# INSTITUTO POTOSINO DE INVESTIGACIÓN CIENTÍFICA Y TECNOLÓGICA, A.C.

## POSGRADO EN GEOCIENCIAS APLICADAS

# Geoquímica, petrogénesis y geocronología del vulcanismo en el Complejo Volcánico Sierra de San Miguelito, Campo Volcánico de San Luis Potosí, México

Tesis que presenta

**Darío Torres Sánchez**

Para obtener el grado de

**Doctor(a) en Geociencias Aplicadas**

**Codirectores de la Tesis:**

**Dr. Sanjeet Kumar Verma**

**Dr. Surendra Pal Verma Jaiswal**

San Luis Potosí, S.L.P., Diciembre 2020

IPICYT

# Constancia de aprobación de la tesis

La tesis "**Geoquímica, petrogénesis y geocronología del vulcanismo en el Complejo Volcánico Sierra de San Miguelito, Campo Volcánico de San Luis Potosí, México**" presentada para obtener el Grado de Doctor(a) en Geociencias Aplicadas fue elaborada por **Darío Torres Sánchez** y aprobada el **quince de diciembre del dos mil veinte** por los suscritos, designados por el Colegio de Profesores de la División de Geociencias Aplicadas del Instituto Potosino de Investigación Científica y Tecnológica, A.C.

**Dr. Sanjeet Kumar Verma**
Codirector de la tesis

**Dr. Surendra Pal Verma Jaiswal**
Codirector de la tesis

**Dr. Fernando Velasco Tapia**
Miembro del Comité Tutoral

**Dr. Aaron Martin**
Miembro del Comité Tutoral

**Dr. José Ramón Torres Hernández**
Miembro del Comité Tutoral


# Créditos Institucionales

Instituto Potosino de Investigación Científica y Tecnológica, A.C., bajo la dirección del Dr. Sanjeet Kumar Verma.

Durante la realización del trabajo el autor recibió una beca académica del Consejo Nacional de Ciencia y Tecnología (No. 336677) y del Instituto Potosino de Investigación Científica y Tecnológica, A. C.

Beca mixta 2018 movilidad en el extranjero del Consejo Nacional de Ciencia y Tecnología (convocatoria no. 291250), se asignó para participar en una estancia de investigación en la Universidad de Leicester, Reino Unido (University of Leicester, UK).

Newton Advence Fellowship, The Royal Society, United Kingdom.

IPICYT

# Instituto Potosino de Investigación Científica y Tecnológica, A.C.

## Acta de Examen de Grado

El Secretario Académico del Instituto Potosino de Investigación Científica y Tecnológica, A.C., certifica que en el Acta 016 del Libro Primero de Actas de Exámenes de Grado del Programa de Doctorado en Geociencias Aplicadas está asentado lo siguiente:

En la ciudad de San Luis Potosí a los 15 días del mes de diciembre del año 2020, se reunió a las 12:00 horas en las instalaciones del Instituto Potosino de Investigación Científica y Tecnológica, A.C., el Jurado integrado por:

| | | |
|---|---|---|
| **Dr. Aaron James Martin _** | **Presidente** | **IPICYT** |
| **Dr. Sanjeet Kumar Verma _** | **Secretario** | **IPICYT** |

a fin de efectuar el examen, que para obtener el Grado de:

DOCTOR EN GEOCIENCIAS APLICADAS

sustentó el C.

**Darío Torres Sánchez**

sobre la Tesis intitulada:

***Geoquímica, petrogénesis y geocronología del vulcanismo en el Complejo Volcánico Sierra de San Miguelito, Campo Volcánico de San Luis Potosí, México***

que se desarrolló bajo la dirección de

**Dr. Sanjeet Kumar Verma _**
**Dr. Surendra Pal Verma Jaiswal (UNAM)**

El Jurado, después de deliberar, determinó

APROBARLO

Dándose por terminado el acto a las 13:45 horas, procediendo a la firma del Acta los integrantes del Jurado. Dando fe el Secretario Académico del Instituto.

A petición del interesado y para los fines que al mismo convengan, se extiende el presente documento en la ciudad de San Luis Potosí, S.L.P., México, a los 15 días del mes de diciembre de 2020.

**Dr. Marcial Bonilla Marín**
Secretario Académico

**Mtra. Ivonne Lizette Cuevas Vélez**
Jefa del Departamento del Posgrado

INSTITUTO POTOSINO DE INVESTIGACIÓN CIENTÍFICA Y TECNOLÓGICA, A.C.
IPICYT
SECRETARÍA ACADÉMICA

# Dedicatoria

A mi prometida Edith Elizondo

A mis padres Darío Torres González y Sonia Laura Sánchez de la Garza

A mi hermana Sonia Alejandra Torres Sánchez

# Agradecimientos

Al Consejo Nacional de Ciencia y Tecnología (CONACYT) por otorgarme una beca de Doctorado en el programa de Doctorado en Geociencias Aplicadas del Instituto Potosino de Investigación de Científica y Tecnologíca (IPICYT).

Al proyecto S-3613 *"Geochemistry and Petrogenesis of the San Luis Potosí Volcanic Field"*, financiado por la Royal Society.

Al Instituto Potosino de Investigación de Científica y Tecnologíca (IPICYT), y a la División de Geociencias Aplicadas por todas las facilidades y apoyos brindados durante la elaboración de este trabajo.

Al departamento de Geología de la Universidad de Leicester, Reino Unido, por la facilidad y apoyo brindado durante los análisis del presente trabajo.

Al Dr. Sanjeet Kumar Verma por su gran apoyo, paciencia, consejos y charlas durante la elaboración de este trabajo de investigación.

Al Dr. Surendra Pal Verma Jaiswal por los grandes consejos, recomendaciones, observaciones como también sus enseñanzas durante todo el período de este trabajo.

Al Dr. Fernando Velasco Tapia por sus consejos y guía durante este proceso, como también por todas las recomendaciones brindadas durante la formación de este trabajo.

A la Dra. Tiffany Barry por su gran apoyo y consejos durante el procesamiento de las muestras y en la interpretación de resultados.

A los Doctores José Ramón Torres Hernández y Aaron James Martin por sus consejos durante la elaboración de este trabajo.

A mis grandes amigos de tanto tiempo: Sahid Abdel, Gerardo Vargas, Jorge Merlo, Adrián Salinas, Jesús Aurelio, Manuel Ligonio, Simón Reyes, por ser grandes amigos y brindarme su amistad por todo este largo tiempo. A las maravillosas personas que conocí durante este trayecto: Pradip, Diego, Salvador, Diego Villanueva y a todos los asesorados y alumnos que los apoye en sus clases y proyectos, muchas gracias a todos.

Al amor de mi vida, Edith Elizondo, quien ha estado conmigo en todo este proceso, el cual no lo hubiese logrado sin tu apoyo incondicional, gracias por siempre estar ahí, por brindarme todo tu apoyo, tu comprensión, tu cariño, durante estos años, gracias por compartir conmigo tantos momentos de felicidad y en ocasiones momentos de dificultad que se han presentado. Edith, gracias por tu amor, y por todo lo que hemos pasado y por todo lo que nos falta por vivir juntos en esta nueva etapa y camino que empezamos y construiremos juntos, te amo mi vida.

# CONTENIDO


Constancia de aprobación de la tesis
Créditos institucionales
Acta de examen
Dedicatorias
Agradecimientos
Lista de tablas V
Lista de figuras VI
Anexos A1
Resumen i
Abstract iii

Introducción 1
1.1 Justificación y objetivos de investigación 5
1.1.1 Justificación 5
1.1.2 Objetivos 5
1.2 Hipótesis 6
1.2.1 Prueba de hipótesis 6
1.3 Esquema de tesis 6
Referencias 8
Capítulo 1 .- Geología Regional–Región sur de la Mesa Central 9
1.1 Estratigrafía de la región sur de la Mesa Central 9
1.2 Geología estructural de la región sur de la Mesa Central 12
1.3 Campo Volcánico San Luis Potosí (CVSLP) 13
1.3a Estratigrafía del CVSLP 13
1.3b Geología estructural del CVSLP 15
Referencias 16
Capítulo 2 .- Trabajo de campo y muestreo 20
2.1 Localización del área de estudio 20

2.2 Geología estructural del CVSSM 21
2.3 Estratigrafía local del CVSSM 22
2.4 Muestreo 28
Referencias 29
Capítulo 3 .- Análisis Petrográfico 31
3.1 Metodología del análisis petrográfico 31
3.2 Características petrográficas de las unidades litológicas del CVSSM 31
Capítulo 4.- Calibración de Fluorescencia de Rayos-X para Elementos Mayores 36
4.1 Presentación del trabajo de investigación publicado 36
Abstract 37
1. Introduction 38
2. Evaluation of Major Element Data for GRMs 38
3. XRF Instrumentation and Intensity Measurements 39
4. Regression Models 39
5. Application of Regression Models for XRF Calibration 41
6. Sensitivities of Major Elements 43
7. Application to Rock Matrices 43
8. Computer Program XRFCalcUnknown 45
9. Conclusions 47
Data Availabillity 47
Conflicts of Interest 47
Acknowledgments 47
References 47
Capítulo 5.- Implicaciones petrogenéticas y tectónicas de rocas volcánicas del Oligoceno-Mioceno del Complejo Volcánico Sierra de San Miguelito, centro de México. 50
5.1 Presentación del trabajo de investigación 50
Abstract 51
1. Introduction 51
2. Geological setting 52
3. Sampling and petrography 54

4. Geochemical analytucal procedures 54
5. Geochemical results 58
6. Discussion 61
7. Conclusions 63
Acknowledgments 64
References 64
Capítulo 6.- Geocronología $^{40}Ar/^{39}Ar$ y petrogenesis del Complejo Volcánico Sierra de San Miguelito, Mesa Central, Mexico (Anexo 3); Manuscrito enviado 66
6.1 Presentación del trabajo de investigación publicado 66
Abstract 68
1. Introduction 68
2. Geological framework 69
3. Materials and methods 71
4. Results 72
5. Discussion 80
6. Conclusions 86
Acknowledfments 86
References 86
Capítulo 7.- Análisis de química mineral 89
7.1 Composiciones minerales 90
7.2 Geotermometría 91
Referencias 93
Capítulo 8 .- Conclusiones 94
8.1 Recomendaciones y futuros trabajos 96

# Anexos


| | |
|---|---|
| Apéndice A.1- Análisis petrográfico | A1 |
| Apéndice A.2- Separación de minerales | A2 |
| Apéndice A.3- Trituración y molienda | A3 |
| Apéndice A.4- Análisis químico de elementos mayores, tierras raras y traza | A4 |
| Apéndice A.5- Análisis de datación Ar/Ar | A5 |
| Apéndice A.6- Análisis isotópicos (Sr-Nd-Pb) | A6 |
| Apéndice A.7- Análisis químico de minerales | A7 |
| Referencias | A9 |

# Lista de Tablas


Tabla 2.1.- Edades de literatura de las unidades litológicas del Complejo Volcánico de la Sierra de San Miguelito. Abreviaciones: SM=San Miguelito; RT=Roca total; FLD=Feldespato; BT=Biotita. 26

Tabla A.1.- Porcentajes modales de las rocas volcánicas del Complejo Volcánico Sierra de San Miguelito. A7

Tabla A.2.-Concetación de elementos mayores, tierras raras y traza de las rocas volcánicas del Complejo Volcánico Sierra de San Miguelito. A8

Tabla A.3.- Composiciones de elementos traza y tierras raras de las rocas volcánicas del Complejo Volcánico Sierra de San Miguelito. Muestras analizadas en el laboratorio ALS Chem, Canadá. A11

Tabla A.4.- Composiciones de elementos mayores, traza y tierras raras de las rocas volcánicas del Complejo Volcánico Sierra de San Miguelito. Muestras analizadas en la Universidad de Leicester, Inglaterra A13

Tabla A.5.- Datos isotópicos de roca total de Sr-Nd de las rocas volcánicas del Complejo Volcánico de la Sierra de San Miguelito A17

Tabla A.6.-Datos isotópicos de roca total de Pb de las rocas volcánicas del Complejo Volcánico de la Sierra de San Miguelito. A18

Tabla A.7.- Datos de edades 40Ar/39Ar age data para las unidades del Complejo Volcánico de la Sierra de San Miguelito A19

Tabla A.8.- Información de química mineral. Abreviaciones B= análisis en borde; C= análisis en el centro. A31

# Lista de Figuras


Figura 1. a) Mapa tectónico regional de la situación actual de la sección oeste de Norteamérica y la provincia del Basin and Range con las subdivisiones de las regiones norte, centro y sur del Basin and Range (Modificado de Cosca et al., 2014); b) Mapa geológico simplificado de la Mesa Central (Modificado de Nieto-Samaniego et al., 2007). 3

Figura 1.1 Mapa geológico de la sección sur de la Mesa Central (Modificado de Nieto-Samaniego et al., 2007). Abreviaciones: SMOc= Sierra Madre Occidental; STFS=Sistema de Fallas San Luis Tepehuanes; TSMFS=Sistema de Fallas Taxco-San Miguel de Allende; EB= Graben El Bajío; S=San Luis Potosí; Z= Zacatecas; A= Aguascalientes. 11

Figura 1.2 Mapa geológico del CVSLP (Tomado y modificado de Tristán-González et al., 2009). Abreviaciones: SLP=San Luis Potosi, VA=Villa de Arista; P=Pinos; GB=Graben Bledos. 1.-Complejo Volcánico Sierra de San Miguelito; 2.- Complejo Volcánico Pinos; 3.- Complejo Volcánico Ahualulco; 4.- Complejo Volcánico la Repartición; 5.- Complejo Volcánico Villa Hidalgo; 6.- Complejo Volcánico Santa María 15

Figura 2.1.- Mapa de ubicación del área de estudio. Abreviaciones: CA= Cabras; CR= Carranco; ES= Escalerillas; SLP= San Luis Potsí; VA= Villa Aldama. 20

Figura 2.2.- Mapa de los sistemas de fallas principales del CVSSM. Abreviaciones: CA= Cabras; CR= Carranco; ES= Escalerillas; SLP= San Luis Potsí; VA= Villa Aldama. 21

Figura 2.3.- Columna litológica simplificada del Complejo Volcánico de la Sierra de San Miguelito. 22

Figura 2.4.- Fotografías de campo representativas de cada unidad litológica del Complejo Volcánico Sierra de San Miguelito. a) Afloramiento masivo de la unidad San Miguelito; b) Afloramiento de bloque masivo de la unidad El Zapote; c) Muestra de mano de la unidad San José, donde se aprecian ; d) Afloramiento de bloque de la unidad Cantera, donde se observan estructuras de fiames; e) Afloramiento de bloque de roca de la unidad Panalillo donde se observan alta cantidad de líticos; f) Afloramiento masivo basáltico de la unidad La Placa; e) Afloramiento de bloques basálticos de la unidad Cabras. 23

Figura 2.5.- Mapa del CVSSM representado las muestras recolectadas en este estudio (estrellas rojas) y muestras compiladas de literatura (círculos azules). 28

Figura 3.1.- Microfotografías en nicoles cruzados (NX) con un aumento de 2.5x de muestras representativas de la unidad máfica Cabras. a) Fenocristales de plagioclasas, olivino y cuarzo con aros de reacción y microcistales de plagioclasa en la matriz; b) Fenocristales de plagioclasas, olivino y cuarzo con aros de reacción y microcistales de plagioclasa y piroxenos en la matriz; c) Fenocristales de plagioclasas con microcristales de plagaioclasa en la matriz. Plg=plagioclasa; Qz= cuarzo; Cpx= clinopiroxeno; Opx= ortopiroxeno; Ol=olivino. 32

Figura 3.2.- Microfotografías en nicoles cruzados (NX) con un aumento de 2.5x de muestras representativas de la unidad intermedia Placa. a) Fenocristales de plagioclasas con texturas de criba y clinopiroxenos y microcistales de plagioclasa en la matriz; b) Fenocristal de cuarzo con aro de reacción inmerso en una matriz vítrea con microcristales de plagioclasas; c) Fenocristales de plagioclasas con texturas de criba y fenocristales de clinopiroxeno inversos en una matriz vítrea con microcristales de plagioclasas; d) Fenocristales de plagioclasa con textura de criba y clinopiroxenos; e) Fenocristales de plagioclasa con textura de criba en una matriz 33

vítrea con microcristales. Plg=plagioclasa; Qz= cuarzo; Cpx= clinopiroxeno; Opx= ortopiroxeno; Ol=olivino.
Figura 3.3.- Microfotografías en nicoles cruzados (NX) con un aumento de 2.5x de muestras representativas de las unidades félsicas. a) Fenocristales de feldespatos alcalinos de la unidad San Miguelito; b) Fenocristales de feldespato potásico y ortopiroxenos con microcristales de cuarzo en la matriz de la unidad San Miguelito; c) Fenocristales de feldespato potásico con microcristales de cuarzo en la matriz de la unidad El Zapote; d) Fenocristales de feldespato potásico, cuarzo y ortopiroxeno de la unidad El Zapote. Qz= cuarzo; FldK= feldespato potásico; Opx= ortopiroxeno. 34
Figura 3.4 Microfotografías en nicoles cruzados (NX) y nicoles paralelo con un aumento de 2.5x de muestras representativas de las unidades ácidas de carácter piroclásitco. a) Fenocristales de clinopiroxeno, ortopiroxeno y feldespatos potásicos de la unidad Cantera; b) Fenocristales de feldespatos potásicos y ortopiroxeno de la unidad Cantera; c) Fenocristales de feldespatos potásicos, ortopiroxeno y clinopiroxeno de la unidad Panalillo; d) Fenocristales de feldespato potásico, ortopiroxeno y clinopiroxeno de la unidad Panalillo. FldK= feldespato potásico; Opx= ortopiroxeno. 35
Figura 7.1 a) Diagrama de clasificación de feldespatos para las rocas del Complejo Volcánico de la Sierra de San Miguelito; b) Diagrama de clasificación de piroxenos para las rocas del Complejo Volcánico de la Sierra de San Miguelito. 90
Figura 7.2 a) Diagrama de Rhodes para ortopiroxenos de las rocas intermedias y básicas del Complejo de la Sierra de San Miguelito; b) Diagrama de Rhodes para clinopiroxenos de las rocas intermedias y básicas del Complejo de la Sierra de San Miguelito. 92
Figura A.1 a) Cortadora con disco de diamante; b) Discos metálicos giratorios para pulido de muestras; c) Vidrios para pulido; d) Láminas delgadas terminadas. A1
Figura A2.- a) Trituradora de quijada ASC. ; b) Cribas de 500, 1000, 2000 µm de espesor; c) Muestra cribada bajo lámpara con luz roja para un secado; d) Triturado y cribado terminado para separado manual. A3
Figura A3.- a) Trituradora de quijada ASC; b) y c) Molino de ágata PLANETARY MONO MILL PULVERISETTE, FRITSCH; d) Polvo de roca terminado A4
Figura A4.- Espectrómetro de masas multi-colector Finnigan MAT 262, NERC Laboratorio Isotópico de Geociencias (NIGL), Keyworth, Inglaterra A7
Figura A5.- Microsonda electrónica Cameca SX100, Open University, Milton Keynes, Inglaterra A8

# Resumen


## Geoquímica, petrogénesis y geocronología del vulcanismo en el Complejo Volcánico Sierra de San Miguelito, Campo Volcánico de San Luis Potosí, México

La presente tesis doctoral describe las características geológicas, petrográficas, geoquímicas y geocronológicas de las rocas volcánicas del Complejo Volcánico Sierra de San Miguelito (CVSSM). El CVSSM se constituye principalmente por rocas volcánicas de composiciones máficas, intermedias y félsicas. Las rocas máficas del presentan texturas porfiríticas con matriz vítrea y un ensamblaje mineral principal compuesto por fenocristales de olivino, clinopiroxeno, ortopiroxeno, y plagioclasas, a su vez, estas rocas se caracterizan por contenidos de 38.12-51.48% de $SiO_2$, 4.59-6.26% MgO y valores de #Mg [#Mg = 100 x ($Mg^{2+}$/$Mg^{2+}$ + $Fe^{2+}$)] que varían entre 41.46 y 55.24. De igual forma, muestran un patrón con enriquecimiento de tierras raras ligeras (REE) y elementos traza menos incompatibles con anomalías negativas de Nb (0.64), Ta, Ba, y P. Las rocas intermedias muestran texturas porfiríticas con matriz vítrea y un ensamblaje mineral principal de fenocristales de clinopiroxeno, ortopiroxeno y plagioclasas. Algo destacable en estas rocas volcánicas, es la interacción entre fenocristales de plagioclasas con texturas de criba junto a plagioclasas con texturas típicas de estos minerales. Muestran contenidos de $SiO_2$ de 57.46-62.24%, MgO de 2.81-5.71% y valores de #Mg [#Mg = 100 x ($Mg^{2+}$/$Mg^{2+}$ + $Fe^{2+}$)] que varían entre 53.04 y 64.13. Presentan un patrón de tierras raras y elementos traza similares a las rocas máficas, con una presencia similar en anomalías de Nb (0.22-0.33), Ta, Ba, y P. Las rocas félsicas contienen texturas porfiríticas en una matriz vítrea con un ensamblaje mineral principal compuesto por fenocristales de cuarzo, feldespato, plagioclasas y ortopiroxenos. Los contenidos de $SiO_2$ y $Al_2O_3$, son de 64.36-82.24%, 10.92-21.26%, respectivamente. Muestran patrones enriquecidos en tierras raras ligeras con una tendencia a la horizontal en tierras raras pesadas, a la vez, es una anomalía negativa pronunciada de Eu, lo cual se asocia a la fraccionación de feldespatos y palgioclasas lo cual coincide con la cantidad de feldespatos y plagioclasas notables

en las rocas félsicas. A su vez, las rocas, muestran anomalías negativas de Nb (0.21-35.38), Ta, Ba y P.

Las características isotópicas de las rocas máficas del CVSSM revelan que se generaron en el manto, lo cual a su vez es demostrable a partir de los valores positivos de $\varepsilon_{Nd(t)}$ (+5.2 - +0.9). Por otro lado, tanto las rocas intermedias, como las rocas félsicas muestran una evolución a partir de componentes corticales, lo cual se asocia a valores negativos de $\varepsilon_{Nd(t)}$ (-2.5 a -1.8).

A partir de las nuevas dataciónes por medio del método de $^{40}Ar/^{39}Ar$ obtenidas para el presente trabajo, junto con la comparación de edades propuestas de trabajos previos, se observó que las rocas del CVSSM se generaron en tres distintos periodos de tiempo. El primer periodo se caracteriza por la formación de lavas félsicas de características efusivas, los cuales dieron lugar a estructuras dómicas. También dentro de este episodio se emplazaron distintos paquetes piroclásticos de distintos espesores, los cuales presentan una composición de igual forma félsica. El segundo periodo se describe como un episodio dominantemente explosivo, en donde, se generaron grandes paquetes piroclásticos de composición félsica junto con la erupción de flujos de lavas aisladas de una composición intermedia. Por último, el tercer periodo se caracteriza por la presencia aislada de flujos de lava masivos de composiciones máficas, principalmente asociados al sistema de fallas.

Los modelos cuantitativos generados en el presente trabajo revelan que las rocas máficas evolucionaron por la fusión parcial de una fuente de manto aproximadamente a los 22–21 Ma, mientras que las rocas intermedias se generaron por fraccionamiento de una fuente máfica la cual presentó distintos niveles de asimilación cortical en un periodo de 32–28Ma. Por último, los modelos revelan que las rocas félsicas se generaron a partir de un proceso de fusión parcial de metasedimentos a niveles de corteza media y superior en un periodo de tiempo que abarca de los 34 a 32Ma.

**Palabras clave:** Geoquímica, Petrogenesis, Rocas volcánicas, Ambiente tectónico, San Luis Potosí, datación $^{40}Ar/^{39}Ar$, Mesa Central, México, isótopos Sr-Nd-Pb.

# Abstract


**Geochemistry, petrogeneis and geochronological of the volcanism from the Sierra de San Miguelito Volcanic Complex, San Luis Potosí Volcanic Field, Mexico**

The present work describes the geological, petrographic, geochemistry and geochronological characteristics from the Sierra de San Miguelito Volcanic Complex (SSMVC) volcanic rocks. The SSMVC mainly of volcanic rocks of mafic, intermediate, and felsic. The mafic rocks display porphyritic textures with vitreous matrix, and a main mineral assemblage of phenocrysts of olivine, clinopyroxene and plagioclases, these rocks are characterized by the contents of 38.12-51.48% $SiO_2$, 4.59-6.26% MgO and #Mg [#Mg = 100 x ($Mg^{2+}$/$Mg^{2+}$ + $Fe^{2+}$)] values that range 41.46 – 55.24. The mafic rocks show light rare earth elements (LREE) and enrichment incompatible trace elements with small negative anomalies of Nb (0.64), Ta, Ba, and P. In the other hand, the intermediate volcanic rocks from SSMVC consist of phenocrysts of clinopyroxene, orthopyroxene and plagioclases with porphyritic textures with a vitreous matrix, these rocks display contents of $SiO_2$ of 57.46-62.24%, MgO of 2.81-5.71% and #Mg [#Mg = 100 x ($Mg^{2+}$/$Mg^{2+}$ + $Fe^{2+}$)] values that range 53.04 to 64.13. Intermediate rocks show LREE and trace elements patterns similar to the mafic volcanic rocks negative anomalies of Nb (0.22-0.33), Ta, Ba, and P. The felsic volcanic rocks of the SSMVC are characterized by porphyritic textures with a vitreous matrix, and a main mineral assemblage of quartz, alkali feldspar, plagioclases and orthopyroxene. The contents of $SiO_2$, $Al_2O_3$, in these rocks are 64.36-82.24%, 10.92-21.26%, respectively. Felsic rocks display an enriched trend in LREE with negative anomalies of Eu, which are probably associated with the fractionation of feldspar. These rocks display negative anomalies of Nb (0.21–35.38), Ta, Ba, and P.

Isotopic characteristics of mafic volcanic rocks from the SSMVC reveals that these rocks were generated in the mantle, which is demonstrable from their positive values of $\varepsilon_{Nd(t)}$ (+5.2 - +0.9). In the other hand, the intermediate rocks and the felsic rocks display involvement of crustal components, as depicted by the negative values of $\varepsilon_{Nd(t)}$ (-2.5 to -1.8).

New $^{40}Ar/^{39}Ar$ ages presented in this work, and in the compilation of previous ages from the area, three main magmatic episodes were defined as follows: (a) the first episode is mainly characterized by the eruption of felsic lavas of effusive characteristics, which formed domes structures and different pyroclastic deposits of felsic composition that were erupted; (b) the second episode is characterized by explosive eruption of pyroclastic deposits of a felsic composition, as well as, lava flows of intermediate composition in isolated area; (c) the third episode is defined by isolated lava flows of mafic compositions, that are located mainly in the edge of fault systems.

Magmatic models generated during the present work reveals that mafic rocks evolved through a partial metling process of the mantle during 22–21 Ma. The intermediate rocks were generated by the fractionation of mafic sources, which presented different levels of crustal assimilation during 32–28 Ma. Finally, the magmatic models display that felsic rocks were generated by partial melting of metasediments at middle-upper continental crust levels during the period of 34 to 32 Ma.

**Keywords:** Geochemistry, Petrogenesis, Volcanic rock, Tecnotic setting, San Luis Potosí, $^{40}Ar/^{39}Ar$ dating, Mesa Central, Mexico, Sr-Nd-Pb isotopes

# INTRODUCCIÓN

La provincia del *Basin and Range* (BR), o también conocida como la provincia de Cuencas y Sierras, ha sido de gran importancia en la comunidad geológica ya que sirve como un claro ejemplo de un sistema montañoso en bloques de escala regional, el cual se ha sido formado por deformación extensional. La BR se extiende desde Canadá pasando por el oeste de los EUA y terminando hacia el noroeste de México (Figura 1a), a su vez, esta provincia se ha descrito como una región montañosa Cenozoica con una configuración actual y una geometría interna derivada de las múltiples fases de deformación extensional conducidos por distintos impulsos geodinámicos (Dickinson, 2002).

La BR es una larga sucesión de estructuras de graben y horst del Cenozoico con una configuración actual y geometría interna derivada de múltiples fases de extensión (Dickinson, 2002). A su vez, las estructuras tanto estructurales como las rocas volcánicas existentes a través de esta provincia, data desde aproximadamente del Oligoceno temprano hasta el Cuaternario (Gans, 1981; Eaton, 1982; Dickinson, 2002).

Se ha propuesto que el inicio de las fases extensivas que dieron lugar a la construcción del BR, y la disminución de la elevación de la superficie se atribuye a la reorganización del límite de placas Pacífico-Norteamerica durante el Cenozoico, y más específicamente al establecimiento del sistema transformante de San Andreas (Cassel et al., 2014; Long, 2019). La disminución en el acoplamiento intraplaca que acompañó a la desaparición de la subducción de la placa Farallón, junto con la conrrespondiente influencia creciente del cizallamiento dextral en el margen de placa, sigue siendo la explicación más aceptada para el control extensional principal del BR (Dickinson, 2002; Long, 2019). La provincia del Basin and Range se ha separado en tres secciones principales como: (i) sección norte; (ii) sección central; (iii) sección sur (Figura 1a; Cosca et al., 2014).

La sección sur del BR se caracteriza principalmente por presentar actividades extensionales syn-transformantes las cuales se han relacionado a la migración rápida de la triple unión de la placa Rivera la cual pasa por Baja California, México hasta su locación actual entre la península de Baja California y el terreno mexicano, como también esta sección presenta una gran cantidad de actividad volcánica a través de la provincia, los cuales tuvieron lugar desde el Paleoceno Tardío, hasta el Mioceno Tardío (House et al., 2001; Spencer et al., 2001; Jones et al., 1992; Dickinson, 2002; Cosca et al., 2014).

Dentro de la sección sur de la BR se encuentra la provincia de la Mesa Central (MC) la cual se localiza en la región centro-norte de México, cubriendo los estados de Chihuahua, Durango, Zacatecas, Aguascalientes, y San Luis Potosí y se ha definido como una meseta elevada la cual provee un registro geológico que abarca desde el Triásico hasta el presente (Nieto-Samaniego et al., 2007, 2019). La MC se encuentra limitada hacia el N y E por la Sierra Madre Oriental, y para el W por la Sierra Madre Occidental (Figura 1b).

La MC se ha divido en dos regiones principales: (i) región norte, la cual se caracteriza principalmente por episodios avanzados de erosión con cuencas aluviales-lacustres, y unidades volcánicas dispersas del Oligoceno al Cuaternario; (ii) región sur, se distingue por presentar un amplio volumen de rocas volcánicas del Paleogeno-Neogeno, cortadas por diversos sistemas de fallas normales (Nieto-Samaniego et al., 1996, 1999, 2007).

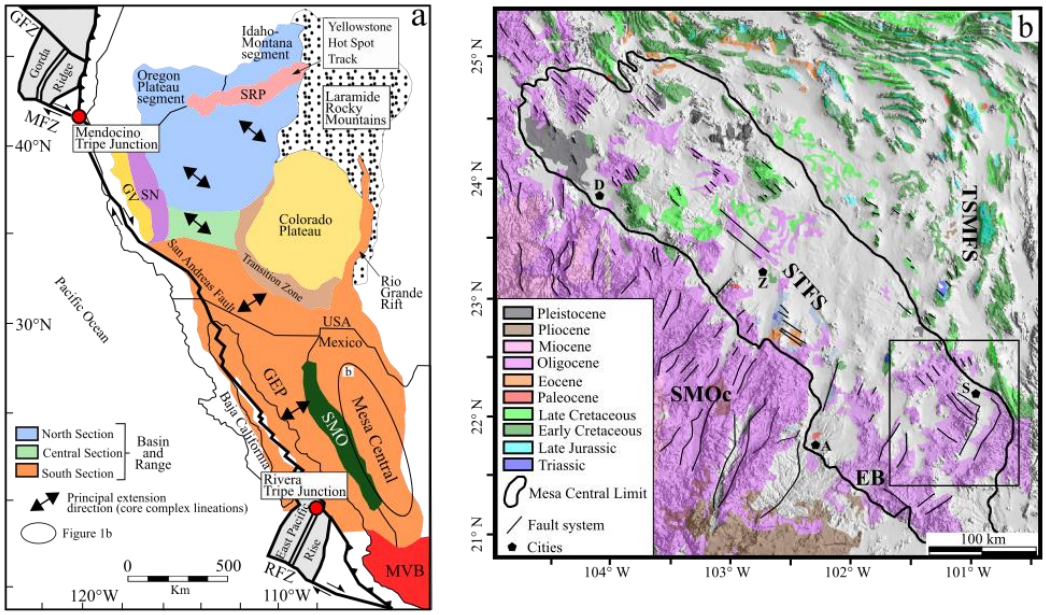


Figura 1. a) Mapa tectónico regional de la situación actual de la sección oeste de Norteamérica y la provincia del Basin and Range con las subdivisiones de las regiones norte, centro y sur del Basin and Range (Modificado de Cosca et al., 2014); b) Mapa geológico simplificado de la Mesa Central. El recuadro negro representa el área de estudio del presente trabajo. (Modificado de Nieto-Samaniego et al., 2007). Abreviaciones: SMOc= Sierra Madre Occidental; STFS= Sistema de Falla San Luis-Tephuanes; TSMFS= Sistema de Fallas Taxco-San Miguel de Allende; EB=Graben El Bajío; S=San Luis Potosí; Z=Zacatecas; A= Aguascalientes; D=Durango

Las estructuras Cenozoicas mayores que conforman a la Mesa Central son:(a) *Falla del Bajío*: la cual presenta dos grupos de fallas con direcciones NW-SE y ENE a NE, ambos grupos proporcionan una forma aserrada al borde norte de El Bajío, en esta zona los desplazamientos mínimos son entre 150 y 250m, en cambio, el segundo segmento presenta una longitud de 80 km aproximadamente y se conforma por una serie de fallas normales de ángulo alto, escalonadas con bloques hundidos al SW;(b) *Sistema de fallas Taxco-San Miguel de Allende:* se constituye por sistemas de falla de dirección N-S. Los principales lineamientos NW-SE que se observan segmentando a este sistema de fallas son los sistemas de fallas San Luis-Tepehuanes y la falla el Bajío; (c) *Sistema de fallas San Luis-Tepehuanes:* de forma general este sistema se caracteriza por una serie de lineamientos de dirección NW-SE en donde su traza coincide burdamente con el límite de los alforamientos de rocas volcánicas cenozoicas pertenecientes a la Sierra Madre Occidental; (d) *Graben de Aguascalientes:* consiste de un graben asimétrico cuya falla principal se ubica hacia el occidente (Nieto-Samaniego et al., 2007).

Dentro de la región sur de la MC se localiza el Campo Volcánico de San Luis Potosí (CVSLP) el cual incluye secuencias volcánicas de composiciones básicas, intermedias y ácidas las cuales hicieron erupción a partir desde el Eoceno hasta el Cuaternario. Los eventos volcánicos del CVSLP tuvieron lugar durante el Oligoceno Tardío y se caracteriza principalmente por riolitas de alto sílice y largos volúmenes de ignimbritas. A su vez, los eventos volcánicos jóvenes en el CVSLP se caracterizan por bajos volúmenes de lavas de composición básica e intermedia (Tristán-González et al., 2009; Aguillón-Robles et al., 2014; Torres-Sánchez et al., 2019). El CVSLP ha sido dividido en seis complejos principales: (i) Complejo Ahualulco; (ii) Complejo Villa Hidalgo; (iii) Complejo La Repartición; (iv) Complejo Pinos; (v) Complejo Santa María; y el (vi) Complejo de la Sierra de San Miguelito (Torres-Hernández et al., 2006; Rodríguez-Ríos et al., 2007; Tristán-González et al., 2009; Aguillón-Robles et al., 2014; López-Loera, 2014; Torres-Sánchez et al., 2019).

Diversos estudios han sido desarrollados dentro del Complejo Volcánico de la Sierra de San Miguelito (p.ej. Tristán-González et al., 2009; Aguillón-Robles et al., 2014; López-Loera, 2014), sin embargo, aún existen distintas ausencias de información, como de modelos complementarios. Dentro de este apartado se muestra una sobrevista sobre las metas y objetivos que se proponen en el presente estudio.

## 1.1 Justificación y objetivos de investigación

### *1.1.1 Justificación*

Diversa información ha sido generada para el Complejo Volcánico de la Sierra de San Miguelito (CVSSM), desde cartografía geológica, geología estructural, petrografía, geoquímica de roca total y datación por el método de K/Ar en roca total. Sin embargo, para una propuesta de un modelo petrogenético se requiere: a) contar con un muestreo representativo, tanto de litología como espacialmente del complejo volcánico; b) establecer una composición modal de las diferentes rocas, como sus características texturales y la composición química tanto de la matriz de la roca como de sus minerales; c) contar con una base de datos completa de geoquímica (elementos mayores y traza), relaciones isotópicas (Sr-Nd-Pb) para cada muestra; d) generar información geocronológica para rocas de las distintas litologías de la zona y elaborar un contraste con las edades propuestas; f) deducir el ambiente tectónico asociado al vulcanismo de la región a través de diagramas de discriminación tectónica convencionales, y de diagramas basados en estadística multivariada.

### *1.1.2 Objetivos*

El objetivo principal de este estudio es el proponer un modelo petrogenético cuantitativo para las rocas volcánicas del Complejo Volcánico Sierra de San Miguelito.

Las metas que se alcanzaron para este trabajo son:

- Descripción de la distribución espacial de las diferentes litologías y su relación con los elementos estructurales de la región.
- Caracterización de los distintos tipos de rocas desde una perspectiva petrográfica, geoquímica e isotópica.
- Evaluación cuantitativa de procesos magmáticos que generaron al vulcanismo en el CVSSM.
- Elaboración de un esquema geocronológico de los eventos magmáticos que forman parte del CVSSM.
- Propuesta de un ambiente tectónico para el vulcanismo del CVSSM.

## 1.2 Hipótesis

Las hipótesis de investigación del presente proyecto son las siguientes:

1. El vulcanismo máfico del Complejo Volcánico de la Sierra de San Miguelito es relacionado a un proceso de fusión parcial del manto.
2. El origen del vulcanismo intermedio del Complejo Volcánico de la Sierra de San Miguelito es relacionado a un proceso de asimilación–cristalización fraccionada con una mezcla de magmas entre rocas félsicas y máficas.
3. El vulcanismo félsico del Complejo Volcánico de la Sierra de San Miguelito se relaciona a un proceso de fusión parcial de distintos niveles de la corteza continental.
4. La actividad magmática tuvo lugar durante el Eoceno Tardío–Mioceno Temprano durante un evento tectónico extensional.

### *1.2.1 Prueba de hipótesis*

Para poder comprobar las hipótesis planteadas anteriormente se ha propuesto las siguientes pruebas:

1. Análisis geoquímico de elementos mayores, traza y tierras raras ayudarán para el entendimiento del ambiente tectónico del vulcanismo.
2. Las nuevas edades Ar/Ar, aportarán al análisis geocronológico para la precisión de las edades de formación.
3. Análisis isotópico se lleva a cabo para el entendimiento de la evolución geodinámica y petrogenesis del Complejo Volcánico de la Sierra de San Miguelito.

## 1.3 Esquema de tesis

El presente trabajo se basa en tres artículos publicados, uno en participación como co-autor y dos publicados como primer autor.

El capítulo **uno** del presente estudio describe las características geológicas de las provincias geológicas de la Mesa Central, así como, del Campo Volcánico de San Luis Potosí. El capítulo **dos** muestra la descripción geológica y el muestreo del área de estudio. El capítulo **tres** presenta los resultados del análisis petrográfico de las rocas

estudiadas en el presente trabajo. El **cuarto** capítulo presenta un artículo publicado en "*Journal of Spectrometry"* donde el autor de este trabajo participó como co-autor. En este artículo se describe la importancia de la aplicación de modelos de regresión lineal ponderada para la calibración de máquinas de fluorescencia de rayos-X a partir de 59 materiales de referencia.

El capítulo **cinco** presenta el primer artículo publicado en la revista "*Journal of South American Earth Sciences*", el cual se enfoca en las características petrográficas y geoquímicas de las rocas máficas y félsicas del Complejo Volcánico de la Sierra de San Miguelito, y se presentan los primeros modelos petrogenéticos que ayuden a explicar un posible origen de las rocas máficas y félsicas del CVSSM. El capítulo **seis** presenta el segundo artículo publicado en la revista *"Lithos",* el cual se enfoca tanto en las conexiones petrogenéticas, como en el contraste de edades entre las rocas básicas, intermedias y ácidas del CVSSM y sus implicaciones en la actividad volcánica Cenozoica de la Mesa Central. El capítulo **siete** presenta las características de química mineral de las distintas unidades del CVSSM, y se propone las temperaturas en las cuales se generaron las distintas rocas volcánicas del CVSSM. El último capítulo (capítulo **ocho**) provee un resumen de los hallazgos principales y sugiere como la investigación puede ser complementada y/o extendida en el área de estudio del presente trabajo.

## Referencias


Aguillón-Robles A., Tristán-González M., Aguirre-Díaz G.J., López-Doncel R.A., Bellon H., Martínez-Esparza G., 2014. Eocene to Quaternary mafic-intermediate volcanism in San Luis Potosí, central Mexico: The transition from Farallon plate subduction to intra-plate continental magmatism. Journal of Volcanology and Geothermal Research 276, 152–172.

Cassel E.J., Breecker D.O., Henry C.D., Larson T.E., Stockli D.F., 2014. Profile of a paleo-orgen: High topography across the present-day Basin and Range from 40 to 23 Ma. Geology 42, 1007-1010.

Cosca, M.A., Thompson, R.A., Lee, J.P., Turner, K.J., Neymark, L.A., Premo, W.R., 2014. $^{40}Ar/^{39}Ar$ geochronology, isotope geochemistry (Sr, Nd, Pb), and petrology of alkaline lavas near Yampa, Colorado: migration of alkaline volcanism and evolution of the northern Rio Grande rift. Geoshpere, 10, 374–400.

Dickinson W.R., 2002. The Basin and Range Province as a composite extensional domain. International Geology Review, 44, 1–38.

Dilek Y., Moores E.M., 1999. A Tibetan model for the early Tertiary western United States. Geological Society of London Journal, 156, 929–941.

Eaton, G. P., 1982. The Basin and Range Province: Origin and Tectonic Significance. Annual Review of Earth and Planetary Science, 10, 409-40.

Gans, P.B., 1981. Geometry of pre-basin and range extension east-central Nevada. EOS 62, 399p.

House M. A., Wernicke B.P., Farley K.A., 2001. Paleogeomorphology of the Sierra Nevada, California, from (U-Th)/He ages in apatite. American Journal of Science, 301, 77–102.

Jones, C.H., Wernicke, B.P., Farmer, G.L., Walker, J.D., Coleman, D.S., McKenna, L.W., Perry, F.V., 1992. Variations across and along a major continental rift: an interdisciplinary study of the Basin and Range province, western USA. Tectonophysics, 213, 57–96.

Long S.P., 2019. Geometry and magnitude of extension in the Basin and Range Province (39°N), Utah, Nevada and California, USA: Constraints from a province-scale cross section. Geological Society of America Bulletin 131, 99-119.

López-Loera, H., 2014. Geofísica para la localización de Agua Subterránea en Ambientes Volcánicos Áridos de la Mesa Central: Caso La Dulcita, Villa de Ramos, San Luis Potosí, México. Boletín de la Sociedad Geológica Mexicana 66, 165–181.

Nieto-Samaniego A.F., Alaniz-Álvarez S.A., Camprubí A., 2007. Mesa Central of México: Stratigraphy, structure, and Cenozoic tectonic evolution. In: Alaniz-Álavarez, S.A., Nieto-Samaniego, Á.F. (eds.), Geology of México: Celebrating the Centenary of the

Geological Society of México. Geological Society of America Special Paper 422, 41–70.

Nieto-Samaniego A.F., Macías-Romo C., Alaniz-Alvarez S.A., 1996. Nuevas edades isotópicas de la cubierta volcánica cenozoica de la parte meridional de la Mesa Central, México. Revista Mexicana de Ciencias Geológicas 13, 117–122. 8

Nieto-Samaniego A.F., Olmos-Moya M.J.P., Levresse G., Alaniz-Alvarez S.A., Abdullin F., Pilar-Martínez A., Xu S, 2019. Thermochronology and exhumation rates of granitic intrusions at Mesa Central, Mexico. International Geology Review, 1-9.

Nieto–Samaniego, A.F., Ferrari, L., Alaniz–Alvarez, S.A., Labarthe–Hernández, G., Rosas–Elguera, J., 1999. Variation of Cenozoic extention and volcanism across the southern Sierra Madre Occidental volcanic province, Mexico. Geological Society of America Bulletin, 111, 347–363.

Rodríguez-Ríos, R., Aguillón-Robles, A., Leroy, J.L., 2007. Evolución petrológica y geoquímica de un complejo de domos topacíferos en el Campo Volcánico de San Luis Potosí (México). Revista Mexicana de Ciencias Geológicas 24, 328–343.

Spencer J.E., Richard S.M., Ferguson C.F., 2001. Cenozoic structure and evolution of the boundary between the Basin and Range and Transition Zone provinces in Arizona, in Erskine M.C., Faulds J.E., Bartley J.M., Rowley P.D., eds, The geologic transition, High Plateaus to Great Basin–a sumposium and field guide. Utah Geological Association Publication, 30, 273–289.

Torres-Hernández, J.R., Labarthe-Hernández, G., Aguillón-Robles, A., Gómez-Anguiano, M., Mata-Segura, J.L., 2006. The pyroclastic dikes of the Tertiary San Luis Potosi volcanic field: Implications on the emplacement of Panalillo ignimbrite. Geofísica Internacional 45, 243–253.

Torres–Sánchez, D., Verma, S.K., Verma, S.P., Velasco–Tapia, F., Torres–Hernández, J.R., 2019. Petrogenetic and tectonic implications of Oligocene–Miocene volcanic rocks from the Sierra de San Miguelito complex, central Mexico. Journal of South American Earth Sciences, 95, 102311.

Tristán-González M., Aguillón-Robles A., Barboza-Gudiño J.R., Torres-Hernández J.R., Bellon H., López-Doncel R., Rodríguez-Ríos R., Labarthe-Hernández G., 2009. Geocronología y distribución espacial del vulcanismo en el Campo Volcánico de San Luis Potosí. Boletín de la Sociedad Geológica Mexicana 61, 287–303.

# CAPITULO 1.-

## GEOLOGÍA REGIONAL–REGIÓN SUR DE LA MESA CENTRAL

En el presente capítulo se presenta una descripción de rasgos geológicos destacables de la región sur de la Mesa Central, y se describen las características geológicas del Campo Volcánico de San Luis Potosí. Las siguientes descripciones aportan nueva información acerca de la estratigrafía, geología estructural, así como de la actividad volcánica de la zona de estudio.

### 1.1 Estratigrafía de la región sur de la Mesa Central

La región sur de la Mesa Central presenta un registro geológico amplio el cual abarca un período de tiempo desde el Mesozoico hasta la época presente (Figura 1.1). Las rocas Mesozoicas en esta región son representadas por dos principales litologías: (i) rocas marinas calcáreas de la secuencia de la Sierra Madre Oriental; (ii) y secuencias del complejo volcano-sedimentario de la Sierra de Guanajuato (Eguiluz de Antaño et al., 2000; Orozco-Esquivel et al., 2002).

Por otro lado, la evidencia magmática para el Cretácico Tardío–Paleoceno (Figura 1.1) es escasa, principalmente representada por cuerpos intrusivos que se acomodan a lo largo de las principales estructuras tectónicas de la MC, y por cuerpos intrusivos graníticos en la Sierra de Guanajuato para el Paleoceno. Para el Eoceno, el vulcanismo corresponde a cuerpos aislados de lavas andesíticas, depósitos piroclásticos y cuerpos riolíticos reportados en el área de San Luis Potosí y Guanajuato (Martínez-Reyes, 1992; Orozco-Esquivel et al., 2002; Nieto-Samaniego et al., 2019).

En cambio, para el Oligoceno se ha reportado un evento volcánico voluminoso el cual formó una cubierta volcánica gruesa de lavas de composición andesitica a riolítica, cuales reposan sobre unidades Mesozoicas (Figura 1.1; Orozco-Esquivel et al., 2002). Orozco-Esquivel et al (2002) agruparon a esta cobertura volcánica del Oligoceno en dos secuencias: (a) *secuencia inferior*, la cual incluye rocas emplazadas antes de la formación del Graben de Villa de Reyes, las cuales presentan una variación composicional de andesitas a riolitas, y en porcentaje bajo, distintos depósitos piroclásticos de composición

riolítica; y, (b) *secuencia superior*, en donde la mayoría de las rocas fueron formadas durante una fase volcánica muy bien definida, la cual inició con el emplazamiento de grandes volúmenes de lavas riolíticas, seguido por un evento ignimbritico voluminoso de composición igualmente riolítica. Una segunda fase volcánica tomo lugar, la cual produjo de igual forma lavas riolíticas y paquetes ignimbritcos, solo que estos a menor escala que la fase anterior.

Para el Mioceno (Figura 2.1), se ha reportado rocas volcánicas de composición basáltica y andesítica intercaladas con los sedimentos que rellenan cuencas continentales cenozoicas, y afloramientos de rocas volcánicas de la misma composición en numerosas localidades aisladas (McDowell y Keizer, 1977; Luhr et al., 1995; Henry y Aranda-Gómez, 2000; Rodríguez-Ríos et al., 2007; Aguillón-Robles et al., 2009).

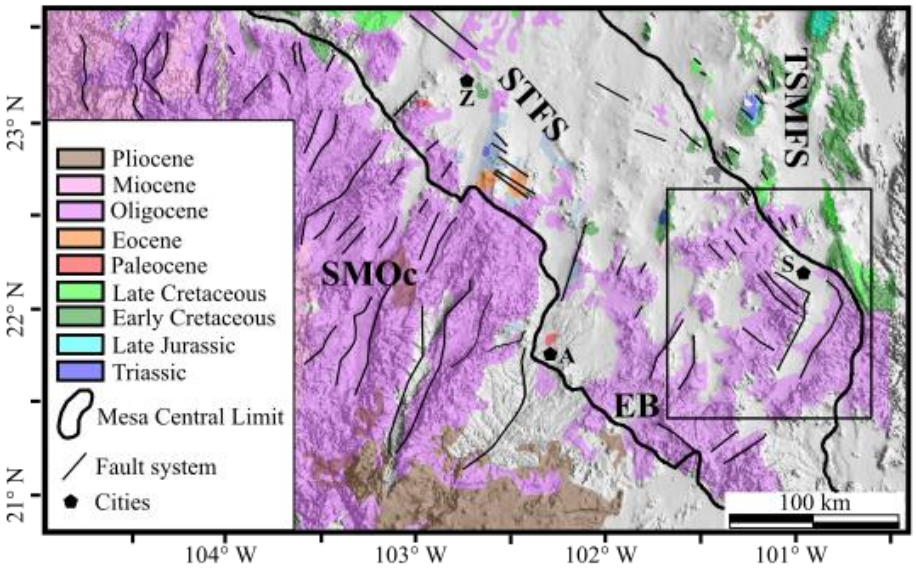


Figura 1.1 Mapa geológico de la sección sur de la Mesa Central (Modificado de Nieto-Samaniego et al., 2007). Abreviaciones: SMOc= Sierra Madre Occidental; STFS=Sistema de Fallas San Luis Tepehuanes; TSMFS=Sistema de Fallas Taxco-San Miguel de Allende; EB= Graben El Bajío; S=San Luis Potosí; Z= Zacatecas; A= Aguascalientes.

Por último, para el Plioceno y Cuaternario (Figura 1.1) se han reconocido rocas volcánicas que afloran principalmente en pequeños conjuntos de aparatos volcánicos como conos cineríticos, flujos de lava y “maares”. Estos cuerpos volcánicos abarcan una composición basáltica alcalina, y corresponden a lavas alcalinas con xenolitos de lerzolita provenientes del manto y de granulita procedentes de la base de la corteza (Labarthe-Hernández et al., 1982; Swanson, 1989; Pier et al., 1989; Schaaf et al., 1994; Aranda-Gómez et al., 2003; Saucedo et al., 2017)

### 1.2 Geología estructural de la región sur de la Mesa Central

La región sur de la Mesa Central se encuentra afectada por distintos sistemas de fallas, entre los cuales se encuentran el sistema de fallas San Luis–Tepehuanes (SFST), la falla El Bajío (FB) y el graben de Aguascalientes (GA; Nieto-Samaniego et al., 2007).

El SFST se caracteriza por un conjunto de lineamientos de dirección NW-SE (Figura 1.1). La porción oriental del SFST se conforma por diversas estructuras de fallas normales con dirección de rumbo NW-SE y buzamiento SW, que conforman diversos sistemas de horst, grabens, y semi-grabens, los cuales presentaron actividad durante el Oligoceno hasta el Mioceno (Labarthe-Hernández y Jiménez-López, 1992; Silva-Romo, 1996; Xu et al., 2004; Nieto-Samaniego et al., 2007). Por otro lado, la porción occidental del SFST se conforma por estructuras de fallas normales con direcciones NW-SE, y en menor número, fallas con rumbos E-W y NE-SW, la actividad principal de estos sistemas de fallas ocurrieron entre el Eoceno y el Oligoceno (Albinson, 1988; Arada-Gómez et al., 2003; Loza-Aguirre, 2005; Nieto-Samaniego et al., 2007).

La FB se caracteriza por mostrar dos segmentos mayores que se extienden desde Celaya hasta Guanajuato (Figura 1.1). El primer segmento de esta estructura se caracteriza por dos grupos de fallas con direcciones NW-SE y ENE, los cuales brindan a este sector una forma aserrada al borde norte de El Bajío (Trujillo-Candelaria, 1985; Nieto-Samaniego et al., 2005). En cambio, el segundo segmento muestra una extensión ~ de 80km de largo y es representada por una serie de fallas normales de ángulo alto, escalonadas y con bloque hundidos al SW (Quintero-Legorreta, 1992; Nieto-Samaniego et al., 2005).

El GA limita al occidente la región sur de la Mesa Central separándola de la Sierra Madre Occidental. Esta estructura consiste de un graben asimétrico cuya falla principal se ubica al occidente y se extiende aproximadamente por 150 km con dirección N–S (Figura 1.2; Jiménez-Nava, 1993; Nieto-Samaniego et al., 2007).

## 1.3 Campo Volcánico San Luis Potosí (CVSLP)

### *1.3a Estratigrafía del CVSLP*

El Campo Volcánico de San Luis Potosí (CVSLP, Figura 1.2) se localiza en la porción sureste de la región sur de la Mesa Central, se definió por primera vez por Labarthe-Hernández et al. (1982) como un campo volcánico conformado por lavas e ignimbritas del Terciario. Actualmente se conoce al CVSLP como un campo volcánico que cubre un área cercana a los 10, 000 $km^2$, y se encuentra formado principalmente por secuencias de lavas y flujos piroclásticos que abarcan una edad desde el Eoceno medio hasta el Cuaternario, y un rango composicional que va desde rocas básicas hasta rocas ácidas (Tristán-González et al., 2009).

Se ha establecido que el CVSLP presentó cinco etapas principales de vulcanismo, donde la primera predominó la emisión de lavas andesiticas durante el Eoceno Medio; la segunda etapa abarcó el Oligoceno Temprano y se compone principalmente por lavas de composición ácida (dacitas y riolítas). La tercera y cuarta etapa se conforman por un vulcanismo félsico y máfico el cual ocurrió durante el Oligoceno Tardío-Mioceno Inferior. La quinta y última etapa se caracteriza por un vulcanismo intraplaca de composición basanítica, la cual abarca principalmente el Cuaternario (Tristán-González et al., 2009; Aguillón-Robles et al., 2012).

En base a la semejanza estratigráfica, geoquímica y geocronológica Tristán-González et al. (2009) dividieron al CVSLP en diversos complejos volcánicos (Figura 2.3), los cuales se han denominado como:

a) ***Ahualulco***: se caracteriza por presentar diversas estructuras volcánicas de composición andesitica, domos riolíticos del Eoceno Medio-Oligoceno Temprano, y flujos piroclásticos asociados a estos. Dentro de este complejo

volcánico también se pueden apreciar derrames de lavas basaníticas del Cuaternario.

b) ***Pinos***: el cual se conforma por derrames de lavas y domos poligenéticos del Oligoceno temprano de un rango composicional principalmente dacítica y riolítica, y derrames pirclásticos asociados a estos.

c) ***Villa Hidalgo***: se caracteriza por mostrar domos y derrames de lava de composición dacítica-andesitica y flujos piroclásticos asociados a estos emplazados durante el Oligoceno. A su vez, dentro de este campo se observan lavas máficas del Cuaternario, las cuales contienen xenolitos tanto de manto como de corteza.

d) ***La Repartición***: se comprende por depósitos de flujos piroclásicos, un conjunto de lavas dacíticas, andesiticas y basálticas. También se presentan diques tuficíticos y acumulaciones de material piroclástico y epiclástico.

e) ***Sierra de San Miguelito***: está formado principalmente por domos de composición riolítica intercalados con un paquete grueso de depósitos piroclásticos del Oligoceno; también, se presenta vulcanismo puntual de composición básica. Algo característico en este complejo es que las secuencias se encuentran afectadas por una gran cantidad de fallas normales de ángulo alto, las cuales se acomodaron en patrón de dominó, formando así semi-fosas tectónicas estrechas.

f) ***Santa María***: se caracteriza por presentar cadenas de domos de composición traquítica hasta riolítica, junto con depósitos piroclásticos asociados a estos. El gran paquete volcánico de este complejo fue afectado por una serie de fallas normales NW-SE. Durante el último evento efusivo de este complejo se inyectaron puntualmente coladas de lavas basálticas a lo largo de fallas normales, principalmente sobre la zona de fallas marginales al SE del Graben de Villa de Reyes.

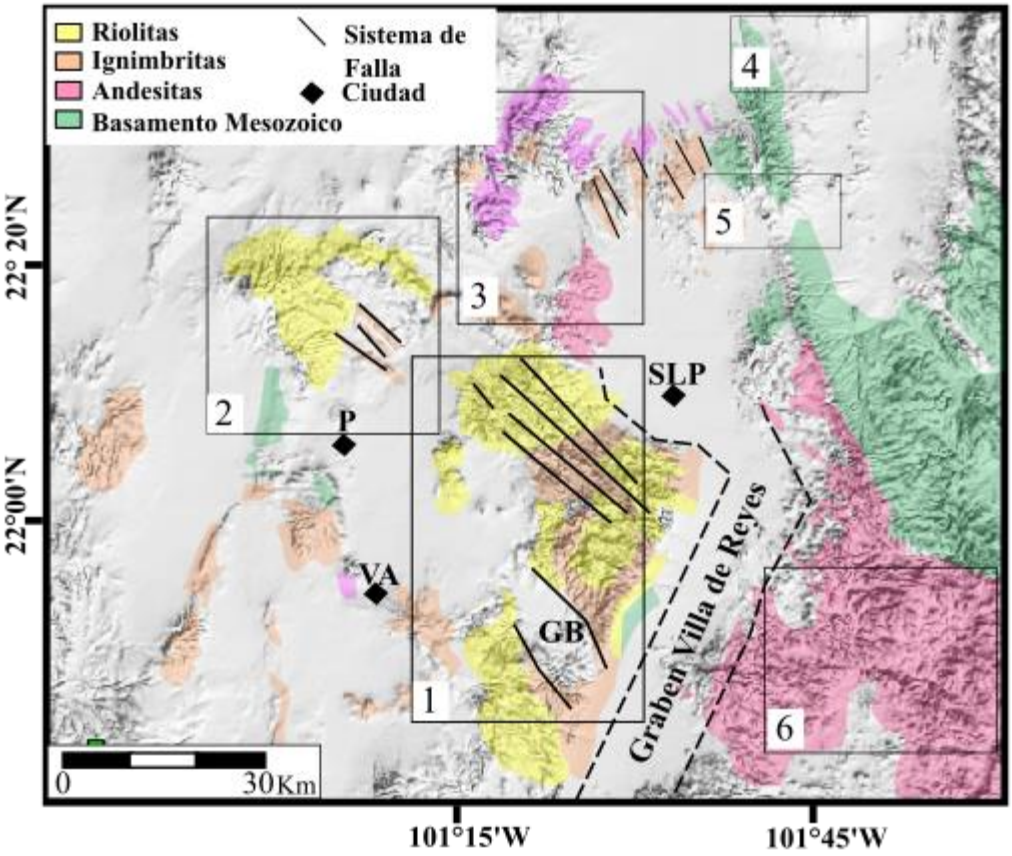


Figura 1.2 Mapa geológico del CVSLP (Tomado y modificado de Tristán-González et al., 2009). Abreviaciones: SLP=San Luis Potosi, VA=Villa de Arista; P=Pinos; GB=Graben Bledos. 1.-Complejo Volcánico Sierra de San Miguelito; 2.- Complejo Volcánico Pinos; 3.- Complejo Volcánico Ahualulco; 4.- Complejo Volcánico la Repartición; 5.- Complejo Volcánico Villa Hidalgo; 6.- Complejo Volcánico Santa María

### *1.3b Geología estructural del CVSLP*

Con respecto a la geología estructural del CVSLP se han caracterizado dos regiones estructurales distintas: (i) el Graben de Villa de Reyes (GVR) localizado entre el Complejo Volcánico de la Sierra de San Miguelito y el Complejo Volcánico Santa María; y (ii) el Graben de Bledos (GB) el cual se localiza hacia el sur del Complejo Volcánico de la Sierra de San Miguelito (Figura 1.2).

El GVR se ha definido como una fosa tectónica de edad Oligocénica, la cual se encuentra rellena por depósitos volcánicos y clásticos de edades que abarcan desde el Oligoceno temprano hasta la época actual (Figura 1.2). Esta estructura presenta una longitud de ~ 200 km y un ancho variable de 10-20 km, y este se limitada por un sistema de fallas de

dirección NE. El fondo de la fosa se conforma por domos exógenos del Oligoceno y en algunos sitios llegan a aflorar como pequeñas cumbres, como se observa en las inmediaciones del poblado de Villa de Reyes (Labarthe-Hernández et al., 1982; Tristán-González, 1986; López-Loera et al., 2013). A su vez, el GVR forma parte de una serie de estructuras tectónicas presentes en la región sur de la Mesa Central las cuales corresponden a la etapa de máxima extensión, y esta estructura se encuentra cruzado por un sistema de fallas de orientación NW-SW las cuales se arreglan en un patrón en dominó (Labarthe-Hernández et al., 1982; Tristán-González, 1986; Nieto-Samaniego et al., 1997; Labarthe-Hernández y De la Huerta-Cobos, 1998; Aranda-Gómez et al., 2000; Torres-Aguilera, 2005; Rodríguez-Ríos, 2009; López-Loera et al., 2013).

Por otra parte, el GB consiste en un valle de ~ 18 km de largo y ~8 km de ancho. Esta estructura se ha considerado como un semi-fosa con dos fallas notables en su margen NE, con rumbos NW y buzamientos al SW. Por otra parte, la edad de las fallas se ha definido entre los 29 Ma y 27 Ma (Labarthe-Hernández y Jiménez-López, 1992). A su vez, esta semi-fosa se encuentra rellenada por depósitos volcánicos de composiciones riolíticas y basálticas como de depósitos conglomeráticos y aluviales (Labarthe-Hernández y De La Huera-Cobos, 1998).

## Referencias


Aguillón-Robles, A., Tristán-González, M., Aguirre-Díaz, G.J., Bellon, H., 2009. Syn-extensional intra-plate trachydacite-rhyolitic dome volcanism of the Mesa Central, southern Sierra Madre Occidental volcanic province, Mexico. Journal of Volcanology and Geothermal Research, 187, 33-52.

Aguillón-Robles, A., Tristán-González, M., López-Doncel, R.A., García-Arreola, M.A., 2012. Trace elements geochemistry and origin of volcanic units from the San Luis Potosí and Río Santa María volcanic fields, Mexico: the bearing of IPC-QMS data. Geofísica Internacional, 51, 293-308.

Albinson, T., 1988. Geologic reconstruction of paleosurfaces in the Sombrerete Colorada, and Fresnillo district, Zacatecas state, Mexico. Economic Geology and the Bulletin of the Society of Econocimic Geologists, 83, 1647-1667.

Aranda-Gómez, J.J., Henry, C.D., Luhr, J., 2000. Evolución tectonomagmática post-paleocénica de la Sierra Madre Occidental y de la porción meridional de la provincia tectónica de Cuencas y Sierras, Mexico. Boletín de la Sociedad Geológica Mexicana, 53, 59-71.

Aranda-Gómez, J.J., Henry, C.D., Luhr, J., McDowell, F.W., 2003. Cenozoic volcanic-tectonic development of northwestern Mexico-A transext across the Sierra Madre Occidental volcanic field and observations on extensión-related magmatism in the southern Basin and Range and Gulf of California tectonic provinces, in Geologic transects across Cordilleran Mexico, D.F., March 25-30, 2003: Universidad Nacional Autónoma de México, Instituto de Geología, Centro de Geociencias, Special publication 1, 71-121.

Eguiluz de Antuaño S., Aranda-García, M., Marret, R., 2000. Tectónica de la Sierra Madre Oriental, México. Boletín de la Sociedad Geológica Mexicana, 53, 1.26.

Henry, C.D., Aranda-Gómez, J.J., 2000. Plate interactions control middle-late Miocene, proto-Gulf and Basin and Range extensión in the southern Basin and Range. Tectonophysics, 318, 1-26.

Jiménez-Nava, F.J., 1993. Aportes a la estratigrafía de Aguascalientes mediante la exploración geohidrológica a profundidad, in Simposio sobre la geología del Centro de México, resúmenes y guía de excursión. Universidad de Guanajuato, Facultad de Minas, Metalurgia y Geología, Extensión Minera, abstracts book 1, 93.

Labarthe-Hernández, G., Tristán-González, M., Aranda-Gómez, J.J., 1982. Revisión estratigráfica del Cenozoico de la parte central del Estado de San Luis Potosí. Folleto Técnico (Open File Report) 85. Universidad Autónoma de San Luis Potosí, Instituto de Geología y Metalurgia.

Labarthe-Hernández, G., Jiménez-López, L.S., 1992. Características físicas y estructrua de lavas e ignimbrita riolíticas en la Sierra de San Miguelito, S.L.P. Instituto de Geología. Universidad Autónoma de San Luis Potosí, Folleto Técnico 144.

López-Loera, H., Tristán-González, M., 2013. Geología y magnetometría aérea del Graben de Villa de Reyes, San Luis Potosí, Mesa Central de México: implicaciones tectónicas y geohidrológicas. Boletín de la Sociedad Geológica Mexicana, 65, 137-156.

Loza-Aguirre, I., 2005. Estudio estructural de la actividad cenozoica del sistema de fallas San Luis-Tepehuanes de la región Zacatecas-San José de Gracia Instituto Tecnológico de Ciudad Madero (Tesis licenciatura).

Luhr, J.F., Pier, J.G., Aranda-Gómez, J.J., Podosek, F., 1995. Crustal contamination in early Basin and Range hawaiites of the Los Encinos volcanic field, central Mexico. Contributions of Mineralogy and Petrology, 118, 321-339.

Martínez-Reyes, J., 1992. Mapa geológico de la Sierra de Guanajuato con resumen de la geología de la Sierra de Guanajuato. Universidad Nacional Autónoma de México, Instituto de Geología, Cartas Geológicas y Mineras, 8.

McDowell, F.W., Keiser, 1977. Timing of mid-Tertiary volcanism in the Sierra Madre Occidental between Durango City and Mazatlan, Mexico. Geological Society of America Bulletin, 88, 1479-1486.

Nieto-Samaniego, A.F., Alaniz-Álvarez, S.A., Labarthe-Hernández, G., 1997. La deformación cenozoica paoslaramídica en la parte meridional de la Mesa Central, Mexico. Revista Mexicana de Ciencias Geológicas, 14, 13-25.

Nieto-Samaniego, Á. F., Alaniz-Álvarez, S. A., Camprubí í Cano, A., 2005. La Mesa Central de México: estratigrafía, estructura y evolución tectónica cenozoica. Boletín de la Sociedad Geológica mexicana, 57, 285-318.

Nieto-Samaniego, A.F., Alaniz-Álvarez, S., Camprubí, A., 2007. Mesa Central of México: Stratigraphy, structure, and Cenozoic tectonic evolution. Geological Society of America, Special Paper, 422, 41-70.

Nieto-Samaniego, A.F., Olmos-Moya M.J., Levresse, G., Alaniz-Alvarez S.A., Abdullin, F., Pilar-Martínez, A., Xu, S., 2020. Thermochronology and exhumation rates of granitic intrusions at Mesa Central, Mexico. International Geology Review, 62, 311-319.

Orozco-Esquivel, M.T., Nieto-Samaniego, A.F., Alaniz-Álvarez, S.A., 2002. Origin of rhyolitic lavas in the Mesa Central, Mexico, by crustal melting related to extension. Journal of Volcanology and Geothermal Research, 118, 37-56.

Pier J.G., Podosek, F.A., Luhr, F., Brannon, J.C., 1989. Spinel-lherzollite-bearing Quaternary volcanic centers in San Luis Potosí, Mexico 2. Sr and Nd Isotopic systematics. Journal of Geophysical Research, 94, 7941-7951.

Quintero-Legorreta, O., 1992. Geología de la región de Comanja, estados de Guanajuato y Jallisco. Universidad Nacional Autónoma de Mexico, Revista del Instituto de Geología, 10, 6-25.

Rodríguez-Ríos, R., Aguillón-Robles, A., Leroy, J.L., 2007. Evolución petrológica y geoquímica de un complejo de domos topacíferos en el Campo Volcánico de San Luis Potosí (Mexico). Revista Mexicana de Ciencias Geológicas, 24, 328-343.

Rodríguez-Ríos, R., Torres-Aguilera, J.M., 2009. Petrología y Geoquímica de un Vulcanismo Bimodal Oligocénico en el Campo Volcánico de San Luis Potosí. Revista Mexicana en Ciencias Geológicas, 26, 658-673.

Saucedo, R., Macías, J. L., Ocampo-Díaz, Y. Z. E., Gómez-Villa, W., Rivera-Olguín, E., Castro-Govea, R., Sánchez-Nuñez, J.M., Layer, P.W., Torres-Hernández, J.R., Carrasco-Núñez, G., 2017. Mixed magmatic–phreatomagmatic explosions during the formation of the Joya Honda maar, San Luis Potosí, Mexico. Geological Society, London, Special Publications, 446, 255-279.

Schaaf, P., Heinrich, W., Besch, T., 1994. Composition and Sm-Nd isotopic data of the lower crust beneath San Luis Potosí, central Mexico: evidence from a granulite-facies xenolith suite. Chemical Geology, 118, 63-84.

Silva-Romo, G. 1996. Estudio de la estratigrafía y estructuras tectónicas de la Sierra de Salinas, Estados de San Luis Potosí y Zacatecas. Universidad Nacional Autónoma de México (Tesis de Maestría), 139.

Swanson, E.R., 1989. A new type of maar volcano from the State of Durango- The El Jagüey-La Breña complex reinterpreted. Revista del Instituto de Geología, 8, 243-248.

Torres-Aguilera, J., 2005. Carácterización petrográfica y geoquímica del vulcanismo bimodal en el semigraben de Bledos, en el Campo Volcánico de San Luis Potosí: San Luis Potosí, Mexico. Universidad Autónoma de San Luis Potosí, Facultad de Ingeniería (Tesis de Maestría).

Tristán-González, M., Aguillón-Robles, A., Barboza-Gudiño, J.R., Torres-Hernández, J.R., Bellon, H., López-Doncel, R.A., Rodríguez-Ríos, R., Labarthe-Hernández, G., 2009. Geocronología y distribución espacial del Campo Volcánico de San Luis Potosí. Boletín de la Sociedad Geológica Mexicana, 61, 287-303.

Tristán-González, M., 1986. Estratigrafía y tectónica del graben de Villa de Reyes en los estados de San Luis Potosí y Guanajuato, Mexico. Universidad Autónoma de San Luis Potosí, Instituto de Geología, Folleto Técnico 107, 91.

Trujillo-Candelaria, J.A., 1985. Origen del fallamiento in Flores-Nuñez, J., ed., Fallamiento de terrenos en Celaya. Sociedad Mexicana de Mecánica de Suelos, 3-9.

Xu, S.S., Nieto-Samaniego, A.F., Alaniz-Álvarez, S.A., 2004. Vertical shear mechanism of faulting and estimation of strain in the Sierra de San Miguelito, Mesa Central, Mexico. Geologica Acta, 2, 189-201.

# CAPITULO 2.-
# TRABAJO DE CAMPO Y MUESTREO

## 2.1 Localización del área de estudio

El Complejo Volcánico de la Sierra de San Miguelito (CVSSM) se localiza en la sección central de México, hacia el borde occidental del estado de San Luis Potosí, México (Figura 2.1), donde forma una extensa sierra en los bordes sur, oeste y noroeste de la ciudad de San Luis Potosí. Desde una perspectiva fisiográfica, el CVSSM forma parte de la provincia de la Mesa Central.

Las vías de acceso hacia el CVSSM son principalmente la carretera estatal No. 80 San Luis Potosí–Guadalajara, con la desviación a la comunidad de Escalerillas y Presa del Peaje, como también el anillo periférico libramiento sur y este con desviación hacia la Cañada del Lobo, Capulines, Iglesia del Desierto, Presa de San José, Villa Magna y Horizontes (Figura 2.1). De igual forma se puede acceder hacia el CVSSM por la Carretera Estatal No. 49 con desviación hacia el poblado Suspiro Picacho y también algunos caminos de terracería que llegan a comunicar pequeñas comunidades con poblados.

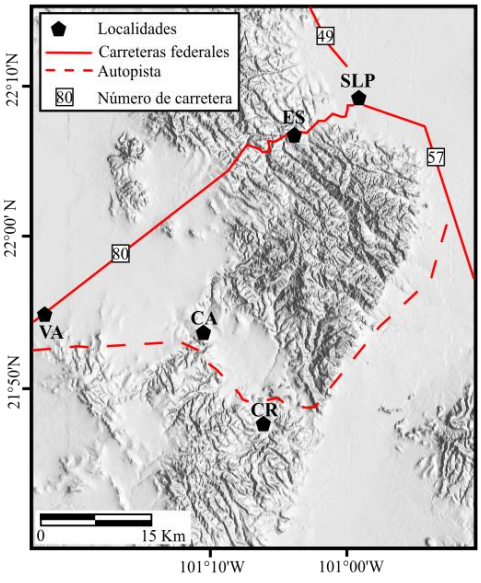


**Figura 2.1.-** Mapa de ubicación del área de estudio. Abreviaciones: CA= Cabras; CR= Carranco; ES= Escalerillas; SLP= San Luis Potsí; VA= Villa Aldama.

## 2.2 Geología estructural del CVSSM

El CVSSM se considera como un área relativamente alta de la región sur de la provincia de la Mesa Central. Los grandes ejes y el alineamiento de domos volcánicos comúnmente indican las orientaciones de largas fallas normales (Xu et al., 2008).

Las estructura geológica principal que limita al CVSSM es el Graben de Villa de Reyes (GVR; Figura 2.2), el cual se caracteriza por ser una fosa tectónica del Oligoceno rellenada por depósitos volcánicos y clásticos de edad del Oligoceno temprano hasta depósitos recientes (López-Loera et al., 2013; Xu et al., 2013). La longitud aproximada del GVR es de 200 km con un ancho variable de 10-20 km, a su vez, el GVR forma parte a las distintas series de estructuras tectónicas de la provincia de la Mesa Central las cuales corresponde a la etapa de máxima extensión del área (Labarthe-Hernández et al., 1982; Tristán-González, 1986; Nieto-Samaniego et al., 1996; Henry y Aranda-Gómez, 1992; López-Loera et al., 2013).

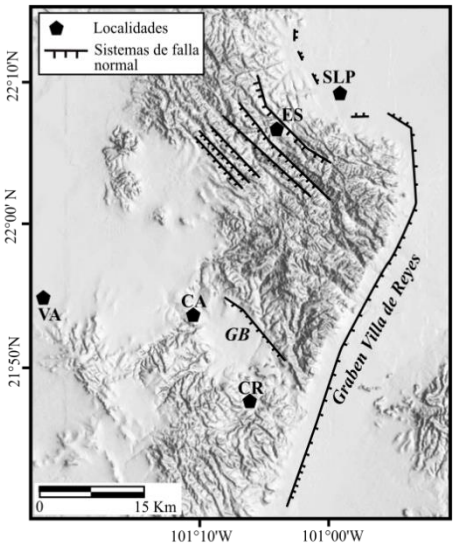


**Figura 2.2.-** Mapa de los sistemas de fallas principales del CVSSM. Abreviaciones: CA= Cabras; CR= Carranco; ES= Escalerillas; SLP= San Luis Potsí; VA= Villa Aldama; GB= Graben de Bledos.

El CVSSM se compone por numerosas fallas normales con rumbos que oscilan entre los 300° y 340°. La mayoría de estas fallas presentan direcciones de buzamiento hacia el SW y varían desde los 45° a los 75° de buzamiento (Xu et al., 2004). Se han clasificado a estas fallas como un sistema *domino* debido a que muestran dirección de buzamiento de falla uniforme, dirección de buzamiento de bloques uniformes y ángulos de buzamientos similares a los bloques (Figura 2.2; Labarthe-Hernández y Jiménez-López, 1992; Xu et al., 2004, 2008, 2013).

## 2.3 Estratigrafía local del CVSSM

La estratigrafía del Complejo Volcánico de la Sierra de San Miguelito cubre desde el Oligoceno hasta el Mioceno temprano. El CVSSM muestra siete unidades litológicas principales (Figura 2.3) las cuales son la unidad San Miguelito, San José, El Zapote, Cantera, La Placa, Panalillo, y Cabras.

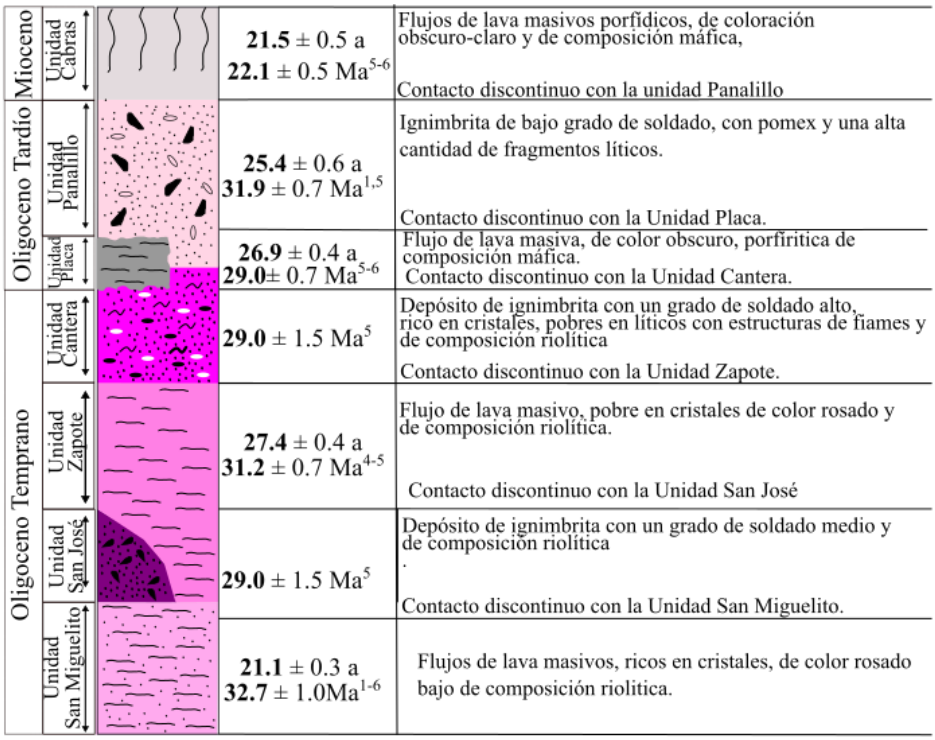


**Figura 2.3.-** Columna litológica simplificada del Complejo Volcánico de la Sierra de San Miguelito. Edades son tomadas de los siguientes autores:[1]Labarthe-Hernández et al. (1982); [2]Tuta et al. (1988); [3]Aguillón-Robles et al. (1994); [4]Aguillón-Robles et al. (2009); [5]Tristán-González et al. (2009); [6]Aguillón-Robles et al. (2014).

La unidad más antigua que se puede encontrar en el CVSSM es la unidad San Miguelito (Figura 2.4a) la cual se caracteriza por ser el principal componente de los domos exógenos que se observan dentro del complejo; además, el grosor de la unidad San Miguelito varía entre los 130 m hasta llegar a espesores amplios de 800m, y se observa que es aún más alta en el centro de los domos (Figura 2.4; Labarthe-Hernández y Jiménez-López, 1992). La mineralogía que se puede observar en rocas de mano consiste principalmente en fenocristales de cuarzo y sanidino embebidos en una matriz desvitrificada.

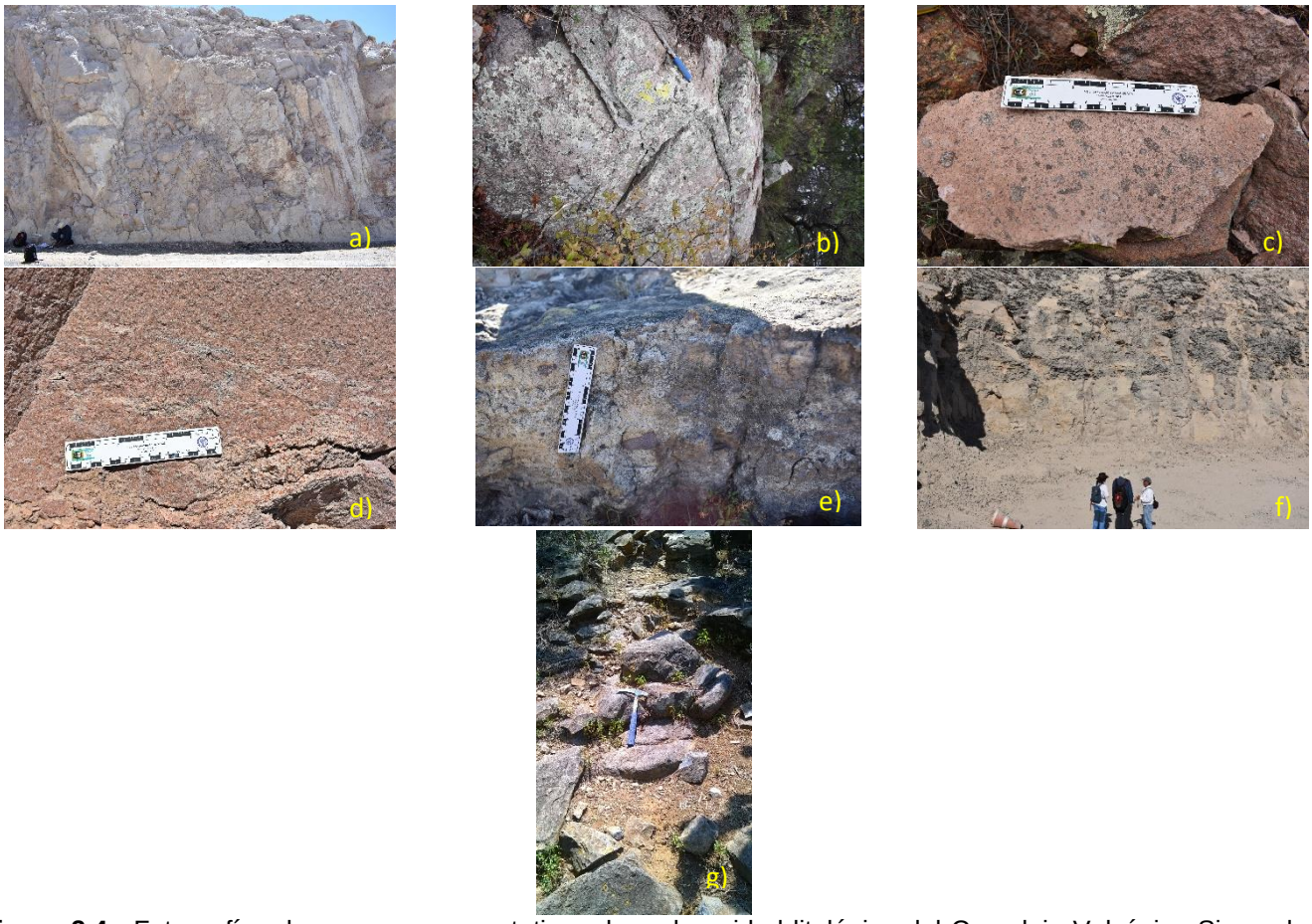


**Figura 2.4.-** Fotografías de campo representativas de cada unidad litológica del Complejo Volcánico Sierra de San Miguelito. a) Afloramiento masivo de la unidad San Miguelito; b) Afloramiento de bloque masivo de la unidad El Zapote; c) Muestra de mano de la unidad San José, donde se aprecian ; d) Afloramiento de bloque de la unidad Cantera, donde se observan estructuras de *fiames*; e) Afloramiento de bloque de roca de la unidad Panalillo donde se observan alta cantidad de líticos; f) Afloramiento masivo basáltico de la unidad La Placa; e) Afloramiento de bloques basálticos de la unidad Cabras.

Estudios previos han reportado edades de roca total por el método de K/Ar de roca total para la unidad San Miguelito (Tabla 2.1; Labarthe-Hernández y Jiménez-López, 1992; Aguillón-Robles et al., 1994, 2014; Tristán-González et al., 2009). La datación por este método ha variado entre los 33 y 30 Ma para la generación de esta unidad. En algunas localidades esta unidad se observa en contacto junto a una unidad riolítica denominada como la unidad El Zapote, como a su vez, con distintas unidades piroclásticas como lo son la unidad Cantera, Panalillo y San José.

La unidad El Zapote, presenta ciertas características similares a la unidad San Miguelito (lavas masivas de composición riolítica con mineralogía de cuarzo y feldespatos), sin embargo, esta unidad presenta distintos espesores; además se concentra en una sola región del Complejo Volcánico de la Sierra de San Miguelito. A su vez, la unidad El Zapote descansa directamente en el tope de la unidad San Miguelito, y a diferencia de esta, la unidad El Zapote presenta texturas de grano fino con tendencia fluida, y pobre en fenocristales. (Figura 2.4b; Labarthe-Hernández y Jiménez-López, 1992). Ha sido datada de igual forma por el método de K/Ar por trabajos previos en una edad de 31 a 27 Ma (Tabla 2.1; Labarthe-Hernández y Jiménez-López, 1992; Aguillón-Robles et al., 2014; Tristán-González et al., 2009).

Entre la unidad San Miguelito y la unidad El Zapote se encuentra una unidad piroclástica la cual se le ha denominado como San José (Figura 2.4c). Esta unidad se caracteriza por localizarse en un sector del CVSSM, como también por espesores de 3 a 15m, consiste principalmente de depósitos de ceniza que se encuentran parcialmente consolidados (Labarthe-Hernández y Jiménez-López, 1992; Tristán-González et al., 2009; Gaytán-Martínez et al., 2017).

La unidad Cantera subyace a la unidad San Miguelito, El Zapote y San José, como a su vez, cubre la mayoría del CVSSM. La unidad Cantera se determina por depósitos piroclásticos altamente compactado caracterizados por pómez y ceniza de colores grisáceas a rosas, abundantes estructuras de fiames y fragmentos líticos de composiciones de arenisca y riolita, inmersos en una matriz vítrea (Figura 2.4d; Labarthe -Hernández y Jiménez-López, 1992; Tristán-González et al., 2009; Caballero -Miranda et al., 2009; Gaytán-Martínez et al., 2017). Diversos autores han datado esta unidad por el método de K/Ar, mostrando una edad de formación de 29 Ma (Labarthe-Hernández y Jiménez-López, 1992; Tristán-González et al., 2009).

La unidad La Placa consiste de flujos de lava masivas de composiciones básicas (Figura 2.4f) las cuales se exponen en afloramientos aislados, mostrando un rango de espesor de 10 a 15m, y se caracteriza por fenocristales de olivino escasos en una matriz vítrea. Estudios previos han datado esta unidad por el método de K/Ar y han reportado edades de 29 a 26 Ma (Tabla 2.1; Tristán-González et al., 2009; Aguillón-Robles et al., 2014).

La unidad de composición ácida más joven dentro del CVSSM, es la unidad denominada ignimbrita Panalillo. Se compone principalmente de depósitos de piroclástiicos de pómez y ceniza, ricos en líticos, y presenta bajos grados de soldamiento en comparación a la unidad ignimbritica Cantera (Figura 2.4e). Estudios previos han asignado esta unidad en 29 a 26 Ma por estar ubicada entre dos unidades fechadas por el método de K/Ar (Tabla 2.1; Labarthe-Hernández y Jiménez-López, 1992; Torres-Hernández et al., 2006; Tristán-González et al., 2009).

La unidad más reciente en el CVSSM es la unidad Cabras, esta unidad, igual que la unidad La Placa, se presenta en afloramientos aislados dentro de la región del complejo, como a su vez, se caracteriza por flujos de lava gruesos (~25 m de espesor) con texturas afaníticas-porfídicas con fenocristales de olivino escasos y composiciones básicas (Figura 2.4g). Tristán-González et al. (2009) y Aguillón-Robles et al. (2014) reportan edades de roca total por el método de K/Ar de 22 a 21 Ma.

Tabla 2.1.- Edades de literatura de las unidades litológicas del Complejo Volcánico de la Sierra de San Miguelito. Abreviaciones: SM=San Miguelito; RT=Roca total; FLD=Feldespato; BT=Biotita.

| Unidad | Edad | Error | Método | Tipo de muestra | Referencia |
|---|---|---|---|---|---|
| Cabras | 21.5 | 0.5 | K/Ar | RT | Aguillon-Robles etal (2014) |
| Cabras | 21.5 | 0.5 | K/Ar | RT | Tristan-González etal. (2009) |
| Cabras | 21.6 | 0.5 | K/Ar | RT | Aguillon-Robles etal (2014) |
| Cabras | 22.1 | 0.5 | K/Ar | RT | Aguillon-Robles etal (2014) |
| Panalillo | 25.4 | 0.6 | K/Ar | RT | Tristan-González etal. (2009) |
| Panalillo | 25.4 | 0.6 | K/Ar | RT | Tristan-González etal. (2009) |
| Panalillo | 25.7 | 0.4 | K/Ar | FLD | Tristan-González etal. (2009) |
| Panalillo | 27.6 | 0.6 | K/Ar | FLD | Labarthe-Hernández etal. (1982) |
| Panalillo | 28.3 | 0.9 | K/Ar | RT | Tristan-González etal. (2009) |
| Panalillo | 28.9 | 0.5 | K/Ar | RT | Tristan-González etal. (2009) |
| Panalillo | 29 | 0.9 | K/Ar | RT | Tristan-González etal. (2009) |
| Panalillo | 29 | 0.9 | K/Ar | RT | Tristan-González etal. (2009) |
| Panalillo | 29.9 | 0.6 | K/Ar | FLD | Labarthe-Hernández etal. (1982) |
| Panalillo | 30.3 | 0.7 | K/Ar | FLD | Labarthe-Hernández etal. (1982) |
| Panalillo | 31.9 | 0.7 | K/Ar | FLD | Labarthe-Hernández etal. (1982) |
| Placa | 26.9 | 0.4 | K/Ar | RT | Tristan-González etal. (2009) |
| Placa | 28 | 0.6 | K/Ar | RT | Tristan-González etal. (2009) |
| Placa | 29 | 0.7 | K/Ar | RT | Aguillon-Robles etal (2014) |
| Zapote | 27.4 | 0.4 | K/Ar | FLD | Tristan-González etal. (2009) |
| Zapote | 28.7 | 0.7 | K/Ar | RT | Aguillon-Robles etal. (2009) |
| Zapote | 31.2 | 0.7 | K/Ar | RT | Tristan-González etal. (2009) |
| SM | 21.1 | 0.3 | K/Ar | RT | Tristan-González etal. (2009) |
| SM | 28.7 | 0.8 | K/Ar | RT | Tristan-González etal. (2009) |
| SM | 29.1 | 0.7 | K/Ar | RT | Tristan-González etal. (2009) |

Tabla 2.1.- *Continuación*

| Unidad | Edad | Error | Método | Tipo de muestra | Referencia |
|---|---|---|---|---|---|
| SM | 29.2 | 0.8 | K/Ar | BT | Aguillon-Robles etal. (1994) |
| SM | 30.3 | 0.9 | K/Ar | RT | Tristan-González etal. (2009) |
| SM | 30.4 | 0.5 | K/Ar | FLD | Tristan-González etal. (2009) |
| SM | 30.7 | 0.7 | K/Ar | RT | Tristan-González etal. (2009) |
| SM | 31 | 0.6 | K/Ar | BT | Labarthe-Hernández etal. (1982) |
| SM | 31.1 | 0.7 | K/Ar | FLD | Tristan-González etal. (2009) |
| SM | 31.1 | 0.3 | K/Ar | RT | Tuta etal. (1988) |
| SM | 31.3 | 0.7 | K/Ar | RT | Tristan-González etal. (2009) |
| SM | 31.6 | 0.9 | K/Ar | RT | Tristan-González etal. (2009) |
| SM | 32 | 0.7 | K/Ar | RT | Tristan-González etal. (2009) |
| SM | 32.3 | 1.6 | K/Ar | FLD | Labarthe-Hernández etal. (1982) |

## 2.4 Muestreo

Para el presente trabajo un total de 41 muestras (Figura 2.5) representativas de las principales unidades litológicas del CVSSM fueron seleccionadas. Lugares en donde se presentan distintos grados de alteración, como a su vez, afloramientos en donde se observa deformación de la roca fueron evitados durante el muestreo.

Los límites estratigráficos y litológicos de las rocas volcánicas fueron dibujados, en gran parte en características geomorfológicas probadas en el campo y después refinados por los análisis petrológicos, geoquímicos y geocronológicos mostrados en las siguientes secciones del presente trabajo.

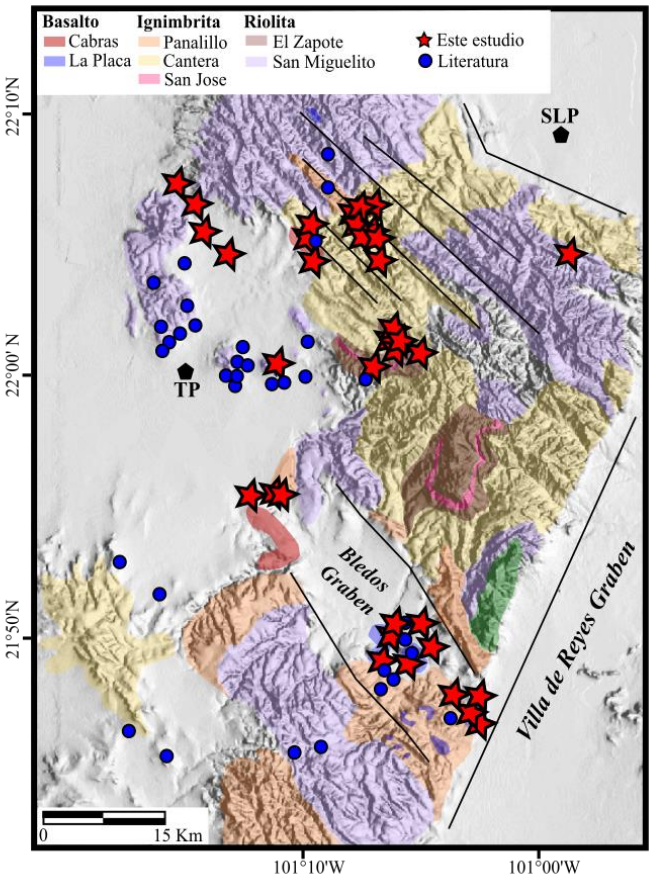


**Figura 2.5.-** Mapa del CVSSM representado las muestras recolectadas en este estudio (estrellas rojas) y muestras compiladas de literatura (círculos azules).

## Referencias


Aguillón-Robles A., Tristán-González M., Aguirre-Díaz G.J., López-Dorcel R.A., Bellon H., Martínez-Esparza G., 2014. Eocene to Quaternary mafic-intermediate volcanism in San Luis Potosí, central Mexico: the transition from Farallon plate subduction to intra-plate continental margin. Journal of Volcanology and Geothermal Research 276, 152-172.

Caballero -Miranda C.I., Torres-Hernández J.R., Alva-Valdivia M., 2009. Anisotropy of magnetic susceptibility analysisi of the Cantera Ignimbrite, San Luis Potosí, Mexico: flow source recognition. Earth Planets Space 61, 173-182.

Gaytán-Martínez R., Noyola-Medrano C., Rojas-Beltrán M.A., 2017. Análisis espectral y petrográfico del Complejo Volcánico Sierra de San Miguelito, S.L.P., México. Ser. Correlación Geológica 33, 49-60.

Henry, C.D, Aranda-Gómez J.J., 2000. Plate interactions control middle-late Miocene, proto-Gulf and Basin and Range extensión in the southern Basin and Range. Tectonophysics 318, 1-26.

Labarthe-Hernández, G., Jiménez-López, L.S., 1992. Características físicas y estructura de lavas e ignimbritas riolíticas en la Sierra de San Miguelito, San Luis Potosí. Instituto Geología, Universidad Autónoma de San Luis Potosí, Folleto Técnico 114, 31.

Labarthe-Hernández, G., Tristán-González, M., Aranda-Gómez, J.J, 1982. Revisión estratigráfica del Cenozoico de la parte central del estado de San Luis Potosí. Universidad Autónoma de San Luis Potosí, Instituto de Geología, Folleto Técnico 85, 208.

López-Loera, H., Tristán-González, M., 2013. Geología y magnetometría 762 aérea del Graben de Villa de Reyes, San Luis Potosí, Mesa Central de México: implicaciones tectónicas y geohidrológicas. Boletín de la Sociedad Geológica Mexicana 65, 137–156.

Nieto-Samaniego, A.F., Macías-Romo, C., Alaniz-Alvarez, S.A., 1996. Nuevas edades isotópicas de la cubierta volcánica cenozoica de la parte meridional de la Mesa Central, México. Revista Mexicana de Ciencias Geológicas 13, 117–122.

Torres-Hernández J.R., Labarthe-Hernández G., Aguillón-Robles A., Gómez-Anguiano M., Mata-Segura J.L, 2006. The pyroclastic dikes of the Tertiary San Luis Potosí volcanic field: Implications on the emplacement of Panalillo Ignimbrite. Geofísica Internacional 45, 243-253.

Tristan-González M., Aguillón-Robles A., Barboza-Gudiño J.R, Torres-Hernández J.R., Bellon H., López-Doncel R., Rodríguez-Ríos R., Labarthe-Hernández G., 2009. Geocronología y distribución espacial del vulcanismo en el Campo Volcánico de San Luis Potosí. Boletín de la Sociedad Geológica Mexicana 61, 287-303.

Tristán-González, M., 1986. Estratigrafía y tectónicas del graben de Villa de Reyes, en los estados de San Luis Potosí y Guanajuato, México. Instituto de Geología, Universidad Autónoma de San Luis Potosí, Folleto Técnico 107, 91.

Tuta Z.H., Sutter J.F., Kesler S.E., Ruiz J., 1988. Geochronology of mercury, tin, and fluorite mineralization in northern Mexico. Economic Geology and the Bulletin of the Society of Economic Geologists 83, 1931-1942.

Xu, S.S., Nieto-Samaniego, A.F., Alaniz-Álvarez, S.A., 2004. Titling mechanisms in domino faults of the Sierra de San Miguelito, central Mexico. Geologica Acta 2, 189–209.

Xu, S.S., Nieto-Samaniego, A.F., Alaniz-Álvarez, S.A., 2013. Origin of superimposed and curved slickenlines in San Miguelito range, Central México. Geologica Acta, 11, 103–112.

Xu, S-S, Nieto-Samaniego, Á.F., Alaniz-Álvarez, S.A., Grajales-Nishimura, J.M., 2008. Evolution of the geometry of normal faults in the Oligocene volcanic field of the Mesa Central, México. Boletín de la Sociedad Geológica Mexicana 60, 71–82.

# CAPITULO 3.-

# ANÁLISIS PETROGRÁFICO

## 3.1 Metodología del análisis petrográfico

Para la elaboración del análisis petrográfico, se elaboraron 20 láminas delgadas de las rocas volcánicas del Complejo Volcánico Sierra de San Miguelito (CVSSM), las cuales se llevaron a cabo en el Laboratorio de Preparación de la Facultad de Ciencias de la Tierra, UANL.

Para una revisión detallada de la metodología de elaboración de las secciones delgadas, se pude revisar la sección A.1 del apartado de Anexos de este trabajo. Las composiciones modales son reportadas en la Tabla A.1 en la sección de Anexos.

## 3.2 Características petrográficas de las unidades litológicas del CVSSM

A partir de las observaciones de campo y petrográficas, las rocas del CVSSM se pueden dividir en tres grupos principales. Para este trabajo se han divido las rocas volcánicas del CVSSM en: a) rocas básicas; b) rocas intermedias; y c) rocas ácidas. En las siguientes secciones se presentarán las características petrográficas principales de estos tres grupos.

### *3.2.1 Rocas básicas*

Las rocas básicas del CVSSM muestran texturas porfiríticas con una limitada presencia de vesículas y una matriz vítrea (Tabla A.1).

El ensamblaje mineral principal que presentan las rocas básicas del CVSSM (Figura 3.1) consiste de fenocristales euhedrales a subhedrales de plagioclasas (10-68%), generalmente mostrando maclas simples (maclas Carlsband) y un zonamiento normal; fenocristales subhedrales de clinopiroxeno que muestran una abundancia aproximada del 6-20%; fenocristales subhedrales de ortopiroxeno (4-7%); como también una pequeña cantidad de microcristales subhedrals a xenoformos de olivino (<6%).

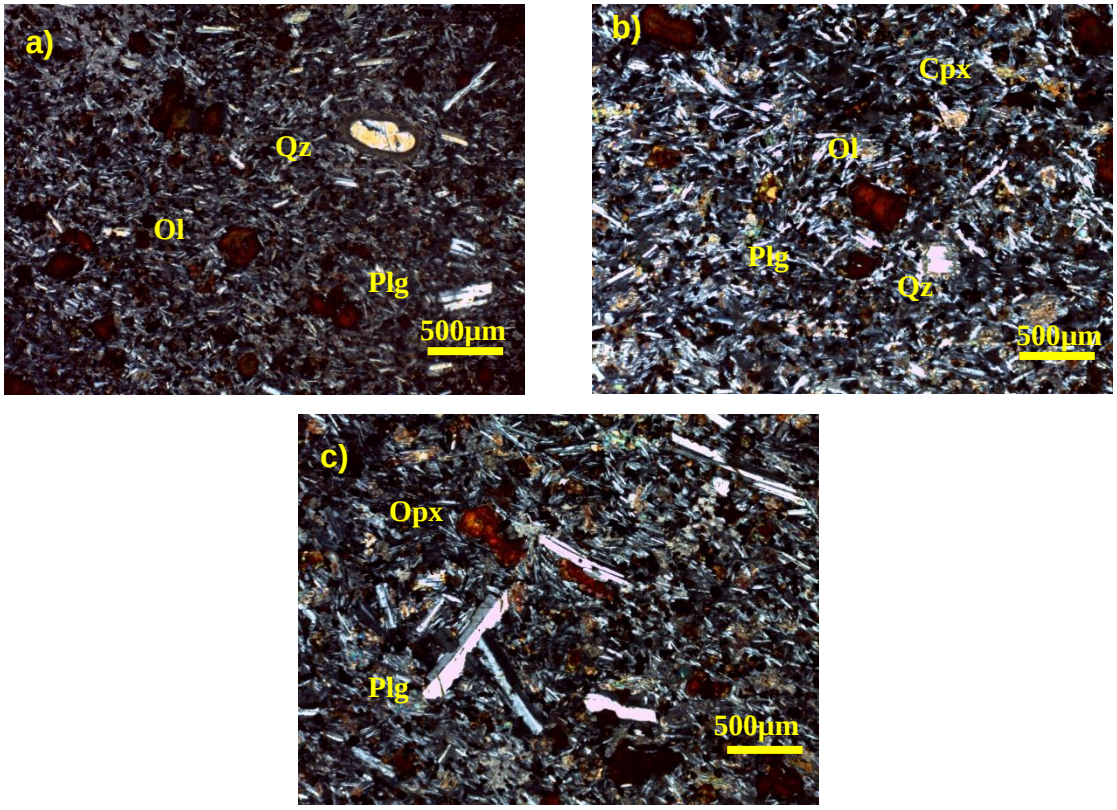


Figura 3.1.- Microfotografías en nicoles cruzados (NX) con un aumento de 2.5x de muestras representativas de la unidad máfica Cabras. a) Fenocristales de plagioclasas, olivino y cuarzo con aros de reacción y microcistales de plagioclasa en la matriz; b) Fenocristales de plagioclasas, olivino y cuarzo con aros de reacción y microcistales de plagioclasa y piroxenos en la matriz; c) Fenocristales de plagioclasas con microcristales de plagaioclasa en la matriz. Plg=plagioclasa; Qz= cuarzo; Cpx= clinopiroxeno; Opx= ortopiroxeno; Ol=olivino.

### *3.2.2 Rocas intermedias*

Las rocas intermedias del CVSSM muestran texturas porfiríticas sin presencia de vesículas, y una matriz vítrea (Tabla A.1).

El ensamblaje mineralógico que muestran las rocas intermedias es similar al de las rocas básicas, con la única diferencia en las proporciones que muestran en ciertos minerales. Las rocas intermedias del CVSSM se componen por: fenocristales euhedrales a subhedrales de plagioclasas (10-68%); fenocristales subhedrales de clinopiroxeno que muestran una abundancia aproximada del 6-20%; fenocristales subhedrales de ortopiroxeno (4-7%); como también cantidad limitada de microcristales subhedrales a xenoformos de olivino (<6%).

Además, las rocas intermedias del CVSSM muestran las siguientes características peculiares: (i) diversas texturas de desequilibrio que incluyen plagioclasas con texturas normales y de criba en la misma muestra; (ii) cristales redondeados y embebidos con aros de reacción de cuarzo; (iii) plagioclasas con zonación mineral compleja, tales como zonación oscilatoria e inversa, o bien, cristales zonados de forma normal e inversa en la misma muestra (Figura 3.2).

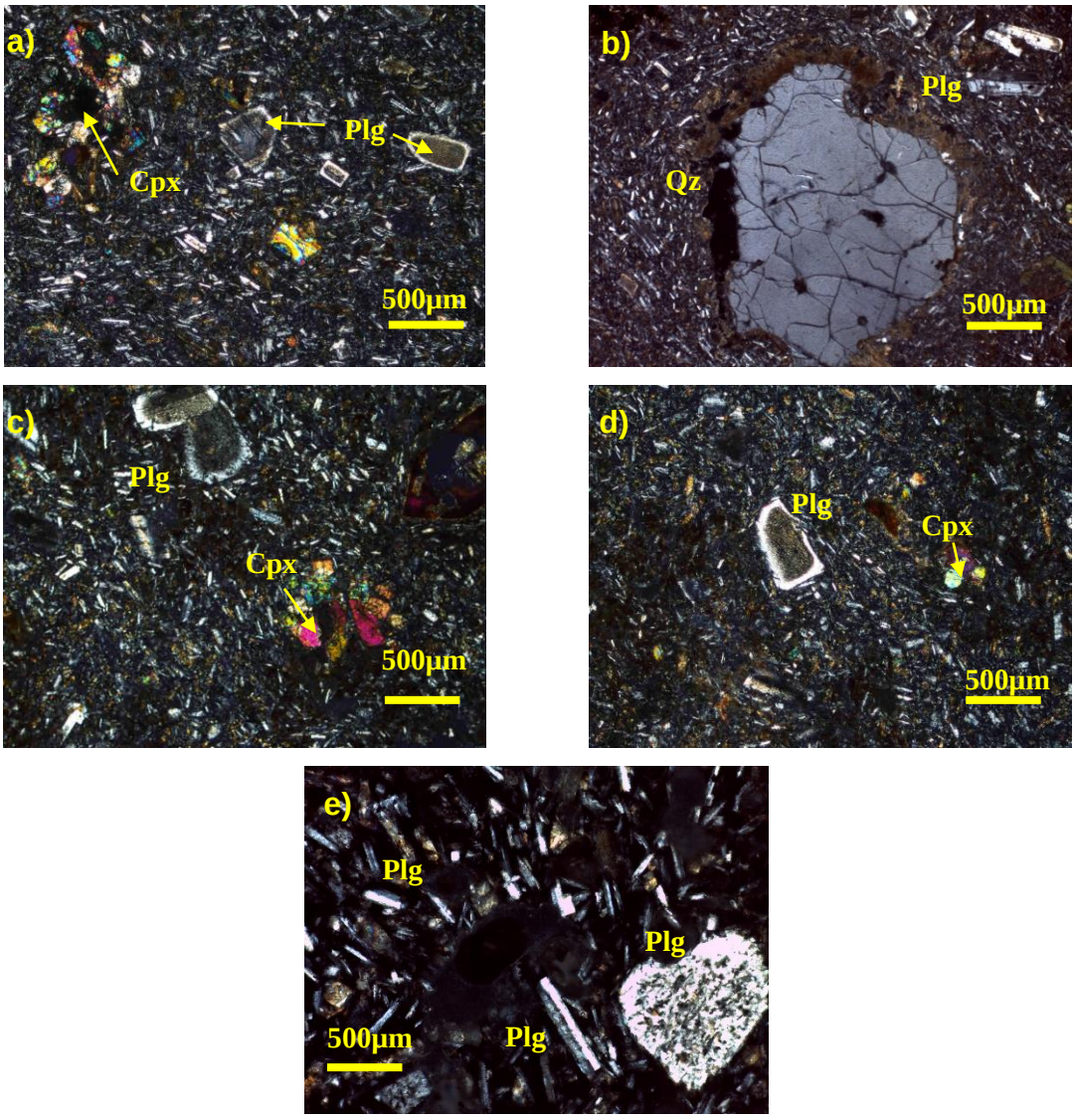


Figura 3.2.- Microfotografías en nicoles cruzados (NX) con un aumento de 2.5x de muestras representativas de la unidad intermedia Placa. a) Fenocristales de plagioclasas con texturas de criba y clinopiroxenos y microcristales de plagioclasa en la matriz; b) Fenocristal de cuarzo con aro de reacción inmerso en una matriz vítrea con microcristales de plagioclasas; c) Fenocristales de plagioclasas con texturas de criba y fenocristales de clinopiroxeno inversos en una matriz vítrea con microcristales de plagioclasas; d) Fenocristales de plagioclasa con textura de criba y clinopiroxenos; e) Fenocristales de plagioclasa con textura de criba en una matriz vítrea con microcristales. Plg=plagioclasa; Qz= cuarzo; Cpx= clinopiroxeno; Opx= ortopiroxeno; Ol=olivino.

*3.2.3 Rocas ácidas*

Las rocas ácidas muestran texturas porfirítcas, con excepción de algunas muestras que muestran texturas porfiriticas fluidales (Tabla A.1; Figura. 3.3).

El ensamblaje mineralógico principal de las rocas ácidas del CVSSM consiste de fenocristales xenoformos de cuarzo (27-41%); fenocristales euhedrales a subhedrales de feldespatos potásicos (11-15%): fenocristales euhedrales a subhedrales de plagioclasas (~44%) con diámetros de 0.5-2 mm; ortopiroxenos subhedrales (1-4%) y fenocristales de clinopiroxenos (1-4%) de un diámetro aproximado de 0.2-0.7 mm.

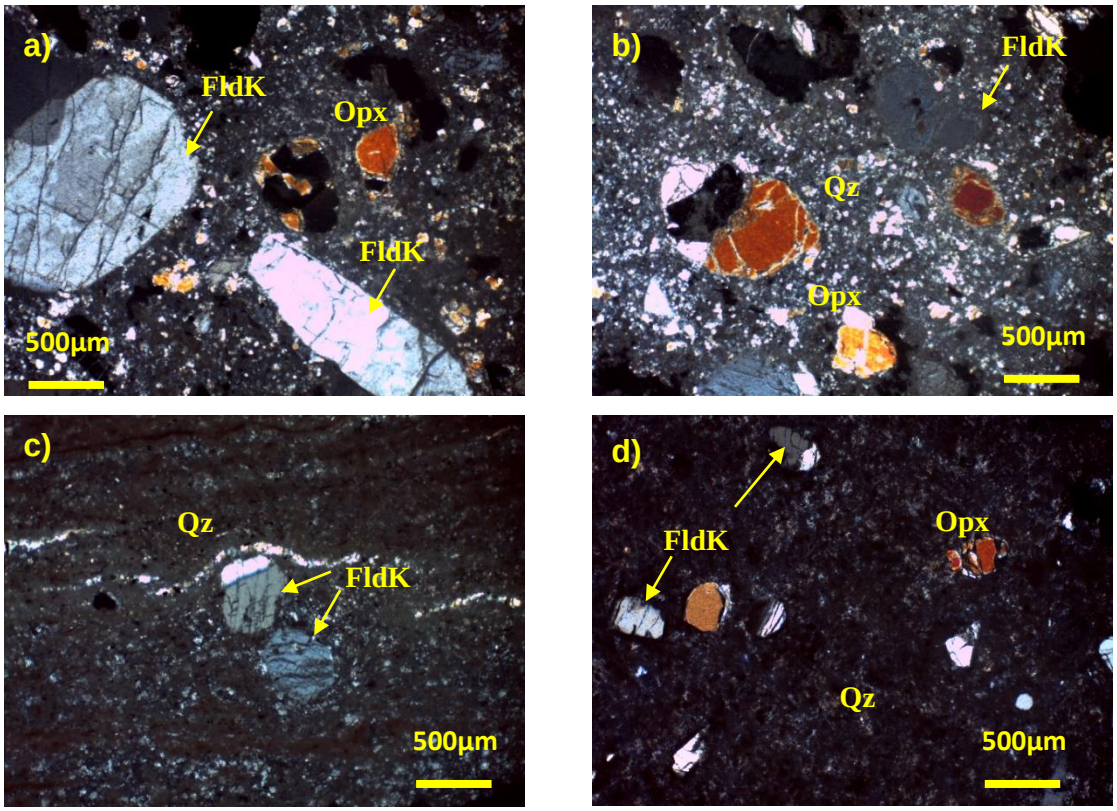


Figura 3.3.- Microfotografías en nicoles cruzados (NX) con un aumento de 2.5x de muestras representativas de las unidades félsicas. a) Fenocristales de feldespatos alcalinos de la unidad San Miguelito; b) Fenocristales de feldespato potásico y ortopiroxenos con microcristales de cuarzo en la matriz de la unidad San Miguelito; c) Fenocristales de feldespato potásico con microcristales de cuarzo en la matriz de la unidad El Zapote; d) Fenocristales de feldespato potásico, cuarzo y ortopiroxeno de la unidad El Zapote. Qz= cuarzo; FldK= feldespato potásico; Opx= ortopiroxeno.

De igual forma las rocas ácidas de carácter piroclástico consisten en depósitos de flujo semi-consolidados y consolidados. Estas muestras de roca presentan texturas porfiríticas y un ensamblaje mineral principal de fenocristales de suhedrales de cuarzo (15-38%), feldespatos potásicos (15-22%) euhedrales a subhedrales, plagioclasas (2-43%), ortopiroxenos subhedrales y xenoformos (2-5%), cristales de clinopiroxeno (2-7%) y en algunas muestras se pueden llegar a observar microcristales de olivinos en poca abundancia (Table A1; Figura 4.4).

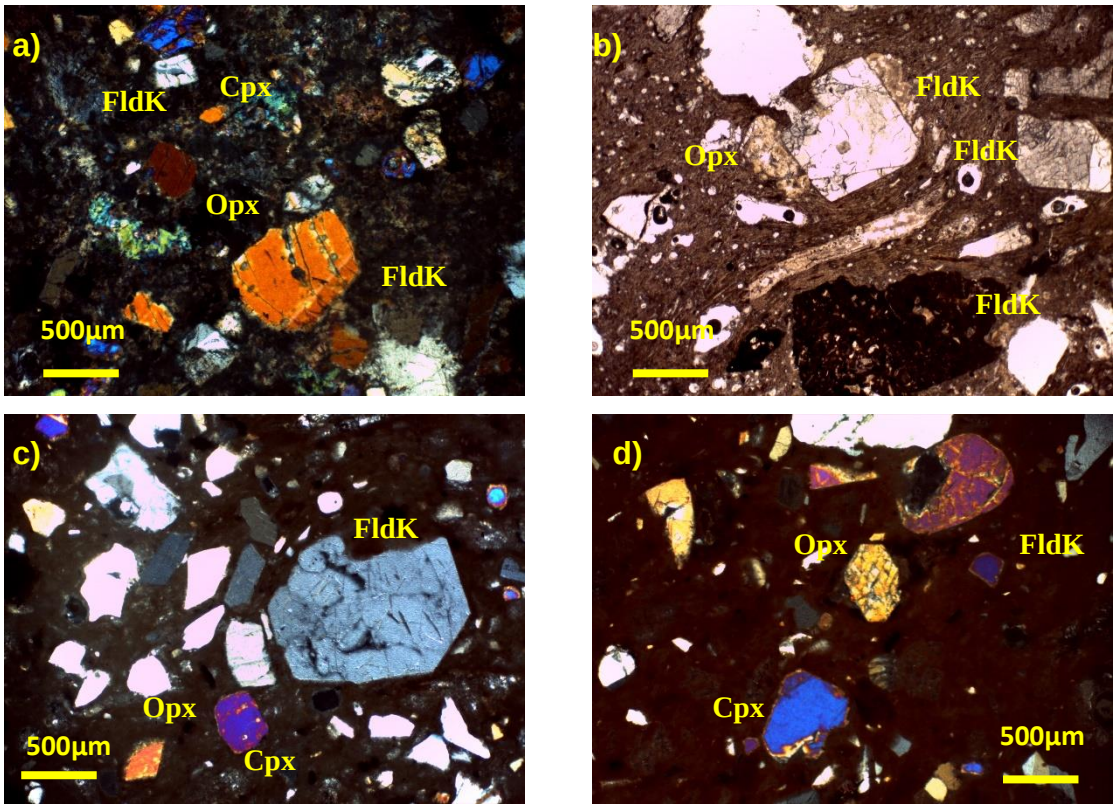


Figura 3.4 Microfotografías en nicoles cruzados (NX) y nicoles paralelo con un aumento de 2.5x de muestras representativas de las unidades ácidas de carácter piroclásitco. a) Fenocristales de clinopiroxeno, ortopiroxeno y feldespatos potásicos de la unidad Cantera; b) Fenocristales de feldespatos potásicos y ortopiroxeno de la unidad Cantera; c) Fenocristales de feldespatos potásicos, ortopiroxeno y clinopiroxeno de la unidad Panalillo; d) Fenocristales de feldespato potásico, ortopiroxeno y clinopiroxeno de la unidad Panalillo. FldK= feldespato potásico; Opx= ortopiroxeno.

# CAPITULO 4.-

# CALIBRACIÓN DE FLUORESCENCIA DE RAYOS-X PARA LA MEDICIÓN DE ELEMENTOS MAYORES

## 4.1 Presentación del trabajo de investigación publicado

El presente artículo de investigación ha sido publicado en *Journal of Spectrometry* en el cual el autor de esta tesis participó activamente. Dentro de este trabajo me encuentro como cuarto co-autor, como a su vez, el primer autor de este trabajo es el Dr. Surendra Pal Verma Jaiswal. Los demás co-autores del presente artículo de investigación son: Dr. Sanjeet Kumar Verma, Dra. M. Abdelaly Rivera-Gómez, Dra. Lorena Díaz-González, Ing. Alejandra Amezcua-Valdez, M.C. Beatriz Adriana Rivera-Escoto, Dr. Mauricio Rosales-Rivera, Dr. John S. Armstrong-Altrin, Dr. Héctor López-Loera, Dr. Fernando Velasco Tapia y el Dr. Kailasa Pandarinath.

Este trabajo de investigación brinda una amplia contribución dentro de la calibración de máquinas de fluorescencia de rayos-X (FRX). Dentro de este trabajo se aplicó tanto regresiones lineales ordinarias (RLO) y modelos de regresión lineal ponderada (RLP) para la calibración y comparación de una máquina de FRX, a través de 59 materiales de referencia geoquímica (MRG). Se obtuvieron archivos a partir de una recopilación actualizada de datos químicos y su procesamiento a partir de pruebas conocidas de discordancia e importancia.

La contribución principal es lo demostrado entre la comparación de los modelos de RLO y RLP, en donde se mostró claramente que este último, con valores generalmente más altos de *r,* es preferible para calibraciones rutinarias de los procedimientos analíticos de máquinas de FRX.

Hindawi
Journal of Spectroscopy
Volume 2018, Article ID 5837214, 13 pages
https://doi.org/10.1155/2018/5837214

*Research Article*

# Statistically Coherent Calibration of X-Ray Fluorescence Spectrometry for Major Elements in Rocks and Minerals

**Surendra P. Verma**[1], **Sanjeet K. Verma**[2], **M. Abdelaly Rivera-Gómez**[3], **Darío Torres-Sánchez**[4], **Lorena Díaz-González**[5], **Alejandra Amezcua-Valdez**[6], **Beatriz Adriana Rivera-Escoto**[7], **Mauricio Rosales-Rivera**[8], **John S. Armstrong-Altrin**[3], **Héctor López-Loera**[2], **Fernando Velasco-Tapia**[9] and **Kailasa Pandarinath**[1]

[1]*Instituto de Energías Renovables, Universidad Nacional Autónoma de México, Temixco, Mor 62580, Mexico*
[2]*División de Geociencias, Instituto Potosino de Investigación en Ciencia y Tecnología, Camino a la Presa San José # 2055, Col. Lomas 4a Sec., San Luis Potosí, SLP 78216, Mexico*
[3]*Instituto de Ciencias del Mar y Limnología, Unidad de Procesos Oceánicos y Costeros, Universidad Nacional Autónoma de México, Circuito Exterior s/n, 04510 CDMX, Mexico*
[4]*Posgrado en Geociencias Aplicadas, Instituto Potosino de Investigación en Ciencia y Tecnología, Camino a la Presa San José # 2055, Col. Lomas 4a Sec., San Luis Potosí, SLP 78216, Mexico*
[5]*Centro de Investigación en Ciencias, Instituto de Investigación en Ciencias Básicas y Aplicadas, Universidad Autónoma del Estado de Morelos, Cuernavaca, Mor 62209, Mexico*
[6]*Posgrado en Ingeniería, Instituto de Energías Renovables, Universidad Nacional Autónoma de México, Temixco, Mor 62580, Mexico*
[7]*División de Materiales Avanzados, Instituto Potosino de Investigación en Ciencia y Tecnología, Camino a la Presa San José # 2055, Col. Lomas 4a Sec., San Luis Potosí, SLP 78216, Mexico*
[8]*Doctorado en Ciencias, Instituto de Investigación en Ciencias Básicas y Aplicadas, Universidad Autónoma del Estado de Morelos, Cuernavaca, Mor 62209, Mexico*
[9]*Universidad Autónoma de Nuevo León, Facultad de Ciencias de la Tierra, Ex–Hacienda de Guadalupe, Carretera Linares–Cerro Prieto km 8, Linares, N.L. 67700, Mexico*

Correspondence should be addressed to Surendra P. Verma; spv@ier.unam.mx

Received 8 August 2018; Revised 8 October 2018; Accepted 19 October 2018; Published 11 December 2018

Academic Editor: Rafal Sitko



We applied both the ordinary linear regression (OLR) and the new uncertainty weighted linear regression (UWLR) models for the calibration and comparison of a XRF machine through 59 geochemical reference materials (GRMs) and a procedure blank sample. The mean concentration and uncertainty data for the GRMs used for the calibrations (Supplementary Materials) (available here) filewere achieved from an up-to-date compilation of chemical data and their processing from well-known discordancy and significance tests. The drift-corrected XRF intensity and its uncertainty were determined from mostly duplicate pressed powder pellets. The comparison of the OLR (linear correlation coefficient $r$~0.9523–0.9964 and 0.9771–0.9999, respectively, for before and after matrix correction) and UWLR models ($r$~0.9772–0.9976 and 0.9970–0.9999, respectively) clearly showed that the latter with generally higher values of $r$ is preferable for routine calibrations of analytical procedures. Both calibrations were successfully applied to rock matrices, and the results were generally consistent with those obtained in other laboratories although the UWLR model showed mostly narrower confidence limits of the mean (slope and intercept) or lower uncertainties than the OLR. Similar sensitivity (~2.69–46.17 kc·s$^{1}$·%$^{1}$ for the OLR and ~2.78–59.69 kc·s$^{1}$·%$^{1}$ for the UWLR) also indicated that the UWLR could advantageously replace the OLR model. Another novel aspect is that the total uncertainty can be reported for individual chemical data. If the analytical instruments were routinely calibrated from the UWLR model, this action would make the science of geochemistry more quantitative than at present.

## 1. Introduction

All modern analytical instruments require some kind of calibration of the instrumental response ($y$-variable) as a function of the concentration ($x$-variable) [1–3]. This calibration is generally achieved through an ordinary least-squares linear regression (OLR) model. However, such a procedure is not strictly valid because all requirements for the statistical validity of the OLR model are not fulfilled. Usually, the assumptions "independent concentration variable $x$ is error-free or less than one-tenth of the error in the dependent response variable $y$" and "error in $y$ is homoscedastic" (i.e., equal errors for all $y$ values) are not satisfied and, therefore, more sophisticated and statistically coherent regression procedures, such as weighted least-squares linear regression (WLR) models, should be used [4–18].

X-ray fluorescence (XRF) spectrometry is among the most popular analytical techniques for the determination of all major and some trace elements in rocks [4, 19–27]. Natural geochemical reference materials (GRMs) are commonly used for XRF calibrations and posterior characterization of those and other GRMs as well as of similar rock and mineral matrices [4, 19, 28–30]. As for most other analytical instruments, XRF spectrometers are also calibrated under the statistically incoherent OLR model.

To apply the WLR and compare it with the OLR, both central tendency (e.g., mean) and dispersion (e.g., confidence limits of the mean) estimates on both $x$-axis (concentration, generally expressed in the unit of % m/m, i.e., mass/mass unit expressed in percent) and $y$-axis (response, in this case XRF intensity, generally reported in the unit of $kc{\cdot}s^{-1}$, i.e., kilo counts per second) variables are required. More precise (and accurate) estimates of the central tendency will also be useful for both types of regressions. Therefore, precise concentrations of GRMs with the respective lowest possible "confidence limits of the mean" (referred hereafter as the "uncertainty" of the measured variable) [2, 17, 18] are required to apply the regression procedure. Sometimes, we had to use also the term "error" (instead of the uncertainty) because the use of the error is widespread in the literature.

We report the following five aspects: (a) evaluation of 59 GRMs to achieve the least possible uncertainties in the mean concentrations of all major elements ($SiO_2$ to $P_2O_5$); (b) the comparison of regression models (OLR and WLR) applied to net drift-corrected XRF intensities before the correction of matrix effects; (c) the second (or final) comparison of both models after achieving the matrix correction as well as for the estimation of sensitivities of the regression models; (d) application of the entire procedure to four GRMs treated as "unknown" samples and their comparison with the previous literature compilations; and (e) development of a computer program to achieve the abovementioned objectives. Thus, the regression equations (intercept and its uncertainty, slope and its uncertainty, and linear correlation coefficient values) for each constituent from $SiO_2$ to $P_2O_5$ and their application to similarly complex rock matrices are presented in this work.

## 2. Evaluation of Major Element Data for GRMs

A total of 59 GRMs (listed in alphabetical order in Table S1; this and four other tables are provided in Supplementary Materials), along with a procedure blank, were used in this study. The procedure blank was a pellet prepared in duplicate with only pure N,N′-Ethylene bis(stearamide) beads without any sample (Section 3). The individual data reported in earlier compilations [31–47] were first compiled in new databases.

The statistical parameters obtained in these early compilations could not be directly used for instrumental calibrations due to the following reasons: (i) the statistical methods used to achieve the statistical estimates were outdated (see [17, 18, 48, 49] for possible reasons), and the inferred statistical values were of low quality (high values of dispersion); (ii) there are still determinations reported during about 30 or more years (postcompilation years) that were not obviously available to those compilers; (iii) the precision of more recent determinations is likely to have improved due to the availability of online computers on most modern instruments; (iv) newer more reliable statistical techniques are now available for improving both precision and accuracy of the statistical inferences, e.g., the use of discordancy tests with the highest power and lowest swamping and masking effects [18, 48, 50–52]; and (v) importantly, new computer programs have been developed by our group [52–54], available at http://tlaloc.ier.unam.mx for download or online processing of data (after previous registration onto our server), which can be advantageously used for efficient processing of experimental databases.

The same kinds of objections are applicable even today for the originator's websites, such as https://gbank.gsj.jp/geostandards/welcome.html for Japanese GRMs or https://crustal.usgs.gov/geochemical_reference_standards for United States GRMs. The statistical information at these websites is based on early compilations (around 30 or more years ago). Furthermore, we were unable to use the recent work [55] because this paper reported significantly larger uncertainty values as compared to those achievable from our new validated statistical procedure [51–54]; besides, updated statistical information on the mean and its uncertainty was not available in [55] for many GRMs used in our work.

The initial databases were complemented by individual data from a large number of posterior publications (~480; Table S1), whose complete listing is available at our server http://tlaloc.ier.unam.mx under the heading of "Quality Control." These major element data were classified according to the analytical method groupings [56]. Data from each method group were considered as a univariate statistical sample. Appropriate discordancy and significance tests were applied from thoroughly automatized software UDASys2 [52] and UDASys3 (unpublished), which, in their "recommended procedure," apply the most powerful five (two new and three conventional) recursive tests with prior application of respective single-outlier tests having nil swamping and low masking effects [48, 57–60]. Although the application of discordancy tests is identical for both UDASys2 and UDASys3, the difference lies in that the latter applies the

significance (ANOVA, F and $t$) tests in order to provide the final results automatically.

The resulting statistical information after the application of well-known discordancy tests at the strict 99% confidence level (mean and uncertainty values rounded according to the flexible rules [18]) is listed in Table S2. These GRM compositional data showed by far the lowest 99% uncertainty (Table S2), much lower than any existing compilation [31–47, 55]. We may also stress once again that this was achieved through an objective combination of discordancy tests having the highest performance and lowest swamping and masking effects [17, 18, 48, 53], i.e., from the methodology having the lowest type I and type II errors and the highest power.

Therefore, the population mean of these GRMs is now known within the narrowest possible 99% confidence limits of the mean to best represent the concentration ($x$) axis in the instrumental calibrations as suggested [2, 5, 7, 10, 17, 18, 53]. These data (in units of % m/m; Table S2) will also be useful for those who wish to achieve instrumental calibrations or simply use them for quality control of their results for rock and mineral matrices.

## 3. XRF Instrumentation and Intensity Measurements

A wavelength dispersive X-ray fluorescence (WDXRF) spectrometer Rigaku ZSX Primus II model (rhodium X-ray tube; 4 kW maximum power) was used for this work. We made the effort to best represent the response ($y$) axis ($x$-ray intensity in the units of kilo counts per second, $kc{\cdot}s^{-1}$) for the calibrations. For each GRM, duplicate (41 samples) or even triplicate (8 samples) pressed powder pellets were prepared. First, an appropriate amount of each GRM was dried overnight in an oven at about 105°C. For each pellet, accurately weighed 3.5 g of moisture-free GRM was thoroughly mixed with accurately weighed 3.0 g pure N,N′-ethylene bis(stearamide) beads, <840 $\mu$m as wax (Sigma-Aldrich), and stored in a desiccator. Pressed powder pellets were prepared at 20 $tons{\cdot}inch^{-2}$ pressure (about 310 MPa). However, for 10 GRMs, sufficient material was not available; therefore, only a single pellet could be prepared but the measured intensity uncertainty ($u_{99}$) at the 99% confidence level was increased by a factor of 2 to take into account the sample preparation variance. Similarly, accurately weighed 6.5 g of pure N,N′-ethylene bis(stearamide) beads, <840 $\mu$m as wax, was pressed to prepare a procedure blank sample. This was done in duplicate.

For the intensity measurements, the optimum instrumental conditions were first established through preliminary experiments prior to the routine measurements (Table S2). Each pellet was run at least 8 to 10 times in a random sequence, along with two drift monitors prepared from two volcanic rocks (basalt and rhyolite) from the San Luis Potosí Volcanic Field, San Luis Potosí (central Mexico).

The peak and background measuring conditions and time periods are also listed in Table S3. Appropriate mean drift corrections from two monitors were applied to all intensity measurements. Both monitors were run randomly 8 to 10 times each day. First, the expected monitor intensity was established as an average value of the first two days when the intensities were fairly stable and reproducible. Then, the average drift correction factors were calculated for each chemical element from the two monitors run in the XRF instrument periodically before and after a set of GRMs used for the calibration. These correction factors were then applied to the bracketed GRMs for the entire period of calibration, including the first two days and analysis of "unknown" samples.

Now, although the X-ray counts may obey a Poisson distribution, we are dealing with average values of count rates, which are likely to follow a normal distribution because of the central limit theorem. A normal distribution of measured intensities was also assured for each pellet from the application of discordancy tests as explained above for GRM concentrations. The intensity results for all pellets from a given GRM were then combined, the tests applied again to the combined data, and new mean and 99% uncertainty values were calculated for X-ray intensity of each GRM. This was done to take into account the variance of the sample preparation method, which was significantly higher than the instrumental variance of intensity measurements for individual pellets. The drift-corrected intensity values and their 99% uncertainties ($kc{\cdot}s^{-1}$) for all GRMs, along with the concentration data and their 99% uncertainties (% m/m), are listed in Table S2.

## 4. Regression Models

Two different regression models (OLR and UWLR) were used and compared in this work. The OLR model most frequently used for instrumental calibrations ($x$-axis concentration and $y$-axis response; GRM concentration and X-ray intensity, respectively, in XRF spectrometry) requires the following assumptions to be fulfilled [4, 7, 10, 12–18]: (i) all errors are in the $y$-axis; (ii) $x$-axis is either error-free or has at most 10% error of the $y$-axis errors; (iii) errors in both axes are normally distributed; and (iv) errors in the $y$-axis are homoscedastic. Some or all of these assumptions are violated in most instrumental calibrations through the OLR model.

Thus, from the literature on the GRMs, it has been demonstrated that the concentration axis is not error-free (see non-zero uncertainties for all GRM concentrations in Table S2) [31–47, 51–53]. One can also clearly see that the errors in the intensity axis are not homoscedastic (see unequal, i.e., heteroscedastic uncertainties for any element in different GRMs in Table S2). For a heteroscedastic linear regression system, even if each error or noise term is still Gaussian, the OLR model is no longer the maximum likelihood estimate and consequently, it is no longer efficient [10]. The main advantage that the WLR has over the OLR is the ability to handle regression situations in which the data points are of varying quality as is the case with most instruments including the XRF spectrometers.

However, the major disadvantage of the WLR is that the approach is based on the assumption that the weights are known exactly. They can be estimated using several different equations or algorithms, but when the weights are produced

from small numbers of replicated observations, the regression parameters can be unpredictably affected [10]. In the example of the XRF calibration that we are presenting, the numbers of observations were relatively large for both the $x$ and $y$ axes (concentration and X-ray intensity parameters). Besides, instead of the sample variance, we used the uncertainty values (that take into account the number of observations in the formula for uncertainty or confidence limits of the mean calculations) [2, 18] for estimating the weight factors. The problem of the sensitivity to outliers in the regression equations [10] was also appropriately handled by discordancy tests programmed in the UDASys and BiDASys software [53, 54, 61].

Therefore, although frequently used, the OLR model is not statistically correct or coherent. The statistically coherent WLR, especially the uncertainty-based WLR (UWLR [17]) model, should be used. The confidence level, such as 95% or 99% (significance level of 5% or 1%, respectively, or $\alpha$ of 0.05 and 0.01, respectively), can be explicitly expressed in the confidence limits of the mean or uncertainty used in the UWLR model as well as to estimate the weight factors [17]. We will deal with the 99% uncertainty to have the type I error small (about 1%). Unfortunately, software of most analytical instruments, including XRF spectrometers, allows only the OLR calibration. Therefore, any sophisticated regression model, such as the UWLR, will have to be applied outside the instrumental software. Thus, the probability concept (99% confidence level) can be explicitly used in the UWLR model for weight factors based on the inverse of the squared 99% uncertainty of the mean.

We now present a synthesis of the regression equations for instrumental calibrations [2, 10, 17, 18, 61].

*4.1. Ordinary Least-Squares Linear Regression (OLR) Model.* Let us assume that we have a series of $n$ reference materials or standard calibrators having individual mean concentrations $x_i$ with respective uncertainties $u_{x_i}$ where $i$ varies from 1 to $n$. In order to calibrate an instrument, each of these $n$ calibrators were run several times, obtaining individual mean responses $y_i$ with respective uncertainties $u_{y_i}$ where $i$ varies from 1 to $n$. Thus, we have $n$ bivariate concentration-response data pairs or calibrators $(x_i,\ y_i)$ with the respective uncertainties $(u_{x_i},\ u_{y_i})$.

We can apply the OLR model to these data for obtaining a calibration equation. The OLR fits a least-squares linear equation to the $n$ pairs $(x_i,\ y_i)$ but does not take into account the respective uncertainties $(u_{x_i},\ u_{y_i})$.

The general regression equation for the OLR is as follows (the subscript O is for the OLR model):

$$y_{\mathrm{O}}\left(\pm u_{y_{\mathrm{O}}}\right) = b_{\mathrm{O}}\left(\pm u_{b_{\mathrm{O}}}\right) + \left[m_{\mathrm{O}}\left(\pm u_{m_{\mathrm{O}}}\right) \times x\right], \tag{1}$$

where $m$ is the slope, $u_m$ is the resulting uncertainty in the slope, $b$ is the intercept, $u_b$ is the resulting uncertainty in the intercept, $x$ is the independent variable, $y_{\mathrm{O}}$ is the dependent variable from the OLR model, and $u_{y_{\mathrm{O}}}$ is the resulting uncertainty in $y$. The following equations allow the calculations of these parameters:

$$m_{\mathrm{O}} = \frac{\sum_{i=1}^{n}\{(x_i - \overline{x}) \times (y_i - \overline{y})\}}{\sum_{i=1}^{n}(x_i - \overline{x})^2}, \tag{2}$$

where $\overline{x}$ and $\overline{y}$ are, respectively, the mean values of the $x$ and $y$ variables:

$$u_{m_{\mathrm{O}}} = \left\{\sqrt{\frac{\sum_{i=1}^{n}(y_i - \widehat{y}_i)^2}{(n-2)\sum_{i=1}^{n}(x_i - \overline{x})^2}}\right\} \times t^{\mathrm{CL}}_{(n-2)}, \tag{3}$$

where $\widehat{y}_i$ is the value of $y_{\mathrm{O}}$ for $x_i$ in equation (1) and $t$ is the Student's $t$ test value for $(n-2)$ degrees of freedom, and the superscript CL is the confidence level, generally 95% or 99%:

$$b_{\mathrm{O}} = \overline{y} - (m_{\mathrm{O}} \times \overline{x}),$$

$$u_{b_{\mathrm{O}}} = \left\{\sqrt{\frac{\sum_{i=1}^{n}(y_i - \widehat{y}_i)^2 \times \sum_{i=1}^{n} x_i^2}{n(n-2)\sum_{i=1}^{n}(x_i - \overline{x})^2}}\right\} \times t^{\mathrm{CL}}_{(n-2)}. \tag{4}$$

It is a general practice in most instrumental calibrations to ignore all uncertainties in equation (1) and use an OLR equation without any error (or uncertainty) as follows:

$$y_{\mathrm{O}} = b_{\mathrm{O}} + [m_{\mathrm{O}} \times x]. \tag{5}$$

The resulting standard deviation values of repeat measurements of unknown samples are reported as the final errors. However, these are only partial errors because the errors in the calibration equation (1) are not taken into account. In this work, we will use equation (1) to report total errors (in fact, 99% uncertainties) for the OLR model.

*4.2. Uncertainty Weighted Least-Squares Linear Regression (UWLR) Model.* For the UWLR model, the $n$ pairs $(x_i,\ y_i)$ of calibrators as well as the respective uncertainties $(u_{x_i},\ u_{y_i})$ are taken into account in order to achieve the best least-squares linear fit.

The uncertainties $u_{x_i}$ in the $x$-axis are first propagated to the $y$-axis, combined with the $u_{y_i}$, and the total uncertainty $u_i$ values on the $y$-axis are used for the weighting factors [2, 10, 17, 18, 61]:

$$u_i = \sqrt{\left(m_{\mathrm{O}} \times u_{x_i}\right)^2 + \left(u_{y_i}\right)^2}. \tag{6}$$

The weights are calculated from $u_i$ as follows:

$$w_i = \frac{n \times (u_i)^{-2}}{\sum_{i=1}^{n}(u_i)^{-2}}, \tag{7}$$

where $w_i$ values have the following property:

$$\sum_{i=1}^{n} w_i = n. \tag{8}$$

Thus, the UWLR fits a linear equation to the $n$ pairs $(x_i,\ y_i)$ with the respective weighting factors $w_i$ as follows (the subscript UW is for the UWLR model):

$$y_{\mathrm{UW}}\left(\pm u_{y_{\mathrm{UW}}}\right) = b_{\mathrm{UW}}\left(\pm u_{b_{\mathrm{UW}}}\right) + \left[m_{\mathrm{UW}}\left(\pm u_{m_{\mathrm{UW}}}\right) \times x\right]. \tag{9}$$

Note that this regression line will pass closer to the data with lesser uncertainty $u_i$. The intercept and slope variables and their uncertainties are calculated from the following equations:

$$m_{\mathrm{UW}} = \frac{\left\{\sum_{i=1}^{n}\left(w_i \times x_i \times y_i\right)\right\} - \left\{n \times \overline{x}_{\mathrm{UW}} \times \overline{y}_{\mathrm{UW}}\right\}}{\left\{\sum_{i=1}^{n}\left(w_i \times x_i^2\right)\right\} - \left\{n \times \left(\overline{x}_{\mathrm{UW}}\right)^2\right\}}, \quad (10)$$

where $\overline{x}_{\mathrm{UW}}$ and $\overline{y}_{\mathrm{UW}}$ are, respectively, the weighted mean values of the $x$ and $y$ variables:

$$u_{m_{\mathrm{UW}}} = \left\{\sqrt{\frac{\sum_{i=1}^{n}\left(y_i - \widehat{y}_{i\mathrm{UW}}\right)^2}{(n-2)\sum_{i=1}^{n}\left(x_i - \overline{x}_{\mathrm{UW}}\right)^2}}\right\} \times t^{\mathrm{CL}}_{(n-2)}, \quad (11)$$

where $\widehat{y}_{i\mathrm{UW}}$ is the value of $y_{\mathrm{UW}}$ for $x_i$ in equation (9):

$$b_{\mathrm{UW}} = \overline{y}_{\mathrm{UW}} - \left(m_{\mathrm{UW}} \times \overline{x}_{\mathrm{UW}}\right),$$

$$u_{b_{\mathrm{UW}}} = \left\{\sqrt{\frac{\sum_{i=1}^{n}\left(y_i - \widehat{y}_{i\mathrm{UW}}\right)^2 \times \sum_{i=1}^{n} x_i^2}{n(n-2)\sum_{i=1}^{n}\left(x_i - \overline{x}_{\mathrm{UW}}\right)^2}}\right\} \times t^{\mathrm{CL}}_{(n-2)}. \quad (12)$$

The best regression equation for a calibration curve should have the following characteristics (without distinguishing the subscripts O and UW): (i) intercept $b$ small approaching to zero; (ii) slope $m$ large; and (iii) both $u_b$ and $u_m$ small. Further, the quality of the regression, whether a calibration curve or any other bivariate relationship, is also expressed as the linear regression coefficient ($r$; $r_{\mathrm{O}}$ and $r_{\mathrm{UW}}$, respectively, for the OLR and UWLR), which is ideally +1.00000 for a calibration curve [5, 18, 61].

## 5. Application of Regression Models for XRF Calibration

*5.1. Original Drift-Corrected Net Intensities and GRM Concentrations: The First Set of Two Regression Equations for Each Element.* The evaluations for both regression types on the drift-corrected net intensity-concentration (Int-Conc) relationships (Table S2) for all major elements from $SiO_2$ to $P_2O_5$ were performed (Table S4), for which the new online software BiDASys was used [61] at http://tlaloc.ier.unam.mx. BiDASys allows the application of the conventional OLR as well as the newly proposed UWLR model [17] and provides the output of all regression parameters in an Excel® file. Contrary to the common practice, we will refrain from showing the numerous $x$-$y$ (variable $x$ is drift-corrected net intensity "Int" and variable $y$ is the GRM concentration "Conc") plots. This is because Table S4 statistically quantifies the visual interpretation of such diagrams. The quality parameters (standard errors $se_b$ and $se_m$, uncertainty $u_b$ and $u_m$, and linear correlation coefficient $r$ and its squared value $R^2$ parameters) are reported in Table S4. Because we are using these several different quality parameters, the concern against the use of solely $R^2$ parameter [62] is not important for comparison purposes.

We will explain the implications of the statistical results for the first element $SiO_2$; the statistics for other elements (Table S4) can be similarly understood. The OLR regression equation from the first row of statistical information in Table S4 is as follows (after the element $SiO_2$, subscript O is for the OLR and p is for provisional concentration; note many decimal places are used for the regression variables in such equations, because these values are not final results, and we should not introduce rounding errors during the calculation stage):

$$C_{\mathrm{SiO_{2Op}}}\left(\pm u_{C_{\mathrm{SiO_{2Op}}}}\right) = 11.47071\,(\pm 4.90411) + \left[0.14325(\pm 0.01605) \times I_{\mathrm{SiO_2}}\left(\pm u_{I_{\mathrm{SiO_2}}}\right)\right]. \quad (13)$$

Similarly, the UWLR equation from the second row of statistical information in Table S4 is as follows:

$$C_{\mathrm{SiO_{2UWp}}}\left(\pm u_{C_{\mathrm{SiO_{2UWp}}}}\right) = -0.01316\,(\pm 2.83181) + \left[0.18539(\pm 0.00927) \times I_{\mathrm{SiO_2}}\left(\pm u_{I_{\mathrm{SiO_2}}}\right)\right]. \quad (14)$$

The implications of these regression equations can be understood from the comparison of the uncertainties of the intercept and slope, which are lower for the UWLR (equation (14)) than for the OLR (equation (13)). This means that the uncertainty of the calculated concentration will be lower for the UWLR than for the OLR. Correspondingly, the $r$ value for the UWLR (0.99004, $n = 60$; $R^2 = 0.98017$) is much higher than that for the OLR (0.95229, $n = 60$; $R^2 = 0.90687$; Table S4). Similar trend in the $r$ (and $R^2$) values was obtained for all other elements except MnO (Table S4).

*5.2. Matrix-Effect-Corrected Intensities and GRM Concentrations: The Second Set of Two Regression Equations for Each Element.* Matrix correction is certainly required because the abovementioned least-squares linear regression fits are far from "perfect" ($r \neq +1.00000$; in fact, $r < 1$; $n = 60$; $r = 0.95229$–$0.99638$ for the OLR and $r = 0.97715$–$0.99760$ for the UWLR; Table S4). There is a vast literature on the subject of matrix effects in XRF and their correction procedures [63–75]. In this study, the Lachance-Traill algorithm [73] was used for the matrix effect correction [63, 71]. This was done outside the XRF instrument software. In a review of the existing algorithms, Rousseau [63] showed that the Lachance-Traill algorithm could be considered as one of the most appropriate procedures for the matrix effect correction because other algorithms have limited application range or lack of accuracy. Thus, for each element from $SiO_2$ to $P_2O_5$, a system of overdetermined equations was solved and the resulting alpha coefficients were used to correct all intensities for matrix effects.

From the alpha coefficients, matrix-corrected intensities and improved concentration values for the GRMs and their uncertainties were calculated iteratively under the condition that the convergence parameter (absolute relative difference

of the GRM calculated and input concentrations) for each compositional constituent ($SiO_2$ to $P_2O_5$) be minimized.

New regression equations for achieving the corrected concentrations were established from the relationship of the calculated GRM concentrations (ConcCalc) and the original GRM concentrations (Conc) given in Table S2, for which the online BiDASys software [61] was used at http://tlaloc.ier.unam.mx. These equations can be formulated from the regression coefficient values given in Table S4 (see ConcCalc-Conc rows corresponding to the OLR and UWLR). Again, we will highlight their significance for $SiO_2$ only.

The OLR regression equation from the third row of statistical information in Table S4 is as follows:

$$C_{\mathrm{SiO_{2O}}}\left(\pm u_{C_{\mathrm{SiO_{2O}}}}\right) = 1.87016\,(\pm 4.2048) + \left[0.96759(\pm 0.07369) \times C_{\mathrm{SiO_{2Oc}}}\left(\pm u_{C_{\mathrm{SiO_{2Oc}}}}\right)\right], \quad (15)$$

where the subscripts O and c stand for the OLR model and calculated concentration (ConcCalc), respectively.

Similarly, the UWLR equation from the fourth row of statistical information in Table S4 is as follows:

$$C_{\mathrm{SiO_{2UW}}}\left(\pm u_{C_{\mathrm{SiO_{2UW}}}}\right) = -0.02185\,(\pm 1.47356) + \left[1.00325(\pm 0.02701) \times C_{\mathrm{SiO_{2UWc}}}\left(\pm u_{C_{\mathrm{SiO_{2UWc}}}}\right)\right], \quad (16)$$

where the subscripts UW and c stand for the UWLR model and calculated concentration (ConcCalc), respectively.

Equations (15) and (16) show that the concentration values from the UWLR would be more reliable (lesser uncertainty values in both intercept and slope) than the OLR model. The $r$ value is higher for the UWLR (0.99704, $n = 60$; $R^2 = 0.99408$; Table S4) than the OLR (0.97710, $n = 60$; $R^2 = 0.95472$).

After the matrix correction, in fact most regression equations are better because all $r$ and $R^2$ values are higher for both OLR and UWLR than without the correction (Table S4; Figure 1 for $r$ only). For the OLR, the matrix correction increased the $r$ values ($n = 60$) from 0.95229–0.99638 ($R^2 = 0.90687 - 0.99277$) to 0.97710–0.99992 ($R^2 = 0.95472 - 0.99994$). Similarly, for the UWLR, this increase was from 0.97715–0.99760 ($R^2 = 0.95472 - 0.99521$) to 0.99704–0.99993 ($R^2 = 0.99408 - 0.99986$). Thus, after matrix correction, all $r$ values increased for both OLR and UWLR. For the UWLR, the $r$ values approached the ideal value of +1.00000 (Figure 1). One has to keep in mind that when the $r$ values are closer to the maximum possible value of 1 (the "ideal" fit), the improvement expressed by the actual (absolute) value of $r$ will apparently be small. However, as long as the $r$ value increases for the UWLR as compared to the OLR (Figure 1; Table S4), we can objectively infer that the UWLR is a better regression model than the OLR.

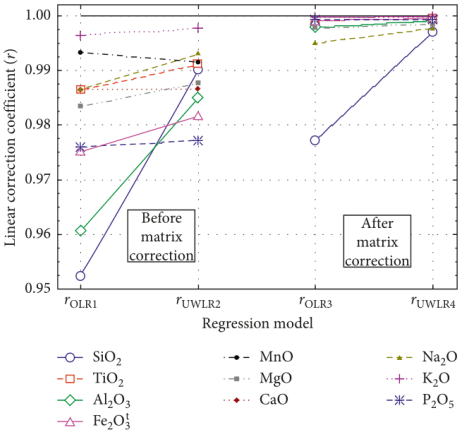


Figure 1: Linear correlation coefficient ($r$) values for the ordinary least-squares linear regression (OLR) and uncertainty-based weighted least-squares linear regression (UWLR) models for the XRF calibration of major elements ($SiO_2$ to $P_2O_5$) in rocks and minerals. OLR1: OLR model 1 for Int-Conc before matrix correction; UWLR2: UWLR model 2 for Int-Conc before matrix correction; OLR: OLR model 3 for ConcCalc-Conc after matrix correction; and UWLR4: UWLR model 4 for ConcCalc-Conc after matrix correction. Symbols are shown as inset. The horizontal line at the $r$ value of 1 represents the "ideal" or "perfect" linear fit.

Before the matrix correction, the intercepts of the Int-Conc regression lines were closer to zero for the UWLR (range ~−0.013 to +0.011) than for the OLR (range ~−2.098 to +11.47) model (Table S4; Figure 2). The same is true for the intercept values (ConcCalc-Conc relationship) after the matrix correction (~−0.025 to +0.021 for the UWLR and ~−0.110 to +1.87 for the OLR).

Finally, the uncertainties on both intercept and slope parameters were mostly lower for the UWLR than the OLR (Table S4). We highlight these differences (lower uncertainties for the UWLR) from dimensionless (free of the measurement units) parameters $\delta u_b$ and $\delta u_m$ defined as follows:

$$\delta u_b = \frac{u_{b_O} - u_{b_{UW}}}{u_{b_{UW}}} \times 100, \qquad \delta u_m = \frac{u_{m_O} - u_{m_{UW}}}{u_{m_{UW}}} \times 100. \quad (17)$$

Plots of these two parameters are presented in Figure 3. If $u_{b_O} > u_{b_{UW}}$, the $\delta u_b$ will be positive, otherwise it will be negative. The same is true for $\delta u_m$. For the comparison of two models OLR and UWLR before the matrix correction, the uncertainty for the UWLR were lower than the OLR for 7 elements (positive $\delta u_b$ and $\delta u_m$), whereas for after the matrix correction, it was so for 8 elements (out of 10; Figure 3). The exceptions were for 3 elements Mno, CaO, and $P_2O_5$ (negative $\delta u_b$ and $\delta u_m$) for the uncertainties before matrix

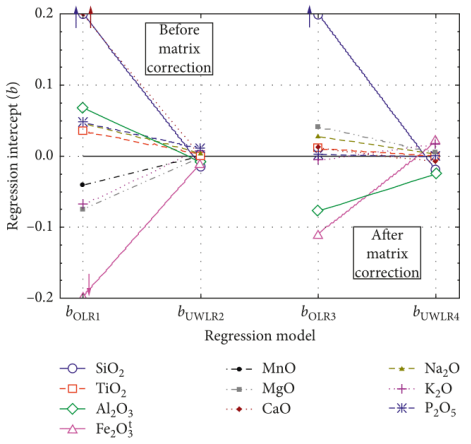


Figure 2: Intercept ($b$) values for the ordinary least-squares linear regression (OLR) and uncertainty-based weighted least-squares linear regression (UWLR) models for the XRF calibration of major elements ($SiO_2$ to $P_2O_5$) in rocks and minerals. Symbols are shown as inset. For abbreviations, see Figure 1. Note some intercept values plotted outside the graph; this is indicated by arrows next to the data point. The horizontal line at the intercept value of zero represents the "ideal" intercept.

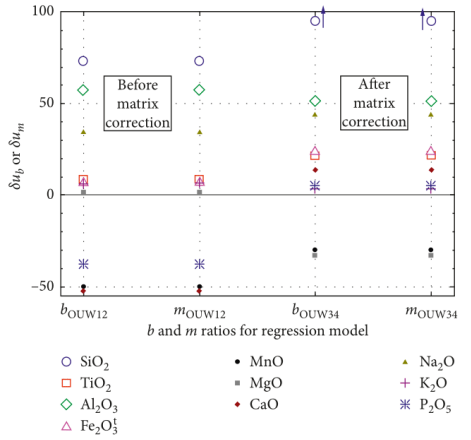


Figure 3: New parameters $\delta u_b$ (for the intercept) and $\delta u_m$ (for the slope) for the evaluation of intercept ($b$) and slope ($m$) of two regression models (OLR: ordinary least-squares linear regression and UWLR: uncertainty-based weighted least-squares linear regression) before (OUW12) and after (OUW34) the matrix correction. The horizontal solid line at the $y$ value of zero represents the line with no difference in the uncertainties of the two models. The arrows indicate that these data plotted above the scale are used for the diagram.

correction and for 2 elements MnO and MgO for those after the matrix correction (Figure 3). Even for the exceptions of the elements MnO and MgO, the UWLR values should be usable (Table S4), i.e., it is not actually necessary to resort to the OLR model for these two exceptions (2 out of 10 cases). Thus, we can use the UWLR model for all purposes.

## 6. Sensitivities of Major Elements

We calculated the sensitivities as the slope of the Conc-IntCorr (GRM concentrations of Table S2 and matrix-corrected intensities of Table S5; see Supplementary Materials at http://tlaloc.ier.unam.mx) from the regression curve (line) for all 10 elements and for both models (Table 1). Because the $r$ values are significantly high (all >0.961, $n = 60$; Table 1) and the residuals are randomly distributed (graphs not shown), the straight line is the most likely, statistically valid fit for the concentration-matrix-corrected intensity data [5, 17, 18]. Therefore, the slope of the regression line represents an average sensitivity value for a given element under the chosen working conditions (Table S3).

The intercept values were closer to zero (zero being the theoretically ideal intercept) for the UWLR regression (~−0.113 to +0.104; Table 1) as compared to the OLR (~−47.8 to +12.3; Table 1). The sensitivity values represented by the slopes of the regression lines (Table 1) were generally similar for both models (~2.69–46.17 $kc{\cdot}s^{-1}{\cdot}\%^{-1}$ for the OLR and ~2.78–59.69 $kc{\cdot}s^{-1}{\cdot}\%^{-1}$ for the UWLR). The sensitivity actually depends on the measuring conditions (Table S3), which were the same for both models.

For the matrix-corrected intensity-concentration (IntCorr-Conc) regressions, the parameters are listed in Table 2. All intercepts for the UWLR model, without exception, were closer to zero as compared to the OLR model. This confirms the superiority of the UWLR model.

## 7. Application to Rock Matrices

The calibrations achieved in this work (Table S4) were applied to the analysis of four GRMs (attapulgite or Fuller's earth clay ATT1; bentonite clay CSB1; granite GH; and tonalite TLM1) taken as "unknown" samples. These GRMs, having similarly complex matrices as the calibration samples, were not included in the calibrations because their mean values were available only from early description or compilations (for ATT1 and CSB1 [76]; for GH [77]; and for TLM1 [78]). We were unsuccessful in complementing these "old" concentration values with newer ones for these GRMs. Therefore, these GRMs were used as unknown samples. They were analysed in exactly the same manner as the calibration samples.

All calculations for the unknown samples were done outside the instrumental software. The drift-corrected net intensities and the corresponding uncertainties were processed from the first set of two regression equations (Int-Conc OLR and UWLR models; Table S4) to obtain provisional concentration and uncertainty values. The

Table 1: Instrumental sensitivities (*x-y*: concentration-matrix-corrected intensity (Conc-IntCorr) regression model; mean and 99% uncertainty) for major elements.

| Element | Regression | | Number of data pairs (calibrators) | Regression equation parameters | | | | | | Quality of regression equation | |
|---|---|---|---|---|---|---|---|---|---|---|---|
| | Variables *x-y* | Model | | Intercept (*b*) | $se_b$ | $u_b$ | Slope (*m*) | $se_m$ | $u_m$ | *r* | $R^2$ |
| $SiO_2$ | Conc-IntCorr | OLR | 60 | −47.8441 | 13.1332 | 34.9772 | 6.3592 | 0.2401 | 0.6395 | 0.96105 | 0.92362 |
| | Conc-IntCorr | UWLR | 60 | 0.1035 | 5.3870 | 14.3471 | 5.3476 | 0.0985 | 0.2623 | 0.99157 | 0.98321 |
| $TiO_2$ | Conc-IntCorr | OLR | 60 | −0.2298 | 0.3000 | 0.7991 | 13.2255 | 0.2889 | 0.7694 | 0.98644 | 0.97307 |
| | Conc-IntCorr | UWLR | 60 | −0.0188 | 0.2637 | 0.7024 | 12.3181 | 0.2539 | 0.6763 | 0.99113 | 0.98235 |
| $Al_2O_3$ | Conc-IntCorr | OLR | 60 | 8.1398 | 4.1673 | 11.0987 | 6.1191 | 0.2269 | 0.6043 | 0.96237 | 0.92615 |
| | Conc-IntCorr | UWLR | 60 | 0.0594 | 3.0552 | 8.1369 | 7.0715 | 0.1663 | 0.4430 | 0.98557 | 0.97135 |
| $Fe_2O_3{}^t$ | Conc-IntCorr | OLR | 60 | 12.2628 | 2.4739 | 6.5886 | 4.3943 | 0.1337 | 0.3561 | 0.97419 | 0.94904 |
| | Conc-IntCorr | UWLR | 60 | 0.0715 | 2.7723 | 7.3835 | 5.4403 | 0.1498 | 0.3991 | 0.98112 | 0.96259 |
| MnO | Conc-IntCorr | OLR | 60 | 2.0367 | 0.2963 | 0.7891 | 46.1686 | 0.6958 | 1.8531 | 0.99348 | 0.98700 |
| | Conc-IntCorr | UWLR | 60 | 0.0147 | 0.7535 | 2.0069 | 59.6875 | 1.7695 | 4.7127 | 0.99160 | 0.98328 |
| MgO | Conc-IntCorr | OLR | 60 | 1.1050 | 1.0231 | 2.7246 | 3.6928 | 0.0901 | 0.2400 | 0.98317 | 0.96662 |
| | Conc-IntCorr | UWLR | 60 | 0.0108 | 0.9641 | 2.5676 | 3.9863 | 0.0849 | 0.2262 | 0.98745 | 0.97505 |
| CaO | Conc-IntCorr | OLR | 60 | −14.3055 | 3.5661 | 9.4974 | 15.4215 | 0.3371 | 0.8977 | 0.98643 | 0.97304 |
| | Conc-IntCorr | UWLR | 60 | −0.0121 | 5.6252 | 14.9814 | 11.5666 | 0.5317 | 1.4160 | 0.98657 | 0.97332 |
| $Na_2O$ | Conc-IntCorr | OLR | 60 | 0.0166 | 0.1553 | 0.4137 | 2.6888 | 0.0571 | 0.1521 | 0.98716 | 0.97449 |
| | Conc-IntCorr | UWLR | 60 | −0.0111 | 0.1154 | 0.3073 | 2.7843 | 0.0424 | 0.1130 | 0.99344 | 0.98692 |
| $K_2O$ | Conc-IntCorr | OLR | 60 | 1.2200 | 0.5896 | 1.5702 | 13.8296 | 0.1431 | 0.3811 | 0.99691 | 0.99383 |
| | Conc-IntCorr | UWLR | 60 | −0.1130 | 0.5491 | 1.4623 | 14.4829 | 0.1333 | 0.3549 | 0.99793 | 0.99587 |
| $P_2O_5$ | Conc-IntCorr | OLR | 60 | −1.7376 | 0.5433 | 1.4469 | 39.1055 | 1.2932 | 3.4442 | 0.96972 | 0.94035 |
| | Conc-IntCorr | UWLR | 60 | 0.0626 | 0.7039 | 1.8747 | 29.4822 | 1.6756 | 4.4624 | 0.96926 | 0.93946 |

*b*, intercept; se, standard error; *u*, uncertainty at 99%; *m*, slope; *r*, linear correlation coefficient; $R^2$, squared linear correlation coefficient.

provisional concentrations were then used to obtain matrix corrections for each sample. The method was iteratively applied with the newer concentrations to obtain the final calculated concentration values (Table 3). These calculated concentration values were used to compute the final mean concentrations ($\bar{x}$) and 99% uncertainties of the mean ($u_{99}$) for each sample from the second sets of regression equations (ConcCalc-Conc, OLR and UWLR models; Table S4). The loss on ignition (LOI) was required to optimise the final results.

The results are listed in Table 3 and compared with the literature compilations [75–77]. On the other hand, because 99% uncertainties were not reported in the original compilations, they were computed for the comparison from the standard deviation, number of determinations, and appropriate two-sided *t* values at 99% confidence level [2, 18].

Firstly, although the mean concentration values determined by the OLR and UWLR models showed a general agreement, the 99% uncertainty values ($u_{99}$; Table 3) were generally lower for the UWLR models, which clearly

Table 2: Regression ($x$-$y$): matrix-corrected intensity-concentration (IntCorr-Conc) parameters.

| Element | Regression | | Number of data pairs (calibrators) | Regression equation parameters | | | | | | Quality of regression equation | |
|---|---|---|---|---|---|---|---|---|---|---|---|
| | Variables $x$-$y$ | Model | | Intercept ($b$) | $se_b$ | $u_b$ | Slope ($m$) | $se_m$ | $u_m$ | $r$ | $R^2$ |
| $SiO_2$ | IntCorr-Conc | OLR | 60 | 10.8541 | 1.6762 | 4.4641 | 0.1452 | 0.0055 | 0.0146 | 0.96105 | 0.92362 |
| | IntCorr-Conc | UWLR | 60 | −0.0148 | 0.9765 | 2.6006 | 0.1848 | 0.0032 | 0.0085 | 0.99157 | 0.98321 |
| $TiO_2$ | IntCorr-Conc | OLR | 60 | 0.0344 | 0.0220 | 0.0587 | 0.0736 | 0.0016 | 0.0043 | 0.98644 | 0.97307 |
| | IntCorr-Conc | UWLR | 60 | 0.0020 | 0.0204 | 0.0542 | 0.0801 | 0.0015 | 0.0040 | 0.99114 | 0.98235 |
| $Al_2O_3$ | IntCorr-Conc | OLR | 60 | −0.1675 | 0.6763 | 1.8011 | 0.1514 | 0.0056 | 0.0150 | 0.96237 | 0.92615 |
| | IntCorr-Conc | UWLR | 60 | −0.0070 | 0.4419 | 1.1769 | 0.1397 | 0.0037 | 0.0098 | 0.98557 | 0.97135 |
| $Fe_2O_3{}^t$ | IntCorr-Conc | OLR | 60 | −2.0576 | 0.5960 | 1.5873 | 0.2160 | 0.0066 | 0.0175 | 0.97419 | 0.94904 |
| | IntCorr-Conc | UWLR | 60 | −0.0092 | 0.5458 | 1.4536 | 0.1772 | 0.0060 | 0.0160 | 0.98112 | 0.96259 |
| MnO | IntCorr-Conc | OLR | 60 | −0.0412 | 0.0067 | 0.0178 | 0.0214 | 0.0003 | 0.0009 | 0.99348 | 0.98700 |
| | IntCorr-Conc | UWLR | 60 | 0.0001 | 0.0134 | 0.0356 | 0.0165 | 0.0007 | 0.0017 | 0.99160 | 0.98328 |
| MgO | IntCorr-Conc | OLR | 60 | −0.0977 | 0.2748 | 0.7319 | 0.2618 | 0.0064 | 0.0170 | 0.98317 | 0.96662 |
| | IntCorr-Conc | UWLR | 60 | −0.0014 | 0.2692 | 0.7168 | 0.2376 | 0.0063 | 0.0167 | 0.98745 | 0.97505 |
| CaO | IntCorr-Conc | OLR | 60 | 1.0561 | 0.2173 | 0.5789 | 0.0631 | 0.0014 | 0.0037 | 0.98643 | 0.97304 |
| | IntCorr-Conc | UWLR | 60 | 0.0064 | 0.4616 | 1.2293 | 0.0853 | 0.0029 | 0.0078 | 0.98657 | 0.97331 |
| $Na_2O$ | IntCorr-Conc | OLR | 60 | 0.0447 | 0.0567 | 0.1511 | 0.3624 | 0.0077 | 0.0205 | 0.98716 | 0.97449 |
| | IntCorr-Conc | UWLR | 60 | 0.0054 | 0.0421 | 0.1122 | 0.3558 | 0.0057 | 0.0152 | 0.99345 | 0.98693 |
| $K_2O$ | IntCorr-Conc | OLR | 60 | −0.0720 | 0.0430 | 0.1146 | 0.0719 | 0.0007 | 0.0020 | 0.99691 | 0.99383 |
| | IntCorr-Conc | UWLR | 60 | 0.0082 | 0.0391 | 0.1042 | 0.0687 | 0.0007 | 0.0018 | 0.99793 | 0.99587 |
| $P_2O_5$ | IntCorr-Conc | OLR | 60 | 0.0537 | 0.0128 | 0.0341 | 0.0241 | 0.0008 | 0.0021 | 0.96972 | 0.94035 |
| | IntCorr-Conc | UWLR | 60 | 0.0010 | 0.0202 | 0.0538 | 0.0320 | 0.0013 | 0.0033 | 0.96929 | 0.93952 |

$b$, intercept; se, standard error; $u$, uncertainty at 99%; $m$, slope; $r$, linear correlation coefficient; $R^2$, squared linear correlation coefficient.

indicates that this model should be used routinely, instead of the conventional OLR model. Secondly, there is also a general agreement among all mean values, especially for granite GH and tonalite TLM1. The two clay samples (ATT1 and CSB1) showed some differences with the preliminary values obtained by the originators of these GRMs [75]. These values for comparison were obtained in only one laboratory. The errors (uncertainties) reported in the literature were underestimated, because they did not include those resulting from the calibrations. Furthermore, the accuracy data of the originator's laboratory were not reported [75], such as the results for established GRMs and their comparison to other laboratories.

## 8. Computer Program XRFCalcUnknown

An online computer program JSpectrom_XRFCalcUnknown will be available at our server https://tlaloc.ier.unam.mx for use for unknown samples, which will guide other users to achieve the UWLR calibration outside of the instrumental software and its routine application to unknown samples. This program incorporates the iteration process to achieve reliable

Table 3: Application of the XRF calibrations for the determination of major elements (mean concentration in % m/m; mass/mass unit expressed in percentage, habitually called wt.% and 99% uncertainty $u_{99}$ or simply $u$) in four rock samples (data reported as rounded value following flexible criteria proposed by [18]) and their comparison with the literature data.

| Rock | Method (ref.) | $SiO_2$ | | $TiO_2$ | | $Al_2O_3$ | | $Fe_2O_3{}^t$ | | MnO | | MgO | | CaO | | $Na_2O$ | | $K_2O$ | | $P_2O_5$ | |
|---|---|---|---|---|---|---|---|---|---|---|---|---|---|---|---|---|---|---|---|---|---|
| | | $\bar{x}$ | $u_{99}$ | $\bar{x}$ | $u_{99}$ | $\bar{x}$ | $u_{99}$ | $\bar{x}$ | $u_{99}$ | $\bar{x}$ | $u_{99}$ | $\bar{x}$ | $u_{99}$ | $\bar{x}$ | $u_{99}$ | $\bar{x}$ | $u_{99}$ | $\bar{x}$ | $u_{99}$ | $\bar{x}$ | $u_{99}$ |
| ATT1 | OLR | 61.7 | 6.1 | 0.4961 | 0.0173 | 10.00 | 0.49 | 4.246 | 0.292 | 0.02394 | 0.00188 | 5.373 | 0.377 | 2.139 | 0.086 | 0.083 | 0.094 | 0.7777 | 0.0378 | 0.8074 | 0.0134 |
| | UWLR | 62.30 | 2.23 | 0.4951 | 0.0143 | 9.666 | 0.321 | 4.402 | 0.235 | 0.02416 | 0.00269 | 6.17 | 0.52 | 2.144 | 0.076 | 0.058 | 0.065 | 0.7781 | 0.0366 | 0.7828 | 0.0125 |
| | [76] | 59.6 | 0.8 | 0.49 | 0.015 | 9.50 | 0.29 | 3.31 | 0.06 | 0.025 | 0.018 | 9.14 | 0.06 | 1.87 | 0.03 | 0.1 | 0.03 | 0.86 | 0.06 | 0.76 | 0.01 |
| CSB1 | OLR | 52.7 | 5.5 | 0.1448 | 0.0157 | 24.60 | 0.71 | 3.493 | 0.289 | 0.01408 | 0.00188 | 1.523 | 0.270 | 1.117 | 0.085 | 2.126 | 0.119 | 0.4169 | 0.0374 | 0.0383 | 0.0060 |
| | UWLR | 52.76 | 2.04 | 0.1343 | 0.0130 | 24.40 | 0.48 | 3.564 | 0.233 | 0.01398 | 0.00268 | 1.604 | 0.398 | 1.105 | 0.075 | 2.123 | 0.083 | 0.4337 | 0.0361 | 0.0357 | 0.0057 |
| | [76] | 55.3 | 0.8 | 0.16 | 0.03 | 21.75 | 0.18 | 3.88 | 0.03 | 0.020 | 0.003 | 1.94 | 0.08 | 1.28 | 0.06 | 2.07 | 0.20 | 0.54 | 0.03 | — | — |
| GH | OLR | 73.3 | 6.5 | 0.0968 | 0.0157 | 13.98 | 0.53 | 1.336 | 0.285 | 0.05084 | 0.00190 | 0.074 | 0.262 | 0.843 | 0.084 | 3.618 | 0.151 | 5.302 | 0.059 | 0.0119 | 0.0059 |
| | UWLR | 73.62 | 2.38 | 0.0861 | 0.0129 | 13.714 | 0.349 | 1.466 | 0.229 | 0.05064 | 0.00271 | 0.038 | 0.390 | 0.828 | 0.074 | 3.625 | 0.105 | 5.216 | 0.057 | 0.0091 | 0.0057 |
| | [77] | 75.8 | 0.39 | 0.08 | 0.07 | 12.50 | 0.16 | 1.34 | 0.2 | 0.05 | 0.009 | 0.03 | 0.18 | 0.69 | 0.13 | 3.85 | 0.11 | 4.76 | 0.05 | 0.08 | 0.03 |
| TLM1 | OLR | 57.7 | 5.7 | 0.8497 | 0.0200 | 17.38 | 0.58 | 7.637 | 0.306 | 0.11614 | 0.00199 | 3.972 | 0.319 | 6.807 | 0.100 | 2.675 | 0.130 | 1.7585 | 0.0403 | 0.1378 | 0.0063 |
| | UWLR | 57.67 | 2.11 | 0.8402 | 0.0165 | 17.046 | 0.386 | 7.682 | 0.247 | 0.11592 | 0.00281 | 4.281 | 0.447 | 6.821 | 0.088 | 2.667 | 0.090 | 1.742 | 0.0390 | 0.1336 | 0.0060 |
| | [78] | 58.85 | 0.35 | 0.820 | 0.013 | 17.48 | 0.25 | 7.67 | 0.15 | 0.105 | 0.013 | 3.3 | 0.08 | 6.67 | 0.08 | 2.98 | 0.07 | 1.67 | 0.08 | 0.15 | 0.013 |

concentrations as demonstrated in this work. Example input data files and a ReadMe document are provided to facilitate the application of JSpectrom_XRFCalcUnknown. One important aspect of the program is that for a sample to be identified as an "unknown" sample, the value of LOI (loss on ignition in percent) should be input in the first sheet of the measured intensity file.

A novel aspect of the present work is that total 99% uncertainty can be calculated for individual datum in a given sample (treated as unknown; Table 3). This innovation if put into practice can entirely change the geochemical literature, and in fact make geochemistry a more quantitative science. Further, if an appropriate GRM is analysed as unknown and the analytical data (both mean and total uncertainly) are reported along with the field samples, the data accuracy can be statistically judged from such reports.

## 9. Conclusions

The XRF spectrometer calibrated under both the OLR and UWLR models clearly showed that the UWLR provides more reliable results (lower uncertainty estimates) than the OLR model commonly practiced for most XRF instruments. The sensitivity and LOD values presented for both models also supported the use of the UWLR model. The UWLR model should therefore be used routinely in such calibrations. The use of a large number of well-characterized GRMs is also recommended for this purpose as illustrated in the present work. The application of our procedure was well documented for the analysis of similarly complex rock matrices. The reporting of total uncertainty values for individual datum is highly recommended for all future geochemical research. This work for the XRF shows that such a practice is easy to achieve in any other analytical calibration procedures. As the major conclusion, we can confirm that the statistically coherent WLR model was shown to perform better than the frequently used conventional statistically incoherent OLR model.

## Data Availability

The list of all compiled references (Table S1) will be available at http://tlaloc.ier.unam.mx. These references are not included with the manuscript because they are too many (~480). Similarly, as stated, the online program JSpectrom_XRFCalcUnknown will also be added onto this web portal http://tlaloc.ier.unam.mx. This program needs to be available online for future use; it cannot be submitted to the journal.

## Conflicts of Interest

The authors declare that they have no conflicts of interest.

## Acknowledgments

This work was supported through the Newton Advanced Fellowship Award (grant NA160116) of the Royal Society, U.K., to the second author (SKV) and from the sabbatical stay of SPV at IPICYT. We are grateful to the Nanoscience and Nanotechnology National Research Laboratory (LINAN), Carbon Nanostructures and Two-Dimensional Systems Laboratory at IPICYT, and Dr. Emilio Muñoz-Sandoval for providing access to the required facilities. M. Abdelaly Rivera-Gómez is grateful to CTIC and DGAPA for a postdoctoral fellowship at the ICML-UNAM. Darío Torres-Sánchez and Mauricio Rosales-Rivera thank CONACYT for the doctoral fellowship. The GRM compilation was initiated long ago in our group by the participation of R. González-Ramírez although the bulk of the work was carried out by the present authors. We are grateful to the IER-UNAM library personnel for efficiently providing some of the literature materials for compilation and to Alfredo Quiroz-Ruiz for the maintenance of the computing facility at IER-UNAM. Diego Villanueva-López helped us during the pressed powder pellet preparation and for checking the correctness of the information in GRM databases.

## Supplementary Materials

Five tables (Tables S1–S5) are provided. (*Supplementary Materials*)

## References

[1] H. R. Rollinson, *Using Geochemical Data: Evaluation, Presentation, Interpretation*, Longman Scientific Technical, Essex, UK, 1993.

[2] J. N. Miller and J. C. Miller, *Statistics and Chemometrics for Analytical Chemistry*, Pearson Prentice Hall, Essex, UK, 2010.

[3] R. G. Brereton, "Chemometrics in analytical chemistry. A review," *Analyst*, vol. 112, pp. 1635–1657, 1987.

[4] M. Guevara, S. P. Verma, F. Velasco-Tapia, R. Lozano-Santa Cruz, and P. Girón, "Comparison of linear regression models for quantitative geochemical analysis: an example using x-ray fluorescence spectrometry," *Geostandards and Geoanalytical Research*, vol. 29, no. 3, pp. 271–284, 2005.

[5] P. R. Bevington, *Data Reduction and Error Analysis for the Physical Sciences*, Mc-Graw Hill Book Company, New York, NY, USA, 1969.

[6] D. York, "Least squares fitting of a straight line with correlated errors," *Earth and Planetary Science Letters*, vol. 5, pp. 320–324, 1969.

[7] A. H. Kalantar, "Weighted least squares evaluation of slope from data having errors in both axes," *Trends in Analytical Chemistry*, vol. 9, no. 5, pp. 149–151, 1990.

[8] K. L. Mahon, "The New "York" regression: application of an improved statistical method to geochemistry," *International Geology Review*, vol. 38, no. 4, pp. 293–303, 1996.

[9] M. E. Zorn, R. D. Gibbons, and W. C. Sonzogni, "Weighted least-squares approach to calculating limits of detection and quantification by modeling variability as a function of concentration," *Analytical Chemistry*, vol. 69, no. 15, pp. 3069–3075, 1997.

[10] N. R. Draper and H. Smith, *Applied Regression Analysis*, John Wiley & Sons, New York, NY, USA, 1998.

[11] A. Schick, "Improving weighted least-squares estimates in heteroscedastic linear regression when the variance is a function of the mean response," *Journal of Statistical Planning and Inference*, vol. 76, no. 1-2, pp. 127–144, 1999.

[12] A. Sayago, M. Boccio, and A. G. Asuero, "Fitting straight lines with replicated observations by linear regression: the least

squares postulates," *Critical Review of Analytical Chemistry*, vol. 34, no. 1, pp. 39–50, 2004.

[13] A. Sayago and A. G. Asuero, "Fitting straight lines with replicated observations by linear regression: Part II. Testing for homogeneity of variances," *Critical Review of Analytical Chemistry*, vol. 34, no. 3-4, pp. 133–146, 2004.

[14] A. G. Asuero, A. Sayago, and A. G. González, "The correlation coefficient: an overview," *Critical Review of Analytical Chemistry*, vol. 36, no. 1, pp. 41–59, 2006.

[15] J. Tellinghuisen, "Weighted least-squares in calibration: what difference does it make?," *Analyst*, vol. 132, no. 6, pp. 536–543, 2007.

[16] S. P. Verma, L. Díaz-González, and R. González-Ramírez, "Relative efficiency of single-outlier discordancy tests for processing geochemical data on reference materials and application to instrumental calibration by a weighted least-squares linear regression model," *Geostandards and Geoanalytical Research*, vol. 33, no. 1, pp. 29–49, 2009.

[17] S. P. Verma, "Geochemometrics," *Revista Mexicana de Ciencias Geológicas*, vol. 29, no. 1, pp. 276–298, 2012.

[18] S. P. Verma, *Análisis Estadístico de Datos Composicionales*, Universidad Nacional Autónoma de México, CDMX, Mexico, 2016.

[19] P. J. Potts, *A Handbook of Silicate Rock Analysis*, Blackie, Glasgow, UK, 1987.

[20] P. J. Potts and P. C. Webb, "X-ray fluorescence spectrometry," *Journal of Geochemical Exploration*, vol. 44, no. 1–3, pp. 251–296, 1992.

[21] M. El Maghraoui, J.-L. Joron, J. Etoubleau, P. Cambon, and M. Treuil, "Determination of forty four major and trace elements in GPMA magmatic rock reference materials using x-ray fluorescence spectrometry (XRF) and instrumental neutron activation analysis (INAA)," *Geostandards Newsletter: Journal of Geostandards and Geoanalysis*, vol. 23, no. 1, pp. 59–68, 1999.

[22] K. Tani, H. Kawabata, Q. Chang, K. Sato, and Y. Tatsumi, "Quantitative analyses of silicate rock major and trace elements by X-ray fluorescence spectrometer: evaluation of analytical precision and sample preparation," *Frontiers in Research of Earth Evolution*, vol. 2, pp. 1–8, 2004.

[23] J. Enzweiler and M. A. Vendemiatto, "Analysis of sediments and soils by x-ray fluorescence spectrometry using matrix corrections based on fundamental parameters," *Geostandards and Geoanalytical Research*, vol. 28, no. 1, pp. 103–112, 2005.

[24] L. P. Bédard, "Neutron activation analysis, atomic absorption and x-ray fluorescence spectrometry review for 2004-2005," *Geostandards and Geoanalytical Research*, vol. 30, no. 3, pp. 183–186, 2006.

[25] K. Nakayama, Y. Shibata, and T. Nakamura, "Glass beads/x-ray fluorescence analysis of 42 components in felsic rocks," *X-Ray Spectrometry*, vol. 36, no. 2, pp. 130–140, 2007.

[26] W. Wu, T. Xu, Q. Hao, Q. Wang, S. Zhang, and C. Zhao, "Applications of x-ray fluorescence analysis of rare earths in China," *Journal of the Rare Earths*, vol. 28, pp. 30–36, 2010.

[27] H. Mashima, "XRF analyses of major and trace elements in silicate rocks calibrated with synthetic standard samples," *Natural Resources of Environment and Humans*, vol. 6, pp. 39–50, 2016.

[28] D. Robinson and M. C. Bennett, "XRF determination of 19 trace elements in international geochemical reference samples," *Geostandards Newsletter*, vol. 5, no. 2, pp. 175–181, 1981.

[29] S. P. Verma, T. Besch, M. Guevara, and B. Schulz-Dobrich, "Determination of twelve trace elements in twenty-seven and ten major elements in twenty-three geochemical reference samples by X-Ray fluorescence spectrometry," *Geostandards Newsletter*, vol. 16, no. 2, pp. 301–309, 1992.

[30] X. Wang, G. Li, Q. Zhang, and Y. Wang, "Determination of major/minor and trace elements in seamount phosphorite by XRF spectrometry," *Geostandards and Geoanalytical Research*, vol. 28, no. 1, pp. 81–88, 2004.

[31] K. Govindaraju, "1987 compilation report on Ailsa Craig Granite AC-E with the participation of 128 GIT-IWG laboratories," *Geostandards Newsletter*, vol. 11, no. 2, pp. 203–255, 1987.

[32] K. Govindaraju, "Report (1980) on three GIT-IWG rock reference samples: anorthosite from Greenland, AN-G; basalte d' Essey-la-Côte, BE-N; granite de Beauvoir, MA-N," *Geostandards Newsletter*, vol. 4, no. 1, pp. 49–138, 1980.

[33] E. S. Gladney and I. Roelandts, "1987 compilation of elemental concentration data for USGS BHVO-1, MAG-1, QLO-1, RGM-1, SCo-1, SDC-1, SGR-1, and STM-1," *Geostandards Newsletter*, vol. 12, no. 2, pp. 253–262, 1988.

[34] K. Govindaraju, "Report (1967-1981) on four ANRT rock reference samples: diorite DR-N, serpentine UB-N, bauxite BX-N, disthene DT-N," *Geostandards Newsletter*, vol. 6, no. 1, pp. 91–159, 1982.

[35] E. S. Gladney and I. Roelandts, "1987 compilation of elemental concentration data for USGS BIR-1, DNC-1 and W-2," *Geostandards Newsletter*, vol. 12, no. 1, pp. 63–118, 1988.

[36] S. Abbey, C. R. McLeod, and W. Liang-Guo, "FeR-1, FeR-2, FeR-3 and FeR-4 Four Canadian iron-formation samples prepared for use as reference materials," Geological Survey of Canada Report, Geological Survey of Canada, Ottawa, ON, Canada, 1983.

[37] K. Govindaraju, "Report (1973-1984) in two ANRT geochemical reference samples: granite GS-N and Potash Feldspar FK-N," *Geostandards Newsletter*, vol. 8, no. 2, pp. 173–206, 1984.

[38] E. S. Gladney, C. E. Burns, and I. Roelandts, "1982 compilation of elemental concentration data for the United States Geological Survey's geochemical exploration reference samples GXR-1 to GXR-6," *Geostandards Newsletter*, vol. 8, no. 2, pp. 119–154, 1984.

[39] E. S. Gladney and I. Roelandts, "1988 compilation of elemental concentration data for USGS geochemical exploration reference materials GXR-1 to GXR-6," *Geostandards Newsletter*, vol. 14, no. 1, pp. 21–118, 1990.

[40] K. Govindaraju, "Report (1984) on two GIT-IWG geochemical reference samples: albite from Italy, AL-I and Iron Formation sample from Greenland, IF-G," *Geostandards Newsletter*, vol. 8, no. 1, pp. 63–113, 1984.

[41] N. Imai, S. Terashima, S. Itoh, and A. Ando, "1994 compilation of analytical data for minor and trace elements in seventeen GSJ geochemical reference samples, "igneous rock series"," *Geostandards and Geoanalytical Research*, vol. 19, no. 2, pp. 135–213, 1995.

[42] S. Terashima, "Elemental concentrations in nine new GSJ rock reference samples," *Geostandards Newsletter*, vol. 14, no. 1, pp. 1–5, 1990.

[43] S. Terashima, S. Itoh, M. Ujiie, H. Kamioka, T. Tanaka, and H. Hattori, "Three new GSJ rock reference samples: rhyolite JR-3, gabbro JGb-2 and hornblendite JH-1," *Geostandards Newsletter*, vol. 17, no. 1, pp. 1–4, 1993.

[44] S. Abbey, "Reference materials: rock samples SY-2, SY-3, MRG-1," Energy, Mines and Resources Canada Report, Natural Resources Canada, Ottawa, ON, Canada, 1979.

[45] K. Govindaraju, "Report (1968-1978) on two mica reference samples: biotite Mica-Fe and phlogopite Mica-Mg," *Geostandards Newsletter*, vol. 3, no. 1, pp. 3–24, 1979.

[46] T. W. Steele and R. G. Hansen, "Major element data (1966-1978) for the six "Nimroc" reference samples," *Geostandards Newsletter*, vol. 3, no. 2, pp. 135–172, 1979.

[47] E. S. Gladney, E. A. Jones, E. J. Nickell, and I. Roelandts, "1988 compilation of elemental concentration data for USGS DTS-1, G-1, PCC-1, and W-1," *Geostandards Newsletter*, vol. 15, no. 2, pp. 199–396, 1991.

[48] V. Barnett and T. Lewis, *Outliers in Statistical Data*, John Wiley & Sons, Chichester, UK, 1994.

[49] K. Hayes, A. Kinsella, and N. Coffey, "A note on the use of outlier criteria in Ontario laboratory quality control schemes," *Clinical Biochemistry*, vol. 40, no. 3-4, pp. 147–152, 2007.

[50] S. P. Verma, L. Díaz-González, J. A. Pérez-Garza, and M. Rosales-Rivera, "Quality control in geochemistry from a comparison of four central tendency and five dispersion estimators and example of a geochemical reference material," *Arabian Journal of Geosciences*, vol. 9, p. 740, 2016.

[51] S. P. Verma, L. Díaz-González, J. A. Pérez-Garza, and M. Rosales-Rivera, "Erratum to: quality control in geochemistry from a comparison of four central tendency and five dispersion estimators and example of a geochemical reference material," *Arabian Journal of Geosciences*, vol. 10, p. 24, 2017.

[52] S. P. Verma, M. Rosales-Rivera, L. Díaz-González, and A. Quiroz-Ruiz, "Improved composition of Hawaiian basalt BHVO-1 from the application of two new and three conventional recursive discordancy tests," *Turkish Journal of Earth Science*, vol. 26, no. 5, pp. 331–353, 2017.

[53] S. P. Verma, R. Cruz-Huicochea, and L. Díaz-González, "Univariate data analysis system: deciphering mean compositions of island and continental arc magmas, and influence of underlying crust," *International Geology Review*, vol. 55, no. 15, pp. 1922–1940, 2013.

[54] M. Rosales Rivera, *Desarrollo de herramientas estadísticas computacionales con nuevos valores críticos generados por simulación computacional*, Universidad Autónoma del Estado de Morelos, Cuernavaca, Morelos, Mexico, 2018.

[55] K. P. Jochum, U. Weis, B. Schwager et al., "Reference values following ISO guidelines for frequently requested rock reference materials," *Geostandards and Geoanalytical Research*, vol. 40, no. 3, pp. 333–350, 2016.

[56] F. Velasco-Tapia, M. Guevara, and S. P. Verma, "Evaluation of concentration data in geochemical reference materials," *Chemie der Erde*, vol. 61, no. 1, pp. 69–91, 2001.

[57] B. Rosner, "On the detection of many outliers," *Technometrics*, vol. 17, no. 2, pp. 221–227, 1975.

[58] F. E. Grubbs and G. Beck, "Extension of sample sizes and percentage points for significance tests of outlying observations," *Technometrics*, vol. 14, no. 4, pp. 847–854, 1972.

[59] R. B. Jain and L. A. Pingel, "On the robustness of recursive outlier detection procedures to nonnormality," *Communications in Statistics - Theory and Methods*, vol. 10, no. 13, pp. 1323–1334, 1981.

[60] R. B. Jain, "Detecting outliers: power and some other considerations," *Communications in Statistics - Theory and Methods*, vol. 10, no. 22, pp. 2299–2314, 1981.

[61] M. Rosales-Rivera, L. Díaz-González, and S. P. Verma, "A new online computer program (BiDASys) for ordinary and uncertainty weighted least-squares linear regressions: case studies from food chemistry," *Revista Mexicana de Ingeniería Química*, vol. 17, no. 2, pp. 507–522, 2018.

[62] J. B. Willet and J. D. Singer, "Another cautionary note about R2: its use in weighted least-squares regression analysis," *American Statistician*, vol. 42, no. 3, pp. 236–238, 1988.

[63] R. M. Rousseau, "Corrections for matrix effects in X-ray fluorescence analysis—a tutorial," *Spectrochimica Acta Part B: Atomic Spectroscopy*, vol. 61, no. 7, pp. 759–777, 2006.

[64] T. Shiraiwa and N. Fujino, "Theoretical calculation of fluorescent x-ray intensities in fluorescent x-ray spectrochemical analysis," *Japanese Journal of Applied Physics*, vol. 5, no. 10, pp. 886–899, 1966.

[65] R. Rousseau and F. Claisse, "Theoretical alpha coefficients for the Claisse-Quintin relation for x-ray spectrochemical analysis," *X-Ray Spectrometry*, vol. 3, no. 1, pp. 31–36, 1974.

[66] R. M. Rousseau, "Fundamental algorithm between concentration and intensity in XRF analysis 2-Practical application," *X-Ray Spectrometry*, vol. 13, no. 3, pp. 121–125, 1984.

[67] R. M. Rousseau, J. P. Willis, and A. R. Duncan, "Practical XRF calibration procedures for major and trace elements," *X-Ray Spectrometry*, vol. 25, no. 4, pp. 179–189, 1996.

[68] A. J. Klimasara, "XRF analysis—theory, experiment, and regression," in *Proceedings of X-Ray Conference (DXC) on Applications of X-Ray Analysis*, Denver, CO, USA, August 1997.

[69] B. Tan and W. Sun, "Correction method for the matrix effect in x-ray fluorescence spectrometric analysis," *X-Ray Spectrometry*, vol. 27, no. 2, pp. 95–104, 1998.

[70] B. I. Kitov, "Calculation features of the fundamental parameter method in XRF," *X-Ray Spectrometry*, vol. 29, no. 4, pp. 285–290, 2000.

[71] A. J. Klimasara, "Logical steps in the automated Lachamp–Triall XRF matrix correction method utilizing an electronic spreadsheet," in *Advances in XRF Analysis*, vol. 42, pp. 53–83, JCPDS-International Centre for Diffraction Data, Newtown Square, PA, USA, 2000.

[72] R. M. Rousseau, "Correction for long-term instrumental drift," *X-Ray Spectrom*, vol. 31, no. 6, pp. 401–407, 2002.

[73] G. R. Lachance and R. J. Traill, "A practical solution to the matrix problem in X-ray analysis," *Canadian Journal of Spectroscopy*, vol. 11, pp. 43–48, 1966.

[74] J. P. Willis and G. R. Lachance, "Comparison between some common influence coefficient algorithms," *X-Ray Spectrometry*, vol. 33, no. 3, pp. 181–188, 2004.

[75] J. P. Willis and G. R. Lachance, "A new approach to correcting theoretical emitted intensities for absorption and enhancement effects," *X-Ray Spectrometry*, vol. 33, no. 3, pp. 204–211, 2004.

[76] J. W. Hosterman and F. J. Flanagan, "USGS reference samples Attapulgite ATT-1 and Bentonite CSB-1," *Geostandards and Geoanalytical Research*, vol. 11, no. 1, pp. 1–9, 1987.

[77] K. Govindaraju, "1995 working values with confidence limits for twenty-six CRPG, ANRT and IWG-GIT geostandards," *Geostandards and Geoanalytical Research*, vol. 19, pp. 1–32, 1995.

[78] F. J. Flanagan, "Rock reference samples, san marcos gabbro, GSM-1 and lakeview mountain tonalite, TLM-1," *Geostandards and Geoanalytical Research*, vol. 10, no. 2, pp. 111–119, 1986.

# CAPITULO 5.-

# IMPLICACIONES PETROGENÉTICAS Y TECTÓNICAS DE ROCAS VOLCÁNICAS DEL OLIGOCENO-MIOCENO DEL COMPLEJO VOLCÁNICO DE LA SIERRA DE SAN MIGUELITO, MÉXICO CENTRAL

## 5.1 Presentación del trabajo de investigación publicado

El presente artículo de investigación ha sido publicado en *Journal of South American Earth Sciences,* en el cual el autor de esta tesis participó activamente. Me encuentro como primer autor y el Dr. Sanjeet K. Verma, Dr. Surendra P. Verma, Dr. Fernando Velasco Tapia y el Dr. José Ramón Torres Hernández son los co-autores del presente artículo de investigación.

El presente trabajo publicado ha contribuido con nuevas descripciones de campo del Complejo Volcánico de la Sierra de San Miguelito (CVSSM), junto con la recolección de nuevas muestras de roca en diferentes localidades dentro del CVSSM, tomando en cuenta trabajos previos de la zona. A su vez, se reportan nuevos datos de concentraciones de elementos mayores y elementos traza para las unidades volcánicas del CVSSM. Una parte en destacar en este estudio, es la innovación en el reporte de las concentraciones de elementos mayores, la cual consiste en estimar el 99% de incertidumbre a partir de la calibración basada en el modelo de regresión lineal de mínimos cuadrados ponderado, como también, en la preparación y medición de *pellets* duplicados, los cuales se midieron 6 veces en una secuencia aleatoria.

De igual forma, en el presente trabajo se reporta los primeros modelos geoquímicos cuantitativos para las rocas volcánicas del CVSSM, tanto para procesos de fusión parcial cortical en las rocas volcánicas de composición ácida, como también, modelos cuantitativos de procesos de mezcla de magmas entre las rocas volcánicas de composición básica y ácida. Los presentes modelos sirvieron para brindar una mejor comprensión en la petrogénesis y la implicación tectónica de las rocas volcánicas del CVSSM.

Torres-Sánchez D., Verma, S.K., Verma, S.P., Velasco-Tapia, F., Torres-Hernández, J.R. (2019). Petrogenetic and tectonic implications of Oligocene-Miocene volcanic rocks from the Sierra de San Miguelito complex, central Mexico. Journal of South American Earth Sciences 95, 102311 .doi: https://doi.org/10.1016/j.jsames.2019.102311

Journal of South American Earth Sciences 95 (2019) 102311

Contents lists available at ScienceDirect

Journal of South American Earth Sciences

journal homepage: www.elsevier.com/locate/jsames

# Petrogenetic and tectonic implications of Oligocene – Miocene volcanic rocks from the Sierra de San Miguelito complex, central Mexico

Darío Torres-Sánchez[a], Sanjeet K. Verma[b,*], Surendra P. Verma[c], Fernando Velasco-Tapia[d], José Ramón Torres-Hernández[e]

[a] Posgrado de la División de Geociencias Aplicadas, Instituto Potosino de Investigación Científica y Tecnológica (IPICYT), Camino a la Presa San José 2055, San Luis Potosí, 78216, Mexico
[b] División de Geociencias Aplicadas, Instituto Potosino de Investigación Científica y Tecnológica (IPICYT), Camino a la Presa San José 2055, San Luis Potosí, 78216, Mexico
[c] Instituto de Energías Renovables, Universidad Nacional Autónoma de México, Temixco, Morelos, 62580, Mexico
[d] Universidad Autónoma de Nuevo León, Facultad de Ciencias de la Tierra, Ex – Hacienda de Guadalupe, Linares, Mexico
[e] Instituto de Geología, Universidad Autónoma de San Luis Potosí, Manuel Nava No. 5. Zona Universitaria, 78240, San Luis Potosí, S.L.P., Mexico

ARTICLE INFO

*Keywords:*
Geochemistry
Petrogenesis
Volcanic rocks
Tectonic setting
San Luis Potosí

ABSTRACT

Paleogene – Neogene volcanic complexes are commonly found in the southern part of the Mesa Central province (MC), Mexico. The Sierra de San Miguelito Complex (SSMC) is located in the southeastern part of the MC and consists of two main phases of Oligocene and Miocene units as follows: (1) basaltic group of porphyritic texture of basalt/trachybasalt compositions; and (2) rhyolite-ignimbrite group of porphyritic texture of trachydacite/trachyte compositions. Chondrite-normalized rare-earth element patterns for the basaltic group display enrichment in light rare earth elements (LREE) and large ion lithophile elements (LILE), whereas the rhyolite-ignimbrite group shows enrichment in LREE and high field strength elements (HFSE). The Eu anomalies within the SSMC become progressively more negative from the basaltic group to the rhyolite-ignimbrite group ($Eu/Eu^* = 1.13$ to 0.02) suggest upper crust (crustal contamination) participates during magma generation. Trace element modelling reveals that the basaltic group evolved through a mixing process between mafic and felsic end – members. In contrast, chondrite-normalized and multi-element models reveal that the rhyolite-ignimbrite group evolved by partial melting of the upper continental crust. New multi-dimensional discrimination diagrams along with the Nb–Ta anomalies reveal that the SSMC volcanic rocks were generated in an extensional environment.

## 1. Introduction

The Mesa Central province (MC) is an elevated plateau located in the central-northern Mexico and is bounded to the N and E by the Sierra Madre Oriental, and toward the W by the Sierra Madre Occidental (Fig. 1a; Nieto-Samaniego et al., 2007). The major fault systems active during the Cenozoic and surrounding as well as within the MC are as follows (Fig. 1b): (a) the El Bajío system at the south; (b) the Taxco-San Miguel de Allende at the west; and (c) the San Luis-Tepehuanes that extends along the MC province. The San Luis-Tepehuanes fault system characterized by a NW-SE lineaments separates the MC into two main regions: (i) northern region, which is characterized by advance stage of erosion with alluvial – lacustrine basins and shows low magmatic evidence from the Oligocene and Quaternary ages; and (ii) southern region that is mainly covered by Paleogene-Neogene volcanic rocks with normal faults (Nieto-Samaniego et al., 1996; 1999, 2007).

At the southern region of the MC, the main volcanic activity is concentrated (Fig. 1b; see the box marked as c) and amplified in Fig. 1c). Previous studies at the southern region of the MC showed that partial melting and fractional crystallization processes of the lower crust in an extensional setting generated felsic magmas in the region (Orozco-Esquivel et al., 2002; Aguillón-Robles et al., 2014; Sieck et al., 2019). Based on the petrographic evidence, Rodríguez-Ríos and Torres-Aguilera (2009) proposed that mafic volcanism exposed in this area is derived from partial melting of the upper mantle and mixing with the overlying crust. In addition, Tristán-González et al. (2009) and Aguillón-Robles et al. (2014) inferred that associated mafic and intermediate magmas were derived in a post-subduction setting from partial melting of the

* Corresponding author.,
*E-mail addresses:* dario.torres@ipicyt.edu.mx, dariotorressan@hotmail.com (D. Torres-Sánchez), sanjeet.verma@ipicyt.edu.mx, sanjeet_vrm@yahoo.com (S.K. Verma), spv@ier.unam.mx (S.P. Verma), fernando.velascotp@uanl.edu.mx (F. Velasco-Tapia), jrtorres@uaslp.mx (J.R. Torres-Hernández).

https://doi.org/10.1016/j.jsames.2019.102311
Received 11 June 2019; Received in revised form 6 August 2019; Accepted 7 August 2019
Available online 12 August 2019
0895-9811/ 

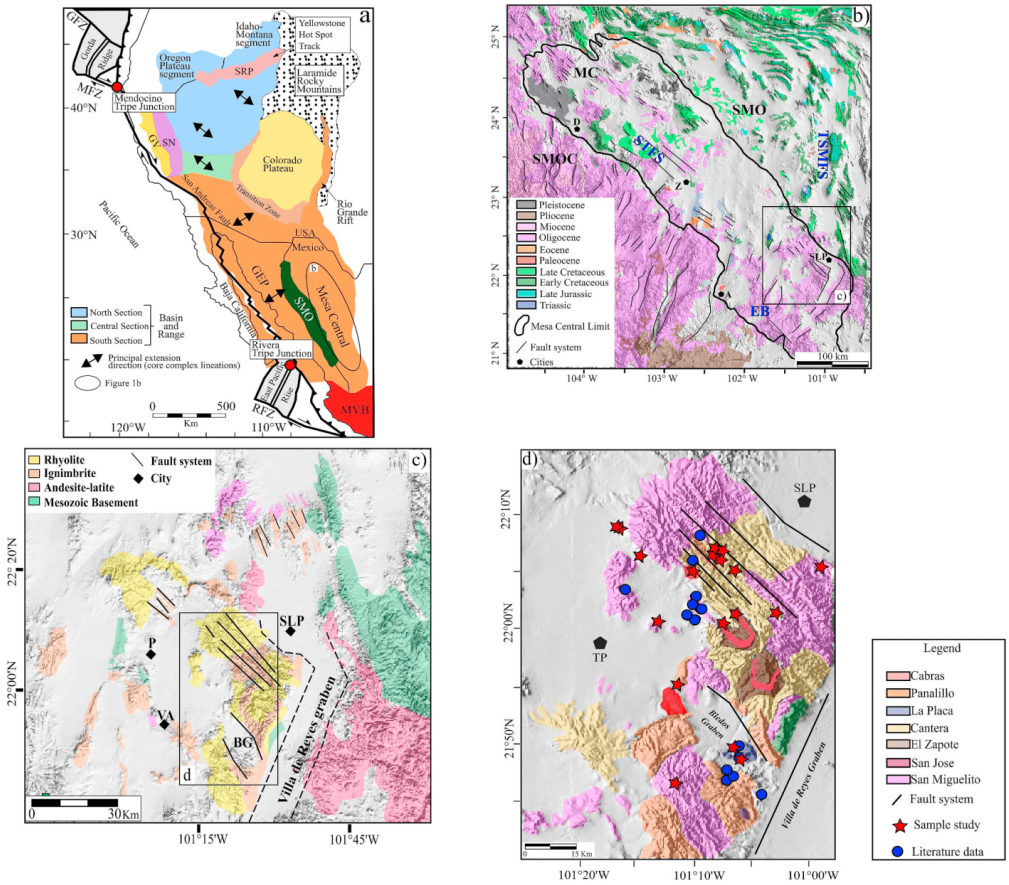


**Fig. 1.** (a) Present-day regional tectonic map of western North America and the Basin and Range province with subdivisions of the northern, central and southern Basin and Range from Jones et al. (1992) and Sonder and Jones (1999). Principal extensional directions established from core complex lineation in each region are simplified and modified from Dickinson (2002) and Cosca et al. (2014); (b) Simplified geological map of the Mesa Central province (modified after Nieto-Samaniego et al., 2007); (c) Geological map of the San Luis Potosí volcanic field (SLPVF; modified after Tristán-González, 1986); (d) Geological map of the Sierra de San Miguelito complex (SSMC), showing the space distribution of the geological units. Abbreviations: GEP – Gulf Extensional Province; SN – Sierra Nevada; RFZ – Rivera Fracture Zone; GV – Great Valley; SRP – Snake River Plain; GFZ – Gorda Fracture Zone; MFZ – Mendocino Fracture Zone; MVB – Mexican Volcanic Belt; STFS – San Luis-Tepehuanes Fault System; TSMFS – Taxco-San Miguel de Allende Fault System; EB – El Bajío Fault System; MC – Mesa Central province; SMO – Sierra Madre Oriental province; SMOC – Sierra Madre Occidental province; the cities are D – Durango; Z – Zacatecas; A – Aguascalientes; TP – Tepetate; SLP – San Luis Potosí; USA – United States of America.

upper mantle. Nevertheless, no detailed geochemical studies have been performed on volcanic rocks from this area. Therefore, in this work, we present a detailed study of field–relationships and geochemistry of volcanic rocks from the Sierra de San Miguelito Complex (SSMC; Fig. 1d) and discuss a quantitative geochemical model to provide a better understanding of the petrogenesis and tectonic implications of the magmatic activity within the southern region of the MC.

## 2. Geological setting

The San Luis Potosí Volcanic Field (SLPVF; Fig. 1c) is located in the southern region of the MC and includes felsic – mafic volcanism, ranging in age from Eocene to Quaternary. The main volcanic event of the SLPVF occurred during late Oligocene and is characterized by high-silica rhyolites and large volume ignimbrites. The youngest volcanic event at the SLPVF was characterized by less voluminous mafic to intermediate lavas (Aguillón-Robles et al., 2014). The SLPVF has been divided into six main volcanic complexes as follows: (i) Ahualulco; (ii) Villa Hidalgo; (iii) La Repartición; (iv) Pinos; (v) Santa María; and (vi) Sierra de San Miguelito (Torres-Hernández et al., 2006; Rodríguez-Ríos et al., 2007; Tristán-González et al., 2009; Aguillón-Robles et al., 2014; López-Loera, 2014).

The Sierra de San Miguelito complex (SSMC; Fig. 1d) consists mainly of Oligocene – Early Miocene rocks of silicic lavas associated to silicic domes, ignimbrite packages, and isolated basaltic volcanism. The volcanic activity of the SSMC was emplaced through fault systems that

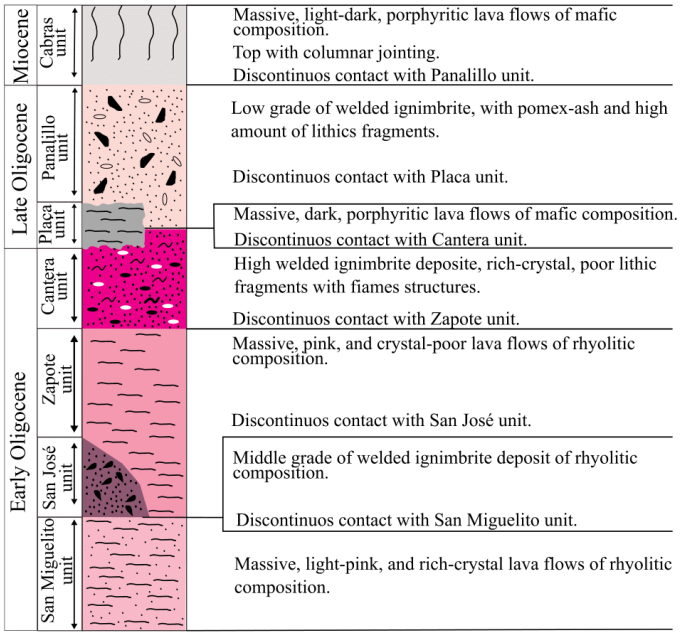


**Fig. 2.** Schematic stratigraphic column for the volcanism in the SSMC.

exhibit a "*domino style geometry*" with strike direction of 300°–340° dip to the SW and titled to NW systematically with dip angles between 12° and 31° (Xu et al., 2004, 2013). The stratigraphy of the SSMC covers the period of Oligocene to Early Miocene and most of the lithology in this complex corresponds to Oligocene. These lithological units could be distributed in three groups as follows: (a) basaltic group (La Placa and Cabras unit); (b) rhyolite group (San Miguelito and El Zapote unit); (c) ignimbrite group (San José, Cantera and Panalillo unit) (Fig. 2). The early Miocene epoch is characterized by the Cabras unit (Figs. 1d and 2).

### 2.1. Basaltic group

The basaltic group is constituted by the La Placa and Cabras units (Fig. 2). Basaltic group displays outcrop in isolated regions of the study area (Fig. 1d). Previous studies (Tristán-González et al., 2009; Aguillón-Robles et al., 2014) have dated the volcanism of the La Placa unit and reported whole-rock K–Ar age of 29 to 26 Ma. The La Placa unit is characterized by massive lava flows that are intercalated with the ignimbrite group (Panalillo and Cantera units). The La Placa unit shows a thickness range from 10 to 15 m and is mainly characterized by scarce phenocrysts and a vitreous matrix. On the other hand, Tristán-González et al. (2009) and Aguillón-Robles et al. (2014) proposed whole-rock K–Ar age of 22 to 21 Ma for the Cabras unit. This unit finds in isolated outcrops of lava flows having a thickness of 25 m and is characterized by aphanitic-porphyritic texture, scarce phenocrysts and rare presence of vesicles in a vitreous matrix (Labarthe-Hernández and Jiménez-López, 1992; Tristán-González et al., 2009; Gaytán-Martínez et al., 2017).

### 2.2. Rhyolite group

The rhyolite group consists of the San Miguelito and El Zapote units (Fig. 2). Previous studies (Labarthe-Hernández and Jiménez-López, 1992; Aguillón-Robles et al., 1994, 2014; Tristán-González et al., 2009) reported whole-rock K–Ar dates for the San Miguelito and El Zapote units ranging from 33 to 21 Ma (Tristán-González et al., 2009). These units consist of lavas flows associated to exogenous domes, whose last eruptive phase formed a thick covering at the top of the domes, known as breccia and vitreous fragments. The thickness of these units are variable (130–800 m), although it is higher at the center of domes. The rhyolite group includes mainly quartz and sanidine phenocrysts embedded in a devitrified and fluidal matrix (Tristán-González, 1986; Labarthe-Hernández and Jiménez-López, 1992; Aguillón-Robles et al., 1994; Tristán-González et al., 2009).

### 2.3. Ignimbrite group

The ignimbrite group is formed by the San José, Cantera and Panalillo units (Fig. 2). Based on stratigraphic aspects Tristán-González et al. (2009) proposed an age of 29 Ma for the San José unit. This unit consists of ash and pyroclastic flows, having a middle-grade of welding and a thickness of ~3–15 m. The San José unit appears in contact with the rhyolite group (San Miguelito and El Zapote unit; Labarthe-Hernández and Jiménez-López, 1992; Tristán-González et al., 2009). In contrast, the Cantera unit was dated at about 29 Ma by the K–Ar method (Labarthe-Hernández and Jiménez-López, 1992; Tristán-González et al., 2009; Gaytán-Martínez et al., 2017). The Cantera unit is characterized by pyroclastic flows of pumice and ash with fiamme structures and lithics fragments. It is present in the major part of the study area and overlays the San Miguelito unit. The Cantera unit shows high-grade of welding and presents an average thickness of 2–30 m.

The Panalillo unit displays variable ages of 29 to 26 Ma (Labarthe-Hernández and Jiménez-López, 1992; Torres-Hernández et al., 2006; Tristán-González et al., 2009), is constituted by pumice – ash pyroclastic flows with a lesser grade of welding, and shows an average

**Table 1**
Petrographic information of the Sierra de San Miguelito complex volcanic rocks.

| Sample | Group | Unit | Lat (N)° | Long(W)° | Texture | Phenocrysts | | | | | | | Groundmass | Disequilibrium type | |
|---|---|---|---|---|---|---|---|---|---|---|---|---|---|---|---|
| | | | | | | Ol | Plg | Opx | Cpx | Qz | FK | Op | | Qz + R | Pl-N-S |
| SLP-01 | Basaltic | Cabras | 21°55′17″ | 101°11′50″ | P | 4 | 10 | 4 | 6 | | | 26 | 50 | | * |
| SLP-02 | Basaltic | La Placa | 21°46′45″ | 101°03′11″ | P | 6 | 68 | | 20 | | | 5 | 1 | | |
| SLP-03 | Basaltic | La Placa | 21°49′47″ | 101°04′42″ | P | 3 | 19 | 7 | 3 | | | 1 | 67 | * | * |
| SLP-06 | Rhyolite-Ignimbre | San Miguelito | 22°05′23″ | 101°13′06″ | P | | | 3 | 1 | 41 | 15 | 30 | 10 | | |
| SLP1712 | Rhyolite-Ignimbrite | San Miguelito | 22°00′03″ | 101°10′51″ | P | | 3 | 1 | | 46 | 10 | 36 | 4 | | |
| SLP-07 | Rhyolite-Ignimbrite | El Zapote | 22°04′12″ | 101°04′45″ | P | | 44 | 4 | 4 | 26 | 15 | | 7 | | |
| SLP1715 | Rhyolite-Ignimbrite | Panalillo | 21°46′47″ | 101°02′13″ | P | 2 | 10 | 18 | 35 | 15 | 15 | 1 | 4 | | |
| SLP-04 | Rhyolite-Ignimbrite | Panalillo | 21°48′45″ | 101°04′11″ | P | 2 | 2 | 9 | 11 | 32 | 14 | 4 | 26 | | |
| SLP1719 | Rhyolite-Ignimbrite | Panalillo | 21°49′02″ | 101°06′08″ | P | | | 4 | | 16 | 22 | 9 | 49 | | |
| SLP1723 | Rhyolite-Ignimbrite | Panalillo | 22°06′06″ | 101°06′35″ | P | | 43 | 1 | | 38 | 15 | | 3 | | |
| SLP1724 | Rhyolite-Ignimbrite | Cantera | 22°05′26″ | 101°06′34″ | P | | | 3 | 6 | 24 | 20 | 6 | 41 | | |
| SLP-05 | Rhyolite-Ignimbrite | San José | 22°01′20″ | 101°04′44″ | P | | | 4 | 2 | 16 | 21 | 5 | 52 | | |

Modal data are presented in percentage (%). Texture: P = porphyritic. Minerals: Ol: olivine; Plg: plagioclase; Opx: orthopyroxene; Cpx: clinopyroxene; Qz: quartz; FK: potassium feldspar; Amp: amphibole; Op: opaque. Disequilibrium type: Qz + R = quartz with reaction rim, Pl-N-S = Plagioclase with normal and sieved texture, * = Presence of Disequilibrium type.

thickness of 20–30 m. This unit shows a high amount of lithics fragments and overlays the Cantera unit, with minor intercalation with the San Miguelito unit in some part of the study area (Tristán-González, 1986; Labarthe-Hernández and Jiménez-López, 1992; Tristán-González et al., 2009; Gaytán-Martínez et al., 2017).

## 3. Sampling and petrography

For this study, we collected representative samples of the main basaltic and rhyolitic-ignimbrite groups from the SSMC. The sampling coordinates are presented in Tables 1 and 2. Modal compositions were determined by point counting on thin section using a Leica petrographic microscope and a PELCON Automatic point counter. In order to obtain a representative mode, approximately 1000 points per sample were counted. Modal composition data are reported in Table 1.

### 3.1. Basaltic group

This group is characterized by porphyritic textures with limited presence of vesicles and a vitreous matrix (Table 1). The main mineral assemblage (Fig. 3a and b) from this unit consists of phenocrysts of euhedral to subhedral plagioclase (10–68%) generally showing Carlsbad twins and normal zoning, subhedral phenocrysts of clinopyroxene (6–20%), subhedral phenocrysts of orthopyroxene (4–7%), and a lesser amount of subhedral to xenoform microcrystals of olivine (< 6%). Furthermore, the basaltic group samples display the following characteristics: (i) diverse disequilibrium textures that include normal and sieved plagioclases in the same sample; (ii) rounded and embayed crystals with reaction rims; and (iii) plagioclase with complex mineral zoning, such as reverse and oscillatory zoning or normally and reversely zoned crystals in the same sample (Fig. 3a and b).

### 3.2. Rhyolite group

The rhyolite group consists of massive flows, which show porphyritic textures, except in some places, where a fluidal texture can be observed. The principal minerals (Fig. 3c and d) consist of phenocrystals of xenoform quartz (27–41%), euhedral to subhedral potassium feldspar (sanidine; 11–15%), euhedral to subhedral plagioclase (44%) with 0.5–2.0 mm of diameter, subhedral orthopyroxene (1–4%) and clinopyroxene (1–4%) of 0.2–0.7 mm of diameter. (Table 1; Fig. 3c and d).

### 3.3. Ignimbrite group

Fresh ignimbrite samples were collected from the SSMC. This group consists of welded and semi–welded pyroclastic flow deposits and represents porphyritic textures. The main minerals (Fig. 3e–g) are subhedral phenocrysts of quartz (15–38%), potassium feldspar (sanidine; 15–22%), plagioclase (2–43%), orthopyroxene (2–5%), and clinopyroxene (2–7%); olivine is present in less abundance in some samples. All subhedral phenocrysts are embedded in a vitreous matrix (Table 1; Fig. 3e–g).

## 4. Geochemical analytical procedures

### 4.1. Major and trace element analysis

Major element for 23 samples were determined by a wavelength dispersive X–ray fluorescence (WD-XRF) spectrometer Rigaku ZSX Primus II at Institute of Scientific and Technological Research of San Luis Potosi, IPICYT (San Luis Potosí, Mexico). The analytical procedures, accuracy, and precision were given by Verma et al. (2018, 2019). The computer program MECUX is available for online use at http://tlaloc.ier.unam.mx. The innovation in reporting major elements consists in estimating total 99% uncertainty from the calibration based on uncertainty-weighted least-squares linear regression model and preparation and measurement of duplicate pellets, each of which run 6 times, in a random sequence, in the XRF instrument. Thus, there is 99% confidence that the true value will be within the interval (mean ± 99% uncertainty) implied from the reported results.

Trace element concentrations were determined in ALS Chemex Laboratories (Vancouver, Canada) using the "*ME–MS81*" method (for more details visit: www.alsglobal.com/geochemistry). Trace element concentrations were obtained by Inductively Coupled Plasma Mass Spectrometry (ICP–MS) with an analytical precision based on geochemical reference materials SY–2 and OREAS146.

Besides new geochemical data for 23 samples, additional literature data for 31 samples from the SSMC were compiled from Leroy et al. (2002; 11 samples); Orozco–Esquivel et al. (2002; 8 samples); Aguillón-Robles et al. (2014; 4 samples) Torres–Hernández et al. (2014; 8 samples). All computations (anhydrous and iron-oxidation ratio adjustments, norm compositions, and rock classifications) were automatically done from the IgRoCS software (Verma and Rivera–Gómez, 2013), with iron–oxidation ratio adjustments proposed by Middlemost (1989). Rock classification was based on the total alkali − silica diagram (TAS–Le Bas et al., 1986; Fig. 4).

**Table 2**
Major element geochemistry and CIPW norms of volcanic rocks from the Sierra de San Miguelito Volcanic Complex, San Luis Potosí, Mexico. *n* = number of analyses of each sample; [Mg# = 100 × ($Mg^{2+}$/($Mg^{2+}$ + $Fe^{2+}$))]. CIPW norms are computed on an ahydrous, 100% adjusted basis and $Fe_2O_3$/FeO ratio after Middlemost (1989), using a program proposed by Verma and Rivera–Gómez (2013).

| Sample | SLP-01 | SLP-02 | SLP1718 | SLP-03 | SLP17-01 | SLP17-02 | SLP17-06 | SLP17-07 |
|---|---|---|---|---|---|---|---|---|
| Rock unit | Cabras | La Placa | La Placa | La Placa | Panalillo | Panalillo | Cantera | Panalillo |
| Rock (TAS) | Foidite, melaephelinite | Foidite, melaephelinite | Potassic trachybasalt | Alkali basalt | Rhyolite | Rhyolite | Rhyolite | Rhyolite |
| Long. (°W) | 101°11′50″ | 101°03′11″ | 101°05′12′ | 101°04′42″ | 101°06′34″ | 101°09′23″ | 101°02′11″ | 101°05′43″ |
| Lat. (°N) | 21°55′17″ | 21°46′45″ | 21°49′47″ | 21°49′47″ | 22°05′26″ | 22°05′09″ | 21°46′46″ | 21°49′48″ |
| *n* | 12 | 12 | 12 | 12 | 12 | 12 | 12 | 12 |
| $SiO_2$ | 39.11 ± 1.50 | 37.38 ± 1.44 | 44.76 ± 1.5 | 46.34 ± 1.54 | 71.01 ± 1.94 | 72.73 ± 1.91 | 66.91 ± 168 | 71.6 ± 1.94 |
| $TiO_2$ | 3.9991 ± 0.039 | 1.7453 ± 0.0225 | 1.7345 ± 0.021 | 2.1155 ± 0.0256 | 0.1137 ± 0.011 | 0.196 ± 0.011 | 0.187 ± 0.0113 | 0.1045 ± 0.0112 |
| $Al_2O_3$ | 15.76 ± 0.314 | 18.556 ± 0.305 | 17.139 ± 0.297 | 15.616 ± 0.302 | 11.245 ± 0.304 | 11.388 ± 0.301 | 18.445 ± 0.303 | 12.726 ± 0.319 |
| $Fe_2O_3^t$ | 14.898 ± 0.131 | 14.657 ± 0.12 | 10.977 ± 0.105 | 11.721 ± 0.111 | 1.608 ± 0.078 | 1.613 ± 0.078 | 2.385 ± 0.079 | 1.611 ± 0.079 |
| MnO | 0.38551 ± 0.003 | 0.34943 ± 0.003 | 0.34366 ± 0.003 | 0.34362 ± 0.003 | 0.01435 ± 0.002 | 0.01786 ± 0.002 | 0.04815 ± 0.00234 | 0.02757 ± 0.0023 |
| MgO | 4.513 ± 0.255 | 6.025 ± 0.251 | 5.177 ± 0.249 | 4.488 ± 0.249 | 0.841 ± 0.263 | 0.845 ± 0.236 | 0.339 ± 0.236 | 0.722 ± 0.236 |
| CaO | 14.355 ± 0.175 | 15.963 ± 0.159 | 12.486 ± 0.143 | 11.74 ± 0.148 | 2.134 ± 0.119 | 2.217 ± 0.119 | 1.035 ± 0.118 | 2.052 ± 0.119 |
| $Na_2O$ | 2.082 ± 0.077 | 2.333 ± 0.073 | 2.642 ± 0.075 | 2.142 ± 0.074 | 0.482 ± 0.069 | 0.613 ± 0.069 | 2.95 ± 0.074 | 0.45 ± 0.069 |
| $K_2O$ | 1.984 ± 0.048 | 1.403 ± 0.045 | 2.406 ± 0.048 | 2.255 ± 0.048 | 5.366 ± 0.065 | 4.012 ± 0.056 | 6.774 ± 0.065 | 4.842 ± 0.061 |
| $P_2O_5$ | 2.4266 ± 0.043 | 0.8962 ± 0.013 | 0.6307 ± 0.010 | 0.7638 ± 0.013 | 0.0442 ± 0.007 | 0.0592 ± 0.007 | 0.1049 ± 0.0068 | 0.0501 ± 0.0067 |
| LOI | 0.496 | 0.692 | 1.703 | 2.481 | 7.146 | 6.31 | 0.824 | 5.818 |
| Sum | 100.005 | 99.999 | 99.998 | 100.005 | 100.004 | 100.001 | 100.002 | 100.003 |
| Q | | | | | 44.63 | 50.71 | 20.74 | 47.33 |
| Or | 11.93 | | 14.59 | 13.81 | 34.19 | 25.34 | 40.43 | 30.42 |
| Ab | 0.44 | | 5.67 | 16.65 | 4.40 | 5.54 | 25.21 | 4.05 |
| An | 28.28 | 36.73 | 28.53 | 27.28 | 11.10 | 11.34 | 4.49 | 10.47 |
| Ne | 9.48 | 10.91 | 9.36 | 1.15 | | | | |
| C | | | | | 0.94 | 2.29 | 4.67 | 3.33 |
| Di-Mg | 11.58 | 2.92 | 15.01 | 11.91 | | | | |
| Di-Fe | 11.76 | 2.78 | 10.28 | 11.22 | | | | |
| Hy-Mg | | | | | 2.26 | 2.25 | 0.85 | 1.91 |
| Hy-Fe | | | | | 1.36 | 1.21 | 1.91 | 1.38 |
| Mt | 3.35 | 3.30 | 3.47 | 2.68 | 0.78 | 0.78 | 1.08 | 0.77 |
| Il | 7.73 | 3.38 | 3.38 | 4.16 | 0.23 | 0.40 | 0.36 | 0.21 |
| Ap | 5.72 | 2.12 | 1.50 | 1.83 | 0.11 | 0.15 | 0.25 | 0.12 |
| Mg# | 41.46 | 49.00 | 54.26 | 47.23 | 60.04 | 60.08 | 28.99 | 56.28 |
| $FeO^t$/MgO | 2.97 | 2.19 | 1.91 | 2.35 | 1.72 | 1.72 | 6.33 | 2.01 |

| Sample | SLP17-08 | SLP17-09 | SLP-04 | SLP17-17 | SLP17-25 | SLP-05 | CR17-04 |
|---|---|---|---|---|---|---|---|
| Rock unit | Panalillo | Panalillo | Panalillo | Panalillo | Panalillo | San José | San Miguelito |
| Rock (TAS) | Rhyolite | Rhyolite | Rhyolite | Rhyolite | Rhyolite | Rhyolite | Rhyolite |
| Long. (°W) | 101°09′24″ | 101°09′2″ | 101°04′11″ | 101°05′11″ | 101°05′45′ | 101°04′44″ | 101°12′33″ |
| Lat. (°N) | 22°05′10″ | 22°05′07″ | 21°48′45″ | 21°48′46″ | 22°05′14″ | 22°01′20″ | 22°00′48″ |
| *n* | 12 | 12 | 12 | 12 | 12 | 12 | 12 |
| $SiO_2$ | 70.98 ± 1.76 | 72.69 ± 1.89 | 78.88 ± 2.01 | 69.4 ± 1.81 | 71.98 ± 1.94 | 68.68 ± 1.63 | 74.32 ± 2.16 |
| $TiO_2$ | 0.2157 ± 0.0113 | 0.2019 ± 0.0114 | 0.0796 ± 0.0111 | 0.2344 ± 0.0115 | 0.1484 ± 0.0112 | 0.1627 ± 0.0112 | 0.0595 ± 0.0111 |
| $Al_2O_3$ | 14.692 ± 0.298 | 13.978 ± 0.309 | 10.895 ± 0.295 | 15.567 ± 0.304 | 10.129 ± 0.297 | 16.971 ± 0.291 | 14.004 ± 0.348 |

(*continued on next page*)

**Table 2** (*continued*)

| Sample | SLP17-08 | SLP17-09 | SLP-04 | SLP17-17 | SLP17-25 | SLP-05 | CR17-04 |
|---|---|---|---|---|---|---|---|
| Rock unit | Panalillo | Panalillo | Panalillo | Panalillo | Panalillo | San José | San Miguelito |
| Rock (TAS) | Rhyolite | Rhyolite | Rhyolite | Rhyolite | Rhyolite | Rhyolite | Rhyolite |
| Long. (°W) | 101°09′24″ | 101°09′2″ | 101°04′11″ | 101°05′11″ | 101°05′45′ | 101°04′44″ | 101°12′33″ |
| Lat. (°N) | 22°05′10″ | 22°05′07″ | 21°48′45″ | 21°48′46″ | 22°05′14″ | 22°01′20″ | 22°00′48″ |
| *n* | 12 | 12 | 12 | 12 | 12 | 12 | 12 |
| $Fe_2O_3^t$ | 2.627 ± 0.079 | 2.401 ± 0.079 | 1.096 ± 0.078 | 2.484 ± 0.079 | 1.619 ± 0.078 | 2.15 ± 0.078 | 1.407 ± 0.079 |
| MnO | 0.02747 ± 0.00233 | 0.03816 ± 0.00235 | 0.03232 ± 0.0023 | 0.11047 ± 0.0023 | 0.0173 ± 0.0023 | 0.04593 ± 0.0023 | 0.01724 ± 0.0023 |
| MgO | 0.076 ± 0.236 | 0.045 ± 0.236 | 0.155 ± 0.236 | 0.737 ± 0.236 | 0.783 ± 0.236 | 0.096 ± 0.236 | 0.019 ± 0.236 |
| CaO | 0.606 ± 0.118 | 0.516 ± 0.118 | 0.924 ± 0.118 | 2.081 ± 0.119 | 2.397 ± 0.119 | 1.075 ± 0.118 | 0.328 ± 0.118 |
| $Na_2O$ | 3.189 ± 0.077 | 2.946 ± 0.079 | 2.416 ± 0.077 | 3.378 ± 0.078 | 0.42 ± 0.069 | 2.822 ± 0.073 | 3.467 ± 0.106 |
| $K_2O$ | 6.61 ± 0.064 | 6.458 ± 0.066 | 4.836 ± 0.058 | 4.948 ± 0.058 | 5.291 ± 0.063 | 6.647 ± 0.061 | 5.554 ± 0.073 |
| $P_2O_5$ | 0.0786 ± 0.0067 | 0.0669 ± 0.0067 | 0.0574 ± 0.0067 | 0.1068 ± 0.0068 | 0.0509 ± 0.0067 | 0.1133 ± 0.0067 | 0.0342 ± 0.0067 |
| LOI | 0.9 | 0.654 | 0.627 | 0.954 | 7.165 | 1.239 | 0.791 |
| Sum | 100.001 | 99.994 | 99.998 | 100.000 | 100.000 | 100.001 | 100.000 |
| Q | 25.30 | 29.25 | 44.17 | 24.92 | 46.25 | 24.25 | 32.01 |
| Or | 39.49 | 38.48 | 28.78 | 29.57 | 33.72 | 39.83 | 33.12 |
| Ab | 27.28 | 25.14 | 20.59 | 28.91 | 3.83 | 24.21 | 29.60 |
| An | 2.52 | 2.14 | 4.24 | 9.74 | 10.92 | 4.66 | 1.42 |
| Ne | | | | | | | |
| C | 1.39 | 1.37 | 0.14 | 1.14 | | 3.50 | 1.79 |
| Di-Mg | | | | | 0.82 | | |
| Di-Fe | | | | | 0.44 | | |
| Hy-Mg | 0.19 | 0.11 | 0.39 | 1.86 | 1.72 | 0.24 | 0.05 |
| Hy-Fe | 2.04 | 1.87 | 0.90 | 2.03 | 1.08 | 1.74 | 1.19 |
| Mt | 1.19 | 1.09 | 0.50 | 1.13 | 0.79 | 0.98 | 0.64 |
| Il | 0.41 | 0.39 | 0.15 | 0.45 | 0.30 | 0.31 | 0.11 |
| Ap | 0.18 | 0.16 | 0.13 | 0.25 | 0.13 | 0.27 | 0.08 |
| Mg# | 7.67 | 5.11 | 28.89 | 46.01 | 58.14 | 11.37 | 3.73 |
| $FeO^t/MgO$ | 31.10 | 48.01 | 6.36 | 3.03 | 1.86 | 20.15 | 66.63 |

| Sample | SLP17-03 | SLP17-04 | SLP17-05 | SLP-06 | SLP-07 | SLP17-30 | SLP17-31 | SM17-03 |
|---|---|---|---|---|---|---|---|---|
| Rock unit | San Miguelito | San Miguelito | San Miguelito | San Miguelito | El Zapote | Zapote | Zapote | San Miguelito |
| Rock (TAS) | Rhyolite | Rhyolite | Rhyolite | Trachydacite | Rhyolite | Rhyolite | Rhyolite | Rhyolite |
| Long. (°W) | 101°07′00″ | 101°07′36″ | 101°07′31″ | 101°13′06″ | 101°04′45″ | 101°06′43″ | 100°58′08″ | 101°14′07′ |
| Lat. (°N) | 22°07′02″ | 22°07′04″ | 22°07′07″ | 22°05′23″ | 22°04′12″ | 22°00′40″ | 22°05′28″ | 22°06′23″ |
| *n* | 12 | 12 | 12 | 12 | 12 | 12 | 12 | 12 |
| $SiO_2$ | 69.43 ± 1.84 | 70.85 ± 1.88 | 68.12 ± 1.64 | 63.75 ± 1.67 | 68.57 ± 1.78 | 72.82 ± 1.96 | 72.36 ± 1.77 | 69.95 ± 2.02 |
| $TiO_2$ | 0.1305 ± 0.0112 | 0.1299 ± 0.0112 | 0.1458 ± 0.0112 | 0.1911 ± 0.0113 | 0.1436 ± 0.0112 | 0.1302 ± 0.0112 | 0.1352 ± 0.0112 | 0.1334 ± 0.0112 |
| $Al_2O_3$ | 17.153 ± 0.329 | 15.643 ± 0.317 | 16.264 ± 0.289 | 21.064 ± 0.317 | 18.084 ± 0.322 | 15.101 ± 0.326 | 14.863 ± 0.295 | 17.027 ± 0.357 |
| $Fe_2O_3^t$ | 1.668 ± 0.079 | 1.645 ± 0.078 | 2.052 ± 0.079 | 1.919 ± 0.078 | 1.771 ± 0.078 | 1.693 ± 0.079 | 1.627 ± 0.078 | 1.456 ± 0.078 |
| MnO | 0.03938 ± 0.0023 | 0.03955 ± 0.0024 | 0.0575 ± 0.0023 | 0.04941 ± 0.00235 | 0.03128 ± 0.00235 | 0.02178 ± 0.0023 | 0.03287 ± 0.0023 | 0.02497 ± 0.00235 |
| MgO | 0.362 ± 0.236 | 0.258 ± 0.236 | 0.194 ± 0.236 | 0.451 ± 0.236 | 0.136 ± 0.236 | 0.071 ± 0.236 | 0.046 ± 0.236 | 0.313 ± 0.236 |
| CaO | 0.751 ± 0.118 | 0.971 ± 0.118 | 1.828 ± 0.118 | 1.097 ± 0.118 | 0.76 ± 0.118 | 0.692 ± 0.118 | 1.018 ± 0.118 | 0.699 ± 0.118 |
| $Na_2O$ | 2.743 ± 0.079 | 2.393 ± 0.078 | 2.764 ± 0.073 | 3.117 ± 0.075 | 3.229 ± 0.079 | 2.938 ± 0.082 | 3.346 ± 0.081 | 2.745 ± 0.082 |
| $K_2O$ | 6.357 ± 0.069 | 6.519 ± 0.071 | 7.082 ± 0.064 | 7.43 ± 0.067 | 6.165 ± 0.064 | 5.812 ± 0.066 | 5.857 ± 0.068 | 6.547 ± 0.073 |

(*continued on next page*)

**Table 2** (*continued*)

| Sample | SLP17-03 | SLP17-04 | SLP17-05 | SLP-06 | SLP-07 | SLP17-30 | SLP17-31 | SM17-03 |
|---|---|---|---|---|---|---|---|---|
| Rock unit | San Miguelito | San Miguelito | San Miguelito | San Miguelito | El Zapote | Zapote | Zapote | San Miguelito |
| Rock (TAS) | Rhyolite | Rhyolite | Rhyolite | Trachydacite | Rhyolite | Rhyolite | Rhyolite | Rhyolite |
| Long. (°W) | 101°07′00″ | 101°07′36″ | 101°07′31″ | 101°13′06″ | 101°04′45″ | 101°06′43″ | 100°58′08″ | 101°14′07″ |
| Lat. (°N) | 22°07′02″ | 22°07′04″ | 22°07′07″ | 22°05′23″ | 22°04′12″ | 22°00′40″ | 22°05′28″ | 22°06′23″ |
| *n* | 12 | 12 | 12 | 12 | 12 | 12 | 12 | 12 |
| $P_2O_5$ | 0.0531 ± 0.0067 | 0.0507 ± 0.0066 | 0.0952 ± 0.0067 | 0.1104 ± | 0.0669 ± 0.0067 | 0.0608 ± 0.0067 | 0.0748 ± 0.0067 | 0.0664 ± 0.0068 |
| LOI | 1.316 | 1.496 | 1.395 | 0.822 | 1.047 | 0.663 | 0.64 | 1.036 |
| Sum | 100.002 | 99.995 | 99.997 | 100.000 | 100.003 | 100.002 | 99.999 | 99.997 |
| Q | 26.92 | 29.54 | 20.55 | 13.94 | 24.20 | 31.72 | 28.07 | 26.95 |
| Or | 38.11 | 39.16 | 42.51 | 44.33 | 36.86 | 34.62 | 34.88 | 39.14 |
| Ab | 23.55 | 20.58 | 23.75 | 26.63 | 27.64 | 25.06 | 28.53 | 23.49 |
| An | 3.43 | 4.56 | 8.58 | 4.77 | 3.37 | 3.06 | 4.60 | 3.07 |
| Ne | | | | | | | | |
| C | 4.59 | 3.06 | 0.97 | 6.22 | 4.93 | 2.89 | 1.36 | 4.36 |
| Di-Mg | | | | | | | | |
| Di-Fe | | | | | | | | |
| Hy-Mg | 0.91 | 0.65 | 0.49 | 1.13 | 0.34 | 0.18 | 0.12 | 0.79 |
| Hy-Fe | 1.35 | 1.33 | 1.70 | 1.48 | 1.40 | 1.33 | 1.28 | 1.12 |
| Mt | 0.76 | 0.75 | 0.94 | 0.87 | 0.81 | 0.77 | 0.74 | 0.66 |
| Il | 0.25 | 0.25 | 0.28 | 0.37 | 0.28 | 0.25 | 0.26 | 0.26 |
| Ap | 0.12 | 0.12 | 0.22 | 0.26 | 0.16 | 0.14 | 0.17 | 0.16 |
| Mg# | 38.40 | 31.06 | 21.36 | 40.30 | 18.07 | 10.75 | 7.51 | 38.17 |
| $FeO^t/MgO$ | 4.15 | 5.74 | 9.52 | 3.83 | 11.72 | 21.46 | 31.83 | 4.19 |

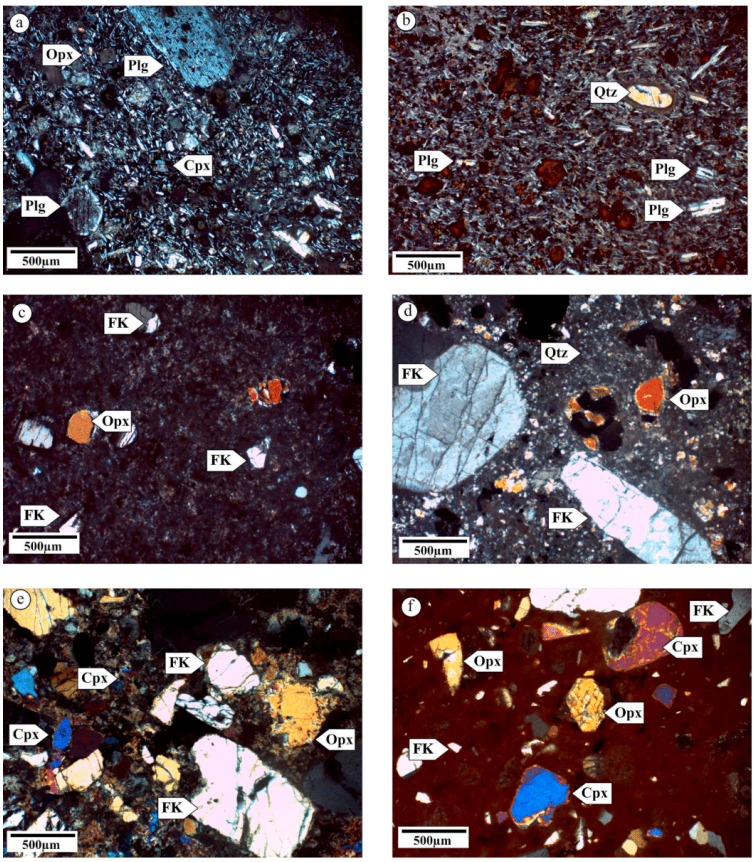


**Fig. 3.** Photomicrographs of the SSMC volcanic rocks. (a) Phenocrysts of plagioclase and quartz with reaction rims in the Cabras unit; b) Phenocrysts of potassium feldspar, clipnopyroxene and orthopyroxene in the Panalillo unit; c) Sieved textures in plagioclase in the Placa unit; d) Phenocrysts of potassium feldspar, orthopyroxene and clinopyroxene in the Cantera unit; e) Phenocrysts of potassium feldspar, orthopyroxene, clinopyroxene in the El Zapote unit; f) Phenocrysts of potassium feldspar, orthopyroxene, clinopyroxene in the San José unit; g) Potassium feldspar phenocrysts and orthopyroxene crystals of porphyritic texture in the San Miguelito unit. Abbreviations of mineral names are reported in Table 1.

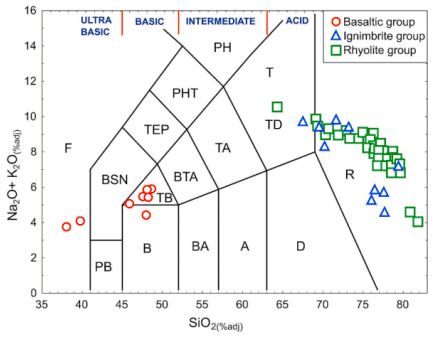


**Fig. 4.** Total Alkali – Silica classification diagram (TAS) for the volcanic rocks from the SSMC (Le Bas et al., 1986) prepared from the adjusted data by using the IgRoCS computer program (Verma and Rivera-Gómez, 2013).

## 5. Geochemical results

### 5.1. Major elements

The basaltic group samples show a foidite to trachybasalt composition (Fig. 4), covering the range of $(SiO_2)_{adj}$ = 38.12–48.01% m/m, $(Al_2O_3)_{adj}$ values of 16.04–18.92% m/m, $(MgO)_{adj}$ values are 4.59–6.14% m/m, $(TiO_2)_{adj}$ = 1.78–4.07% m/m and Mg# (calculated as $100 \times Mg^{2+}/(Mg^{2+}+Fe^{2+})$), ranges from 41.46 to 54.26. Most of the samples of this group are nepheline normative (n = 4; Table 2).

In contrast, the rhyolite-ignimbrite group samples display a rhyolitic composition, with the exception of one sample that shows trachydacite composition. The rhyolite-ignimbrite group samples contain 64.36–79.43% m/m $(SiO_2)_{adj}$, relatively high $(Al_2O_3)_{adj}$ ranging from 10.92 to 21.26% m/m. $(MgO)_{adj}$ values are 0.01–0.91% m/m, $(TiO_2)_{adj}$ = 0.06–0.24% m/m and Mg# ranges from 3.73 to 60.07; most of the samples are hypersthene normative (n = 19; Table 2).

### 5.2. Trace elements

Trace element compositions of the basaltic group samples include Sc = 21–28 ppm ($\mu g.g^{-1}$), Cr = 100–240 ppm, Ni = 7–92 ppm, and

**Table 3**
Trace and rare earth element geochemistry of volcanic rocks from the Sierra de San Miguelito Volcanic Complex, San Luis Potosí, Mexico.

| Sample | SLP-01 | SLP-02 | SLP1718 | SLP-03 | SLP17-01 | SLP17-02 | SLP17-06 | SLP17-07 | SLP17-08 | SLP17-09 | SLP-04 | SLP17-17 |
|---|---|---|---|---|---|---|---|---|---|---|---|---|
| Rock unit | Cabras | La Placa | La Placa | La Placa | Panalillo | Panalillo | Cantera | Panalillo | Panalillo | Panalillo | Panalillo | Panalillo |
| Rock (TAS) | Foidite, melaephelinite | Foidite, melaephelinite | Potassic trachybasalt | Alkali basalt | Rhyolite | Rhyolite | Rhyolite | Rhyolite | Rhyolite | Rhyolite | Rhyolite | Rhyolite |
| Long. (°W) | 101°11′50″ | 101°03′11″ | 101°05′12′ | 101°04′42″ | 101°06′34″ | 101°09′23″ | 101°02′11″ | 101°05′43″ | 101°09′24″ | 101°09′2″ | 101°04′11″ | 101°05′11″ |
| Lat. (°N) | 21°55′17″ | 21°46′45″ | 21°49′47″ | 21°49′47″ | 22°05′26″ | 22°05′09″ | 21°46′46″ | 21°49′48″ | 22°05′10″ | 22°05′07″ | 21°48′45″ | 21°48′46″ |
| Ba | 376 | 288 | 691 | 966 | 392 | 171 | 219 | 308 | 70 | 54.7 | 28.5 | 389 |
| Co | 43 | 32 | 22 | 27 | 2 | | | | | 1 | | 3 |
| Cr | 240 | 100 | 230 | 240 | | 10 | | | | | | 10 |
| Cs | 0.37 | 1.11 | 6.48 | 1.35 | 14.15 | 13.75 | 13.25 | 25.5 | 5.74 | 6.11 | 13.3 | 10.3 |
| Cu | 35 | 11 | 10 | 10 | 3 | 3 | 2 | 3 | 4 | 2 | 2 | 4 |
| Ga | 25.1 | 21.2 | 19.5 | 20.3 | 19.2 | 17.2 | 21 | 22.3 | 23.8 | 24.8 | 18.5 | 18.4 |
| Hf | 6 | 4.3 | 6.1 | 5.9 | 5 | 5.2 | 6 | 6.1 | 8.7 | 8.6 | 3.8 | 4.9 |
| Nb | 27.1 | 13.6 | 12.4 | 13.6 | 20.4 | 17.9 | 22.8 | 19.6 | 38.4 | 38.6 | 18.2 | 16.5 |
| Ni | 92 | 7 | 26 | 46 | 3 | 2 | 2 | 2 | | | | 2 |
| Pb | 4 | 8 | 11 | 10 | 26 | 19 | 38 | 25 | 35 | 34 | 22 | 26 |
| Rb | 14.2 | 21.7 | 94 | 90.1 | 248 | 203 | 349 | 249 | 271 | 274 | 369 | 282 |
| Sc | 23 | 28 | 21 | 21 | 7 | 6 | 8 | 8 | 2 | 2 | 4 | 5 |
| Sr | 519 | 371 | 435 | 441 | 511 | 221 | 30.2 | 367 | 7.8 | 7.2 | 15.2 | 72.4 |
| Ta | 1.7 | 0.9 | 0.8 | 0.8 | 1.9 | 1.6 | 2 | 2 | 2.6 | 2.7 | 2.1 | 1.8 |
| Th | 2.1 | 2.56 | 7.14 | 6.24 | 19.8 | 20.9 | 29.9 | 30.5 | 27.8 | 27.4 | 35.2 | 23.8 |
| U | 0.84 | 0.66 | 1.36 | 1.34 | 4.84 | 4.08 | 7.68 | 6.63 | 4.83 | 5.66 | 9.01 | 6.94 |
| V | 229 | 161 | 145 | 138 | 11 | 8 | 8 | 5 | 39 | 33 | 41 | 13 |
| Y | 32.8 | 27 | 24.7 | 35.7 | 41.3 | 45.7 | 67 | 64.8 | 47.3 | 55.5 | 75.9 | 55.3 |
| Zn | 125 | 110 | 100 | 104 | 97 | 75 | 70 | 99 | 127 | 106 | 42 | 55 |
| Zr | 277 | 177 | 242 | 254 | 112 | 158 | 181 | 169 | 251 | 249 | 73 | 129 |
| La | 28.8 | 16.5 | 27 | 33.6 | 20.3 | 60.2 | 60.9 | 52.8 | 60.4 | 78.6 | 19.9 | 22.1 |
| Ce | 61.7 | 37 | 59 | 68.8 | 43.1 | 66.1 | 136.5 | 102 | 102.5 | 138 | 50.1 | 51.9 |
| Pr | 8.38 | 4.85 | 7.49 | 8.87 | 6.58 | 15.55 | 17.15 | 16.25 | 15.45 | 19.85 | 7.02 | 6.67 |
| Nd | 37.4 | 22.1 | 32.5 | 37.7 | 27.9 | 58.9 | 66.7 | 63.4 | 55.3 | 74.3 | 29.5 | 26.4 |
| Sm | 8.53 | 5.11 | 6.86 | 8.03 | 8.76 | 14.15 | 16.3 | 14.95 | 10.95 | 14.15 | 9.46 | 7.45 |
| Eu | 2.54 | 1.79 | 1.57 | 1.82 | 0.27 | 0.47 | 0.39 | 0.38 | 0.16 | 0.19 | 0.08 | 0.35 |
| Gd | 7.6 | 5.36 | 5.91 | 7.45 | 8.11 | 10.85 | 13.6 | 13.2 | 8.99 | 10.95 | 10.7 | 7.72 |
| Tb | 1.15 | 0.84 | 0.88 | 0.8 | 1.29 | 1.55 | 2.16 | 2.1 | 1.47 | 1.75 | 1.99 | 1.38 |
| Dy | 6.72 | 5.65 | 5.24 | 6.89 | 7.88 | 8.89 | 12.7 | 12.9 | 9.59 | 10.8 | 13.25 | 9.32 |
| Ho | 1.24 | 1.05 | 0.96 | 1.35 | 1.55 | 1.65 | 2.51 | 2.48 | 1.9 | 2.17 | 2.68 | 1.9 |
| Er | 3.47 | 2.85 | 2.77 | 3.81 | 4.38 | 4.49 | 6.89 | 6.79 | 5.3 | 5.94 | 7.83 | 5.59 |
| Tm | 0.48 | 0.4 | 0.36 | 0.51 | 0.68 | 0.67 | 1.01 | 1.1 | 0.9 | 0.97 | 1.24 | 0.91 |
| Yb | 2.83 | 2.84 | 2.5 | 3.39 | 4.28 | 4.22 | 6.64 | 6.71 | 5.53 | 6.31 | 7.72 | 5.81 |
| Lu | 0.39 | 0.4 | 0.35 | 0.5 | 0.62 | 0.59 | 0.88 | 0.96 | 0.82 | 0.93 | 1.1 | 0.84 |

| Sample | SLP17-25 | SLP-05 | CR17-04 | SLP17-03 | SLP17-04 | SLP17-05 | SLP-06 | SLP-07 | SLP17-30 | SLP17-31 | SM17-03 |
|---|---|---|---|---|---|---|---|---|---|---|---|
| Rock unit | Panalillo | San José | San Miguelito | San Miguelito | San Miguelito | San Miguelito | San Miguelito | El Zapote | Zapote | Zapote | San Miguelito |
| Rock (TAS) | Rhyolite | Rhyolite | Rhyolite | Rhyolite | Rhyolite | Rhyolite | Trachydacite | Rhyolite | Rhyolite | Rhyolite | Rhyolite |
| Long. (°W) | 101°05′45′ | 101°04′44″ | 101°12′33″ | 101°07′00″ | 101°07′36″ | 101°07′31″ | 101°13′06″ | 101°04′45″ | 101°06′43″ | 100°58′08″ | 101°14′07′ |
| Lat. (°N) | 22°05′14″ | 22°01′20″ | 22°00′48″ | 22°07′02″ | 22°07′04″ | 22°07′07″ | 22°05′23″ | 22°04′12″ | 22°00′40″ | 22°05′28″ | 22°06′23″ |
| Ba | 410 | 119.5 | 6.8 | 21.2 | 34.8 | 167.5 | 255 | 62.1 | 107 | 47.8 | 254 |

(*continued on next page*)

**Table 3** (*continued*)

| Sample | SLP17-25 | SLP-05 | CR17-04 | SLP17-03 | SLP17-04 | SLP17-05 | SLP-06 | SLP-07 | SLP17-30 | SLP17-31 | SM17-03 |
|---|---|---|---|---|---|---|---|---|---|---|---|
| Rock unit | Panalillo | San José | San Miguelito | San Miguelito | San Miguelito | San Miguelito | San Miguelito | El Zapote | Zapote | Zapote | San Miguelito |
| Rock (TAS) | Rhyolite | Rhyolite | Rhyolite | Rhyolite | Rhyolite | Rhyolite | Trachydacite | Rhyolite | Rhyolite | Rhyolite | Rhyolite |
| Long. (°W) | 101°05′45′ | 101°04′44″ | 101°12′33″ | 101°07′00″ | 101°07′36″ | 101°07′31″ | 101°13′06″ | 101°04′45″ | 101°06′43″ | 100°58′08″ | 101°14′07′ |
| Lat. (°N) | 22°05′14″ | 22°01′20″ | 22°00′48″ | 22°07′02″ | 22°07′04″ | 22°07′07″ | 22°05′23″ | 22°04′12″ | 22°00′40″ | 22°05′28″ | 22°06′23″ |
| Co | 2 | | | 2 | | 1 | | 1 | 1 | | 1 |
| Cr | | 10 | 10 | | | | | | | | |
| Cs | 9.05 | 11.75 | 5.18 | 18.1 | 17.35 | 20.4 | 11.9 | 14.8 | 13.25 | 13.5 | 13.05 |
| Cu | 3 | 2 | 5 | 2 | 2 | 2 | 2 | 3 | 2 | 2 | 2 |
| Ga | 15.9 | 23.1 | 42.8 | 24.6 | 23.2 | 23.1 | 22.2 | 23 | 21.6 | 23.1 | 22.7 |
| Hf | 4.6 | 6 | 8.9 | 4.8 | 4.4 | 4 | 4.8 | 5.8 | 5.6 | 5.4 | 5.6 |
| Nb | 13.3 | 23 | 100.5 | 26.1 | 24.5 | 25.1 | 20.8 | 23.3 | 21.3 | 25.2 | 21.6 |
| Ni | 1 | | 2 | 1 | | | 2 | 1 | 2 | | 2 |
| Pb | 22 | 35 | 62 | 37 | 36 | 33 | 32 | 40 | 33 | 38 | 33 |
| Rb | 183 | 336 | 397 | 407 | 390 | 403 | 319 | 368 | 330 | 369 | 315 |
| Sc | 5 | 7 | | 10 | 10 | 10 | 7 | 8 | 8 | 9 | 8 |
| Sr | 648 | 19.9 | 5.6 | 16 | 158.5 | 117.5 | 32.8 | 14.5 | 18.1 | 12.9 | 30.2 |
| Ta | 1.2 | 2.1 | 9.7 | 2.5 | 2.4 | 2.5 | 1.9 | 2.2 | 2 | 2.4 | 2 |
| Th | 21.9 | 34 | 18.25 | 33.8 | 31.2 | 31 | 25.3 | 29.2 | 26.7 | 37.9 | 30.8 |
| U | 6.15 | 6.31 | 6.65 | 6.78 | 6.58 | 5.74 | 4.23 | 4.48 | 5.33 | 6.22 | 5.17 |
| V | 17 | 26 | | | | | 8 | | 5 | | 8 |
| Y | 37.6 | 69.7 | 16.9 | 68.7 | 56.3 | 57.8 | 39 | 14.4 | 26 | 70.1 | 51.3 |
| Zn | 62 | 64 | 130 | 71 | 96 | 75 | 70 | 76 | 69 | 65 | 68 |
| Zr | 132 | 161 | 135 | 120 | 108 | 92 | 121 | 147 | 144 | 143 | 152 |
| La | 55.9 | 76 | 6.6 | 61.7 | 47.2 | 43.5 | 37.9 | 22 | 44.9 | 73.5 | 54.5 |
| Ce | 88 | 107 | 16.6 | 132 | 113.5 | 107 | 86.5 | 63.4 | 90.5 | 127 | 107 |
| Pr | 14.5 | 20.6 | 1.25 | 17.85 | 13.1 | 12.5 | 10.05 | 3.51 | 13.2 | 20.4 | 16.3 |
| Nd | 53 | 77.4 | 4 | 67.6 | 49.6 | 46.7 | 37.1 | 10.1 | 49.3 | 76.3 | 62.2 |
| Sm | 10.2 | 15.8 | 1.18 | 15.3 | 11.15 | 10.2 | 8.39 | 1.82 | 10.4 | 16.75 | 13.9 |
| Eu | 0.36 | 0.33 | 0.05 | 0.13 | 0.11 | 0.07 | 0.43 | 0.22 | 0.37 | 0.18 | 0.38 |
| Gd | 7.86 | 13.2 | 1.4 | 12.55 | 9.15 | 8.92 | 7.7 | 1.8 | 7.6 | 13.8 | 11.55 |
| Tb | 1.21 | 2.03 | 0.35 | 1.99 | 1.57 | 1.61 | 1.23 | 0.44 | 1.15 | 2.21 | 1.79 |
| Dy | 7.22 | 12.6 | 2.64 | 13.05 | 10.2 | 10.6 | 7.67 | 2.86 | 6.66 | 13.75 | 10.7 |
| Ho | 1.4 | 2.49 | 0.61 | 2.59 | 2.06 | 2.22 | 1.5 | 0.64 | 1.24 | 2.56 | 2 |
| Er | 3.82 | 6.67 | 2.03 | 7.24 | 6.19 | 6.43 | 4.1 | 2.09 | 3.33 | 7.22 | 5.23 |
| Tm | 0.61 | 1.06 | 0.35 | 1.15 | 1 | 1.06 | 0.61 | 0.39 | 0.56 | 1.12 | 0.8 |
| Yb | 3.61 | 6.38 | 2.59 | 7.16 | 6.17 | 6.61 | 3.9 | 2.69 | 3.62 | 6.92 | 4.8 |
| Lu | 0.55 | 0.94 | 0.36 | 1.01 | 0.91 | 0.99 | 0.56 | 0.41 | 0.51 | 1.02 | 0.71 |

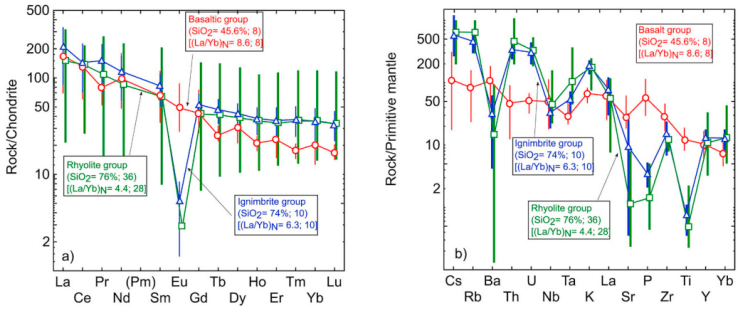


**Fig. 5.** (a) Chondrite–normalized rare–earth element (REE) plot for the SSMC samples (values taken from McDonough and Sun, 1995; mean value of silica and mean value of $(La/Yb)_N$ ratios along with the number of samples are also included for each rock groups). (b) Primitive mantle–normalized multi–element plot for the SSMC samples (values taken from McDonough and Sun, 1995; mean value of silica and mean value of $(La/Yb)_N$ ratios along with the number of samples are also included for each rock groups).

variable concentration of LILE (Ba = 288–966 ppm; Sr = 371–519 ppm; Table 3). The chondrite-normalized REE diagram (Fig. 5a) shows an enrichment in light REE (LREEs) and heavy REEs (HREEs; $(La/Yb)_{CN}$ = 3.9–7.3), as well as small Eu anomalies Eu (Eu/Eu* = 0.70–1.15), the subscript $_{CN}$ refers to the chondrite normalized value, chondrite values are from McDonough and Sun (1995; Fig. 5a). Total REE concentration of the basaltic group varies from 101.09 to 176.63 ppm. The primitive mantle-normalized multi-element diagram (Fig. 5b) for the basaltic group samples display slightly flat patterns in incompatible elements with Nb (Nb/Nb* = 0.20–0.78), Ta (Ta/Ta* = 0.21–0.90) and P anomalies (Fig. 5b).

Trace element concentrations of the rhyolite-ignimbrite group samples are characterized by Sc = 2.0–10 ppm, Cr = 1.2–10 ppm, Ni = 0.60–14 ppm, and enriched and variable concentrations of LILE (e.g. Ba = 6.8–410 ppm, Sr = 5.6–648 ppm; Table 3). The chondrite-normalized REE diagram (Fig. 5a) displays an enrichment in LREEs and highly variable heavy REEs (HREEs) ($(La/Yb)_{CN}$ = 1.7–10.5), as well higher Eu anomalies as compared to the basaltic group. The strong negative Eu (Eu/Eu* = 0.02–0.36) anomalies are probably consistent with plagioclase fractionation, either in the solid residuum left by partial melting (Rollinson, 1993). The primitive mantle-normalized multielement diagram for the rhyolite-ignimbrite group shows enriched patterns in incompatible elements with Nb (Nb/Nb* = 0.26–1.06), Ti (Ti/Ti* = 0.04–0.28), Ba and P anomalies (Fig. 5b).

## 6. Discussion

### 6.1. Alteration effects

The loss–on–ignition (LOI) values for the basaltic group display a range from 0.496 to 2.48%. The LOI of the rhyolitic-ignimbrite group shows the range from 0.627 to 1.49%, except four samples that display high values > 5% m/m. Therefore, the effect of post–emplacement alteration on elemental mobility could be considered for only some samples. As probably an alteration-independent index for geochemical diversity, Zr concentration implements a significant correlation with other elements and can be used to test their mobility (Pearce et al., 1992; Wang et al., 2016). Similarly, in this work, elements including $(TiO_2)_{adj}$, Ba, Rb, V, Nb, and Sr, for volcanic rocks plotted against Zr to evaluate their mobility during alteration (graph not shown) displayed a statistically significant correlation. Therefore, these elements could be considered relatively immobile during alteration and are useful in understanding of petrogenetic interpretation.

### 6.2. Petrogenetic processes

Petrography analysis has revealed disequilibrium evidence in the basaltic group rocks, whereas (Eu/Eu*) and (Th/Yb) bivariate plots show a limited contribution of the continental crust in their petrogenesis (Fig. 6a – b). In order to explore the effects of magma mixing between the felsic group and mafic group magmas, a mixing model were developed between two samples L2 and SLP01. Sample L2 has the most felsic nature with $SiO_{2(adj)}$ = 79.41 %m/m, $MgO_{(adj)}$ = 0.04 %m/m (values reported by Leroy et al., 2002), sampled in the study area, and sample SLP01 has more mafic characteristics i.e., $SiO_{2(adj)}$ = 39.81% m/m, $MgO_{(adj)}$ = 4.59 %m/m for the SSMC (Fig. 7a and b). It is clear from Fig. 7 that the basaltic group lavas plot close to the representative mixing curve, but also show shift of some points from the modelled mixing curve, probably as a result of the prior fractional crystallization process.

The $(Gd/Yb)_{PM}$ versus Eu/Eu* and Nb/Yb versus Th/Yb ratios of the rhyolite-ignimbrite group rocks from the SSMC may be comparable to

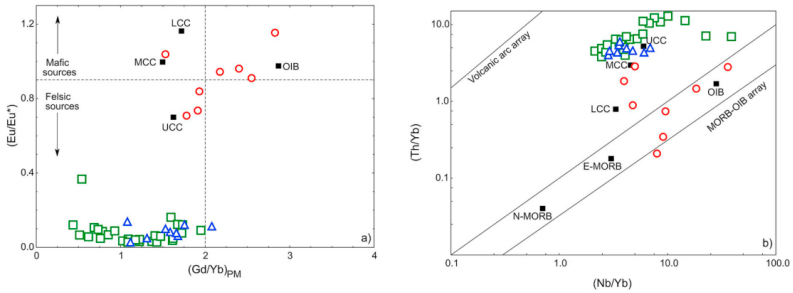


**Fig. 6.** Geochemical variation diagrams for volcanic rocks from the SSMC. (a) (Eu/Eu*) – $(Gd/Yb)_{PM}$ diagram; (b) (Nb/Yb) – (Th/Yb) diagram. Abbreviations: N – MORB– normal Mid – Ocean Ridge basalt; E – MORB – enriched Mid – Ocean Ridge basalt; OIB – Ocean Island basalt; LCC – lower continental crust; MCC – middle continental crust; UCC – upper continental crust.

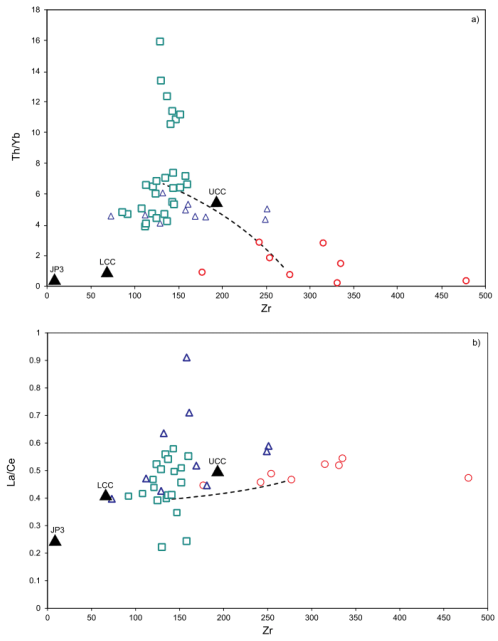


**Fig. 7.** (a) Zr–Th/Yb and (b) Zr–La/Ce variation diagrams for the basaltic group and rhyolite-ignimbrite group rocks from the SSMC showing mixing model. JP3: hornblende pyroxenite sample represent an enriched mantle (taken from Heinrich and Besch, 1992); LCC: lower continental crust (value taken from Rudnick and Gao, 2003); UCC: upper continental crust (value taken from Rudnick and Gao, 2003).

the continental crust (Fig. 6a – b), especially when the uncertainty in the average crustal compositions could be taken into account.

A quantitative treatment was carried out to represent a partial melting process for the rhyolitic-ignimbrite group of the SSMC by applying the modal batch partial melting equations reported by Zou (2007). Trace and rare-earth element compositions from the average upper and lower continental crust reported by Rudnick and Gao (2003) were used as the crustal source ($C_o$). The mineralogical compositions of crustal reservoirs were as follows: for lower crust (LCC): 0.30 Pl + 0.30Cpx + 0.20 Gt + 0.10Amp + 0.05Opx + 0.05Op and upper crust (UCC): 0.50 Pl + 0.10Fsp + 0.15Bt + 0.05Amp + 0.30Qtz + 0.01Ap (see more detail in Velasco-Tapia, 2017). The partial melting models for the rhyolite-ignimbrite group were carried out for melting degrees of 20–50% (F = 0.2–0.5). The results obtained were used to elaborate chondrite-normalized REE plots (Fig. 8a – b). The rhyolite-ignimbrite group rocks showed patterns with comparable features with the upper continental crust and their derived liquids. Thus, the crustal melting process may have taken place at different depths with conditions of the upper continental crust.

### 6.3. Tectonic setting

#### 6.3.1. Evaluation of Nb and Ta anomalies

The evaluation of the Nb and Ta anomalies has been described statistically by Verma (2015, 2019) for basic, intermediate, and acid magmas from the Mexican Volcanic Belt, numerous continental and island arcs, continental rifts or extensional areas, including continental collision setting around the world. In this work, we have calculated these values for the basic and acid rocks from the SSMC rocks and compared them with the compilation of Verma (2015) in Table 4. The calculated value for Nb and Ta anomaly values for basic (0.604 ± 0.343 and 0.53 ± 0.33), and acid (0.676 ± 0.218 and 1.189 ± 0.445) units could be considered similar to the continental rift or extension areas of the Eastern Anatolia (Turkey) and the Rio Grande rift, New Mexico (USA) and different from the continental arcs (Table 4). Therefore, the volcanic rocks from SSMC may have been derived from the rifting or extensional environment.

#### 6.3.2. Subduction or continental crust sensitive parameters

Subduction – continental crust signal parameters were proposed and used to identify the subduction or continental crust contribution in a tectonic environment (Verma, 2009, 2015, 2019). Higher values of these parameters, especially those having LILE in the numerator and HFSE in the denominator, reflect contribution from the subduction process. Alternatively or concurrently, high values of these parameters may also represent a significantly higher influence from the continental crust. This is especially applied for evolved intermediate and acid rocks (Verma and Verma, 2018). These considerations make it difficult to unambiguously infer the tectonic implications from evolved rocks. Nevertheless, we used 6 such parameters (two listed below; others in the Supplementary file) for statistically comparing between the SSMC and Rio Grande rift, New Mexico (RG) rocks.

The $(LILE4/LREE3)_E$ parameter is the "four LILE to three LREE" ratio and $(LILE5/HFSE5)_E$ parameter is the "five LILE to five HREE" ratio as follows:

$$\{LILE4/LREE3\}_E = \frac{[(K_{sa}/K_E) + (Rb_{sa}/Rb_E) + (Ba_{sa}/Ba_E) + (Sr_{sa}/Sr_E)]/4}{[(La_{sa}/La_E) + (Ce_{sa}/Ce_E) + (Nd_{sa}/Nd_E)]/3} \quad (1)$$

$$\{LILE5/LHFSE5\}_E = \frac{[(K_{sa}/K_E) + (Rb_{sa}/Rb_E) + (Cs_{sa}/Cs_E) + ((Ba_{sa}/Ba_E)) + (Sr_{sa}/Sr)_E]/5}{[(Ti_{sa}/Ti_E) + (P_{sa}/P_E) + (Zr_{sa}/Zr_E) + ((Hf_{sa}/Hf_E)) + (Ta_{sa}/Ta_E)]/5} \quad (2)$$

where the subscript "sa" stands for the sample and "E" for bulk silicate earth (normalization values from McDonough and Sun, 1995).

The basaltic group from the SSMC shows lower values for 2 parameters $(LILE4/LREE3)_E$ and $(LILE4/HFSE4)_E$ than the Central American Volcanic Arc (CAVA); the other 3 parameters show overlapping confidence interval of the mean; and the remaining parameter $(LREE3/HFSE5)_E$ cannot be compared because of the lack of information for the CAVA (Table 5). On the other hand, the SSMC basaltic rocks show overlapping values for all 4 parameters with the RG rocks (Table 5). These results imply that the SSMC basaltic group rocks might be considered similar to the Rio Grande basic rocks but different from the CAVA.

The SSMC rhyolite-ignimbrite group samples display overlapping values for 4 out of 5 parameters with the CAVA; $(LREE3/HFSE5)_E$ cannot be compared whereas $(LILE4/LREE3)_E$ shows lower value for the SSMC than the CAVA. On the other hand, the SSMC evolved rocks show overlapping ranges for both parameters $(LILE4/HFSE4)_E$ and $(LREE3/HFSE5)_E$ that can be compared with the RG (Table 5). These results are also consistent with the similarities of the SSMC with the RG.

Thus, for both basaltic and evolved rocks, the similarity of the SSMC with the RG and at least some significant differences between the SSMC and the CAVA can be inferred. This may imply similarity of the tectonic regime of the SSMC and RG and differences of the SSMC and CAVA regions.

#### 6.3.3. Multi–dimensional discrimination diagrams

New multi–dimensional discrimination diagrams were also used to infer the tectonic setting, because conventional bivariate and ternary diagrams for tectonic discrimination were shown to work unsatisfactorily (Verma, 2010). The failure of the older diagrams is based

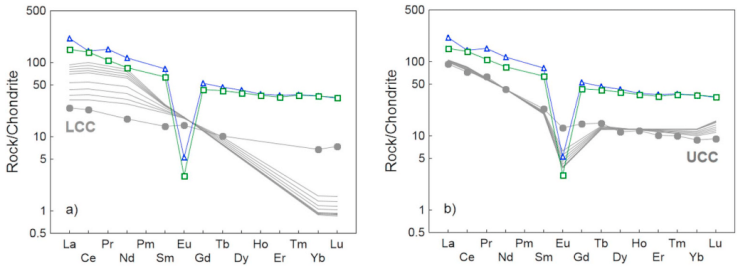


**Fig. 8.** (a) Chondrite – normalized rare – earth element patterns for the Lower Continental Crust (LCC) and (b) Chondrite – normalized rare – earth element patterns for the Upper Continental Crust (UCC); for both figures partial melts (solid gray lines) were generated at degree of melting F = 0.2–0.5, applying a batch melting equation by Zou (2007) for comparison of rhyolite-ignimbrite group rocks (average value, n = 46). Gray circles line correspond to LCC or UCC normalized pattern.

**Table 4**
Statistical information on the Nb and Ta anomaly (with respect to Ba and La) for mafic and felsic rocks from San Miguelito Complex (SSMC), San Luis Potosí Mexico (this work) and comparison with other arcs and continental rifts (taken from Verma, 2015).

| Area | Magma type | $\{Nb/Nb^*\}_{pm}$ | | $\{Ta/Ta^*\}_{pm}$ | |
|---|---|---|---|---|---|
| | | Mean ± standard deviation (number of samples) $\bar{x} \pm s$ (n) | 99% Confidence limits (CL) of the mean | Mean ± standard deviation (number of samples) $\bar{x} \pm s$ (n) | 99% Confidence limits (CL) of the mean |
| Sierra de San Miguelito Volcanic Complex | Basic | 0.604 ± 0.343 (8) | 0.179–1.029 | 0.53 ± 0.33 (4) | (0) – 1.49 |
| | Acid | 0.676 ± 0.218 (25) | 0.554–0.798 | 1.189 ± 0.445 (38) | 0.92–1.457 |
| *Continental arcs* | | | | | |
| Central American Volcanic Arc | Basic | 0.13 ± 0.06 (59) | 0.11–0.15 | 0.18 ± 0.11 (34) | 0.13–0.23 |
| | Acid | 0.105 ± 0.040 (25) | 0.083–0.127 | 0.105 ± 0.029 (4) | 0.020–0.189 |
| Andes (Chile) | Basic | 0.20 ± 0.05 (29) | 0.17–0.23 | 0.147 ± 00.037 (9) | 0.17–0.23 |
| | Acid | 0.177 ± 0.031 (49) | 0.165–0.189 | 0.194 ± 0.034 (41) | 0.180–0.208 |
| Andes (Peru) | Acid | 0.25 ± 0.10 (37) | 0.21–0.30 | 0.26 ± 0.11 (33) | 0.21–0.31 |
| Andes (Ecuador) | Basic | 0.079 ± 0.009 (7) | 0.065–0.090 | – – | – – |
| | Acid | 0.106 ± 0.018 (210) | 0.103–0.110 | 0.17 ± 0.07 (16) | 0.11–0.22 |
| *Continental rifts or extensional areas* | | | | | |
| San Juan volcanic field, Colorado (USA) | Acid | 0.12 ± 0.05 (7) | 0.06–0.19 | – – | – – |
| Rio Grande rift, New Mexico (USA) | Basic | 0.7 ± 0.5 (29) | 0.5–1.0 | 0.8 ± 0.5 | 0.5–1.1 |
| Central Mexican Volcanic Belt | Basic | 0.54 ± 0.25 (38) | 0.43–0.65 | 0.75 ± 0.16 (30) | 0.67–0.84 |
| | Acid | 0.152 ± 0.033 (194) | 0.146–0.158 | 0.22 ± 0.05 (184) | 0.21–0.23 |
| Eastern Anatolia (Turkey) | Basic | 0.782 ± 0.014 (20) | 0.773–0.791 | 0.784 ± 0.038 (20) | 0.760–0.809 |
| | Acid | 0.50 ± 0.13 (25) | 0.43–0.58 | 0.680 ± 0.017 (24) | 0.580–0.779 |

**Table 5**
Statistical information of subduction signal for the Sierra de San Miguelito complex (SSMC). Rio Grande Rift (RG; data compiled from Duncker et al., 1991; Gibson et al., 1992; McMillan et al., 2000) and Central American Volcanic Arc (CAVA; data compilation by Verma, 2015).

| Parameter | SSMC | | | RG | | | CAVA |
|---|---|---|---|---|---|---|---|
| | n | $\bar{x}$ | $u_{99}$ | n | $\bar{x}$ | $u_{99}$ | 99% confidence limit of the mean |
| Basic | | | | | | | |
| $(LILE4/LREE3)_E$ | 8 | 1.67 | 0.82 | 21 | 1.44 | 0.272 | 2.7–3.2 |
| $(LILE5/HFSE5)_E$ | 4 | 3.30 | 7.2 | 1 | 3.75 | – | 4.1–5.7 |
| $(LILE4/HFSE4)_E$ | 8 | 1.47 | 0.58 | 45 | 1.884 | 0.064 | 4.2–5.7 |
| $(LREE3/HFSE5)_E$ | 4 | 1.25 | 1.32 | 22 | 2.13 | 0.48 | – |
| (LILE4/HREE3) | 4 | 10.29 | 0.366 | – | – | – | 7.8–9.1 |
| (LILE4/LREE4) | 4 | 2.07 | 2.09 | – | – | – | 2.8–3.03 |
| Acid | | | | | | | |
| $(LILE4/LREE3)_E$ | 29 | 2.80 | 0.396 | – | – | – | 3.4–4.5 |
| $(LILE5/HFSE5)_E$ | 29 | 13.48 | 2.0 | – | – | – | 3.7–16.0 |
| $(LILE4/HFSE4)_E$ | 37 | 15.71 | 0.61 | 4 | 10.87 | 4.14 | 4.3–16.0 |
| $(LREE3/HFSE5)_E$ | 30 | 2.5 | 0.68 | 1 | 3.03 | – | – |
| (LILE4/HREE3) | 37 | 13.93 | 0.58 | – | – | – | 6.0–28.0 |
| (LILE4/LREE4) | 29 | 2.772 | 0.119 | – | – | – | 2.1–7.0 |

on the following criteria: (a) use of limited databases to construct them; (b) the problem of closed or constant sum compositional variables not attended in older diagrams; and (c) eye–fitted tectonic field boundaries in the older diagrams. All these problems have been solved in the multidimensional solutions (Armstrong–Altrin, 2015; Verma, 2015, 2019; Verma and Amstrong–Altrin, 2016; Verma et al., 2012, 2013, 2015). Therefore, new multi–dimensional discrimination diagrams for basic and acid rocks, which are based on log–ratio transformation, linear discrimination and canonical analysis, were used for tectonic interpretation.

The new multi–dimensional discrimination diagrams (Verma and Agrawal, 2011; Verma et al., 2013) indicated a within–plate setting for the SSMC volcanic rocks (Fig. 9). The findings of new multi-dimensional discrimination diagrams are coherent with the syn-transform extension regime and intraplate volcanism that was produced during the Oligocene to Miocene within the southern Basin and Range province (western USA, northwestern Mexico; Dickinson, 2002; Cosca et al., 2014).

More constraints, especially the study of basic volcanic rocks and underlying crust from this and surrounding areas and appropriate well-constrained thermochemical models, are required before a comprehensive petrogenetic and tectonic model could be put forth. This should constitute future studies.

## 7. Conclusions

The following conclusions, based on the results and observations, can be summarized:

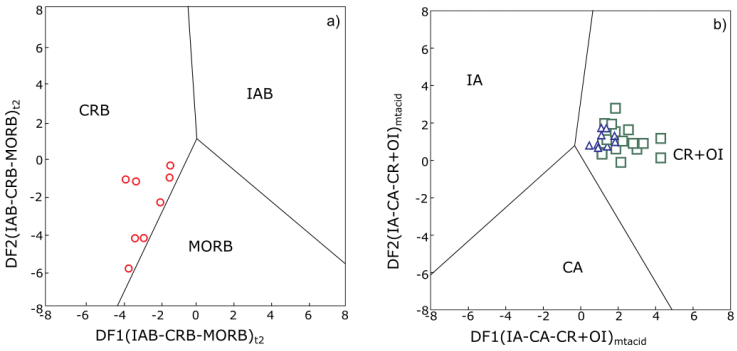


**Fig. 9.** (a) Discriminant – function multidimensional diagrams based on log – - transformed ratios of major and trace elements for tectonic discrimination of the basic units from the SSMC (Verma and Agrawal, 2011). (b) Discriminant – function multidimensional diagrams based on log – - transformed ratios of major and trace elements for tectonic discrimination of the acid units from the SSMC (Verma et al., 2013).

1. The San Miguelito volcanic complex is constituted by the basaltic components of trachybasalt, basalt, and foidite compositions and the rhyolite-ignimbrite component of rhyolitic and trachyte compositions.
2. Basaltic group rocks from the San Miguelito volcanic complex show foidite to trachybasalt composition. The REE chondrite-normalized patterns display an enrichment in LREE, a small or absent Eu-anomaly and a flat-shape for HREE. The primitive mantle normalized diagram shows slightly flat patterns in incompatible elements with small or absent anomalies of Nb, Ta, and P. In contrast, the rhyolite-ignimbrite group rocks display a trachydacite and rhyolite compositions. The REE chondrite-normalized patterns show an enrichment in LREE, a negative Eu-anomaly and a flat shape for HREE. The primitive mantle normalized diagram shows an enrichment in incompatible elements with negative anomalies in Nb, Ti, Ba and P.
3. Geochemical features indicated that the basaltic group rocks from the San Miguelito volcanic complex were derived from mantle through crustal evolution by relatively small amount of magma mixing processes with felsic volcanism. The felsic volcanic rocks were generated by partial melting of the upper continental crust.
4. New multi–dimensional tectonic discrimination diagrams indicate that these volcanic rocks are related to within–plate setting. This is consistent with Nb– and Ta anomalies as well with the syn-transform extension regime from the Basin and Range province.

## Acknowledgements

The first author (DTS) is thankful to the National Council of Science and Technology (CONACYT), Mexico for his doctoral fellowship [grant # 336677]. SKV is grateful to Newton Advanced Fellowship award–The Royal Society, UK for the grant [NA160116]. We are also grateful to two anonymous reviewers and Associate Editor Prof. Reinhardt Fuck for their constructive comments and suggestions.

## Appendix A. Supplementary data

Supplementary data to this article can be found online at https://doi.org/10.1016/j.jsames.2019.102311.

## References

Armstrong–Altrin, J.S., 2015. Evaluation of two multi–dimensional discrimination diagrams from beach and deep sea sediments from the Gulf og Mexico and their application to Precambrian clastic sedimentary rocks. Int. Geol. Rev. 57, 1446–1461.
Aguillón-Robles, A., Aranda-Gómez, J.J., Solorio Munguía, J.G., 1994. Geología y tectónica de un conjunto de domos riolíticos del Oligoceno medio en el sur del Estado de San Luis Potosí, México. Rev. Mex. Ciencias Geol. 11, 29–42.
Aguillón-Robles, A., Tristán-González, M., Aguirre-Díaz, G.J., López-Doncel, R.A., Bellon, H., Martínez-Esparza, G., 2014. Eocene to Quaternary mafic-intermediate volcanism in San Luis Potosí, central Mexico: the transition from Farallon plate subduction to intra-plate continental magmatism. J. Volcanol. Geotherm. Res. 276, 152–172.
Cosca, M.A., Thompson, R.A., Lee, J.-P., Turner, K.J., Neymark, L.A., Premo, W.R., 2014. $^{40}Ar/^{39}Ar$ geochronology, isotope geochemistry (Sr, Nd, Pb), and petrology of alkaline lavas near Yampa, Colorado: migration of alkaline volcanism and evolution of the northern Rio Grande rift. Geosphere 10, 374–400.
Dickinson, W.R., 2002. The Basin and Range province as a composite extensional domain. Int. Geol. Rev. 44, 1–38.
Duncker, K.E., Wolff, J.A., Harmon, R.S., Leat, P.T., Dickin, A.P., Thompson, R.N., 1991. Diverse mantle and crustal components in lavas of the NW Cerros del Rio volcanic field, Rio Grande Rift, New Mexico. Contrib. Mineral. Petrol. 108, 331–345.
Gaytán-Martínez, R., Noyola-Medrano, C., Rojas-Beltrán, M.A., 2017. Análisis espectral y petrográfico del Complejo Volcánico Sierra de San Miguelito, S.L.P., México. Ser. Correlación Geol. 33, 49–60.
Gibson, S.A., Thompson, R.N., Leat, P.T., Dickin, A.P., Morrison, M.A., Hendry, G.L., Mitchell, J.G., 1992. Asthenosphere-derived magmatism in the Rio Grande rift, western USA: implications for continental break-up. In: Storey B, C., Alabaster, T., Pankhurst, R.J. (Eds.), Magmatism and the Causes of Continental BreakUp. Geological Society Special Publication, London, UK, pp. 61–89.
Heinrich, W., Besch, T., 1992. Thermal history of the upper mantle beneath a young back-arc extensional zone: ultramafic xenoliths from San Luis Potosí, Central Mexico. Contrib. Mineral. Petrol. 111, 126–142.
Jones, C.H., Wernicke, B.P., Farmer, G.L., Walker, J.D., Coleman, D.S., McKenna, L.W., Perry, F.V., 1992. Variations across and along a major continental rift: an interdisciplinary study of the Basin and Range province, western USA. Tectonophysics 213, 57–96.
Labarthe-Hernández, G., Jiménez-López, L.S., 1992. Características físicas y estructura de lavas e ignimbrita riolíticas en la Sierra de San Miguelito, S.L.P. Universidad Autónoma de San Luis Potosí, Instituto de Geología. Folleto Técnico 114.
Le Bas, M.J., Maitre, R.W.L., Streickensen, A., Zanettin, B., 1986. A chemical classification of volcanic rocks based on the total alkali–silica diagram. J. Petrol. 27, 745–750.
Leroy, J.L., Rodríguez–Ríos, R., Dewonck, S., 2002. The topaz–bearing rhyolites from the San Luis Potosí area (Mexico): characteristics of the lava and growth conditions of topaz. Bull. Soc. Geol. Fr. 173, 579–588.
López-Loera, H., 2014. Geofísica para la localización de Agua Subterránea en Ambientes Volcánicos Áridos de la Mesa Central: Caso La Dulcita, Villa de Ramos, San Luis Potosí, México. Bol. Soc. Geol. Mex. 66, 165–181.
McDonough, W.F., Sun, S.–S., 1995. The composition of the Earth. Chem. Geol. 120, 223–253.
McMillan, N.J., Dickin, A.P., Haag, D., 2000. Evolution of magma source regions in the Rio Grande rift, southern New Mexico. Geol. Soc. Am. Bull. 112, 1582–1593.
Middlemost, E.A.K., 1989. Iron oxidation ratios, norms and the classification of volcanic rocks. Chem. Geol. 77, 19–26.
Nieto–Samaniego, A.F., Macías–Romo, C., Alaniz–Alvarez, S.A., 1996. Nuevas edades isotópicas de loa cubierta volcánica cenozoica de la parte meridional de la Mesa Central, México. Rev. Mex. Ciencias Geol. 13, 117–122.
Nieto–Samaniego, A.F., Ferrari, L., Alaniz–Alvarez, S.A., Labarthe–Hernández, G., Rosas–Elguera, J., 1999. Variation of cenozoic extensión and volcanism across the southern Sierra Madre Occidental volcanic province, Mexico. Geol. Soc. Am. Bull. 111, 347–363.
Nieto–Samaniego, A.F., Alaniz-Álvarez, S.A., Camprubí, A., 2007. Mesa central of méxico: stratigraphy, structure, and cenozoic tectonic evolution. In: In: Alaniz-Álavarez, S.A., Nieto-Samaniego, Á.F. (Eds.), Geology of México: Celebrating the Centenary of the Geological Society of México 422. Geological Society of America Special Paper, pp. 41–70.
Orozco–Esquivel, M.T., Nieto–Samaniego, A.F., Alaniz–Alvarez, S.A., 2002. Origin of rhyolitic lavas in the Mesa Central, Mexico by crustal melting related to extension. J. Volcanol. Geotherm. Res. 118, 37–56.
Pearce, J.A., van der Laan, S.R., Arculus, R.J., Murton, B.J., Ishii, T., Peate, D.W., Parkinson, I.J., 1992. Boninite and harzburgite from Leg 125 (Bonin–Mariana forearc): a case study of magma genesis during the initial stages of subduction. Proc. Ocean Drill. Program Sci. Results 623–659.

Rodríguez–Ríos, R., Aguillón–Robles, A., Leroy, J.L., 2007. Evolución petrológica y geoquímica de un complejo de domos topacíferos en el Campo Volcánico de San Luis Potosí (México). Rev. Mex. Ciencias Geol. 24, 328–343.
Rodríguez-Ríos, R., Torres-Aguilera, J., 2009. Evolución petrológica y geoquímica del vulcanismo bimodal oligocénico en el campo volcánico de San Luis Potosí (México). Rev. Mex. Ciencias Geol. 26, 658–673.
Rollinson, H.R., 1993. Using of Geochemical Data: Evaluation, Presentation, Interpretation. Longman Scientific and Technical, New York.
Rudnick, R.L., Gao, S., 2003. Composition of the continental crust. Treatise Geochem. 3, 659.
Sieck, P., López-Doncel, R., Dávila-Harris, P., Aguillón-Robles, A., Wemmer, K., Maury, R.C., 2019. Almandine garnet-bearing rhyolites associated to bimodal volcanism in the Mesa Central of Mexico: geochemical, petrological and geochronological evolution. J. South Am. Earth Sci. 92, 310–328.
Sonder, L.J., Jones, C.H., 1999. Western United States extension: how the west was widened. Annu. Rev. Earth Planet Sci. 27, 417–462.
Torres-Hernández, J.R., Labarthe-Hernández, G., Aguillón-Robles, A., Gómez-Anguiano, M., Mata-Segura, J.L., 2006. The pyroclastic dikes of the Tertiary San Luis Potosi volcanic field: implications on the emplacement of Panalillo ignimbrite. Geofis. Int. 45, 243–253.
Torres–Hernández, J.R., Siebe–Grabach, C., Aguillón–Robles, A., Rodríguez–Ríos, R., 2014. Geocronología y características geoquímicas de un conjunto de domos riolíticos terciarios en el Campo Volcánico de San Luis Potosí, México. Bol. Soc. Geol. Mex. 66, 183–197.
Tristán-González, M., 1986. Estratigrafía y tectónica del Graben de Villa de Reyes, en los estados de San Luis Potosí y Guanajuato, México. Universidad Autónoma de San Luis Potosí, Instituto de Geología Folleto Técnico 107.
Tristán–González, M., Aguillón–Robles, A., Barboza–Gudiño, J.R., Torres–Hernández, J.R., Bellon, H., López–Doncel, R., Rodríguez–Ríos, R., Labarthe–Hernández, G., 2009. Geocronología y distribución espacial del vulcanismo en el Campo Volcánico de San Luis Potosí. Bol. Soc. Geol. Mex. 61, 287–303.
Velasco-Tapia, F., 2017. Volcanic ash-beds of the upper Cretaceous san felipe formation, Sierra Madre oriental (Northeastern Mexico): provenance and petrogenesis based on conventional and statistical tools applied to geochemical data. In: In: Veress, B., Szigethy, J. (Eds.), Horizons in Earth Science Research 16. Nova Publishers Inc., pp. 67–99.
Verma, S.P., 2009. Continental rift setting for the central part of the Mexican Volcanic Belt: a statistical approach. Open Geol. J. 3, 8–129.
Verma, S.P., 2010. Statistical evaluation of bivariate, ternary and discriminant function tectonomagmatic discrimination diagrams. Turk. J. Earth Sci. 19, 185–238.
Verma, S.P., 2015. Present state of knowledge and new geochemical constraints on the central part of the Mexican Volcanic Belt and comparison with the Central American Volcanic Arc in terms of near and far trench magmas. Turk. J. Earth Sci. 24, 399–1460.
Verma, S.P., 2019. Road from Geochemistry to Geochemometrics. Springer, Singapore978-981-13-9277-1 (in press).
Verma, S.P., Agrawal, S., 2011. New tectonic discrimination diagrams for basic and ultrabasic volcanic rocks through log-transformed ratios of high field strength elements and implications for petrogenetic processes. Rev. Mex. Ciencias Geol. 28, 24–44.
Verma, S.P., Armstrong–Altrin, J.S., 2016. Geochemical discrimination of siliciclastic sediments from active and passive margin settings. Sediment. Geol. 332, 1–12.
Verma, S.P., Rivera–Gómez, M.A., 2013. Computer programs for the classification and nomenclature of igneous rocks. Episodes 36, 115–124.
Verma, S.P., Verma, S.K., 2018. Petrogenetic and tectonic implications of major and trace element and radiogenic isotope geochemistry of Pliocene to Holocene rocks from the Tacaná Volcanic Complex and Chiapanecan Volcanic Belt, southern Mexico. Lithos 312, 274–289.
Verma, S.K., Pandarinath, K., Verma, S.P., 2012. Statistical evaluation of tectonomagmatic discrimination diagrams for granitic rocks and proposal of new discriminant function–based multi–dimensional diagrams for acid rocks. Int. Geol. Rev. 54, 325–347.
Verma, S.P., Pandarinath, K., Verma, S.K., Agrawal, S., 2013. Fifteen new discriminant–function–based multi–dimensional robust diagrams for acid rocks and their application to Precambrian rocks. Lithos 168, 113–123 169.
Verma, S.K., Oliveira, E.P., Verma, S.P., 2015. Plate tectonic settings for Precambrian basic rocks from Brazil by multidimensional tectonomagmatic discrimination diagrams and their limitations. Int. Geol. Rev. 57, 1566–1581.
Verma, S.P., Verma, S.K., Rivera-Gómez, M.A., Torres-Sánchez, D., Díaz-González, L., Amezcua-Valdez, A., Rivera-Escoto, B.A., Rosales-Rivera, M., Armstrong-Altrin, J.S., López-Loera, H., Velasco-Tapia, F., Pandarinath, K., 2018. Statistically coherent calibration of X-ray fluorescence spectrometry for major elements in rocks and minerals. J. Spectrosc. 1–13.
Verma, S.P., Rosales-Rivera, M., Rivera-Gómez, M.A., Verma, S.K., 2019. Comparison of matrix-effect corrections for ordinary and uncertainty weighted linear regressions and determination of major element mean concentrations and total uncertainties of sixty-two international geochemical reference materials from wavelength-dispersive X-ray fluorescence spectrometry. Colloquium Spectroscopicum Internationale XLI O.XR.1, p. 180, Mexico City, June 9-14, 2019.
Wang, T., Wang, Z., Yana, Z., Ma, Z., He, S., Fua, C., Wang, D., 2016. Geochronological and geochemical evidence of amphibolite from the Hualong Group, northwest China: implication for the early Paleozoic accretionary tectonics of the Central Qilian belt. Lithos 248–251, 12–21.
Xu, S.S., Nieto–Samaniego, A.F., Alaniz–Alvarez, S.A., 2004. Titling mechanisms in domino faults of the Sierra de San Miguelito, central Mexico. Geol. Acta 2, 189–209.
Xu, S.S., Nieto–Samaniego, A.F., Alaniz–Álvarez, S.A., 2013. Origin of superimposed and curved slickenlines in San Miguelito range, Central México. Geol. Acta 11, 103–112.
Zou, H., 2007. Quantitative Geochemistry. Imperial College Press, London.

# CAPITULO 6.-

# GEOCRONOLOGÍA $^{40}Ar/^{39}Ar$ Y PETROGENÉSIS DEL COMPLEJO VOLCÁNICO DE LA SIERRA DE SAN MIGUELITO, MESA CENTRAL, MÉXICO

## 6.1 Presentación del trabajo de investigación publicado

El presente artículo de investigación ha sido publicao en *LITHOS* en donde el autor del presente trabajo de tesis participó activamente. Dentro de este trabajo me encuentro como primer autor y el Dr. Sanjeet Kumar Verma, la Dra. Tiffany Barry, el Dr. Surendra Pal Verma y el Dr. José Ramón Torres Hernández son los co-autores del presente artículo de investigación.

Este trabajo de investigación ha contribuido con nueva información dentro del Complejo Volcánico de la Sierra de San Miguelito (CVSSM). Dentro de este trabajo se ha presentado nueva información geocronológica para las unidades volcánicas del CVSSM por el método de $^{40}Ar/^{39}Ar$, la cual sirvió como apoyo para que, junto con la información de datación realizada por trabajos previos, se elaborara una limitación entre los distintos episodios magmáticos dentro del CVSSM. De igual forma, en el presente trabajo se reporta nuevos datos isótopicos (Sr-Nd-Pb), que junto a información isotópica de la provincia de Sierras y Cuencas (Basin and Range), sirvieron para la generación de modelos que muestran el comportamiento de la fuente de las rocas volcánicas del CVSSM.

A su vez, en el presente trabajo se muestra que el CVSSM no exhibe un bimodalismo en la composición de las rocas, como se pensaba en trabajos previos, sino, el CVSSM exhibe un rango composicional amplio (rocas básicas, intermedias y ácidas). De igual forma, en el trabajo se reporta nuevos modelos cuantitativos de procesos de fusión parcial del manto para las rocas básicas, modelos de asimilación y cristalización fraccionada para las rocas intermedias y modelos de fusión parcial cortical para las rocas ácidas, los cuales brindaron una mejor comprensión en la evolución de las rocas volcánicas del CVSSM.

Por último, una contribución importante dentro de este trabajo es la discusión entre las limitaciones petrogenéticas de la información de edades, datos geoquímicos e isotópicos a través del área de estudio dentro del contexto tectónico del desarrollo de la sección sur de la provincia de Sierras y Cuencas (Basin and Range). Es de igual importancia destacar que para el momento en que el presente trabajo ha sido publicado se ha generado un nuevo esquema propuesto por Verma (2020), el cual llega a invalidar los procedimientos existentes de discriminación tectónica. Este nuevo esquema será aplicado para futuros trabajos dentro del CVSSM.

## Referencias

Verma S.P., 2020. Comprehensive multidimensional tectonomagmatic discrimination from log-ratio transformed major and trace elements. Lithos 362-363, 105476.

Torres-Sánchez D., Verma, S.K., Barry, T.L., Verma, S.P., Torres-Hernández, J.R. (2020). $^{40}Ar/^{39}Ar$ geochronology and petrogenesis of the Sierra de San Miguelito Volcanic Complex, Mesa Central, Mexico. Lithos 370-371, 105613 .doi: https://doi.org/10.1016/j.lithos.2020.105613

Lithos 370–371 (2020) 105613

Contents lists available at ScienceDirect

Lithos

journal homepage: www.elsevier.com/locate/lithos

Research Article

# $^{40}Ar/^{39}Ar$ geochronology and petrogenesis of the Sierra de San Miguelito Volcanic Complex, Mesa Central, Mexico

Darío Torres-Sánchez [a], Sanjeet K. Verma [b,*], Tiffany L. Barry [c,*], Surendra P. Verma [d], José Ramón Torres-Hernández [e]

[a] Posgrado de la División de Geociencias Aplicadas, Instituto Potosino de Investigación Científica y Tecnológica (IPICYT), Camino a la Presa San José 2055, San Luis Potosí 78216, Mexico
[b] División de Geociencias Aplicadas, Instituto Potosino de Investigación Científica y Tecnológica (IPICYT), Camino a la Presa San José 2055, San Luis Potosí 78216, Mexico
[c] School of Geography, Geology and the Environment, University of Leicester, University Road, Leicester LE1 7RH, UK
[d] Instituto de Energías Renovables, Universidad Nacional Autónoma de México, Temixco, Morelos 62580, Mexico
[e] Instituto de Geología, Universidad Autónoma de San Luis Potosí, Manuel Nava No. 5. Zona Universitaria, 78240 San Luis Potosí, S.L.P., Mexico

ARTICLE INFO

*Article history:*
Received 6 March 2020
Received in revised form 20 May 2020
Accepted 28 May 2020
Available online 06 June 2020

*Keywords:*
Geochemistry
$^{40}Ar/^{39}Ar$ dating
Petrogenesis
Mesa Central
San Luis Potosí
Mexico

ABSTRACT

The southern part of the Mesa Central (MC) province, Mexico, is formed of several Cenozoic volcanic complexes. The Sierra de San Miguelito Complex (SSMC) is in the south-eastern part of the MC. The SSMC consists of: (1) mafic volcanic rocks of porphyritic texture and trachybasalt/basalt compositions; (2) intermediate volcanic rocks of porphyritic texture and basaltic-trachyandesite, basaltic andesite and andesite compositions; and (3) silicic volcanic rocks of porphyritic texture and rhyolite composition. New $^{40}Ar/^{39}Ar$ dating results, in combination with major- and trace-element data, and Sr-Nd-Pb isotope data, are used to investigate the petrogenesis and geodynamic evolution of SSMC. The $^{40}Ar/^{39}Ar$ radiometric age data constrains the magmatic events in the SSMC to between 34 and 21 Ma. Chondrite-normalized rare-earth element patterns are distinct for each volcanic succession; mafic and intermediate lavas have relatively flat light rare earth element (LREE) and large ion lithophile element (LILE) patterns, whereas the silicic volcanic rocks show enrichment in LREE and high field strength elements (HFSE). Within each volcanic phase, the total rare-earth element concentrations increase from mafic to silicic, and the size of the negative Eu anomalies progressively increase ($Eu/Eu^*$ from 0.02 to 1.04). The initial $^{87}Sr/^{86}Sr$ ratios are widely distributed (from 0.70344 to 0.71973) whereas the initial $^{143}Nd/^{144}Nd$ ratios are somewhat low and show a narrower range (0.51245 to 0.51287), indicating the mafic magmas derived from a slightly heterogeneous source. Geochemical modelling of the mafic volcanic rocks reveals two sources of magma: (1) a parental magmas generated from melting underlying lithospheric mantle; and (2) a second lithospheric melt contaminated by lower crust. Intermediate magmas evolved from assimilation and fractional crystallization (AFC) processes of both lithospheric melts, at shallower levels. The silicic volcanic rocks in the area, however, were probably derived from partial melting of sedimentary rocks within the upper–middle continental crust. New multidimensional tectonic discrimination diagrams, combined with the magmatic model, indicates that volcanic activities in the region were generated in an extensional environment.


## 1. Introduction

The Basin and Range (BR) province is one of the most prominent tectonic features across the western part of the North American plate (Fig. 1a). The BR extends from Canada through the western USA to north-western Mexico (Fig. 1a) and is a composite Cenozoic taphrogen with a present configuration and internal geometry derived from multiple phases of extension (Dickinson, 2002). Late Paleocene, Mid-Miocene and Pliocene *syn*-transform extension within the southern BR (western USA and north-western Mexico) have been related to rapid migration of the Rivera triple junction past Baja California to its current location between the tip of the Baja Peninsula and mainland Mexico (Fig. 1a; Dickinson, 2004; Cosca et al., 2014). Features of Middle to Late Cenozoic extension and magmatism generated through BR have been extensively studied (e.g. Berglund et al., 2012; Cosca et al., 2014; Dickinson, 2002, 2004; Jones et al., 1992). Nevertheless, its origin, dynamics and evolution are still a much-debated topic of discussion within the earth sciences (e.g., Atwater, 1970; Coney and Harms, 1984; Cosca et al., 2014; Glazner and Bartley, 1984; Henry and

* Corresponding authors.
*E-mail addresses:* dario.torres@ipicyt.edu.mx (D. Torres-Sánchez), sanjeet.verma@ipicyt.edu.mx (S.K. Verma), tlb2@leicester.ac.uk (T.L. Barry), spv@ier.unam.mx (S.P. Verma), jrtorres@uaslp.mx (J.R. Torres-Hernández).

https://doi.org/10.1016/j.lithos.2020.105613
0024-4937/

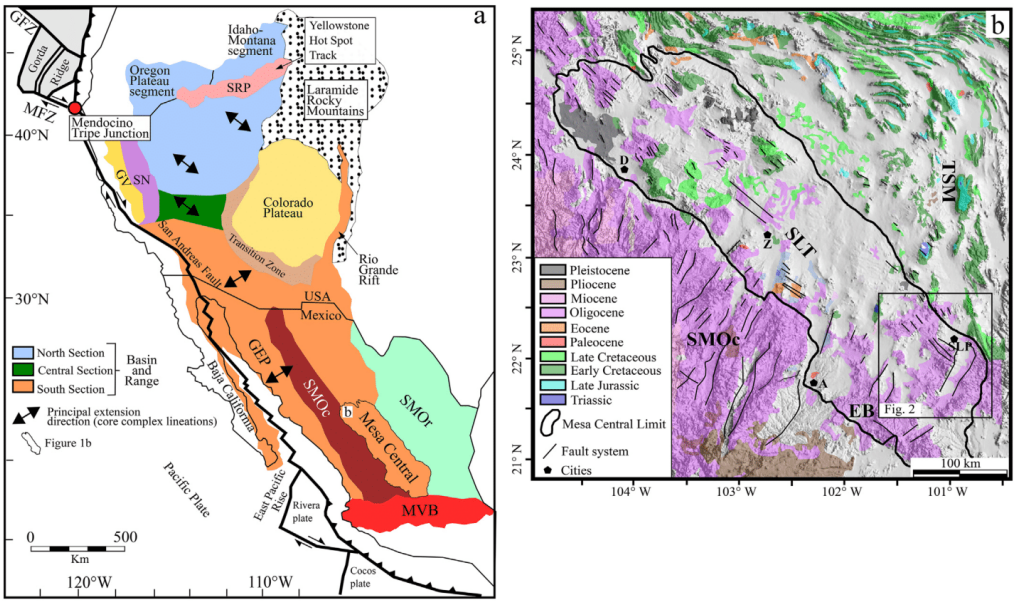


**Fig. 1.** (a) Present-day regional tectonic map of western North America and Basin and Range province with subdivisions of the northern, central and southern Basin and Range from Jones et al. (1992) and Sonder and Jones (1999) (modified from Cosca et al., 2014); (b) Simplified geological map of the Mesa Central province (modified from Nieto-Samaniego et al., 2007) showing Triassic metamorphic and sedimentary basement; Late Jurassic sediments and sandstones; Early Cretaceous limestone; Late Cretaceous sediments and sandstones; Paleocene plutonic rocks; Eocene silicic volcanism; Oligocene silicic and pyroclastic volcanism; Miocene mafic volcanism; Pliocene mafic volcanism; and Pleistocene mafic volcanism. Abbreviations are as follows: GEP-Gulf Extensional Province; MFZ-Mendocino Fracture Zone; MVB-Mexican Volcanic Belt; RFZ-Rivera Fracture Zone; GFZ-Gorda Fracture Zone; SRP-Snake River Plain; SN-Sierra Nevada; GV-Great Valley: STFS-San Luis Tepehuanes Fault Systems; TSM-Taxco-San Miguel de Allende Fault System; EB-El Bajío Fault System; SMOc-Sierra Madre Occidental province; SMOr-Sierra Madre Oriental; USA-United States of America; D-Durango city; Z-Zacatecas city; A-Aguascalientes city; SLP-San Luis Potosí city.

Aranda-Gómez, 2000; Parsons, 1995; Severinghaus and Atwater, 1990; Wernicke et al., 1988).

The Mesa Central (MC) province, Mexico, sits within the southern limits of the BR. The province is within an elevated plateau that extends across central-northern Mexico and is bound to the north and east by the Sierra Madre Oriental (SMOr) and to the south and west by the Sierra Madre Occidental (SMOc; Fig. 1b; Nieto-Samaniego et al., 2007). Within MC there are several fault systems (Fig. 1b): (i) the NW-SE trending El Bajío (EB) in the south; (ii) the Taxco-San Miguel de Allende (TSM) in the west; and (iii) the San Luis-Tepehuanes (SLT) extending within the Mesa Central. The MC is divided into two main regions by ~1600 km long lineament towards the NW direction: (a) the northern region, which is characterized by advanced stages of erosion, alluvial-lacustrine basin development, and only a low volume of magmatic activity during the Oligocene and Quaternary; whereas (b) the southern region, is mainly covered by Paleogene-Neogene volcanic rocks and cross-cut by several normal faults (Fig. 2a; Nieto-Samaniego et al., 1996,Nieto-Samaniego et al., 1999, Nieto-Samaniego et al., 2007). Several geological, geophysical and geochemical studies have been carried out within the southern region of the MC (i.e., Aguirre-Díaz and Labarthe-Hernández, 2003; Labarthe-Hernández et al., 1982; López-Loera and Tristán-González, 2013; Nieto-Samaniego et al., 2007; Orozco-Esquivel et al., 2002; Sieck et al., 2019), but the origin, evolution, timing, and cause of the volcanism is still poorly constrained.

One of the mostly poorly understood parts of the MC is the bimodal Sierra de San Miguelito Complex (SSMC; Fig. 2b) in the south (i.e., Labarthe-Hernández et al., 1982; Rodríguez-Ríos et al., 2007). Limited geological work has been done on the area of SSMC but the essential information, such as robust age constraints and detailed geochemical and radiogenic isotope data, is still missing. So far, the volcanic rocks have predominantly been dated by the K—Ar method that has several substantial drawbacks (Clay et al., 2015), including much larger uncertainties than Ar—Ar ages (Lee, 2015). Thus, the timing and origin of the highly evolved explosive rhyolitic volcanism in the SSMC, relative to the spatially associated basaltic volcanism remains enigmatic.

In this work, we present new $^{40}Ar/^{39}Ar$ ages along with whole-rock chemistry and Sr-Nd-Pb isotope data of the magmatic units across the area. We present the age, geochemical and isotopic constraints on the mafic, intermediate and silicic rocks in the area and discuss their petrogenesis in the context of the development of the southern parts of the Basin and Range.

## 2. Geological framework

The southern region of the MC is mainly characterized by widespread Cenozoic faults that commonly bound basins filled with fluvial and lacustrine deposits. These faults reflect a complex tectonic stress regime that was generated during the Mid- to Late Cenozoic and marks a continuous extension to the BR (Fig. 1b). The region is underpinned by a Mesozoic basement comprising marine calcareous rocks of the SMOr, and volcanic-flysch sequences of the Sierra de Guanajuato Complex (Centeno-García, 2017; Orozco-Esquivel et al., 2002).

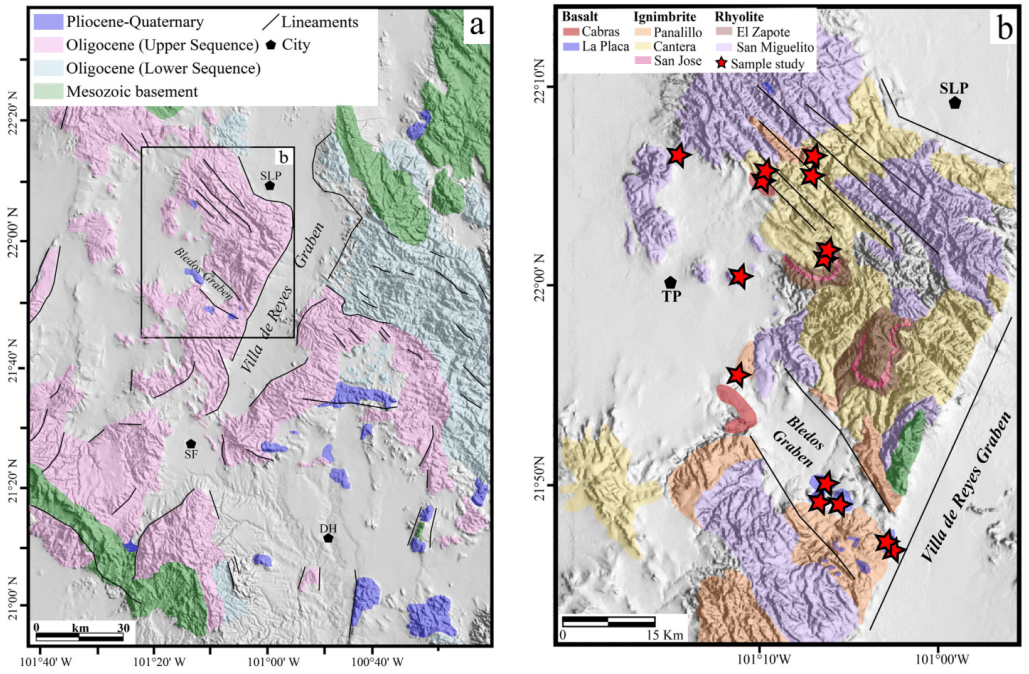


**Fig. 2.** (a) Simplified geological map showing the division of the stratigraphic units and the location of the main stratigraphy of the southern Mesa Central province (Modified after Orozco-Esqueviel, et al., 2002); (b) Geological map of the Sierra de San Miguelito complex (SSMC). Basalt from late Oligocene to Miocene; Ignimbrite and Rhyolite from early Oligocene to late Oligocene. Abbreviations are as follows: SLP-San Luis Potosí city, SF-San Felipe city, DH-Dolores Hidalgo city, TP-Tepetate city.

Prior to the Oligocene, there is little evidence of Cenozoic cover sequence within the MC. During the Paleocene, a few post-Laramide granite intrusions occurred within the southern part of the MC (Angeles-Moreno et al., 2017). By the Eocene, continental sandstones and conglomerates were deposited along with intermittent pyroclastic deposits and mafic-intermediate lavas (Aranda-Gómez and McDowell, 1998; Labarthe-Hernández et al., 1982). Regional extension occurred across the southern part of the MC, beginning in the Eocene, but continuing through the Miocene, forming NW-SE and NE-SW oriented grabens that suggest episodes of extension during this period (Nieto-Samaniego et al., 1996). These basins were later filled with alluvial and lacustrine deposits (Nieto-Samaniego et al., 1996).

During the Oligocene, a voluminous magmatic event took place within the southern region of the MC, forming a thick volcanic succession of mafic, intermediate and silicic volcanic rocks. This magmatic event has been divided into a lower and upper sequence (Fig. 2a; Orozco-Esquivel et al., 2002). The lower sequence comprises mainly of altered intermediate volcanic rocks and semi-altered pyroclastic deposits. The ages of the lower sequence have been reported as 32.8 ± 0.9 to 29.5 ± 1.5 Ma by K—Ar technique (Cerca-Martínez et al., 2000; Labarthe-Hernández et al., 1982). The upper sequence consists predominantly of silicic domes, the majority associated with lava and pyroclastic deposits. The domes are aligned along subsidiary faults or fractures parallel to the direction of the major fault systems through the area (Orozco-Esquivel et al., 2002). The ages of this sequence have previously been reported as 30.1 ± 0.8 to 27.0 ± 0.7 Ma by K—Ar technique (Nieto-Samaniego et al., 1996), despite it being situated on top the lower sequence. No clearly defined caldera structures have been identified for the upper sequence, but rare pyroclastic dikes, underlying the domes, have been observed with a similar orientation to the regional faults (Torres-Hernández et al., 2006). The uppermost part of the upper sequence is represented by a small number of isolated outcrops of mafic and intermediate volcanic rocks that erupted during the late Oligocene-Miocene (Orozco-Esquivel et al., 2002).

The SSMC is situated within the upper sequence and is mainly bounded by the Villa de Reyes Graben (Fig. 2a; Nieto-Samaniego et al., 1999, 2007). The volcanic activity of the SSMC was emplaced through fault systems that exhibit a "*domino style geometry*" with strike direction of 300°-340° dip to the SW and NW systematically with dip angles between 12° and 31° (Xu et al., 2004). The stratigraphy of the SSMC covers the Epoch of Oligocene to early Miocene (Fig. 3). Lithologically, the units can be categorized into three types: (a) mafic volcanic rocks (Cabras unit); (b) intermediate volcanic rocks (La Placa unit); (c) silicic volcanic rocks (San Miguelito, San José, El Zapote, Cantera and Panalillo units).

### 2.1. Mafic volcanic rocks

The mafic volcanic rocks consist of the Cabras unit (Fig. 3). This unit is found as isolated outcrops of lava, displaying a thickness of <25 m, and is mainly characterized by an aphanitic-porphyritic texture, scarce olivine phenocrysts, and rare vesicles in a vitreous matrix (Torres-Sánchez et al., 2019; Tristán-González et al., 2009). Tristán-González et al. (2009) and Aguillón-Robles et al. (2014) presented whole-rock K—Ar ages of 22 to 21 Ma for this unit.

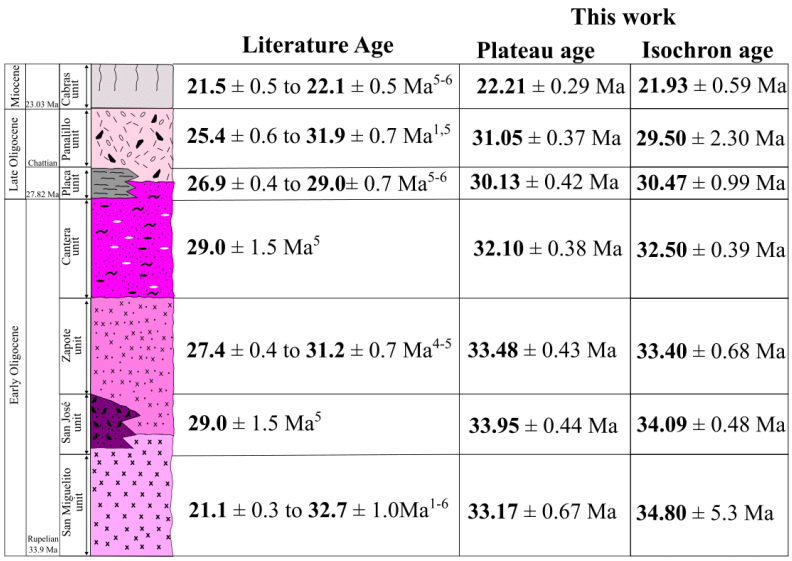


**Fig. 3.** Schematic stratigraphic column of the volcanic rocks from the SSMC. Ages from this study were taken from Table 4. Literature age are taken from the following: [1]Labarthe-Labarthe-Hernández et al. (1982); [2]Tuta et al. (1988); [3]Aguillón-Robles et al. (1994); [4]Aguillón-Robles et al. (2009); [5] Tristán-González et al. (2009); [6] Aguillón-Robles et al. (2014).

*2.2. Intermediate volcanic rocks*

The intermediate volcanic rocks comprise of the La Placa unit (Fig. 3); previous studies (Aguillón-Robles et al., 2014; Tristán-González et al., 2009) have reported whole-rock K—Ar ages of 29 to 26 Ma. This unit consists of massive lavas flows that are only exposed in isolated outcrops, displaying a thickness range from 10 to 15 m, and characterized by scarce olivine phenocrysts in a vitreous matrix.

*2.3. Silicic volcanic rocks*

The most voluminous rock type in the SSMC is the silicic volcanic rocks represented by the San Miguelito, San José, El Zapote, Cantera and Panalillo units (Fig. 3). The San Miguelito and El Zapote units consist of exogenous lava domes, which during the final stages of development erupted thick breccias on the top. The overall thickness of the San Miguelito and El Zapote units is variable (130–800 m) and is higher at the center of the domes. Previous studies (Aguillón-Robles et al., 1994, 2014; Tristán-González et al., 2009) reported whole-rock K—Ar dates of 33 to 21 Ma for the San Miguelito and El Zapote units. In some places, between the San Miguelito and El Zapote units, lies the San José unit, though elsewhere El Zapote sits directly on top the San Miguelito unit. The San José unit is 3–15 m thick and consists of ash and a pyroclastic deposit which is mildly welded (Tristán-González et al., 2009).

Above the El Zapote unit, is the Cantera unit - a highly welded pyroclastic deposit characterized by grayish white to pink pumice and ash, abundant fiamme and lithic fragments of rhyolite and sandstone compositions, in a devitrified glassy matrix. It's thickness varies between 2 and 30 m thick. The unit covers much of the SSMC and overlays the San Miguelito unit. Previously, the Cantera unit has been dated at about 29 Ma by K—Ar method (Caballero-Miranda et al., 2009; Tristán-González et al., 2009).

Finally, the youngest silicic rocks in the area are the Panalillo unit, previously dated at 29 to 26 Ma (Torres-Hernández et al., 2006; Tristán-González et al., 2009). It is mainly composed of a pumice-ash pyroclastic deposit which is lithic-rich and is slightly less welded than the Cantera below. It has an average thickness of 20–30 m (Torres-Sánchez et al., 2019; Tristán-González et al., 2009).

## 3. Materials and methods

*3.1. Sampling and petrography*

For this study, representative samples of the main lithological units from the SSMC were selected. The locations of weathering, deformation and veins were avoided during sampling and only fresh samples were collected for $^{40}Ar/^{39}Ar$ dating and geochemical analysis. Stratigraphic and lithological boundaries for volcanic rocks were drawn, largely on geomorphologic characteristics tested in the field and later refined by petrological, geochemical and geochronological analyses. Modal compositions were determined at the Institute of Scientific and Technological Research of San Luis Potosí (IPICYT, San Luis Potosí, Mexico) by point counting on thin sections using a Leica petrographic microscope and a PELCON Automatic point counter (Table S1).

*3.2. $^{40}Ar/^{39}Ar$ geochronology*

Radiometric $^{40}Ar/^{39}Ar$ dating was undertaken using feldspar crystals (silicic samples) and whole rock pieces (mafic samples). Samples selected for radiometric dating were crushed, sieved, and washed repeatedly with de-ionized water, and the 250–350 μm fragments were selected. These fragments were again cleaned ultrasonically in acetone and de-ionized water, dried using the hot plate, and packaged in aluminum foil packets of 10 × 10 mm size prior to irradiation.

Irradiation was carried out at the McMaster Nuclear Reactor (McMaster University, Canada) for 101 h. Cadmium shielding was used, and the samples were held in position 8D. Neutron flux was monitored using biotite mineral standard GA1550 (99.738 ± 0.104 Ma;

Renne et al., 2011). Standards were packed for irradiation either side of the unknown samples and analyzed using the single grain fusion method, in a 1059 nm CSI fiber laser and MAP215–50 mass spectrometer. J values were calculated by linear extrapolation between two measured J values, and a 0.5% error on J is used. The values for J for each sample are reported in Table S3 (see the supplementary material file).

Irradiated samples were loaded into an ultra-high vacuum system and a 1059 nm CSI fiber laser was focused into the sample chamber and used to step-heat the sample. After passing through a liquid-nitrogen trap, extracted gases were cleaned for 5 min using three SAES AP-10 getters, two running at 450 °C and one at room temperature. Following this, the gases were let into a MAP 215–50 mass spectrometer for measurement, with the mass discrimination value for $^{40}Ar/^{36}Ar$ measured at 283. System blanks were measured before and after every two sample analyses. Gas clean-up and inlet was fully automated, with measurement of $^{40}Ar$, $^{39}Ar$, $^{38}Ar$, $^{37}Ar$, and $^{36}Ar$, each for ten scans, and the final measurements are extrapolations back to the inlet time.

### 3.3. Whole rock geochemistry

Fifteen samples were jaw crushed and then powdered in an agate bowl obtaining a 400 μm mesh fine powder. Major elements were determined on fusion beads prepared from pre-ignited powders, which were fused with lithium metaborate flux (80% lithium metaborate and 20% lithium tetraborate) in a ratio of 1:5. Trace elements were determined on pressed powder pellets made with a mixture of 7 g of sample and 7% PVA (Polyvinyl Alcohol) solution. Analyses were carried out at the University of Leicester, United Kingdom, in a PANalytical Axios Advanced x-ray fluorescence (XRF) spectrometer. Internal standards BH-1, WS-1, BCS375, BCS 376, MRG-1 and NIM-D were analyzed to monitor precision and accuracy of the results. The analytical precision ($2\sigma$) and accuracy were considered between 2 and 5% for major and < 2% for trace elements. Rare earth element concentrations were determined at the University of Leicester by a Thermo Scientific ICAP-Qc quadrupole ICP mass spectrometer. Samples were prepared using a standard HF-$HNO_3$ digestion. Seven geochemical reference materials (BHVO-1, NIM-G, MRG-1, JSd-1, JSd-2, JSD-3, and JR-1) were used to calibrate and evaluate the analytical data quality.

### 3.4. Isotopic analyses

Twelve samples from the SSMC were analyzed for Sr, Nd, and Pb isotope compositions. Samples were prepared and analyzed following the procedures of Kempton et al. (1995) and Royse et al. (1998). The Sr, Nd, and Pb isotope compositions were analyzed as metal species on single Ta, double *Re*—Ta and single Re filaments, respectively, using a Finnigan MAT 262 multi-collector mass spectrometer at the NERC Isotope Geosciences Laboratory (NIGL), Keyworth, UK. Samples were leached for ~1 h in 6 M HCl at 50 °C prior to digestion by a standard HF-$HNO_3$ procedure. Blanks for Sr, Nd, and Pb were less than 125 pg, 275 pg, and 325 pg, respectively. $^{87}Sr/^{86}Sr$ was normalized during run time to $^{87}Sr/^{86}Sr = 0.1194$ and $^{143}Nd/^{144}Nd$ was normalized to a value of $^{143}Nd/^{144}Nd = 0.7219$. Sample data are reported relative to accepted values of 0.710177 for $^{87}Sr/^{86}Sr$ in the NBS987 standard and 0.512128 for $^{143}Nd/^{144}Nd$ in the La Jolla standard. Based on repeated runs of NBS981, the reproducibility of the Pb isotope ratios was ~0.1%. Pb isotopes were corrected relative to the average standard Pb isotopic compositions of Todt et al. (1996). Measured values were age corrected based on the new $^{40}Ar/^{39}Ar$.

## 4. Results

### 4.1. Petrography

According to field and microscopic observations, the mafic and intermediate volcanic rocks from the SSMC (Fig. 4a-b; Table S1) are characterized by porphyritic textures. The main mineral assemblages represent euhedral-subhedral phenocrysts of plagioclase (10–64%), subhedral clinopyroxene (4–20%), subhedral-anhedral orthopyroxene (1–6%) and a lesser amount of subhedral-anhedral olivine (3–8%). The phenocrysts range in size from 0.1 to 0.5 mm, in a vitreous matrix (Fig. 4a-b; Table S1). Additionally, the rocks display the following characteristics: (a) diverse disequilibrium textures that include normal and sieved plagioclases crystals in the same rock samples; (b) rounded and embayed crystals of quartz with reaction rims of microcrysts of pyroxene; and (c) plagioclase with complex mineral zoning, such as reverse and oscillatory zoning, or normally zoned crystals, in the same rock sample (Fig. 4a-b).

In contrast, the silicic volcanic rocks display porphyritic textures with mineral assemblages that consist of phenocrysts of anhedral quartz (15–46%), euhedral to subhedral sanidine (10–22%), euhedral to subhedral plagioclase (2–43%), subhedral orthopyroxene (1–18%) and subhedral clinopyroxene (3–35%) embedded in a vitreous matrix showing a phenocryst size ranging from 0.2–0.7 mm of diameter (Fig. 4c-g).

### 4.2. $^{40}Ar/^{39}Ar$ geochronology

A total of 12 samples were analyzed; four dates were obtained from whole rock fragments (mafic-intermediate volcanic rocks), and eight from sanidine crystals (silicic volcanic rocks). Table 4 presents the summary of the $^{40}Ar/^{39}Ar$ plateau and correlation dating results from the SSMC. Spectra and correlation diagrams are shown in Fig. 8a–n, whereas step-heating results are reported in Table S3. Errors on the age spectrum and correlation diagrams represent the analytical precision at $\pm 2\sigma$ level.

The sanidine phenocrysts of rhyolite sample SLP17–11 (San Miguelito volcanic unit) show a spectrum with argon-loss defined by steps 1–3. A slightly flat age spectrum is defined by steps 4–6 with a plateau age of 33.17 ± 0.67 Ma (Fig. 5a). Moreover, this sample yielded an isochron age of 34.80 ± 5.4 Ma (Fig. 5b) with MSWD = 13, due to the spread of the error of the isochron data of this sample; therefore the isochron age should not be considered reliable. We use the more robust plateau age instead.

Sanidine phenocrysts of the San José unit (sample SLP17–29) yielded a slightly disturbed spectrum with a plateau age of 33.95 ± 0.44 Ma (Fig. 5c) over fourteen steps with 98.1% of released $^{39}Ar$. Similarly, this sample yielded an isochron age of 34.09 ± 0.48 Ma (Fig. 5d) with a MSWD = 1.7. The isochron indicates that some presence of excess argon, which is also supported by the trend of the age spectrum.

$^{40}Ar$—$^{39}Ar$ analyses of sanidine phenocrysts from the rhyolitic sample SLP17–28 (El Zapote volcanic unit) produced a nearly ideal flat age spectrum, with some low ages at 11–14 steps. Steps 8–14 define a plateau age of 33.48 ± 0.43 Ma (Fig. 5e) with 90.2% of released $^{39}Ar$. This sample yielded an isochron age of 33.40 ± 0.68 Ma (Fig. 5f) with MSWD = 2.2. The isochron age is nearly correlated to the plateau age, lending confidence to the result.

Analyses of sanidine crystals from the Cantera unit (sample SLP17–24) shows a nearly flat spectrum with exception of some slightly higher ages on the first two and the last three steps, and a lower age in step 8. Step 3–7 yielded a flat spectrum age of 32.10 ± 0.38 Ma (Fig. 5g) with 86% of released $^{39}Ar$. The isochron for this samples yielded an age of 32.50 ± 0.39 Ma (Fig. 5h) with MSWD = 1.3. The isochron age and plateau age are nearly correlated, hence, both ages can be considered reliable.

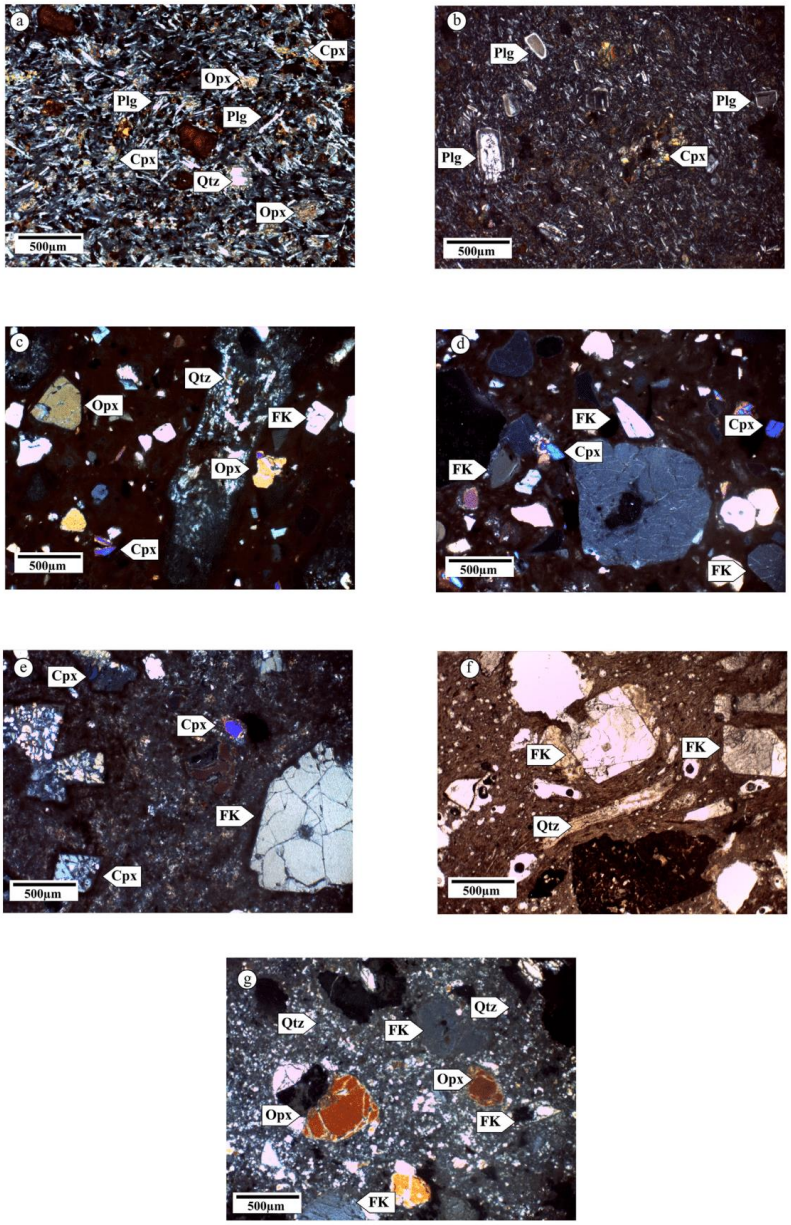


**Fig. 4.** Microphotographs of the SSMC volcanic rocks. (a) Phenocrysts of plagioclase, orthopyroxene, clinopyroxene and quartz with reaction rims from the Cabras unit; (b) Phenocrysts of plagioclase with sieved textures, microcrystals of clinopyroxene from the Placa unit; (c) Phenocrysts of potassium feldspar, orthopyroxene, clinopyroxene and microcrystals of quartz from the Panalillo unit; (d) Phenocrysts of potassium feldspar, orthopyroxene and clinopyroxene from the Cantera unit; (e) Phenocrysts of potassium feldspar and clinopyroxene from El Zapote unit; (f) Phenocrysts of potassium feldspar and bands filled with quartz from the San José unit; (g) Phenocrysts of potassium feldspar, orthopyroxene with microcrystals of quartz from the San Miguelito unit. Abbreviations of mineral names are as follows: FK-potassium feldspar; Plg-plagioclases; Opx-Orthopyroxene; Cpx-clinopyroxene.

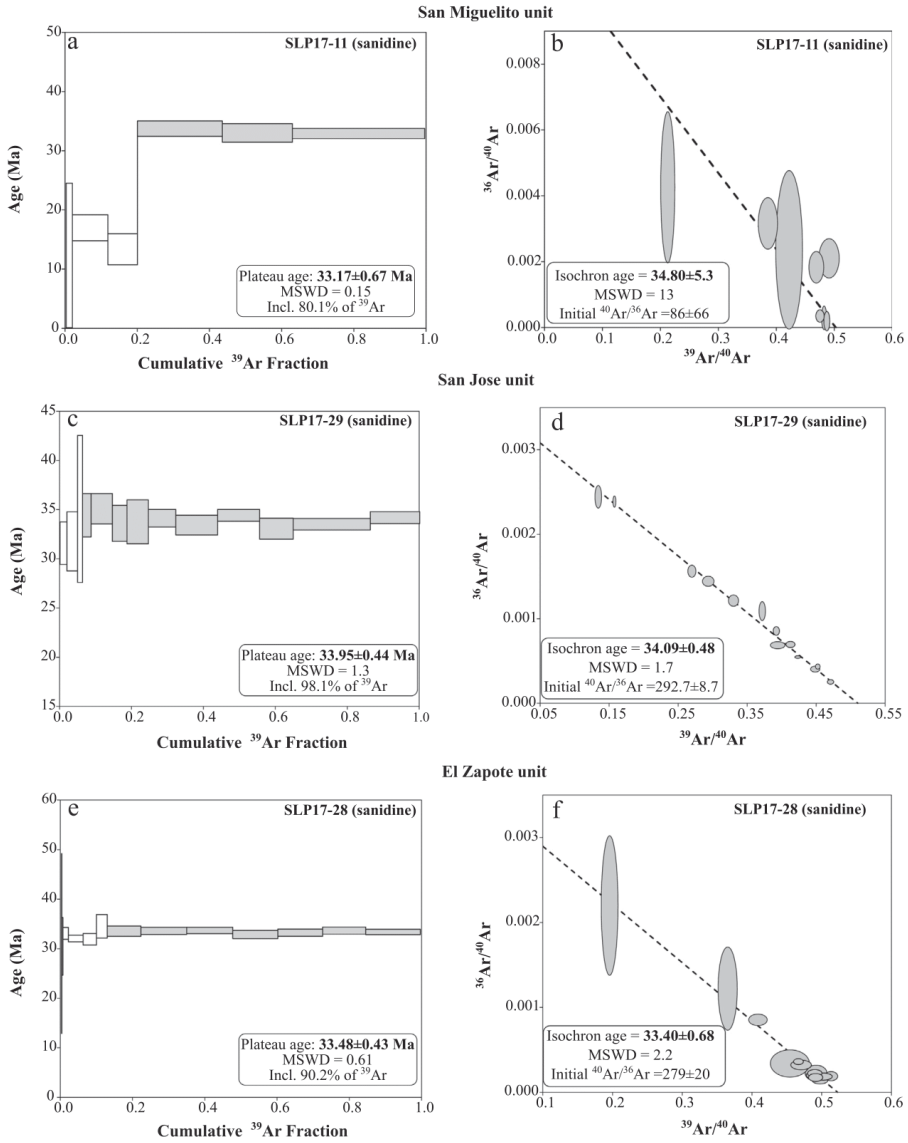


**Fig. 5.** $^{40}Ar/^{39}Ar$ age spectrum and respective isotope isochron diagram for the volcanic rocks. See text for discussion.

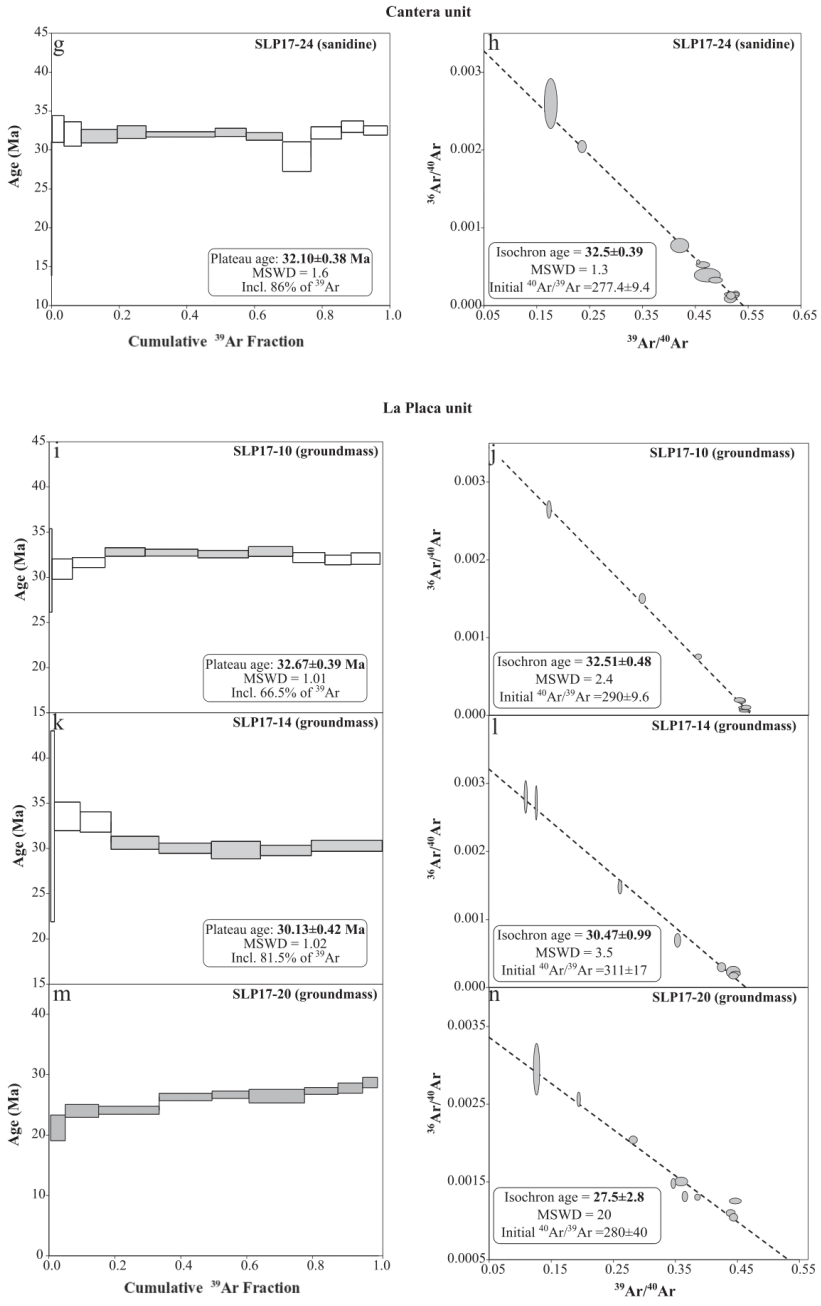


**Fig. 5** (*continued*).

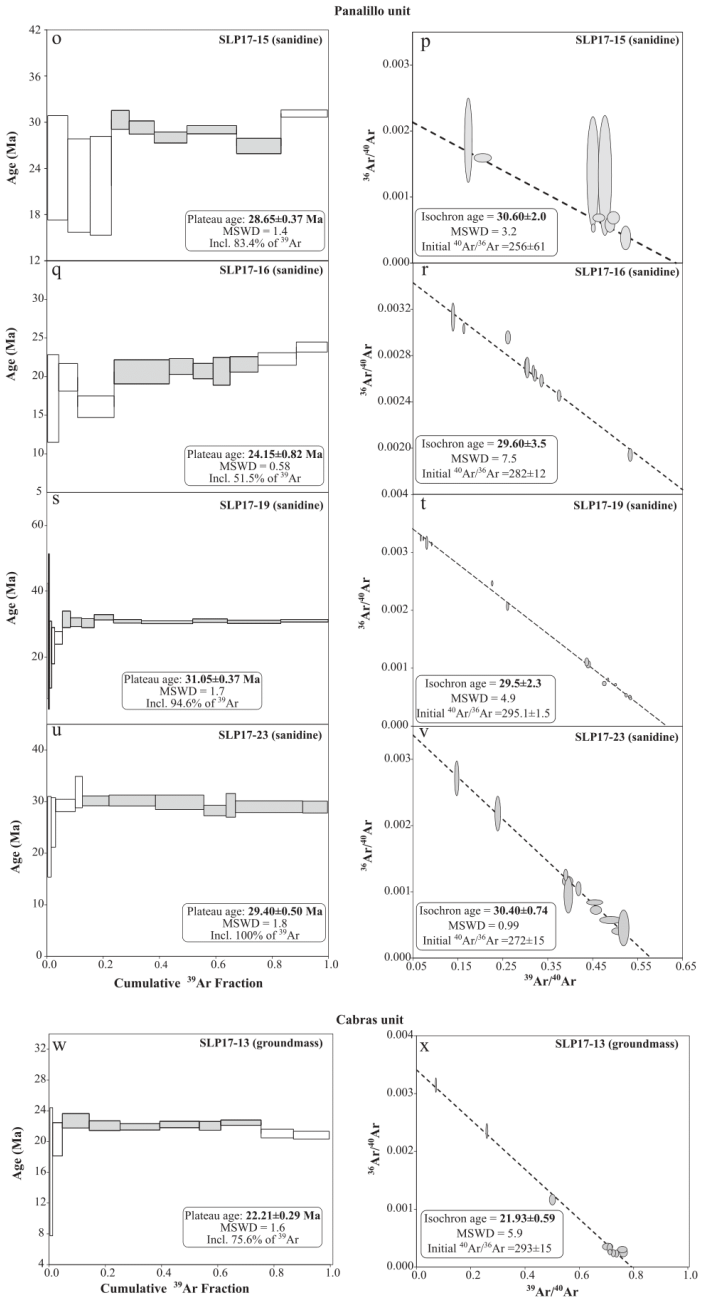


**Fig. 5** (*continued*).

Groundmass from andesite and basalt samples of La Placa unit (SLP17–10; SLP17–14; SLP17–20) yielded nearly flat spectrum with some lower ages in the initial steps. For this unit, the spectrum ages yielded a range between 32.67 ± 0.39 and 30.13 ± 0.42 Ma (Fig. 5i, k, m), with ~66–81% of released $^{39}$Ar. The isochrons for this unit show a range ages between 27.00 and 32.67 ± 0.42 Ma (Fig. 5j, l, n) with ~3.5–20 MSWD. The isochrons indicate some excess argon, which may be related to the age spectrum form. However, the concordance between the plateau and the isochron ages gives a confidence to the age of this unit.

$^{40}$Ar—$^{39}$Ar analyses from sanidine of the samples SLP17–15 and SLP17–16 (Panalillo unit) shows a disturbed spectrum with a trend of argon loss profile with a plateau age of 28.65 ± 0.37 Ma and 24.15 ± 0.82 Ma (Fig. 5o, q, s, u) respectively and a $^{39}$Ar release of 83.4 and 51.5%, with an isochron age of 30.60 ± 2.0 Ma and 29.60 ± 3.5 Ma (Fig. 5p, r, t, v). However, for the same unit, the samples SLP17–19 and SLP17–23 yielded a plateau age of 31.05 ± 0.37 Ma and 29.40 ± 0.50 Ma, with 94.6 and 100% of $^{39}$Ar released respectively; these samples show an ideal flat age spectrum. The isochron of the samples SLP17–19 and SLP17–23 presents an age of 29.50 ± 2.30 Ma with MSWD = 4.9 and 30.40 ± 0.74 Ma with MSWD = 0.99, respectively.

The groundmass of SLP17–13 sample (Cabras unit; Fig. 5w) yielded a plateau age of 22.21 ± 0.29 Ma with 75.6% of $^{39}$Ar released. The spectrum for this sample is slightly saddle-shaped. The isochron shows an isochron age of 21.93 ± 0.59 Ma (Fig. 5x) with MSWD = 5.9.

### 4.3. Whole-rock geochemical compositions

New major and trace element geochemical data for 15 samples from the SSMC are reported in Table 1. Besides 15 samples, additional literature geochemical data for 68 samples (Table S2 in the Supplementary Excel file) from the SSMC were compiled from the following references: Orozco-Esquivel et al. (2002, n = 4 samples); Leroy et al. (2002, n = 4 samples); Rodríguez-Ríos and Torres Aguilera (2009, *n* = 15 samples); Torres-Hernández et al. (2014, n = 8 samples); Aguillón-Robles et al. (2014, n = 14 samples); and Torres-Sánchez et al. (2019, *n* = 23 samples).

All data were processed in the IgRoCS software (Verma and Rivera-Gómez, 2013) to automatically determine the magma and rock types under the Middlemost (1989) option for Fe-oxidation adjustment, which allowed us to strictly follow the IUGS recommendations for rock classification and nomenclature (Le Bas et al., 1986). Thus, all major element data were treated in exactly the same manner. The use of 100% adjusted data on an anhydrous basis and after Fe-oxidation adjustment helps minimize the effect of analytical errors and element mobility and makes the use of the TAS diagram more consistent with the IUGS scheme.

The new data from the SSMC combined with the literature data (Orozco-Esquivel et al., 2002; Leroy et al., 2002; Rodríguez-Ríos and Torres Aguilera, 2009; Torres-Hernández et al., 201; Aguillón-Robles et al., 2014; and Torres-Sánchez et al., 2019), are presented in the conventional TAS diagram (Fig. 6a; Le Bas et al., 1986). The samples plot in a wide compositional range including basalt, trachybasalt, basaltic andesite, andesite and rhyolite (Fig. 6a). These samples show a range of calc-alkaline to shoshonitic affinity (Fig. 6b), although caution is required in the use of a diagram without having Ca in it (Sheth et al., 2002).

From the new data (Table 1), we summarize the following characteristics. The mafic rock samples record values of $(SiO_2)_{adj}$ = 48.33–51.48% m/m, $(MgO)_{adj}$ = 5.71–6.26% m/m, $(TiO_2)_{adj}$ = 1.97–2.86% m/m, and Mg-number (Mg#) = 48.99–55.24. The Cr and Ni contents are in the ranges of 92.02–234.35 μg/g and 3.50–83.25 μg/g, respectively. The intermediate rocks display more variable contents of $(SiO_2)_{adj}$ = 57.46–62.24% m/m, $(MgO)_{adj}$ = 2.81–5.71% m/m, $(TiO_2)_{adj}$ = 0.88–1.50% m/m. Their Mg# ranges from 53.04 to 64.13, Cr from 20.72 to 239.0 μg/g, Ni from 3.5 to 42.7 μg/g. The silicic rocks have high $(SiO_2)_{adj}$ = 76.56–82.24% m/m, $(MgO)_{adj}$ = 0.03–0.18% m/m, $(TiO_2)_{adj}$ = 0.59–0.24% m/m, and Mg# = 8.42–27.61, with Cr and Ni contents are in the ranges of 11.36–34.82 and 0.9–3.6 μg/g, respectively.

The chondrite-normalized rare earth element (REE; McDonough and Sun, 1995) plots of the new data (Table 1) are shown in Fig. 7a–c. The mafic volcanic rocks display a relatively flat pattern with a slight enrichment in light REE (LREE; $(La/Sm)_{CN}$ = 1.91–2.05; $(La/Yb)_{CN}$ = 3.76–6.44; Fig. 7a), with a small negative or positive Eu anomaly ($Eu/Eu^*$ = 1.03–1.09). Total REE concentrations of the mafic volcanic rocks vary from about 101.66 to 152.84 μg/g. The intermediate volcanic rocks show total REE content ranging from about 125.5 to 181.3 μg/g (one sample having very low REEs; Fig. 7b). The intermediate rocks also display enrichment in LREE (Fig. 6b; $(La/Sm)_{CN}$ = 2.02–2.43; $(La/Yb)_{CN}$ = 5.13–6.41), but also show a relatively small negative Eu anomaly ($Eu/Eu^*$ = 0.12–0.82). The silicic volcanic rocks display total REE content of 37.45–439.75 μg/g, enriched LREE patterns (Fig. 7c; $(La/Sm)_{CN}$ = 1.21–5.82; $(La/Yb)_{CN}$ = 1.16–13.10) but also show large negative Eu anomalies ($Eu/Eu^*$ = 0.03–0.36).

Primitive mantle-normalized multi-element (McDonough and Sun, 1995) diagrams of mafic volcanic rocks from SSMC display almost flat patterns (Fig. 7d). In general, the mafic volcanic rocks are enriched in highly incompatible LILE (i.e., Rb, U, LREE) relative to the moderately incompatible HFSE (e.g., Nb, Ta, Th and HREE). Normalized trace element patterns are enriched in incompatible elements with low Nb anomalies ($Nb/Nb^*$ = 0.64). The intermediate rocks display enrichment in LILE, relative to the incompatible HFS (Fig. 7e) and enrichment in incompatible elements with low Nb ($Nb/Nb^*$ = 0.22–0.33), Ti ($Ti/Ti^*$ = 0.39–0.51), Ba and P anomalies. The silicic volcanic rocks from the SSMC are enriched in incompatible LILE compared to incompatible HFS elements (Fig. 7f). Normalized patterns of silicic rocks display an enrichment in incompatible elements with low Nb anomalies ($Nb/Nb^*$ = 0.21–35.38) and strong Ti ($Ti/Ti^*$ = 0.01–0.13), Ba, Sr, and P anomalies.

The Nb and Ti anomalies are important to understanding the crustal contamination because mafic rocks from extensional or rift tectonic settings have lesser anomalies than intermediate and silicic rocks (Verma, 2020a), which shows that mafic magmas are likely to have lesser crustal assimilation effects as compared to intermediate and silicic rocks. Intermediate and silicic rocks from the SSMC are likely to have more residence time in the crust as compared to mafic rocks. The lesser crustal residence time is especially true for relatively primary mafic magmas having high MgO, Mg#, Ni, and Cr.

### 4.4. Whole-rock Sr-Nd-Pb isotope data

Whole-rock Sr, Nd, Pb isotopic data for the SSMC volcanic rocks are listed in Table 2. Due to the scarcity of isotope information in the study area, literature data from the southern region of the BR were compiled and plotted in all isotope diagrams (Fig. 8a–d). Isotopic data from the BR were taken from: Duncker et al. (1991, n = 14); Johnson and Thompson (1991, n = 17); Kempton et al. (1991, *n* = 35); Gibson et al. (1992, n = 20); Bradshaw et al. (1993, n = 14); Davis and Hawkesworth (1995, n = 19); Rogers et al. (1995, n = 26); McMillan et al. (2000, n = 26) and Christiansen et al. (2007, n = 8).

Strontium-Nd and initial $\varepsilon_{Nd}(t)$ values for SSMC volcanic rocks are plotted in Fig. 8a, together with isotope data from the BR volcanic rocks. The mafic volcanic rocks of the SSMC display initial $^{87}Sr/^{86}Sr$ isotopic ratios ($I_{Sr}$) of 0.70344 and 0.70496 and positive $\varepsilon_{Nd}(t)$ values of +5.2 and + 0.9 (Table 2). The intermediate volcanic rocks from the SSMC show $I_{Sr}$ that range from 0.70540 to 0.70581 and negative $\varepsilon_{Nd}(t)$ values of −1.8 to −2.5 (Table 2). For silicic volcanic rocks the $I_{Sr}$ ratios range from 0.70719 to 0.71973 and negative $\varepsilon_{Nd}(t)$ values ranging from −0.2 to −2.7 (Table 2). The mafic volcanic rocks plot within the mantle array and overlap the mafic BR volcanic rocks. Intermediate-silicic volcanic rocks plot below the bulk earth line, which suggests

**Table 1**
Representative whole rock compositions of volcanic rocks from the Sierra de San Miguelito Volcanic Complex, San Luis Potosi, Mexico (major elements in weight percent (also known as % m/m) and trace and rare earth elements in μg/g).

| Sample | SLP17–11 | SLP17–12 | SLP17–29 | SLP17–28 | SLP17–24 | SLP17–10 | SLP17–14 | SLP17–20 | SMB17–01 | SMB17–02 |
|---|---|---|---|---|---|---|---|---|---|---|
| Rock unit | San Miguelito | | San José | El Zapote | Cantera | La Placa | | | | |
| Rock (TAS) | Rhyolite | Rhyolite | Rhyolite | Rhyolite | Rhyolite | Andesite | Basalt | Andesite | Andesite | Andesite |
| Long. (°W) | 101°14′06" | 101°10′51" | 101°05′44' | 101°05′45" | 101°06′34" | 101°09′23" | 101°02′11" | 101°05′43" | 101°09′24" | 101°09′2" |
| Lat. (°N) | 22°06′23" | 22°00′03" | 22°01′23" | 22°05′14" | 22°05′26" | 22°05′09" | 21°46′46" | 21°49′48" | 22°05′10" | 22°05′07" |
| $SiO_2$ | 77.63 | 76.53 | 79.15 | 77.07 | 78.01 | 62.88 | 51.23 | 56.89 | 61.86 | 61.27 |
| $TiO_2$ | 0.13 | 0.06 | 0.11 | 0.11 | 0.10 | 0.89 | 1.96 | 1.49 | 0.91 | 0.92 |
| $Al_2O_3$ | 12.57 | 13.75 | 11.54 | 12.69 | 12.20 | 16.73 | 16.34 | 15.79 | 15.57 | 16.12 |
| $Fe_2O_3^t$ | 1.39 | 1.34 | 1.25 | 1.24 | 1.28 | 6.55 | 11.80 | 8.23 | 6.78 | 7.02 |
| MnO | 0.02 | 0.02 | 0.01 | 0.01 | 0.01 | 0.11 | 0.17 | 0.14 | 0.11 | 0.12 |
| MgO | 0.18 | 0.07 | 0.04 | 0.07 | 0.17 | 2.84 | 6.23 | 5.65 | 3.25 | 3.07 |
| CaO | 0.45 | 0.29 | 0.37 | 0.37 | 0.38 | 5.46 | 8.84 | 6.94 | 5.56 | 6.18 |
| $Na_2O$ | 2.26 | 3.41 | 2.08 | 2.44 | 1.59 | 2.70 | 2.73 | 2.41 | 2.66 | 2.54 |
| $K_2O$ | 5.43 | 4.57 | 5.12 | 5.44 | 5.38 | 3.15 | 0.94 | 1.71 | 3.11 | 2.89 |
| $P_2O_5$ | 0.02 | 0.01 | 0.02 | 0.01 | 0.01 | 0.22 | 0.28 | 0.39 | 0.23 | 0.23 |
| LOI | 0.63 | 0.76 | 0.96 | 0.89 | 1.23 | 0.53 | 0.31 | 1.19 | 0.60 | 0.76 |
| Sum | 100.70 | 100.81 | 100.65 | 100.35 | 100.37 | 102.07 | 100.84 | 100.83 | 100.65 | 101.12 |
| Q | 42.06 | 38.01 | 46.42 | 41.02 | 47.14 | 17.35 | 1.50 | 12.30 | 16.80 | 16.60 |
| Or | 32.09 | 27.02 | 30.38 | 32.35 | 32.10 | 18.43 | 5.58 | 10.21 | 18.47 | 17.11 |
| Ab | 19.13 | 28.87 | 17.67 | 20.78 | 13.58 | 22.61 | 23.21 | 20.60 | 22.62 | 21.53 |
| An | 2.10 | 1.37 | 1.71 | 1.78 | 1.84 | 23.98 | 29.70 | 27.49 | 21.46 | 24.09 |
| Ne | 2.20 | 2.69 | 1.96 | 2.15 | 3.12 | | | | | |
| C | 1.50 | 1.30 | 1.04 | 1.11 | 1.42 | 12.04 | 22.71 | 18.95 | 12.14 | 11.74 |
| Di-Mg | 0.63 | 0.60 | 0.56 | 0.56 | 0.58 | 2.25 | 2.62 | 2.89 | 2.37 | 2.44 |
| Di-Fe | 0.25 | 0.11 | 0.21 | 0.21 | 0.19 | 1.67 | 3.74 | 2.86 | 1.74 | 1.75 |
| Hy-Mg | 0.05 | 0.02 | 0.05 | 0.02 | 0.02 | 0.50 | 0.65 | 0.91 | 0.54 | 0.53 |
| Hy-Fe | 27.11 | 13.05 | 8.42 | 13.95 | 27.61 | 53.04 | 55.24 | 64.14 | 55.53 | 53.25 |
| Mt | 6.95 | 17.22 | 28.12 | 15.94 | 6.78 | 2.08 | 1.70 | 1.31 | 1.88 | 2.06 |
| Il | 42.06 | 38.01 | 46.42 | 41.02 | 47.14 | 17.35 | 1.50 | 12.30 | 16.80 | 16.60 |
| Ap | 32.09 | 27.02 | 30.38 | 32.35 | 32.10 | 18.43 | 5.58 | 10.21 | 18.47 | 17.11 |
| Mg# | 19.13 | 28.87 | 17.67 | 20.78 | 13.58 | 22.61 | 23.21 | 20.60 | 22.62 | 21.53 |
| $FeO^t$/MgO | 2.10 | 1.37 | 1.71 | 1.78 | 1.84 | 23.98 | 29.70 | 27.49 | 21.46 | 24.09 |
| Ba | 197.987 | 3.993 | 84.426 | 56.488 | 93.939 | 553.860 | 243.011 | 815.147 | 541.437 | 561.683 |
| Co | 1.174 | 0.681 | 0.745 | 0.879 | 0.684 | 16.790 | 33.135 | 27.095 | 2.581 | 17.910 |
| Cr | 11.381 | 11.365 | 34.817 | 12.732 | 14.384 | 103.450 | 92.022 | 238.981 | 20.717 | 108.275 |
| Cs | 9.426 | 3.656 | 4.574 | 11.994 | 7.751 | 3.245 | 0.950 | 0.945 | 0.583 | 2.853 |
| Cu | 2.102 | 4.915 | 2.438 | 3.041 | 2.502 | 8.883 | 13.950 | 10.996 | 7.900 | 8.300 |
| Ga | 22.550 | 48.024 | 21.436 | 23.497 | 22.506 | 19.931 | 25.484 | 19.267 | 19.600 | 20.900 |
| Hf | 6.364 | 11.285 | 6.022 | 6.772 | 6.043 | 6.308 | 4.290 | 6.412 | 5.817 | 5.578 |
| Nb | 22.111 | 124.387 | 21.488 | 23.509 | 23.281 | 13.252 | 13.638 | 12.944 | 12.872 | 12.091 |
| Ni | 1.355 | 1.576 | 2.337 | 1.025 | 2.036 | 6.921 | 3.483 | 42.683 | 6.800 | 3.500 |
| Pb | 26.661 | 51.671 | 28.743 | 29.351 | 27.019 | 10.886 | 4.164 | 8.495 | 10.723 | 9.958 |
| Rb | 213.350 | 290.797 | 144.259 | 250.091 | 181.507 | 66.264 | 15.721 | 60.949 | 50.935 | 42.022 |
| Sc | 15.384 | 8.264 | 1.316 | 7.121 | 2.242 | 24.478 | 34.975 | 24.756 | 21.682 | 23.251 |
| Sr | 27.560 | 2.458 | 14.007 | 16.071 | 23.189 | 276.837 | 311.042 | 390.274 | 252.612 | 294.668 |
| Th | 28.959 | 44.084 | 27.782 | 30.295 | 25.802 | 9.562 | 2.751 | 7.037 | 9.073 | 8.010 |
| U | 4.414 | 6.664 | 5.752 | 4.297 | 5.005 | 2.766 | 0.599 | 1.242 | 2.721 | 2.653 |
| V | 7.029 | 2.210 | 16.231 | 1.605 | 2.670 | 91.165 | 140.290 | 116.680 | 105.382 | 99.617 |
| Y | 45.551 | 22.808 | 43.756 | 13.331 | 33.373 | 25.781 | 28.204 | 37.810 | 22.901 | 27.477 |
| Zn | 52.222 | 163.443 | 52.300 | 59.009 | 63.020 | 82.635 | 82.039 | 91.125 | 79.200 | 81.000 |
| Zr | 170.859 | 166.115 | 158.115 | 165.630 | 152.773 | 237.990 | 182.985 | 266.598 | 235.385 | 217.393 |
| La | 40.62 | 6.26 | 50.45 | 19.69 | 22.90 | 24.98 | 16.50 | 33.71 | 21.63 | 22.46 |
| Ce | 96.46 | 11.68 | 80.28 | 58.29 | 58.65 | 56.28 | 36.23 | 68.91 | 46.83 | 46.21 |
| Pr | 11.61 | 1.34 | 15.58 | 3.43 | 7.02 | 7.42 | 4.85 | 9.06 | 6.69 | 6.66 |
| Nd | 48.15 | 5.11 | 67.79 | 11.13 | 30.04 | 32.71 | 23.30 | 41.11 | 5.04 | 30.33 |
| Sm | 10.73 | 1.76 | 14.24 | 2.13 | 6.80 | 7.21 | 5.48 | 8.64 | 1.05 | 6.43 |
| Eu | 0.51 | 0.09 | 0.29 | 0.27 | 0.27 | 1.62 | 1.99 | 2.33 | 0.26 | 1.58 |
| Gd | 10.35 | 2.38 | 12.77 | 2.58 | 7.41 | 7.06 | 5.87 | 8.72 | 6.41 | 6.69 |
| Tb | 1.68 | 0.58 | 2.07 | 0.46 | 1.45 | 1.04 | 0.97 | 1.29 | 0.99 | 1.01 |
| Dy | 9.91 | 4.24 | 12.32 | 3.23 | 9.39 | 6.07 | 5.72 | 7.39 | 5.51 | 6.01 |
| Ho | 1.91 | 0.93 | 2.38 | 0.68 | 1.91 | 1.16 | 1.15 | 1.46 | 1.08 | 1.19 |
| Er | 5.59 | 3.01 | 6.81 | 2.25 | 5.52 | 3.30 | 3.30 | 4.25 | 3.14 | 3.50 |
| Tm | 0.69 | 0.44 | 0.75 | 0.29 | 0.62 | 0.34 | 0.39 | 0.51 | 0.28 | 0.33 |
| Yb | 5.01 | 3.68 | 5.89 | 2.75 | 5.14 | 3.00 | 2.99 | 3.57 | 2.86 | 3.07 |
| Lu | 0.75 | 0.55 | 0.88 | 0.41 | 0.78 | 0.45 | 0.46 | 0.58 | 0.45 | 0.47 |
| TREE | 229.90 | 37.45 | 254.17 | 103.42 | 146.27 | 144.05 | 101.66 | 181.26 | 125.46 | 127.95 |
| $(La/Yb)_{CN}$ | 5.51 | 1.16 | 5.82 | 4.87 | 3.03 | 5.66 | 3.75 | 6.41 | 5.13 | 4.97 |
| $(La/Sm)_{CN}$ | 2.47 | 2.18 | 2.26 | 5.82 | 2.04 | 2.21 | 1.91 | 2.43 | 2.02 | 2.14 |
| $(Gd/Yb)_{CN}$ | 1.67 | 0.52 | 1.75 | 0.76 | 1.17 | 1.90 | 1.59 | 1.97 | 1.81 | 1.76 |
| $(La/Yb)_{PM}$ | 5.52 | 1.16 | 5.83 | 4.88 | 3.03 | 5.67 | 3.76 | 6.42 | 5.14 | 4.98 |
| $(La/Sm)_{PM}$ | 2.48 | 2.19 | 2.27 | 5.84 | 2.04 | 2.22 | 1.92 | 2.43 | 2.02 | 2.15 |
| $(Gd/Yb)_{PM}$ | 1.68 | 0.53 | 1.76 | 0.76 | 1.17 | 1.91 | 1.59 | 1.98 | 1.82 | 1.76 |
| $(Eu/Eu^*)$ | 0.15 | 0.13 | 0.07 | 0.36 | 0.11 | 0.70 | 1.09 | 0.82 | 0.12 | 0.73 |
| $(Nb/Nb^*)$ | 0.70 | 35.38 | 0.69 | 1.76 | 1.37 | 0.32 | 0.64 | 0.22 | 0.33 | 0.29 |
| $(Ti/Ti^*)$ | 0.04 | 0.06 | 0.03 | 0.13 | 0.04 | 0.39 | 1.02 | 0.51 | 0.43 | 0.42 |

| Sample | SLP17–15 | SLP17–16 | SLP17–19 | SLP17–23 | SLP17–13 |
|---|---|---|---|---|---|
| Rock unit | Panalillo | | | | Cabras |
| Rock (TAS) | Rhyolite | Rhyolite | Rhyolite | Rhyolite | Basalt |
| Long. (°W) | 101°02′13" | 101°05′11" | 101°06′08" | 101°06′35" | 101°10′50" |
| Lat. (°N) | 21°46′47" | 21°48′46" | 21°49′02" | 22°06′06" | 21°55′17" |
| $SiO_2$ | 75.93 | 82.28 | 76.62 | 78.25 | 47.76 |
| $TiO_2$ | 0.20 | 0.06 | 0.24 | 0.15 | 2.83 |
| $Al_2O_3$ | 12.24 | 9.74 | 11.99 | 11.23 | 15.59 |
| $Fe_2O_3^t$ | 2.43 | 0.92 | 2.34 | 1.66 | 13.73 |
| MnO | 0.03 | 0.02 | 0.02 | 0.01 | 0.20 |
| MgO | 0.12 | 0.08 | 0.03 | 0.02 | 5.64 |
| CaO | 1.13 | 0.51 | 0.44 | 0.30 | 8.87 |
| $Na_2O$ | 2.53 | 2.55 | 2.51 | 2.61 | 3.39 |
| $K_2O$ | 5.02 | 3.94 | 5.12 | 5.49 | 1.27 |
| $P_2O_5$ | 0.05 | 0.01 | 0.04 | 0.02 | 0.71 |
| LOI | 0.64 | 0.47 | 0.92 | 0.70 | 0.39 |
| Sum | 100.32 | 100.57 | 100.27 | 100.43 | 100.38 |
| Q | 38.88 | 50.82 | 41.11 | 41.03 | 0.00 |
| Or | 29.81 | 23.27 | 30.50 | 32.57 | 7.59 |
| Ab | 21.51 | 21.57 | 21.41 | 22.17 | 29.03 |
| An | 5.31 | 2.46 | 1.94 | 1.36 | 23.85 |
| Ne | 0.71 | 0.38 | 1.63 | 0.50 | – |
| C | 2.18 | 0.95 | 1.80 | 1.29 | 2.58 |
| Di-Mg | 1.10 | 0.41 | 1.06 | 0.75 | 3.07 |
| Di-Fe | 0.38 | 0.11 | 0.46 | 0.29 | 5.44 |
| Hy-Mg | 0.12 | 0.02 | 0.09 | 0.05 | 1.66 |
| Hy-Fe | 12.42 | 19.98 | 3.55 | 3.34 | 48.99 |
| Mt | 18.22 | 10.35 | 70.19 | 74.68 | 2.19 |
| Il | 38.88 | 50.82 | 41.11 | 41.03 | 0.00 |
| Ap | 29.81 | 23.27 | 30.50 | 32.57 | 7.59 |
| Mg# | 21.51 | 21.57 | 21.41 | 22.17 | 29.03 |
| $FeO^t/MgO$ | 5.31 | 2.46 | 1.94 | 1.36 | 23.85 |
| Ba | 518.985 | 23.390 | 499.326 | 37.639 | 304.315 |
| Co | 2.026 | 0.853 | 1.115 | 0.593 | 43.183 |
| Cr | 18.347 | 14.968 | 11.565 | 12.659 | 234.352 |
| Cs | 8.323 | 9.347 | 1.596 | 1.843 | 0.333 |
| Cu | 3.919 | 1.670 | 4.026 | 2.862 | 36.438 |
| Ga | 18.087 | 19.209 | 24.249 | 23.983 | 26.990 |
| Hf | 6.578 | 4.276 | 11.171 | 9.380 | 6.068 |
| Nb | 15.766 | 19.431 | 34.377 | 40.481 | 25.028 |
| Ni | 1.861 | 3.599 | 0.904 | 1.674 | 83.257 |
| Pb | 22.503 | 16.621 | 21.886 | 26.949 | 3.066 |
| Rb | 157.642 | 237.321 | 85.363 | 121.351 | 10.359 |
| Sc | 13.620 | 4.740 | 0.896 | 1.349 | 26.952 |
| Sr | 64.817 | 12.268 | 29.233 | 5.279 | 425.171 |
| Th | 23.395 | 36.907 | 17.217 | 25.063 | 2.130 |
| U | 5.197 | 8.373 | 4.350 | 5.222 | 0.740 |
| V | 8.874 | 32.621 | 9.936 | 37.868 | 183.768 |
| Y | 49.555 | 75.276 | 35.823 | 39.647 | 32.536 |
| Zn | 53.115 | 27.636 | 93.980 | 85.772 | 98.530 |
| Zr | 239.542 | 85.699 | 428.562 | 274.831 | 266.834 |
| La | 89.25 | 20.22 | 45.42 | 46.26 | 26.45 |
| Ce | 195.11 | 52.90 | 104.44 | 98.96 | 55.06 |
| Pr | 22.48 | 7.46 | 14.60 | 14.99 | 7.73 |
| Nd | 91.68 | 34.91 | 64.06 | 64.10 | 37.28 |
| Sm | 16.08 | 10.37 | 12.40 | 12.52 | 8.18 |
| Eu | 1.23 | 0.11 | 0.94 | 0.16 | 2.75 |
| Gd | 15.27 | 11.60 | 11.87 | 11.87 | 8.42 |
| Tb | 2.00 | 2.30 | 1.86 | 1.91 | 1.24 |
| Dy | 11.05 | 14.47 | 10.65 | 11.44 | 7.00 |
| Ho | 1.99 | 2.98 | 2.06 | 2.26 | 1.30 |
| Er | 5.57 | 8.94 | 5.95 | 6.63 | 3.47 |
| Tm | 0.60 | 1.08 | 0.63 | 0.69 | 0.38 |
| Yb | 4.63 | 8.56 | 5.35 | 6.17 | 2.79 |
| Lu | 0.70 | 1.24 | 0.82 | 0.92 | 0.45 |
| TREE | 439.75 | 159.82 | 265.58 | 262.77 | 152.84 |
| $(La/Yb)_{CN}$ | 3.59 | 1.21 | 2.24 | 2.29 | 2.05 |
| $(La/Sm)_{CN}$ | 2.67 | 1.10 | 1.79 | 1.56 | 2.44 |
| $(Gd/Yb)_{CN}$ | 13.13 | 1.61 | 5.78 | 5.11 | 6.44 |
| $(La/Yb)_{PM}$ | 3.60 | 1.21 | 2.25 | 2.30 | 2.06 |
| $(La/Sm)_{PM}$ | 2.68 | 1.10 | 1.80 | 1.56 | 2.44 |
| $(Gd/Yb)_{PM}$ | 0.25 | 0.03 | 0.24 | 0.04 | 1.03 |
| (Eu/Eu*) | 0.21 | 1.63 | 0.69 | 1.53 | 0.84 |
| (Nb/Nb*) | 0.04 | 0.01 | 0.06 | 0.04 | 1.07 |
| (Ti/Ti*) | 13.10 | 1.60 | 5.77 | 5.10 | 6.43 |

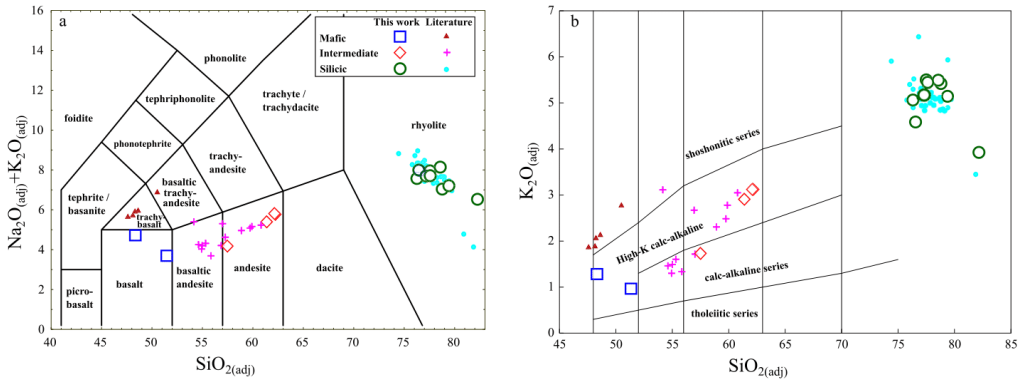


**Fig. 6. (a)** Total Alkali–Silica classification diagram for the volcanic rocks from the SSMC (TAS; Le Bas et al., 1986); **(b)** $K_2O_{(adj)}$–$SiO_{2(adj)}$ diagram of Peccerillo and Taylor (1976). Literature data were taken from the following sources: Orozco-Esquivel et al. (2002); Leroy et al. (2002); Rodríguez-Ríos and Torres-Aguilera (2009); Torres-Hernández et al. (2014); Aguillón-Robles et al. (2014); and Torres-Sánchez et al. (2019).

these rocks may have originated from partial melting of the continental crust.

Lead isotopic compositions of the SSMC volcanic rocks are summarized in Table 3. The rocks are plotted in Fig. 8b, together with the BR isotopic data. The graph also depicts the Northern Hemisphere reference line (NHRL; Zindler and Hart, 1986). The variations in Pb isotopic ratios for the mafic volcanic rocks are 18.925 and 18.962 for $(^{206}Pb/^{204}Pb)_i$, 15.303 and 15.329 for $(^{207}Pb/^{204}Pb)_i$, and 38.571 and 38.909 for $(^{208}Pb/^{204}Pb)_I$ (Table 3). For intermediate rocks, the initial values for $(^{206}Pb/^{204}Pb)_i$, $(^{207}Pb/^{204}Pb)_i$, $(^{208}Pb/^{204}Pb)_i$ ratios show a range of 18.891–18.934, 15.149–15.248, 38.864–38.902 (Table 3), respectively. The silicic volcanic rocks from the SSMC display $(^{206}Pb/^{204}Pb)_i$, $(^{207}Pb/^{204}Pb)_i$, $(^{208}Pb/^{204}Pb)_i$ ratios between 18.889 and 19.005, 14.521–15.217, and 38.831–39.016 (Table 3), respectively. In the Pb isotope diagrams (Fig. 8b), the SSMC mafic volcanic rocks plot above the NHRL with a trend towards depleted mantle (DM) just as the mafic rocks from the BR. The intermediate and silicic volcanic rocks from the SSMC partially overlap and plot above the NHRL with a trend towards enriched mantle type II (EMII) like the silicic volcanic rocks from the BR.

## 5. Discussion

### 5.1. Implications of $^{40}Ar/^{39}Ar$ data

For several years, it has been shown that the K—Ar method presents a major disadvantage over the Ar—Ar method. Compared with K/Ar dating, the $^{40}Ar/^{39}Ar$ technique has the advantage of requiring a much lower quantity of sample and uses only a single sample aliquot for analysis (Jourdan, 2012). Consequently, K—Ar ages tend to have much larger uncertainties than Ar—Ar ages (Lee, 2015). Therefore, when comparing $^{40}Ar/^{39}Ar$ ages with ages obtained by another method, it should be kept in mind that only the total uncertainty should be considered (Couilé et al., 2003).

A database of K—Ar ages have been compiled from the SSMC (Table S3). Data were compiled from: a) Labarthe-Hernández et al. (1982; $n = 6$); b) Tuta et al. (1988; n = 1); c) Aguillón-Robles et al. (1994; $n = 1$); d) Aguillón-Robles et al. (2009; n = 1); e) Tristán-González et al. (2009; n = 23); f) Aguillón-Robles et al. (2014; n = 4). New $^{40}Ar/^{39}Ar$ radiometric data demonstrate that volcanism in the SSMC starts from late Eocene, about 34 Ma, with the emplacement of the San Miguelito volcanic unit. The youngest age is obtained from the Cabras volcanic unit (about 21.9 Ma), indicating that the volcanism of the SSMC was active until the late Miocene.

The new $^{40}Ar/^{39}Ar$ data display three possible phases of magmatism in the SSMC (Fig. 9). The first phase is characterized by the generation of rhyolitic domes (San Miguelito and El Zapote unit); these domes were accompanied with effusive events of rhyolitic ignimbrites (San José and Cantera unit). The onset of the magmatic activity is constrained by Ar—Ar age of about 34 Ma (Fig. 9). The second phase, defined as re-activation of magmatic sources, is occupied by the eruption of intermediate volcanic rocks (La Placa unit), followed by, effusive magmatism of rhyolitic ignimbrites, between ~32.5 and 29.5 Ma (Panalillo unit). The third and final phase is characterized by emplacement of mafic volcanic rocks (Cabras unit), which represent a last period of activity, at about 22 Ma; this age is well constrained by $^{40}Ar/^{39}Ar$ ages, however, K—Ar shows high levels of uncertainty (Fig. 9).

The evidence of these three main phases observed in the SSMC leads to important observations of the evolution of the southern region of the MC: (1) high volumes of rhyolite ignimbrite volcanism between the late Eocene and the middle Oligocene; (2) the southern region of MC is comprised of three different compositional volcanic activities since middle Oligocene to early Miocene, with $SiO_2$ varying widely from about 37.4% m/m to 79.9% m/m (Table S2). The bimodal volcanism, as proposed previously (Rodríguez-Ríos and Torres Aguilera, 2009; Aguillón-Robles et al., 2014), does not seem to be valid.

### 5.2. Petrogenetic implications

Since the negative Nb anomaly in the volcanic rocks likely reflects a source, (Nb/Yb) vs. (Th/Yb) (Fig. 10a) can be used to investigate source characteristics (Pearce, 2008). In the diagram, it can be inferred that the mafic sample (SLP17–13) from the SSMC is mantle derived, while SLP17–14 (mafic rock) displays a lower continental crust signature; in contrast, the intermediate and silicic volcanic rocks of the SSMC display an interaction with middle and upper continental crust.

In order to explore the evolution of the magmatic rocks of the SSMC, petrogenetic mechanisms have been tentatively quantified using different methods. These different models aim at testing the relationship between the more evolved magma and the less differentiated magmas of the SSMC.

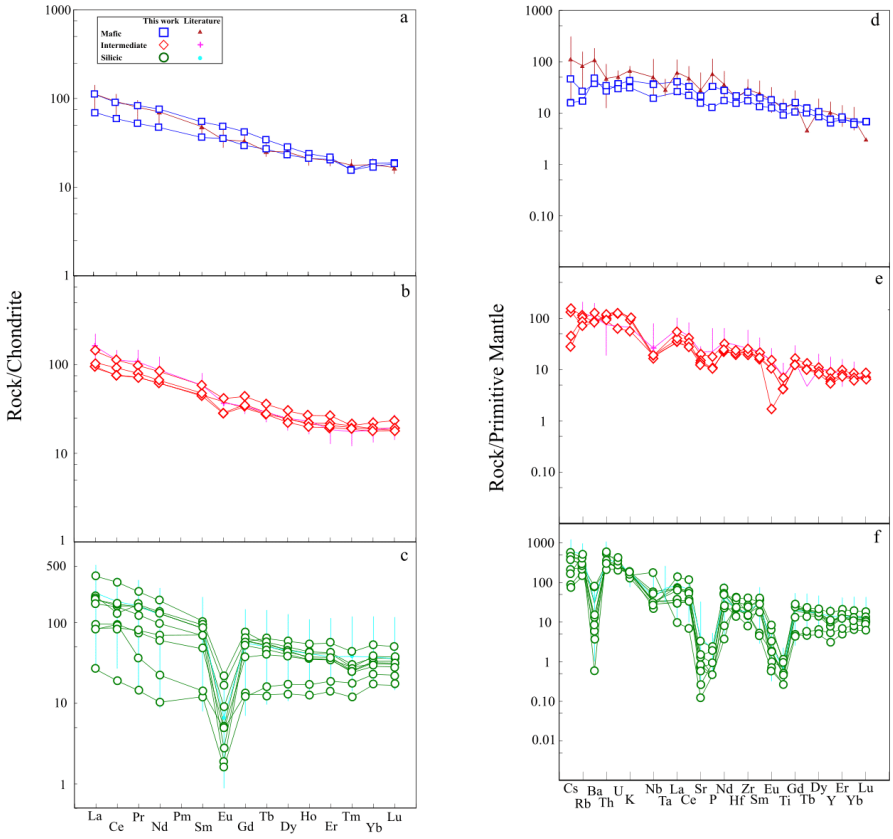


**Fig. 7. (a–c)** Chondrite-normalized rare-earth element (REE) diagrams for the SSMC rocks (chondrite values for normalization taken from McDonough and Sun, 1995); **(d–f)** Primitive-mantle normalized multielement diagrams for the SSMC rocks (primitive mantle values for normalization taken from McDonough and Sun, 1995). Symbols are same as in Fig. 5. Literature data were taken from the following sources: Orozco-Esquivel et al. (2002); Leroy et al. (2002); Rodríguez-Ríos and Torres-Aguilera (2009); Torres-Hernández et al. (2014); Aguillón-Robles et al. (2014) and Torres-Sánchez et al. (2019).

*5.2.1. Origin of the mafic volcanic rocks*

Thus far, the origin of the mafic volcanic rocks from the SSMC has been poorly discussed. Some authors described that these types of rocks in the area have presented a process of magma mixing during their rise to the surface (e.g., Rodríguez-Ríos and Torres-Aguilera, 2007; Torres-Sánchez et al., 2019). Therefore, it is worthwhile to explore the petrogenetic possibilities for these volcanic rocks.

The mafic samples (SLP17–13 and SLP17–14) from the SSMC plot nearby in the $SiO_{2\ (adj)}$ vs $^{87}Sr/^{86}Sr_{(i)}$ diagram (Fig. 10b), although the sample SLP17–14 is shifted towards the mantle-crust mixing lines. A small progressive signature of $^{87}Sr/^{86}Sr_{(i)}$ with $SiO_{2\ (adj)}$ from the sample SLP17–13 towards SLP17–14 may suggest an AFC process. Moreover, sample SLP17–14 could indicate a possible consequence of mixing between mantle-derived magma and crustal melt. This trend converges to a mantle-derived magma composition with an appropriate $^{87}Sr/^{86}Sr_{(i)}$ isotope ratio (0.70344–0.70496; Table 2). On the other hand, this may indicate derivation of the mafic samples (SLP17–13 and SLP17–14) from a heterogeneous mantle source.

In this context, an additional model has been tested. The initial Sr-Nd-Pb isotope ratios are useful to distinguish both mantle source and crustal involvement during magmatism. However, the $^{206}Pb/^{204}Pb$ ratio effectively distinguishes between the various mantle reservoirs, whereas the other isotope values can be used to infer the crustal component (Harangi et al., 2007). Therefore, following the model proposed by Harangi et al. (2007) (Fig. 10c), it can be interpreted that mafic samples from SSMC show two different sources.

The sample SLP17–13 shows a trend to an enriched-mid ocean ridge basalt (*E*-MORB) mantle without any style of mixing process (Fig. 10c). On the other hand, SLP17–14 yields a trend towards a mantle-lower crust mixing line (Fig. 10c), which may suggest a small crustal component in the genesis of this sample.

To support the idea of two different sources in the mafic rocks from the SSMC, a partial melting model of the mantle has been developed following the batch model equations reported by Zou (2007). Data of lherzolite xenolith (sample SD7; Dávalos-Elizondo et al., 2016) were used to represent lithospheric mantle composition. A mineralogical

**Table 2**
Whole-rock Sr and Nd isotopic data for volcanic rocks from the Sierra de San Miguelito Complex. (age data for in situ-growth corrections were taken from Table 4). For $\varepsilon Nd_t$ CHUR values for $^{143}Nd/^{144}Nd = 0.512630$ and $^{147}Sm/^{144}Nd = 0.1960$ were taken from Faure (1977). Rb, Sr, Sm and Nd concentrations were taken from Table 1).

| Sample | Rock unit | Magma type | Age | Rb (ppm) | Sr (ppm) | $^{87}Rb/^{86}Sr$ | $^{87}Sr/^{86}Sr$ | ±2σ | $^{87}Sr/^{86}Sr_{(i)}$ | Sm (ppm) | Nd (ppm) | $^{147}Sm/^{144}Nd$ | $^{143}Nd/^{144}Nd$ | ±2σ | $^{143}Nd/^{144}Nd_{(i)}$ | $\varepsilon Nd_t$ |
|---|---|---|---|---|---|---|---|---|---|---|---|---|---|---|---|---|
| SLP17–13 | Cabras | Basic | 22.21 | 10.36 | 425.17 | 0.07049 | 0.70346 | 6 | 0.70344 | 8.18 | 37.28 | 0.13271 | 0.51289 | 10 | 0.51287 | +5.2 |
| SLP17–14 | La Placa | Basic | 30.13 | 15.72 | 311.04 | 0.14622 | 0.70502 | 6 | 0.70496 | 5.48 | 23.30 | 0.14210 | 0.51266 | 18 | 0.51264 | +0.9 |
| SLP17–10 | La Placa | Inter. | 32.67 | 66.26 | 276.84 | 0.69248 | – | – | | 7.21 | 32.71 | 0.13330 | 0.51249 | 9 | 0.51246 | −2.5 |
| SLP17–20 | La Placa | Inter. | 27.50 | 60.95 | 390.27 | 0.45181 | 0.70557 | 6 | 0.70540 | 8.64 | 41.11 | 0.12707 | 0.51252 | 7 | 0.51249 | −2.0 |
| SMB17–01 | La Placa | Inter. | 30.00 | 50.94 | 252.61 | 0.58333 | 0.70606 | 7 | 0.70581 | 1.05 | 5.04 | 0.12628 | 0.51249 | 13 | 0.51247 | −2.4 |
| SMB17–02 | La Placa | Inter. | 30.00 | 42.02 | 294.67 | 0.41257 | 0.70592 | 20 | 0.70575 | 6.43 | 30.33 | 0.12822 | 0.51252 | 7 | 0.51249 | −1.8 |
| SLP17–11 | San Miguelito | Acid | 33.17 | 213.35 | 27.56 | 22.39592 | 0.71995 | 7 | 0.70940 | 10.73 | 48.15 | 0.13474 | 0.51249 | 6 | 0.51246 | −2.5 |
| SLP17–12 | San Miguelito | Acid | 33.00 | 290.80 | 2.46 | 342.26587 | – | – | – | 1.76 | 5.11 | 0.20808 | 0.51262 | 8 | 0.51258 | −0.2 |
| SLP17–15 | Panalillo | Acid | 28.65 | 157.64 | 64.82 | 7.03621 | 0.71005 | 6 | 0.70719 | 16.08 | 91.68 | 0.10608 | 0.51248 | 8 | 0.51245 | −2.7 |
| SLP17–16 | Panalillo | Acid | 28.65 | 237.32 | 12.27 | 55.96519 | 0.73354 | 7 | 0.71078 | 10.37 | 34.91 | – | – | – | – | – |
| SLP17–19 | Panalillo | Acid | 31.05 | 85.36 | 29.23 | 8.44796 | 0.71258 | 8 | 0.70886 | 12.40 | 64.06 | 0.11702 | 0.51254 | 8 | 0.51252 | −1.4 |
| SLP17–23 | Panalillo | Acid | 29.4 | 121.35 | 5.28 | 66.50392 | 0.74749 | 11 | 0.71973 | 12.52 | 64.10 | 0.11812 | 0.51254 | 8 | 0.51251 | −1.4 |
| SLP17–24 | Cantera | Acid | 32.1 | 181.51 | 23.19 | 22.64472 | 0.72170 | 7 | 0.71138 | 6.80 | 30.04 | 0.13698 | 0.51249 | 8 | 0.51247 | −2.3 |
| SLP17–28 | El Zapote | Acid | 33.48 | 250.09 | 16.07 | 45.02054 | 0.73799 | 6 | 0.71659 | 2.13 | 11.13 | 0.11587 | 0.51249 | 8 | 0.51247 | −2.3 |
| SLP17–29 | San José | Acid | 33.95 | 144.26 | 14.01 | 29.79568 | – | – | – | 14.24 | 67.79 | 0.12706 | 0.51248 | 9 | 0.51245 | −2.6 |

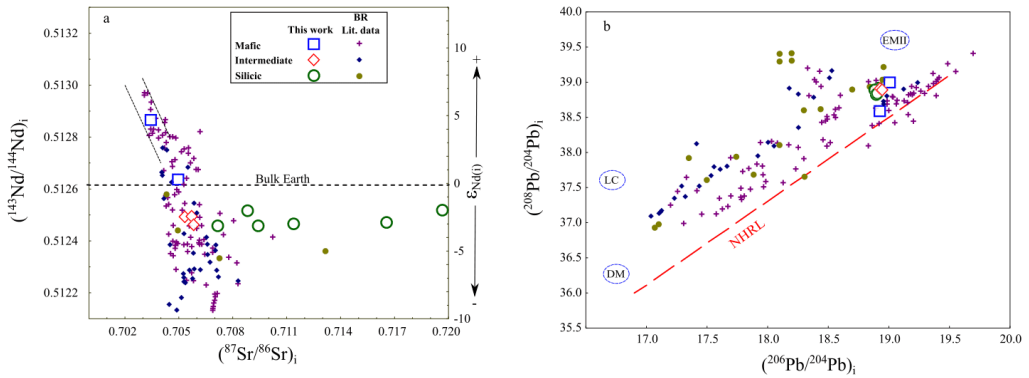


**Fig. 8.** Sr, Nd (modified after Verma, 1984) and Pb isotope plots of SSMC volcanic rocks compared to southern Basin and Range igneous rocks. (a) $^{143}Nd/^{144}Nd$ versus $^{87}Sr/^{86}Sr$ and $\varepsilon_{Nd}$ plot of SSMC volcanic rocks; (b) $^{206}Pb/^{204}Pb$ versus $^{208}Pb/^{204}Pb$ plot SSMC volcanic rocks. Abbreviations: BR-Basin and Range; LC-Lower Crust; DM-Depleted Mantle; EMII–Enriched Mantle type-II; NHRL-Northern Hemisphere Reference Line. Compositions from DM, EMII are taken from Faure (1986) and NHRL values are taken from Zindler and Hart (1986). Literature data were taken from the following sources: Duncker et al. (1991); Johnson and Thompson (1991); Kempton and Fitton (1991); Gibson et al. (1992); Bradshaw et al. (1993); Davis and Hawkesworth (1995); Rogers et al. (1995); McMillan et al. (2000); and Christiansen et al. (2007).

**Table 3**
Whole-rock Pb isotopic data for volcanic rocks from the Sierra de San Miguelito Complex (age data for correction were taken from Table 4; element concentrations of Th, U and Pb were taken from Table 1).

| Sample | Rock unit | Magma type | Age | Th (ppm) | U (ppm) | Pb (ppm) | $^{206}Pb/^{204}Pb$ | $^{207}Pb/^{204}Pb$ | $^{208}Pb/^{204}Pb$ | $^{206}Pb/^{204}Pb_{(i)}$ | $^{207}Pb/^{204}Pb_{(i)}$ | $^{208}Pb/^{204}Pb_{(i)}$ |
|---|---|---|---|---|---|---|---|---|---|---|---|---|
| SLP17–13 | Cabras | Basic | 22.21 | 2.13 | 0.74 | 3.066 | 18.928 | 15.614 | 38.571 | 18.925 | 15.329 | 38.571 |
| SLP17–14 | La Placa | Basic | 30.13 | 2.751 | 0.599 | 4.164 | 18.965 | 15.665 | 38.909 | 18.962 | 15.303 | 38.909 |
| SLP17–10 | La Placa | Inter. | 32.67 | 9.562 | 2.766 | 10.886 | 18.939 | 15.667 | 38.902 | 18.934 | 15.149 | 38.902 |
| SLP17–20 | La Placa | Inter. | 27.5 | 7.037 | 1.242 | 8.495 | 18.894 | 15.664 | 38.864 | 18.891 | 15.248 | 38.864 |
| SMB17–01 | La Placa | Inter. | 30 | 9.073 | 2.721 | 10.723 | 18.936 | 15.666 | 38.894 | 18.932 | 15.205 | 38.893 |
| SMB17–02 | La Placa | Inter. | 30 | 8.01 | 2.653 | 9.958 | 18.938 | 15.665 | 38.889 | 18.933 | 15.227 | 38.889 |
| SLP17–11 | San Miguelito | Acid | 33.17 | 28.959 | 4.414 | 26.661 | 18.900 | 15.666 | 38.885 | 18.897 | 15.016 | 38.885 |
| SLP17–12 | San Miguelito | Acid | 33 | 44.084 | 6.664 | 51.671 | 18.905 | 15.661 | 38.831 | 18.903 | 15.154 | 38.831 |
| SLP17–15 | Panalillo | Acid | 28.65 | 23.395 | 5.197 | 22.503 | 18.909 | 15.665 | 38.881 | 18.906 | 15.122 | 38.881 |
| SLP17–16 | Panalillo | Acid | 28.65 | 36.907 | 8.373 | 16.621 | 19.013 | 15.680 | 39.016 | 19.005 | 14.521 | 39.016 |
| SLP17–19 | Panalillo | Acid | 31.05 | 17.217 | 4.35 | 21.886 | 18.896 | 15.660 | 38.858 | 18.892 | 15.217 | 38.858 |
| SLP17–23 | Panalillo | Acid | 29.4 | 25.063 | 5.222 | 26.949 | 18.897 | 15.659 | 38.861 | 18.894 | 15.162 | 38.861 |
| SLP17–24 | Cantera | Acid | 32.1 | 25.802 | 5.005 | 27.019 | 18.907 | 15.666 | 38.889 | 18.903 | 15.112 | 38.889 |
| SLP17–28 | El Zapote | Acid | 33.48 | 30.295 | 4.297 | 29.351 | 18.892 | 15.668 | 38.876 | 18.889 | 15.045 | 38.876 |
| SLP17–29 | San José | Acid | 33.95 | 27.782 | 5.752 | 28.743 | 18.922 | 15.669 | 38.913 | 18.918 | 15.078 | 38.913 |

**Table 4**
Summary of $^{40}Ar/^{39}Ar$ ages of volcanic rocks from the Sierra de San Miguelito volcanic complex.

| Sample | Plateau age (Ma) ± 2σ | $^{39}Ar$ released (%) | Isochron age (Ma) ± 2σ | MSWD |
|---|---|---|---|---|
| *a) San Miguelito Unit* | | | | |
| SLP17–11 | 33.17 ± 0.67 | 80.1 | 34.80 ± 5.30 | 13 |
| *b) San José Unit* | | | | |
| SLP17–29 | 33.95 ± 0.44 | 98.1 | 34.09 ± 0.48 | 1.7 |
| *c) El Zapote Unit* | | | | |
| SLP17–28 | 33.48 ± 0.43 | 90.2 | 33.40 ± 0.68 | 2.2 |
| *d) Cantera Unit* | | | | |
| SLP17–24 | 32.10 ± 0.38 | 86 | 32.50 ± 0.39 | 1.3 |
| *e) La Placa Unit* | | | | |
| SLP17–10 | 32.67 ± 0.39 | 66.5 | 32.51 ± 0.48 | 2.4 |
| SLP17–14 | 30.13 ± 0.42 | 81.5 | 30.47 ± 0.99 | 3.5 |
| SLP17–20 | – | – | 27.5 ± 2.8 | 20 |
| *f) Panalillo Unit* | | | | |
| SLP17–19 | 31.05 ± 0.37 | 94.6 | 29.50 ± 2.30 | 4.9 |
| SLP17–23 | 29.40 ± 0.50 | 100 | 30.40 ± 0.74 | 0.99 |
| SLP17–15 | 28.65 ± 0.37 | 83.4 | 30.60 ± 2.00 | 3.2 |
| SLP17–16 | 24.15 ± 0.82 | 51.5 | 29.60 ± 3.5 | 7.5 |
| *g) Cabras Unit* | | | | |
| SLP17–13 | 22.21 ± 0.29 | 75.6 | 21.93 ± 0.59 | 5.9 |

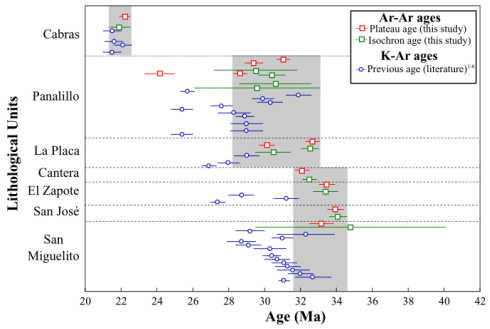


**Fig. 9.** Distribution of age from each SSMC unit. Gray shadow represents three main eruptive events of the SSMC. Previous age was taken from: [1] Labarthe-Hernández et al. (1982); [2] Tuta et al. (1988); [3] Aguillón-Robles et al. (1994); [4] Aguillón-Robles et al. (2009); [5] Tristán-González et al. (2009); [6]Aguillón-Robles et al. (2014).

arrangement of 0.45 Ol + 0.35 Opx + 0.2 Cpx was considered for the partial melting model. Melting degrees for the partial melting model that were used as F = 0.01 to 0.2 (Fig. 10d). The mafic sample (SLP17–13) could be produced by approximately 3–7% of partial melting of the mantle of a lherzolite composition, whereas sample SLP17–14 indicates a trend towards the partial melting line for granulite (Fig. 10d), suggesting lower crustal contamination of a mantle-derived melt. Such a melt regime could exist during an extensional phase within the area. In this context, it is noteworthy that the two mafic samples (SLP17–13 and SLP17–14) displayed different ages i.e., 30 Ma and 22.2 Ma, respectively. Thus, the differences in their initial isotopic composition from the older mafic sample (SLP17–14; 30 Ma) to the youngest mafic sample (SLP17–13; 22.2 Ma), may, on the other hand, represent a temporal switch over from melting the lithospheric- to asthenosphere-derived mafic magmas. However, more detailed sampling and analysis of mafic magmas of different ages is required to resolve these different petrogenetic possibilities. We do not consider one sample each for a statistically representative evidence to pursue further these arguments.

*5.2.2. Origin of the silicic volcanism*

The origin of the silicic volcanic rocks from the SSMC have been discussed by several authors (i.e., Orozco-Esquievel et al., 2002; Rodríguez-Ríos and Torres-Aguilera, 2009; Aguillón-Robles et al., 1994, 2014), that proposed that the silicic volcanic rocks were derived from the partial melting of granulites from the lower continental crust. Recently, Torres-Sánchez et al. (2019) have proposed a first quantitative model for these volcanic rocks that indicated the silicic volcanic rocks were derived from melts of the upper continental crust. According to Xu et al. (2008), if the magmas are derived from partial melt of mafic granulites from the lower crust, the magma produced would have a metaluminous and calc-alkaline signature and are thus inadequate to account for the silicic volcanic rocks from the SSMC. Therefore, in this work we propose a new quantitative model for the partial melting processes that derived the generation of the silicic volcanism in the SSMC.

A crustal partial melting model was developed applying the batch melting equation reported by Zou (2007). Compositions of intermediate granulite were taken from Schaaf et al. (1994) (sample LP89). The mineralogical arrangements of continental crust reservoirs considered for the model are: 0.4Plg + 0.3Cpx + 0.2Gt + 0.05Opx + 0.05Amph. Melting degrees for the partial melting model were F = 0.1 to 0.9 (Fig. 10d). The bivariate model (Fig. 10d) displays that high grades of melting of intermediate granulites can explain the different silicic volcanic rocks of the SSMC (Fig. 10d).

*5.2.3. Assimilation-fractional crystallization processes (AFC)*

Fractional crystallization processes are generally combined with the assimilation of the wall rocks surrounding the magma chamber (DePaolo, 1981). The amount of assimilated material correlates to the quantity of magma that has crystallized through cooling (DePaolo, 1981).

For a better understanding of the processes that involved the evolution of the intermediate rocks from the SSMC an initial quantitative treatment was carried out to represent the assimilation-fractional crystallization (AFC) processes applying the equations proposed by DePaolo (1981). The isotopic composition of a basaltic magma (sample SLP1713, $SiO_2$ = 47.76% m/m) was taken to represent an initial magma ($C_0$), as well as the composition of metasediments (sample LP51; Schaaf et al., 1994), as a representative of the assimilated wall-rock ($C_A$). A mineralogical arrangement of 0.45Plg + 0.1Amph + 0.2Bt + 0.1Ap + 0.05Ol + 0.05Ksp + 0.05Zr was considered for the fractional crystallization process. Partition coefficients were taken from Villemant et al. (1981) and McKenzie and O'Nions (1991). Isotopic AFC models (Fig. 11) were calculated considering the ratios for $r = 0.1$, $r = 0.3$, $r = 0.5$, $r = 0.7$ and $r = 0.9$ of the assimilation to the fractional crystallization, as well as a fraction of magma remaining F = 0.9 to 0.1.

The AFC modelling yields a better fit to isotopic data, indicating that most of the intermediate rocks of the SSMC experience variable degrees of assimilation ($r > 0.3$) of metasediments combined with fractional crystallization. The model reveals ~35 to 40% of assimilation of metasediments from the continental crust (Fig. 11).

*5.3. Tectonic settings*

In this work, we use new multi-dimensional discrimination diagrams to infer the plate tectonic setting, due to conventional bivariate and ternary diagrams revealing several problems related to statistical treatment of compositional data. The most important reason for this failure is related to the use of limited databases, problems of closed or constant sum compositional variables, and eye-fitted tectonic field boundaries and distribution of compositional data (Verma et al., 2012;

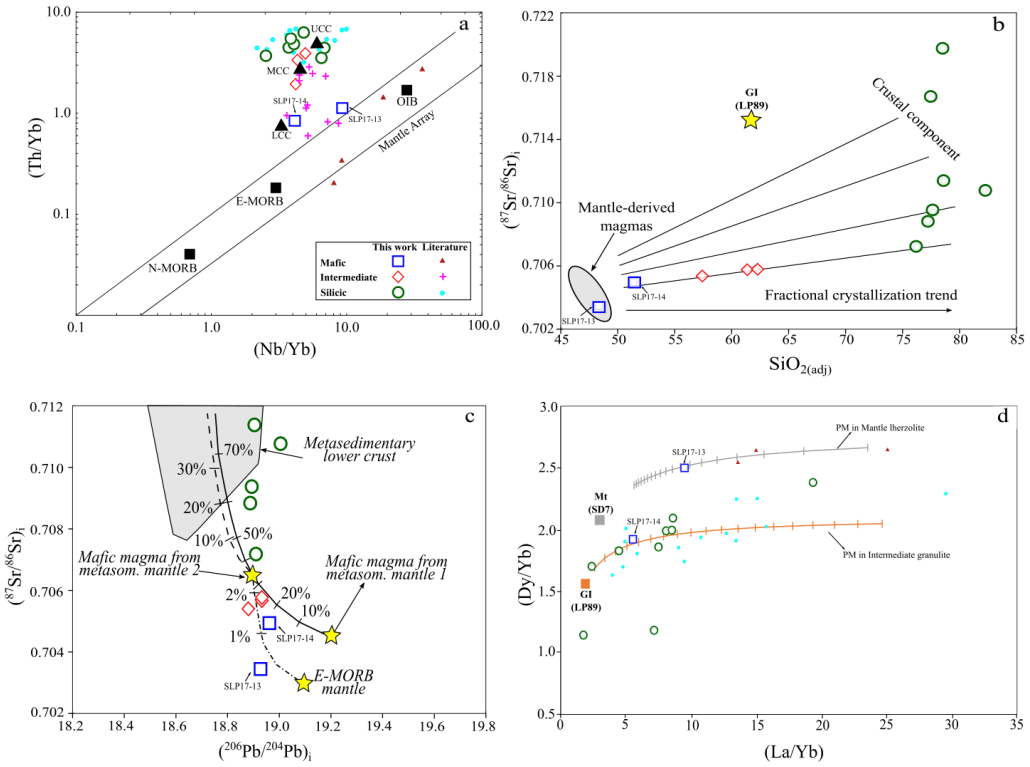


**Fig. 10.** a) (Th/Yb)–(Nb/Yb) diagram for volcanic rocks from the SSMC; (b) $SiO_{2(adj)}$ vs $^{87}Sr/^{86}Sr_{(i)}$ for the SSMC volcanic rocks. The positive correlation trends can be explained either by AFC processes or mixing between mantle-derived mafic magmas and crustal components, whereas the near-horizontal trend indicates closed-system fractional crystallization.; (c) Petrogenetic modelling for the genesis of the SSMC mafic volcanic rocks based on the variation of $^{87}Sr/^{86}Sr_{(i)}$ vs $^{206}Pb/^{204}Pb_{(i)}$. Model is taken and modify after Harangi et al. (2007); (d) (La/Yb) –(Dy/Yb) partial model, values of granulite and mantle taken from Schaaf et al. (1994). Each small bar represents 5% of melting for the orange line (granulite melting) and 1% of melting for the gray line (mantle melting). Literature data were taken from the following sources: Orozco-Esquivel et al. (2002); Leroy et al. (2002); Rodríguez-Ríos and Torres-Aguilera (2009); Torres-Hernández et al. (2014); Aguillón-Aguillón-Robles et al. (2014) and Torres-Sánchez et al. (2019). Abbreviations: *E*-MORB-Enriched Mid-Ocean Ridge; GI-Intermediate Granulite; LCC-Lower Continental Crust; MCC-Middle Continental Crust; Mt-Mantle composition; N-MORB-Normal Mid-Ocean Ridge; OIB-Ocean Island Basalt; UCC-Upper Continental Crust.

Verma et al., 2013). Therefore, new multidimensional discrimination diagrams proposed by Agrawal et al. (2008), Verma and Verma (2013) and Verma et al. (2013) for mafic, intermediate and silicic rocks were used for tectonic interpretation.

In the multidimensional discrimination diagrams by Agrawal et al. (2008) the mafic volcanic rocks from the SSMC were discriminated as within-plate (CR + OI; Fig. 12a) setting. This was also the case for intermediate and silicic rocks (Fig. 12b-c; Verma and Verma, 2013 and Verma et al., 2013). Conventional Sr—Nd isotope diagram (Fig. 12d) was used for comparison of the SSMC volcanic rocks with compiled literature data from continental rifts (Verma and Verma, 2018). The mafic volcanic rocks from the SSMC display a trend towards the mantle array, as well as the evolved rocks (intermediate and silicic volcanic rocks) continental rift rocks. The Nb and Ta anomalies in the primitive mantle-normalized diagrams for the SSMC rocks also support these findings. More detailed sampling and additional data in future could be evaluated from the most recent multidimensional tectonomagmatic models (Verma, 2020b) for better understanding the evolution of the tectonic regime through time from the Oligocene to the Quaternary.

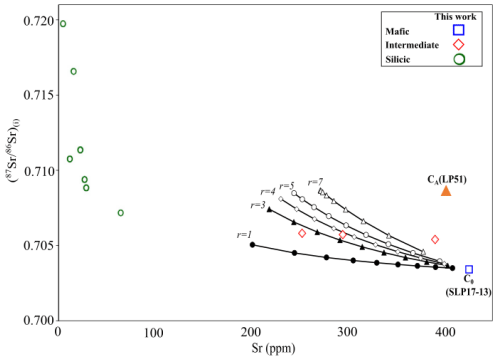


**Fig. 11.** Sr vs $^{87}Sr/^{86}Sr_{(i)}$ assimilation and fractional crystallization model for the intermediate volcanic rocks from the SSMC, values of metasediments were taken from Schaaf et al. (1994). Abbreviations: Co-Initial magma; CA-assimilated wall-rock.

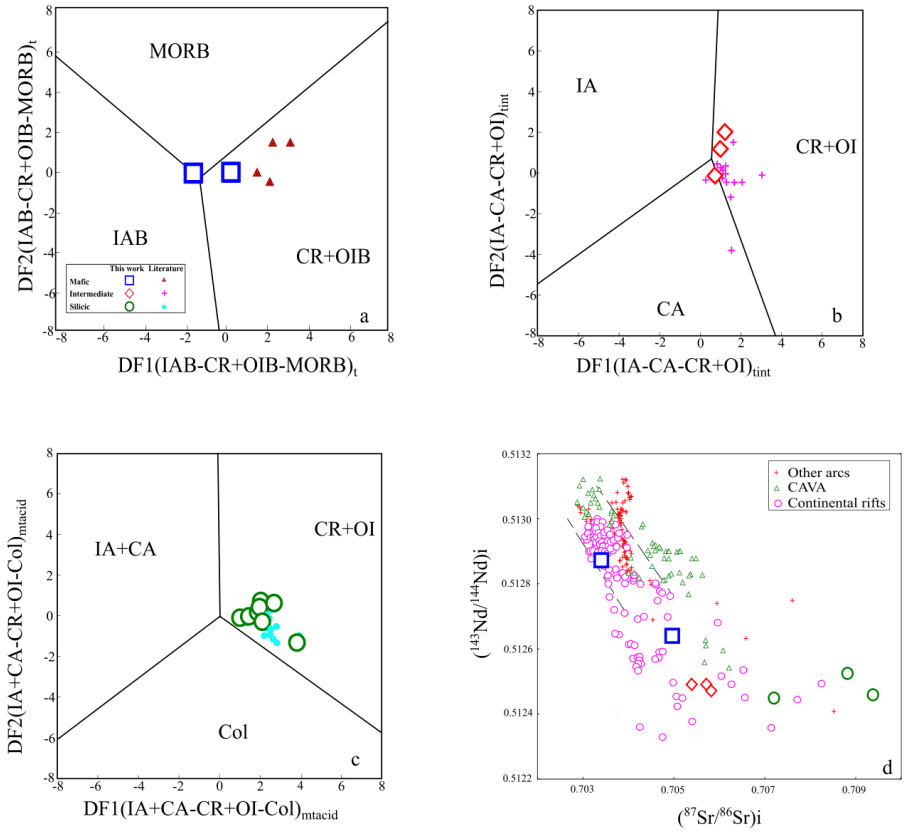


**Fig. 12.** a) Major-trace element based multidimensional discrimination diagram for mafic rocks (Verma and Agrawal, 2011); b) Major-trace element based multidimensional discrimination diagram for intermediate rocks (Verma and Verma, 2013); c) Immobile trace element based multidimensional discrimination diagram for silicic rocks (Verma et al., 2013) from the SSMC. d) Conventional Sr—Nd isotope diagram for the SSMC. Abbreviations: CAVA-Central American Volcanic Arc; Col-Collision; CR + OI-combined continental rift and ocean island; CR + OIB-combined continental rift and ocean island basalt; IA-Island Arc; IA + CA-combined island arc and continental arc; IAB-Island Arc Basalt; MORB-Mid-Ocean Ridge.

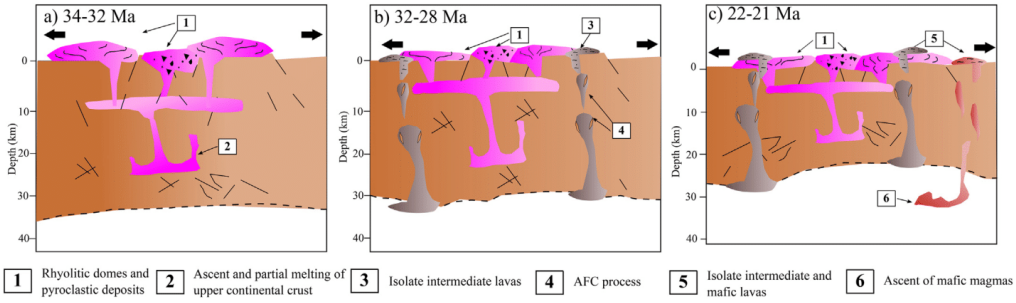


**Fig. 13.** Schematic diagram showing the evolution of the SSMC volcanic rocks between 34 Ma and 21 Ma. a) Generation and ascent of rhyolites and ignimbrites volcanic rocks during the late Eocene to early Oligocene; b) Ascent and assimilation and fractional crystallization of intermediate volcanic rocks during the late Oligocene; c) Emplacement of mafic volcanic rocks at the early Miocene. Black arrows represent continental crust extensional regime; thickness values of the continental crust were taken from Nieto-Samaniego et al. (2007); the figure was modified after Aguillon-Robles et al. (2014) and Sieck et al. (2019).

### 5.4. Geodynamic implications

The petrological observations indicate that the Cenozoic units from the SSMC were derived from a lithospheric mantle source that was heterogeneously enriched by continental contributions. Some authors suggest that the volcanic rocks from the SSMC were generated by a transitional subduction-intraplate setting from 42 to 31 Ma (Aguillón-Robles et al., 2014). Similarly, Tristán-González et al. (2009) proposed that Eocene-Oligocene (42–32 Ma) magmatism was associated with a typical convergence regime of continental volcanic arc and the Miocene (22–20 Ma) volcanic rocks were generated in an intra-plate regime. Rodríguez-Ríos et al. (2007) suggested that the silicic volcanic rocks evolved through a partial melting of a Precambrian lower continental crust (granulite facies).

However, the present study reveals that silicic volcanic rocks of the SSMC were generated through melting of intermediate granulites at 34–32 Ma. Meanwhile, intermediate volcanic rocks were erupted during the early Oligocene (~32–29 Ma) derived from lithospheric mantle melts with contaminated by metasediments. Mafic volcanism was produced at 21 Ma through low degree partial melting of the lithospheric mantle. The observations and data from the present study may be used to hypothesize the magmatic evolution of the SSMC volcanic rocks during late Eocene to early Miocene by extensional regimes (Fig. 13).

If the geological observations are considered, it is apparent that the Eocene to Miocene volcanism in the study area was developed synchronously with the tectonic exhumation of the volcanic rocks from the BR and southern region of the MC. These observations may be used to discuss the nature of the Cenozoic extension systems that produced the volcanic rocks across the southern section of the BR.

## 6. Conclusions

From the integrated petrography, geochemistry, geochronological and isotopic data obtained from the SSMC, the following conclusions can be drawn:

1. The magmatic rocks of the SSMC have a wide composition range of trachybasalt, basalt, basaltic trachyandesite, basaltic andesite, andesite and rhyolite. They display porphyritic textures with disequilibrium features in the mafic volcanic rocks. Although there is a wide range of compositions documented in this study, there is no evidence for synchronous bimodality therefore does not show true bimodal volcanism.
2. Geochemical features indicate that the mafic volcanic rocks from the SSMC were derived from two sources: one derived from the lithospheric mantle alone, and a second source involving a lower crustal component. On the other hand, intermediate volcanic rocks derived from assimilation and fractional crystallization processes of the mafic melt. It is likely that the silicic volcanic rocks were derived from partial melting of mid continental crust granulites.
3. Volcanism was active in the SSMC between 34 and 21 Ma. Magmas were erupted through three episodes: an initial phase characterized by domes and rhyolite ignimbrites, followed by a second phase of volcanism represented by intermediate rocks intercalated with pyroclastic rocks of rhyolite composition; a third phase is characterized by isolated mafic lavas.
4. Magmatic rocks of the SSMC were probably formed in a within-plate (CR + OI) setting, during BR related extension, in the late Eocene to Miocene time, although more detailed sampling and analyses are required to better document the time-related tectonic evolution.

## Declaration of Competing Interest

This paper has not been published elsewhere, nor is it under consideration of any other journal. It is an original contribution, authors have contributed to its development, and there is no conflict of interest.

## Acknowledgments

This study was funded by the Royal Society, UK under grant [NA160116]. SKV and TLB are grateful to the Newton Advanced Fellowship award–The Royal Society, UK. The first author (DTS) acknowledges the National Council of Science and Technology (CONACYT), Mexico for his doctoral fellowship [Grant # 336677], whose doctoral thesis is in preparation under the guidance of SKV. DTS also thanks Dr. Tiffany Barry for his 6 months stay at University of Leicester to perform geochemical, mineralogical, geochronological and isotopic studies. We thank Dr. Alison Halton for running and recalculating the Ar—Ar dating work at The Open University, Milton Keynes, UK. We also thank Dr. Ian Millar and the team at NERC Isotope Geoscience Laboratory (NIGL), Keyworth, UK. We much appreciate two anonymous journal reviewers for their several constructive comments and the "Editor-in-Chief" Prof. Michael Roden for efficient handling of our manuscript.

## Appendix A. Supplementary data

Supplementary data to this article can be found online at https://doi.org/10.1016/j.lithos.2020.105613.

## References

Aguillón-Robles, A., Aranda-Gómez, J.J., Solorio-Munguía, J.G., 1994. Geología y tectónica de un conjunto de domos riolíticos del Oligoceno medio en el sur del Estado de San Luis Potosí, México. Rev. Mex. Cienc. Geol. 11, 29–42.

Aguillón-Robles, A., Tristán-González, M., Aguirre-Díaz, G.J., Bellon, M., 2009. Syn-extensional intra-plate trachydacite-rhyolitic dome volcanism of the Mesa Central, southern Sierra Madre Occidental volcanic province. Mexico. J. Volcanol. Geotherm. Res. 187, 33–52.

Nieto-Samaniego, A.F., Ferrari, L., Alaniz-Alvarez, S.A., Labarthe-Hernández, G., Rosas-Elguera, J., 1999. Variation of Cenozoic extension and volcanism across the southern Sierra Madre Occidental volcanic province, Mexico. Geol. Soc. Am. Bull. 111, 347–363.

Torres-Sánchez, D., Verma, S.K., Verma, S.P., Velasco-Tapia, F., Torres-Hernández, J.R., 2019. Petrogenetic and tectonic implications of Oligocene–Miocene volcanic rocks from the Sierra de San Miguelito complex, central Mexico. J. South Am. Earth Sci. 95, 102311.

Agrawal, S., Guevara, M., Verma, S.P., 2008. Tectonic discrimination of basic and ultrabasic rocks through log-transformed ratios of immobile trace elements. *Int. Geol. Rev.* 50, 1057–1079.

Aguillón-Robles, A., Tristán-González, M., Aguirre-Díaz, G.J., López-Doncel, R.A., Bellon, H., Martínez-Esparza, G., 2014. Eocene to Quaternary mafic-intermediate volcanism in San Luis Potosí, central Mexico: the transition from Farallon plate subduction to intra-plate continental magmatism. J. Volcanol. Geotherm. Res. 276, 152–172.

Aguirre-Díaz, G.J., Labarthe-Hernández, G., 2003. Fissure ignimbrites: Fissure-source origin for voluminous ignimbrites of the Sierra Madre Occidental and its relationship with Basin and Range faulting. Geology 31, 773–776.

Angeles-Moreno, E., Nieto-Samaniego, A.F., Ruiz-González, F.J., Levresse, G., Alaniz-Alvarez, S.A., Moya, M.D.J.P.O., Miranda-Avilés, R., 2017. The transition between shortening and extensional regimes in central Mexico recorded in the tourmaline veins of the Comanja granite. J. South Am. Earth Sci. 73, 65–77.

Aranda-Gómez, J.J., McDowell, F.W., 1998. Paleogene extension in the Southern Basin and Range Province of Mexico: Syndepositional tilting of Eocene red beds and Oligocene volcanic rocks in the Guanajuato mining district. *Int. Geol. Rev.* 40, 116–134.

Atwater, T.M., 1970. Implications of plate tectonics for the Cenozoic tectonic evolution of North America. Geol. Soc. Am. Bull. 81, 3513–3536.

Berglund, H.T., Sheehan, A.F., Murray, M.H., Roy, M., Lowry, A.R., Nerem, R.S., Blume, F., 2012. Distributed deformation across the Rio Grande rift, Great Plains, and Colorado Plateau. Geology 40, 23–26.

Bradshaw, T.K., Hawkesworth, C.H., Gallagher, K., 1993. Basaltic volcanism in the Southern Basin and Range: no role for a mantle plume. Earth Planet. Sci. Lett. 116, 45–62.

Caballero-Miranda, C.I., Torres-Hernández, J.R., Alva-Valdivia, M., 2009. Anisotropy of magnetic susceptibility analysis of the Cantera Ignimbrite, San Luis Potosi, México: flow source recognition. Earth Planets Space 61, 173–182.

Centeno-García, E., 2017. Mesozoic tectono-magmatic evolution of Mexico: an overview. Ore Geol. Rev. 81, 1035–1052.

Cerca-Martínez, L.M., Aguirre-Díaz, G.J., López-Martínez, M., 2000. The geologic evolution of the southern Sierra de Guanajuato; a documented example of the transition from the Sierra Madre Occidental to the Mexican Volcanic Belt. *Int. Geol. Rev.* 42, 131–151.

Christiansen, E.H., Haapala, I., Hart, G.L., 2007. Are Cenozoic topaz rhyolites the erupted equivalents of Proterozoic rapakivi granites? Examples from the western United States and Finland. Lithos 97, 219–246.

Clay, P.L., Buseman, H., Sherlock, S.C., Barry, T.L., Kelley, S.P., McGarvie, D.W., 2015. $^{40}Ar/^{39}Ar$ ages and residual volatile contents in degassed subaerial and subglacial volcanic rocks from Iceland. Chem. Geol. 403, 99–110.

Coney, P.J., Harms, T.A., 1984. Cordilleran metamorphic core complexes: Cenozoic extensional relics of Mesozoic compression. Geology 12, 550–554.

Cosca, M.A., Thompson, R.A., Lee, J.P., Turner, K.J., Neymark, L.A., Premo, W.R., 2014. $^{40}Ar/^{39}Ar$ geochronology, isotope geochemistry (Sr, Nd, Pb), and petrology of alkaline lavas near Yampa, Colorado: migration of alkaline volcanism and evolution of the northern Rio Grande rift. Geosphere 10, 374–400.

Couilé, E., Quidelleur, X., Gillot, P.Y., Courtillot, V., Lefévre, J.C., Chiesa, S., 2003. Comparative K-Ar and Ar/Ar dating of Ethiopian and Yemenite Oligocene volcanism: implications for timing and duration of the Ethiopian traps. Earth Planet. Sci. Lett. 206, 477–492.

Dávalos-Elizondo, M.G., Aranda-Gómez, J.J., Levresse, G., de la Cruz Cervantes, K.E., 2016. Química mineral y geoquímica de xenolitos del manto del campo volcánico Santo Domingo, San Luis Potosí: Evidencias de procesos metasomáticos del manto bajo porciones de la Mesa Central, México. Rev. Mex. Cienc. Geol. 33, 81–104.

Davis, J.M., Hawkesworth, C.H., 1995. Geochemical and tectonic transitions in the evolution of the Mogollon–Datil Volcanic Field, New Mexico, U.S.A. Chem. Geol. 119, 31–53.

DePaolo, D.J., 1981. Trace element and isotopic effects of combined wall rock assimilation and fractional crystallization. Earth Planet. Sci. Lett. 53, 189–202.

Dickinson, W.R., 2002. The Basin and Range province as a composite extensional domain. Int. Geol. Rev. 44, 1–38.

Dickinson, W.R., 2004. Evolution of the north American Cordillera. Annu. Rev. Earth Planet. Sci. 32, 13–45.

Duncker, K.E., Wolf, J.A., Harmon, R.S., Leat, P.T., Dickin, A.P., Thompson, R.N., 1991. Diverse mantle and crustal components in lavas of the NW Cerros del Rio volcanic field, Rio Grande Rift, New Mexico. Contrib. Mineral. Petrol. 108, 331–345.

Faure, G., 1986. Principles of Isotope Geology. Second edition. Wiley & Sons (589 p).

Gibson, S.A., Thompson, R.N., Leat, P.T., Dickin, A.P., Morrison, M.A., Hendry, G.L., Mitchell, J.G., 1992. Magmatism and the Causes of Continental Break–up. Geol. Soc. Spec. Pub. 68, 61–89 Storey, B.C., Alabaster, T., Pankhurst, R.J. (eds).

Glazner, A.F., Bartley, J.M., 1984. Timing and tectonic setting of Tertiary low-angle normal faulting and associated magmatism in the southwestern United States. Tectonics 3, 385–396.

Harangi, S., Downes, H., Thirlwall, M., Gméling, K., 2007. Geochemistry, petrogenesis and geodynamic relationships of Miocene calc-alkaline volcanic rocks in the Western Carpathian Arc, Eastern Central Europe. J. Petrol. 48, 2261–2287.

Henry, C.D., Aranda-Gómez, J.J., 2000. Plate interactions control middle-late Miocene, proto-Gulf and Basin and Range extension in the southern Basin and Range. Tectonophysics 318, 1–26.

Johnson, C.M., Thompson, R.A., 1991. Isotopic composition of Oligocene mafic volcanic rocks in the northern Rio Grande Rift: evidence for contributions of ancient intraplate and subduction magmatism to evolution of the lithosphere. J. Geophys. Res. 96, 13593–13608.

Jones, C.H., Wernicke, B.P., Farmer, G.L., Walker, J.D., Coleman, D.S., McKenna, L.W., Perry, F.V., 1992. Variations across and along a major continental rift: an interdisciplinary study of the Basin and Range province, western USA. Tectonophysics 213, 57–96.

Jourdan, F., 2012. The $^{40}Ar/^{39}Ar$ dating technique applied to planetary science and terrestrial impacts. Aust. J. Earth. Sci. 59, 199–244.

Kempton, P.D., Fitton, J.G., 1991. Isotopic and trace element constraints on the composition and evolution of the lithosphere beneath the southwestern United States. J. Geophys. Res. 96, 13713–13735.

Kempton, P.D., Downes, H., Sharkov, E.V., Vetrin, V.R., Ionov, D.A., Carswell, D.A., Beard, A., 1995. Petrology and geochemistry of xenoliths from the Northern Baltic shield: evidence for partial melting and metasomatism in the lower crust beneath an Archaean terrane. Lithos 36, 157–184.

Labarthe-Hernández, G., Tristán-González, M., Aranda-Gómez, J.J., 1982. Revisión estratigráfica del Cenozoico de la parte central del estado de San Luis Potosí. Universidad Autónoma de San Luis Potosí, Instituto de Geología, Folleto Técnico 85, 208.

Le Bas, M., LeMaitre, R.W., Streckeisen, A., Zanettin, B., 1986. A chemical classification of volcanic rocks base on the total alkali-silica diagram. J. Petrol. 27, 745–750.

Lee, J.K., 2015. Ar–Ar and K–Ar Dating. In: Rink, W.J., Thompson, J.W. (Eds.), Encyclopedia of Scientific Dating Methods. Springer, Netherlands, pp. 58–73.

Leroy, J.L., Rodríguez-Ríos, R., Dewonck, S., 2002. The topaz-bearing rhyolites from the San Luis Potosí area (Mexico): characteristics of the lava and growth conditions of topaz. Bulletin de la Société Géologique de France 173, 579–588.

López-Loera, H., Tristán-González, M., 2013. Geología y magnetometría aérea del Graben de Villa de Reyes, San Luis Potosí, Mesa Central de México: implicaciones tectónicas y geohidrológicas. Bull.Soc.geol.Fr. 65, 137–156.

McDonough, W.F., Sun, S.S., 1995. The composition of the Earth. Chem. Geol. 120, 223–253.

McKenzie, D., O'Nions, R.K., 1991. Partial melt distributions from inversion of rare earth element concentrations. J. Petrol. 32, 1021–1091.

McMillan, N.J., Dickin, A.P., Haag, D., 2000. Evolution of magma source regions in the Rio Grande rift, southern New Mexico. Geol. Soc. Am. Bull. 112, 1582–1593.

Middlemost, E.A.K., 1989. Iron oxidation ratios, norm and the classification of volcanic rocks. Chem. Geol. 77, 19–26.

Nieto-Samaniego, A.F., Macías-Romo, C., Alaniz-Alvarez, S.A., 1996. Nuevas edades isotópicas de la cubierta volcánica cenozoica de la parte meridional de la Mesa Central, México. Rev. Mex. Cienc. Geol. 13, 117–122.

Nieto-Samaniego, A.F., Alaniz-Álvarez, S.A., Camprubí, A., 2007. Mesa Central of México: Stratigraphy, structure, and Cenozoic tectonic evolution. In: Alaniz-Álvarez, S.A., Nieto-Samaniego, Á.F. (Eds.), Geology of México: Celebrating the Centenary of the Geological Society of México. Geological Society of America Special Paper vol. 422, pp. 41–70.

Orozco-Esquivel, M.T., Nieto-Samaniego, Á.F., Alaniz-Álvarez, S.A., 2002. Origin of rhyolitic lavas in the Mesa Central, Mexico, by crustal melting related to extension. J. Volcanol. Geotherm. Res. 188, 37–56.

Parsons, T., 1995. The Basin and Range Province. In: Olsen, K.H. (Ed.), Continental Rifts: Evolution, Structure. Tectonics. Developments in Geotectonics. Elsevier, Amsterdam, pp. 277–324.

Pearce, J.A., 2008. Geochemical fingerprinting of oceanic basalts with applications to ophiolite classification and the search for Archean oceanic crust. Lithos 100, 14–48.

Peccerillo, A., Taylor, S.R., 1976. Geochemistry of Eocene calc–alkaline volcanic rocks from the Kastamonu Area, Northern Turkey. Contrib. Mineral. Petrol. 58, 63–81.

Renne, P.R., Blaco, G., Ludwig, K.R., Mundil, R., Min, K., 2011. Response to the comment by W.H. Schwarz et al. on "Joint determination of $^{40}K$ decay constants and $^{40}Ar^*/^{40}K$ for the fish Canyon sanidine standard, and improved accuracy for $^{40}Ar/^{39}Ar$ geochronology" by P.R. Renne et al. (2010). Geochim. Cosmochim. Acta 75, 5097–5100.

Rodríguez-Ríos, R., Torres-Aguilera, J.M., 2009. Evolución petrológica y geoquímica del vulcanismo bimodal Oligocénico en el campo volcánico de San Luis Potosí (México). Rev. Mex. Cienc. Geol. 26, 658–673.

Rodríguez-Ríos, R., Aguillón-Robles, A., Leroy, J.L., 2007. Evolución petrológica y geoquímica de un complejo de domos topacíferos en el Campo Volcánico de San Luis Potosí (México). Rev. Mex. Cienc. Geol. 24, 328–343.

Rogers, N.W., Hawkesworth, C.J., Ormerod, D.S., 1995. Late Cenozoic basaltic magmatism in the Western Great Basin, California and Nevada. J. Geophys. Res. 100, 10287–10301.

Royse, K.R., Kempton, P.D., Darbyshire, D.P.F., 1998. Procedure for the analysis of rubidium–strontium and samarium–neodymium isotopes at the NERC Isotope Geosciences Laboratory. NIGL Report Series 121, 28.

Schaaf, P., Heinrich, W., Besch, T., 1994. Composition and Sm-Nd isotopic data of the lower crust beneath San Luis Potosí, Central Mexico: evidence from a granulite-facies xenolith suite. Chem. Geol. 118, 1–4.

Severinghaus, J., Atwater, T., 1990. Cenozoic geometry and thermal state of the subducting slabs beneath western North America. In: Wernicke, B. (Ed.), Basin and Range Extension. Geological Society of America Memories vol. 176, pp. 1–22.

Sheth, H.C., Torres-Alvarado, I.S., Verma, S.P., 2002. What is the "calc-alkaline rock series"? Int. Geol. Rev. 44, 686–701.

Sieck, P., López-Doncel, R., Dávila-Harris, P., Aguillón-Robles, A., Wemmer, K., Maury, R.C., 2019. Almandine garnet–bearing rhyolites associated to bimodal volcanism in the Mesa Central of Mexico: geochemical, petrological and geochronological evolution. J. S. Am. Earth Sci. 92, 310–328.

Sonder, L.J., Jones, C.H., 1999. Western United States extension: how the west was widened. Annu. Rev. Earth Planet. Sci. 27, 417–462.

Todt, W., Cliff, R.A., Hanser, A., Hofmann, A.W., 1996. Evaluation of a $^{202}Pb–^{205}Pb$ Double Spike for High-Precision Lead Isotope Analysis. Earth Processes: Reading the Isotopic Code. pp. 429–437.

Torres-Hernández, J.R., Labarthe-Hernández, G., Aguillón-Robles, A., Gómez-Anguiano, M., Mata-Segura, J.L., 2006. The pyroclastic dikes of the Tertiary San Luis Potosi volcanic field: Implications on the emplacement of Panalillo ignimbrite. Geofis. Int. 45, 243–253.

Torres-Hernández, J.R., Siebe-Grabach, C., Aguillón-Robles, A., Rodríguez-Ríos, R., 2014. Geocronología y características geoquímicas de un conjunto de domos riolíticos terciarios en el Campo Volcánico de San Luis Potosí, México. Boletin de la Soc. Geol. Mex. 66, 183–197.

Tristán-González, M., Aguillón-Robles, A., Barboza-Gudiño, J.R., Torres-Hernández, J.R., Bellon, H., López-Doncel, R., Rodríguez-Ríos, R., Labarthe-Hernández, G., 2009. Geocronología y distribución espacial del vulcanismo en el Campo Volcánico de San Luis Potosí. Boletin de la Soc. Geol. Mex. 61, 287–303.

Tuta, Z.H., Sutter, J.F., Kesler, S.E., Ruiz, J., 1988. Geochronology of mercury, tin, and fluorite mineralization in northern Mexico. Economic Geology and the Bulletin of the Society of Economic Geologists 83, 1931–1942.

Verma, S.P., 1984. Sr and Nd isotopic evidence for petrogenesis of mid-Tertiary felsic volcanism in the Mineral District of Zacatecas, Zac. (Sierra Madre Occidental), Mexico. Isotope Geoscience 2, 37–53.

Verma, S.P., 2020a. Road from Geochemistry to Geochemometrics. Springer, Singapore (669 p).

Verma, S.P., 2020b. Comprehensive multidimensional tectonomagmatic discrimination from log-ratio transformed major and trace elements. Lithos 362–363, 105476.

Verma, S.P., Agrawal, S., 2011. New tectonic discrimination diagrams for basic and ultrabasic volcanic rocks through log-transformed ratios of high field strength elements and implications for petrogenetic processes. Rev. Mex. Cienc. Geol. 28, 24–44.

Verma, S.P., Rivera-Gómez, M.A., 2013. Computer programs for the classification and nomenclature of igneous rocks. Episodes 36, 115–124.

Verma, S.P., Verma, S.K., 2013. First 15 probability-based multi-dimensional discrimination diagrams for intermediate magmas and their robustness against post-emplacement compositional changes and petrogenetic processes. Turk. J. Earth. Sci. 22, 931–995.

Verma, S.P., Verma, S.K., 2018. Petrogenetic and tectonic implications of major and trace element and radiogenic isotope geochemistry of Pliocene to Holocene rocks from the Tacaná Volcanic complex and Chiapanecan Volcanic Belt, southern Mexico. Lithos 312–313, 274–289.

Verma, S.K., Pandarinath, K., Verma, S.P., 2012. Statistical evaluation of tectonomagmatic discrimination diagrams for granitic rocks and proposal of new discriminant–function–based multi–dimentsional diagrams for acid rocks. Int. Geol. Rev. 54, 325–347.

Verma, S.P., Pandarinath, K., Verma, S.K., Agrawal, S., 2013. Fifteen new discriminant-function-based multi-dimensional robust diagrams for acid rocks and their application to Precambrian rocks. Lithos 168–169, 113–123.

Villemant, B., Jaffrezic, H., Joron, J.L., Treuil, M., 1981. Distribution coefficients of major and trace elements-Fractional crystallization in the alkali basalt series of Chaine-Des-Puys (Massif Central, France). Geochim. Cosmochim. Acta 45, 1997–2016.

Wernicke, B., Axen, G.J., Snow, J.K., 1988. Basin and Range extensional tectonics at the latitude of Las Vegas, Nevada. Geol. Soc. Am. Bull. 100, 1738–1757.

Xu, S.-S., Nieto-Samaniego, Á.F., Alaniz-Álvarez, S.A., Grajales-Nishimura, J.M., 2008. Evolution of the geometry of normal faults in the Oligocene volcanic field of the Mesa Central, México. Boletin de la Soc. Geol. Mex. 60, 71–82.

Xu, S.S., Nieto-Samaniego, A.F., Alaniz-Álvarez, S.A., 2004. Titling mechanisms in domino faults of the Sierra de San Miguelito, Central Mexico. Geol. Acta 2, 189–209.

Zindler, A., Hart, S., 1986. Chemical geodynamics. Annu. Rev. Earth Planet. Sci. 14, 493–571.

# CAPITULO 7.-

## ANÁLISIS QUÍMICO DE MINERALES

En este estudio se aplicó un método de combinación de técnicas tanto de Microsonda Electrónica (Electron Probe Microanalysis, EMPA), para llevar el análisis cuantitativo de los minerales y de Micrsocopía de Barrido Electrónico (Scanning Electron Microscope, SEM) para la toma de imágenes de retrodispersión de electrones de alta resolución para los minerales analizados.

El análisis químico aplicando el método EMPA se lleva a cabo bombardeando la muestra con un haz de electrones acelerados a 10-20 kV. El haz electrónico de 10 µm de diámetro se enfoca sobre una superficie pulida de la muestra. Esta emite rayos-X característicos de cada elemento los cuales son analizados en un detector de dispersión de energía o en uno de dispersión de longitud de onda. El análisis cuantitativo con EMPA se encuentra limitado generalmente a elementos de Z >11. Los elementos con concentraciones > 0.05% son detectados sin dificultad, aunque no es posible distinguir iones con diferentes estados de oxidación (Johnson y Maxwell, 1981).

Los resultados obtenidos para el presente estudios se obtuvieron en el Departamento de Geología de la Open Universty de Milton Keynes, Inglaterra. El equipo utilizado fue una microsonda electrónica Cameca SX100. Se seleccionaron 5 muestras de las unidades (2 muestras de composición félsicas, 2 muestras de composición intermedia y 1 muestra de composición básica) del Complejo Volcánico de la Sierra de San Miguelito.

La medición se llevó a cabo acelerando una corriente de 10 nA con un voltaje de 15 kV. Los tiempos de conteo de los picos fueron de 10 a 40s y para la corrección de matriz se utilizó una rutina de PhiRhoZ. Los siguientes elementos fueron medidos utilizando una espectroscopia de longitud de onda dispersiva: K, Al, Si, Fe, Mn, Ca, P, Ti, Na and Mg.

La microsonda fue calibrada usando los estándares minerales naturas de: Feldespato (K,Al,Si), hematita (Fe), bustamita (Mn, Ca), apatito (P), rutilo (Ti), jadeíta (Na) y fosterita (Mg). Detalles adicionales del análisis de microsonda son reportados en el apartado de Anexos A7.

En los siguientes apartados se presentará los resultados obtenidos por este método, como también, el procesamiento de los mismos. A su vez, los datos obtenidos se reportan en la Tabla A8 en la sección de anexos.

## 7.1 Composiciones minerales

A partir de la abundancia mineral conocida de las rocas volcánicas del Campo Volcánico de la Sierra de San Miguelito, las composiciones minerales fueron obtenidas de fenocristales de plagioclasas, clinopiroxenos y olivinos para cada uno de los tipos de rocas (máficas, intermedias y ácidas; Tabla A8).

Las composiciones de plagioclasas en las rocas máficas e intermedias indican que estas muestran un rango composicional de $An_{32-69}$ a $Ab_{29-42}$ (Figura 7.1a) Por otro lado las rocas ácidas muestran un rango composicional de plagioclasas de $An_{29-28}$ a $Ab_{65-66}$ (Figura 7.1a), de igual forma, en las rocas ácidas se puede observar la presencia de feldespatos alcalinos, los cuales muestran concentraciones de albita (Ab) y ortoclasa (Or) con abundancias de 65-66 y 5.16 a 5.40 respectivamente.

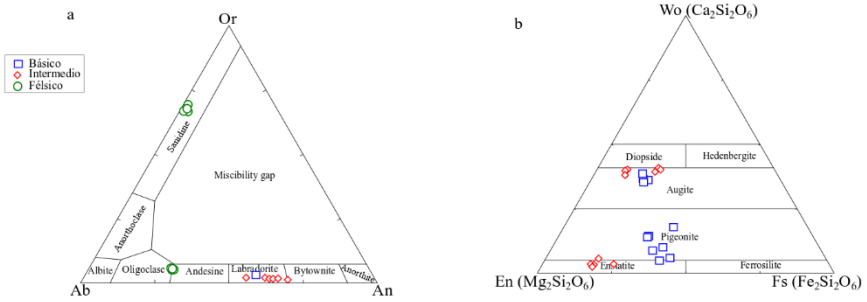


Figura 7.1 a) Diagrama de clasificación de feldespatos para las rocas del Complejo Volcánico de la Sierra de San Miguelito; b) Diagrama de clasificación de piroxenos para las rocas del Complejo Volcánico de la Sierra de San Miguelito.

Los feldespatos alcalinos muestran un contenido el cual difiere a la de los fenocristales de plagioclasa ($Ab_{29-42}$ y $Or_{2-25}$), que sugiere que la cristalización de los dos estilos de feldespatos no se encuentra en equilibrio (Figura 7.1ª).

Por otro lado, las rocas máficas e intermedias muestran dos estilos de piroxenos (Figura 7.1b). Los clinopiroxenos tanto de las rocas máficas muestran una composición de auguita ($Wo_{36-39}$ y $En_{44-45}$; Figura 7.1b), mientras que los ortopiroxenos correspondientes muestran composiciones de enstatita ($En_{76-79}$ y $Wo_{3-5;}$ Figura 7.1b). El rango composicional de las rocas intermedias ($En_{44-51}$ y $Wo_{35-39}$) marca una similitud a las rocas máficas, lo cual indican que cristalizaron en equilibrio.

## 7.2 Geotermometría

El cálculo de temperaturas en equilibrio tanto de las rocas ácidas y básicas del Campo Volcánico de la Sierra de San Miguelito fue desarrollado siguiendo las ecuaciones de termómetros propuestas por Putirka (2008) tanto para plagioclasa-feldespatos alcalinos-líquido, termómetros de ortopiroxeno y clinopiroxeno. La ecuación correspondiente de cada uno de estos se reportan en la sección de Anexos en la Tabla A9.

Sin embargo, se debe de prestar atención en el uso de estas ecuaciones empíricas que no llegan a presentar incertidumbres en los coeficientes de los términos, la evaluación de estas se dispone a tratar en futuras investigaciones.

Las temperaturas de equilibrio en ortopiroxenos en las unidad intermedia de La Placa presenta valores promedio de 967° a 905°C (total de análisis puntuales de 10), en contrario, las rocas básicas (unidad Cabras) las cuales muestran un valor promedio de 1241°C (total de análisis puntuales de 7). De igual forma, estas temperaturas fueron calculadas siguiendo un valor de presión experimental de 1GPa.

Dentro del diagrama de Rhodes (Figura 7.2a), se observa que los valores de ortopiroxenos de las rocas intermedias muestran una tendencia hacia una remoción de ortopiroxeno lo cual puede marcar una fraccionación dentro de la evolución del magma lo cual es coherente con los modelos de asimilación y cristalización fracciona plantados previamente. Por el contrario, la unidad básica del CVSSM (Figura 7.2a) muestra una tendencia hacia una diferenciación, lo cual remarca que el proceso principal de generación de las rocas básicas dentro del complejo es un proceso de fusión parcial.

Las rocas intermedias muestran temperaturas de clinopiroxeno de 973-1014°C, a partir de presiones experimentales de 1GPa (total de análisis puntuales de 9), por otro lado, las rocas básicas muestran un valor de 1392°C (total de análisis puntuales de 6). Este último valor de temperatura fue calculado siguiendo un valor de presión experimental de 1GPa.

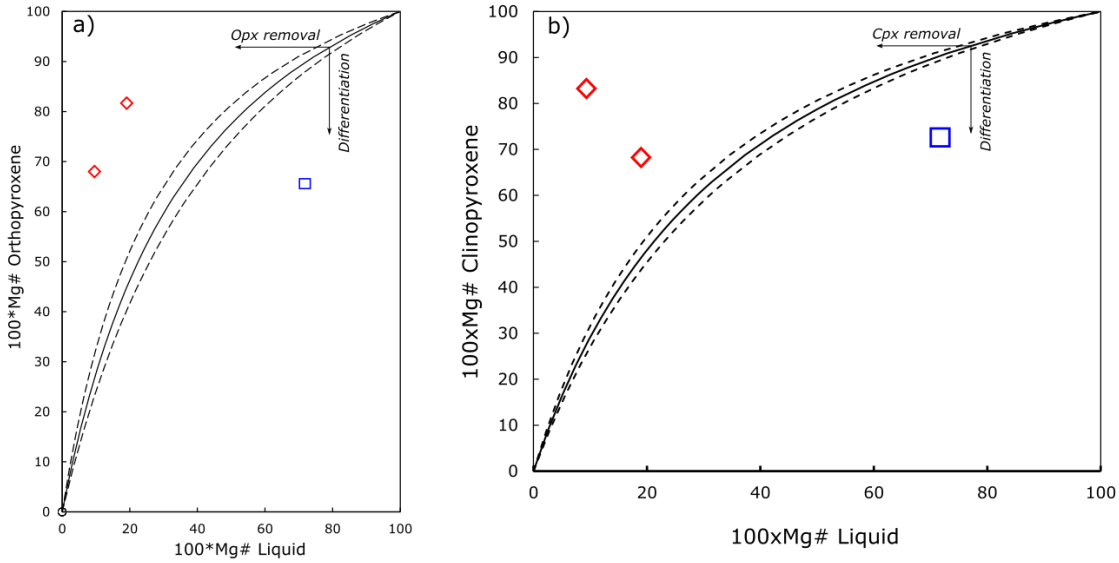


Figura 7.2 a) Diagrama de Rhodes para ortopiroxenos de las rocas intermedias y básicas del Complejo de la Sierra de San Miguelito; b) Diagrama de Rhodes para clinopiroxenos de las rocas intermedias y básicas del Complejo de la Sierra de San Miguelito. Valores promedios de las rocas intermedias (rombo color rojo) y básicas (cuadrado en color azul).

El diagrama de Rhodes (Figura 7.2b) para los clinopiroxenos muestra que las rocas intermedias tienden en una dirección de remoción de clinopiroxeno lo cual, igual que con los ortopiroxenos, demuestran una fraccionación dentro de la evolución del magma, como lo indica el modelo de asimilación y cristalización fraccionada. En contraste a esto, la unidad de composición básica (Figura 7.2b) muestra una tendencia hacia una diferenciación, lo cual confirma que el proceso principal de generación en este estilo de rocas fue un proceso de fusión parcial.

Por otro lado, los valores de temperatura de equilibrio en feldespatos alcalinos de las unidades félsicas muestran un rango promedio de 854° a 880°C, estas temperaturas fueron calculadas siguiendo un valor de presión experimental de 1 GPa, a partir de un total de 12 análisis puntuales en el centro y borde del cristal.

## Referencias

Johnson W.M., Maxwell J.A., 1981. Rock and Mineral Analysis. Wiley, New York.

Putirka K.D., 2008. Thermometers and barometers for volcanic systems. Reviews in Mineralogy and Geochemistry 69, 61-120.

# CAPITULO 8.-

## CONCLUSIONES

La elaboración del presente trabajo aporta nueva información petrogenética para la comprensión de la evolución de las rocas magmáticas, como también limita los distintos episodios magmáticos dentro de la región. Las principales limitaciones en este trabajo se presentan en la corta extensión de los afloramientos de las rocas de composiciones básicas e intermedias, como también la accesibilidad de ciertas regiones del área de estudio.

A pesar de las limitaciones el presente trabajo demuestra que el CVSSM no presenta un comportamiento bimodal, si no que exhibe un rango composicional amplio que incluye rocas de composición básicas, intermedias y ácidas; como también, un contraste en modelos petrogenéticos propuestos por trabajos previas. En estos trabajos previos se proponía que las rocas félsicas fueron desarrolladas por procesos de fusión parcial de la corteza continental inferior, sin embargo, en este trabajo se reporta que las rocas félsicas se originaron a partir de la fusión parcial en niveles medio-superior de la corteza continental; como también, no se había propuesto modelos cuantitativos que ayuden a comprender los procesos magmáticos que generaron el magmatismo básico e intermedio. De igual forma la información generada en el presente trabajo apoyan las cuatro hipótesis enlistadas en la sección 1.2.

Los resultados se simplifican en:

1. El CVSSM se constituye por rocas de composición amplia. Entre las rocas básicas se encuentran rocas de composición traquibasáltica, basáltica y foidítica, a su vez, las rocas intermedias presentan composiciones traquiandesítica basáltica, andesita basáltica y andesítica. Por último las rocas ácidas del CVSSM muestran composiciones riolíticas y traquíticas.

2. Los tres tipos de rocas presentes en el CVSSM muestran texturas porfiríticas, como a su vez, se muestran texturas de desequilibrio en las rocas básicas e intermedias. El ensamble mineralógico principal de las rocas básicas del CVSSM se caracteriza por fenocristales de plagioclasa, olivino, clinopiroxeno y ortopiroxeno, por otra parte, las rocas intermedias presentan fenocristales similares con la excepción de la abundancia de ellos. De igual forma, los fenocristales principales de las rocas ácidas del CVSSM son feldespatos alcalinos (sanidino), plagioclasas, piroxenos (ortopiroxenos y clinopiroxenos).
3. La información geocronológica muestra que el vulcanismo del CVSSM inició hace 34 Ma hasta los 21 Ma. Los magmas del CVSSM se formarón a través de tres episodios, un primer episodio caracterizado por estructuras de domos y de piroclásticos de composiciones riolíticas; la segunda fase de vulcanismo es representada por rocas intermedias intercaladas con rocas piroclásticas de composición riolítica; y por último la tercera fase consiste en lavas de composición máfica aisladas.
4. Las características geoquímicas de las rocas máficas del CVSSM muestran un enriquecimiento en tierras raras ligeras, como también, un enriquecimiento en elementos traza menos incompables, junto con valores positivos de $\varepsilon_{Nd(t)}$ (+5.2 - +0.9), lo cual marca una fuente del manto. A su vez, las rocas intermedias del CVSSM muestran patrones de tierras raras y traza similares a las rocas básicas, con la diferencia de pequeñas anomalías negativas de Eu, como también, estas rocas muestran valores negativos de $\varepsilon_{Nd(t)}$ (-2.5 a -1.8), lo cual indica una contribución de la corteza en la evolución de este estilo de rocas. Por último, las rocas félsicas muestran patrones de enriquecimiento en tierras raras ligeras con pronunciadas anomalías negativas de Eu, lo que marca un fraccionamiento de feldespatos, de igual forma, las composiciones isotópicas de las rocas félsicas muestran valores negativos de $\varepsilon_{Nd(t)}$ (-2.6 a -0.2), lo que nos indica una contribución de la corteza en la generación evolutiva de este estilo de rocas.

5. La modelación de procesos magmáticos de las rocas del CVSSM revelan que las rocas máficas evolucionaron por la fusión parcial de una fuente de manto litosférico, principalmente de fuentes lherzolíticas a nivels de fusión (~15-20%) aproximadamente a los 22–21 Ma, mientras que las rocas intermedias se generaron por fraccionamiento de una líquido parental máfico el cual presentó distintos niveles de asimilación ($r$ > 0.3) con una corteza compuesta por metasedimentos en un periodo de 32–28Ma. Por último, los modelos revelan que las rocas félsicas se generaron a partir de un proceso de fusión parcial de metasedimentos a niveles de corteza media y superior en un periodo de tiempo que abarca de los 34 a 32Ma.
6. Las rocas magmáticas del CVSSM se indican que fueron generadas a partir de un ambiente tectónico intra-placa durante el Eoceno hasta el Mioceno, lo cual puede ser correlacionado con las anomalías de Nb y Ta. Esto puede ser relacionado al régimen extensional de la provincia del Basin and Range.

### 8.1 Recomendaciones y futuros trabajos

El presente trabajo marca una iniciativa para futuros trabajos dentro del Complejo Volcánico de la Sierra de San Miguelito. A partir de los resultados obtenidos en el presente trabajo, se recomienda que para próximas investigaciones se marquen un enfoque en el estudio a profundidad de las rocas máficas de la región, ya que la comprensión de estas rocas junto con información de la corteza subyacente en el área, brindará modelos petrogenéticos y tectónicos integrales.

De igual forma, la aplicación de modelos cuantitativos de inversión en rocas máficas del complejo, permitirán evaluar los procesos de fusión parcial que dieron origen a estos estilos de magmas. Es importante señalar que modelos más confiables pueden ser preparados si se cuenta con una base más amplia de coeficientes de partición y un mayor número de datos analíticos confiables de elementos traza. Estos modelos podrías ser de alta confiabilidad, y representativos, si se cuantifica los coeficientes de partición en las rocas magmáticas del complejo por medio de mediciones directas, por ejemplo, por el método de *Laser Ablation* ICP-MS.

# ANEXOS

## A.1 Análisis Petrográfico

Se elaboraron 20 láminas delgadas para efectuar el análisis petrográfico. La preparación de las mismas se llevó a cabo en el Laboratorio de Preparación de la Facultad de Ciencias de la Tierra, UANL.

El procedimiento que se llevó a cabo para la elaboración de las secciones delgadas es el siguiente:

a) **Corte:** el fragmento de la roca fue cortada con una sierra de disco diamantado (Fig. A1a) para obtener cubos de una medida de 4x2x3 cm.
b) **Pulido:** se seleccionó una de las caras del cubo para ser pulido utilizando un disco metálico (Fig. A1b), al cual se le agrega agua y polvo abrasivo de SiC (Carburo de Silicio) de una granulometría de 200 µm, hasta obtener una superficie plana. La superficie obtenida fue pulida en una placa de vidrio, utilizando agua y polvos abrasivos de distinta granulometría (400, 600, 800 µm).
c) **Pegado:** la superficie pulida se pegó sobre un portaobjetos de vidrio con un agente cementante incoloro e isótropo (mezcla de resina epóxica KÖRAPOX 439; mezcla de resina cristalizados en relación 2:1).
d) **Corte final:** una vez pegado el cubo de roca en el portaobjetos se cortó con un disco de diamante más fino hasta obtener un espesor de ~1 mm.
e) **Pulido final:** la sección obtenida se sometió a un pulido (Fig. Ac, d) como el anteriormente mencionado hasta obtener un espesor aproximado de 25-30 µm. El proceso fue controlado principalmente siguiendo los colores de interferencia de la tabla de Michel Levy para los minerales base presentes (p ej. plagioclasas, cuarzo).

La mineralogía se determinó en base a las características reportadas en literatura especializada (Heinrich, 1970; Philpotts, 1989; McKenzie et al., 1996; Vernon, 2004; Higgins, 2006). De igual forma, las composiciones modales fueron determinadas por conteo en láminas delgadas usando un microscopio petrográfico Leica y un contador semi-Automático PELCON, esto fue determinado en el Instituto Potosino de Investigación Científica y Tecnológica, San Luis Potosí (IPICYT).

**Figura A.1 a)** Cortadora con disco de diamante; **b)** Discos metálicos giratorios para pulido de muestras; **c)** Vidrios para pulido ; **d)** Láminas delgadas terminadas.

## A.2 Separación de minerales

La separación de minerales se llevó a cabo a partir de la trituración de 12 rocas a partir de un triturador de quijada ASC (Fig. A2a), obteniendo fragmentos de aproximadamente de 3-4 mm, los cuales pasaron por tres distintas cribas de 500, 1000, 2000 µm respectivamente (Fig. A2b). Una vez separada la granulometría deseada se pasa a secar la muestra húmeda con una lámpara de luz roja (Fig. A2c, d) por aproximadamente 30 minutos.

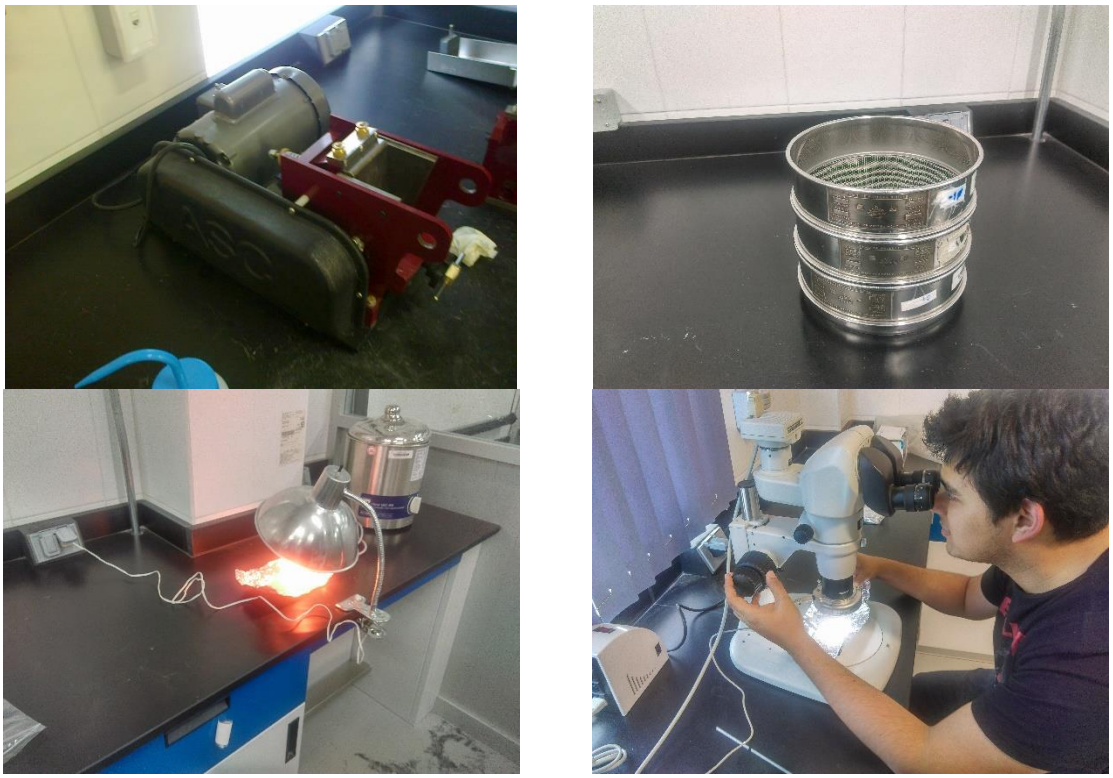

**Figura A2.- a)** Trituradora de quijada ASC. ; **b)** Cribas de 500, 1000, 2000 µm de espesor; **c)** Muestra cribada bajo lámpara con luz roja para un secado; **d)** Triturado y cribado terminado para separado manual.

Al finalizar el secado, se separaron cristales de sanidino de aproximadamente de 1-3 mm de longitud para las rocas félsicas y fragmentos de roca de ~ 1-4 mm de longitud para las rocas máficas con ayuda de un microscopio estereoscópico Nikon. Los fragmentos y minerales separados fueron seleccionados considerando la menor cantidad de imperfecciones en los cristales y fragmentos, como a su vez, se recolectaron la mayor cantidad de minerales sin estar rotos.

### A.3 Trituración y molienda

Las muestras recolectadas pasaron por un procesamiento de molienda, el cual tiene el fin de realizar el análisis geoquímico de elementos mayores, tierras raras, traza e isótopos

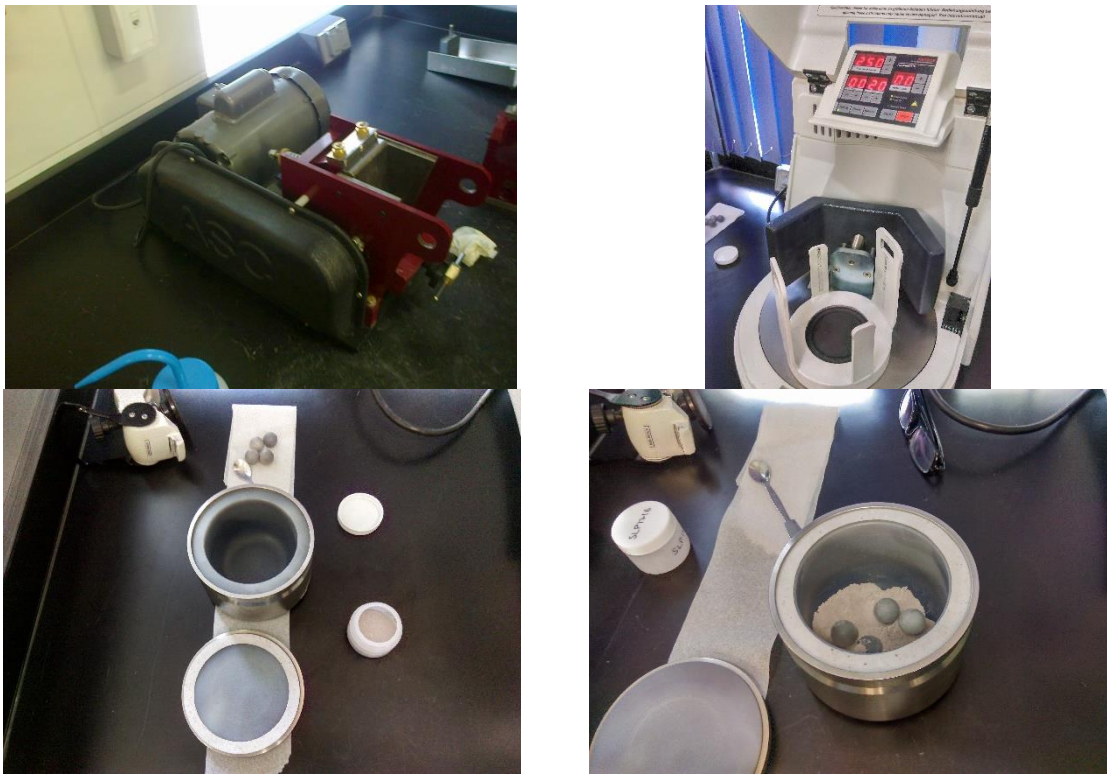

**Figura A3.- a)** Trituradora de quijada ASC; **b) y c)** Molino de ágata PLANETARY MONO MILL PULVERISETTE, FRITSCH; **d)** Polvo de roca terminado.

En este proceso se retiró la capa superficial a cada roca, a fin de contar con una muestra con la menor cantidad de alteración posible, considerando una cantidad aproximada de 500 g.

La roca una vez libre de alteración, se procesó en una triturada de quijada ASC (Fig. A3a), para así reducir los fragmentos a un tamaño aproximado de 0.3-0.5 cm, los cuales se pasaron a pulverizar utilizando un molino de ágata PLANETARY MONO MILL PULVERISETTE, FRITSCH (Fig. A3b, c), generando polvo de roca con un tamaño de partícula aproximado de 75-38 µm.

## A.4 Análisis químico de elementos mayores, tierras raras y traza

Los análisis de elementos mayores, tierras raras y traza se dividieron en dos partes. La primera parte consistió en el análisis de 23 muestras, las cuales se prepararon siguiendo la metodología previamente mencionada. Los elementos mayores fueron determinados por fluorescencia de rayos-X de longitud de onda dispersiva (WD-XRF) Rigaku ZSX Primus II en el Instituto Potosino de Investigación Científica y

Tecnológica (IPICYT), San Luis Potosí. Los procedimientos analíticos, exactitud y precisión son dados por Verma et al. (2018). Las concentraciones de elementos traza y tierras raras fueron determinados en los laboratorios ALS Chemex, Canadá usando el método *ME-MS81,* para más información de este método se puede consultar en www.alsglobal.com/geochemistry. Las concentraciones de elementos traza y tierras raras se obtuvieron por Espectrometría de Masas con Plasma Acoplado Inductivamente, con una precisión analítica basa en materiales de referencia geoquímica SY-2 Y OREAS146.

En la segunda parte de análisis, se seleccionaron 15 muestras, las cuales fueron trituradas siguiendo la metodología previamente descrita. Los análisis de esta segunda parte fueron analizados en la Universidad de Leicester, Inglaterra. Los elementos mayores fueron determinados en perlas de fusión preparadas a partir de polvos pre-calentadas las cuales fueron fundidas con metaborato de litio (80% de metaborato de Li y 20% de tetraborato de Li) en una relación de 1:5. Los elementos traza fueron determinados a partir de pellets de polvo prensados elaboradas con una mezcla de 7g de muestra y una solución de 7% PVA (Alcohol Polivinilo). Los análisis se llevaron a cabo en la Universidad de Leicester, Inglaterra usando una fluorescencia de rayos-X PANalytical Arios. Los estándares internos utilizados fueron BH-1, WS-1, BCS375, BCS 376, MRG-1 y NIM-D los cuales a su vez fueron analizados para el monitoreo de la precisión y exactitud de los resultados. La precisión analítica y exactitud fue considerada entre 2-5% para los elementos mayores y <2% para elementos traza. Las concentraciones de tierras raras fueron determinadas de igual forma en la Universidad de Leicester, Inglaterra por un espectrómetro de masas ICP quadruple Thermo Scientific ICAP-Qc. Las muestras fueron preparadas usando una digestión estándar de HF-$HNO_3$. Siete materiales de referencia (BHVO-1, NIM-G, MRG-1, JSd-1, JSd-2, JSD-3, y JR-1) fueron usados para la calibración y control de calidad del análisis

### A.5 Análisis de datación $^{39}Ar/^{40}Ar$

La irradiación de 12 muestras fue llevada a cabo en el reactor Nuclear McMaster (Universidad de Canadá) por cerca de 101 horas. Se utilizó blindaje de

cadmio y las muestras se mantuvieron en la posición 8D. El flujo de neutrones fue monitoreado usando el estándar de mineral biotita GA1550 (99.738 ± 0.104 Ma; Renne et al., 2011).

Los análisis se llevaron a cabo en el laboratorio de Ar/Ar de la Open University, Milton Keynes, Inglaterra. Los estándares fueron empaquetados para irradiación a cada lado de las muestras y analizados utilizando el método de fusión de grano único, con una fibra de laser CSI de 1059 nm y un espectrómetro de masas MAP215-50. Los valores J fueron calculados por extrapolación linear entre dos valores J medidos y un error de 0.5%.

Las muestras irradiadas fueron cargadas en un sistema de vacío y una fibra de laser CSI de 1059 nm fue enfocado dentro de la cámara de muestras y fue usado para el calentamiento escalonado por muestra. Los sistemas de blancos fueron medidos antes y después de cada dos análisis de muestra. La limpieza y entrada de gas es totalmente automatizada con la medición de $^{40}Ar$, $^{39}Ar$, $^{38}Ar$, $^{37}Ar$, y $^{36}Ar$ por cada 10 escaneos.

### A.6 Análisis isotópicos (Sr-Nd-Pb)

Se seleccionaron 12 muestras representativas de las unidades litológicas del Complejo Volcánico de la Sierra de San Miguelito, en las cuales se analizaron las composiciones isotópicas de Sr, Nd y Pb.

Las muestras fueron preparadas y analizadas siguiendo los procedimientos de Kempton (1995) y Royse et al., (1998). Las composiciones isotópicas de Sr, Nd, y Pb fueron analizados como especímenes metálicos en filamentos individual de Ta, filamento doble Re-Ta y filamento individual de Re, respectivamente, usando un espectrómetro de masas multi-colector Finnigan MAT 262 (Fig. A4) en el NERC Laboratorio Isotópico de Geociencias (NIGL), Keyworth, Inglaterra.


**Figura A4.-** Espectrómetro de masas multi-colector Finnigan MAT 262, NERC Laboratorio Isotópico de Geociencias (NIGL), Keyworth, Inglaterra

Las muestras fueron lixiviadas aproximadamente 1 hora en 6M HCl a 50°C antes de la digestión por un procedimiento estándar de HF- $HNO_3$. Blancos para Sr, Nd y Pb fueron menos que 125 pg, 275pg y 325 pg, respectivamente.

Las relaciones de $^{87}Sr/^{86}Sr$ fueron normalizadas durante el tiempo de corrida a $^{87}Sr/^{86}Sr = 0.1194$ y la relación $^{143}Nd/^{144}Nd$ al valor de $^{143}Nd/^{144}Nd = 0.7219$. Los datos de muestra se informan en relación con los valores aceptados de los estándares NBS987 de $^{87}Sr/^{86}Sr = 0.710177$ y 0.512128 de $^{143}Nd/^{144}Nd$ para el estándar La Jolla. Basado en corridas repetidas de NBS981, la reproducibilidad de relaciones de isótopicos de Pb es ~ 0.1%. Las relaciones de Pb fueron corregidas relativamente al estándar promedio de composiciones isotópicas de Pb de Todt et al., (1996). Los valores medidos fuer corregidos en edad a partir de los datos obtenidos por datación de Ar.

## A.7 Análisis químico de minerales

En este estudio se aplicó un método de Microsonda Electrónica (Electron Prove Microanalysis, EMPA), para llevar el análisis cuantitativo de los minerales para la toma de imágenes de retrodispersión de electrones de alta resolución para los minerales analizados.

Los análisis se llevaron a cabo en el Departamento de Geología de la Open University, Milton Keynes, Inglaterra. El equipo utilizado fue una microsonda electrónica Cameca SX100 (Fig. A5) Se seleccionaron 15 muestras del CVSSM, las cuales abarcaron la litología presente en el área, como también el ensamblaje mineralógico que se determinó en el análisis petrográfico.

La medición se llevó a cabo acelerando una corriente de 10 nA con un voltaje de 15 kV. Los tiempos de conteo de los picos fueron de 10 a 40s y para la corrección de matriz se utilizó una rutina de PhiRhoZ. Los siguientes elementos fueron medidos utilizando una espectroscopia de longitud de onda dispersiva: K, Al, Si, Fe, Mn, Ca, P, Ti, Na and Mg. La microsonda fue calibrada usando los estándares minerales naturas de: Feldespato (K,Al,Si), hematita (Fe), bustamita (Mn, Ca), apatito (P), rutilo (Ti), jadeíta (Na) y fosterita (Mg). Los límites de detección de la microsonda electrónica Cameca SX100 dependen del elemento y de la matriz de la muestra analizada, en donde puede variar desde algunas decenas hasta algunas centenas de ppm (típicamente en orden de 0.02%).

**Figura A5.-** Microsonda electrónica Cameca SX100, Open University, Milton Keynes, Inglaterra

## Referencias


Heinrich, E.W.N., 1970; Identificación microscópica de los minerales; URMO, Bilbao España, 456 pp.

Higgins, M. D. (2006). Quantitative textural measurements in igneous and metamorphic petrology. Cambridge university press.Johnson y Maxwell.

Kempton, P.D., Downes, H., Sharkov, E.V., Vetrin, V.R., Ionov, D.A., Carswell, D.A. and Beard, A., 1995. Petrology and geochemistry of xenoliths from the Northern Baltic shield: evidence for partial melting and metasomatism in the lower crust beneath an Archaean terrane. Lithos 36, pp.157-184.

McKenzie, W. S., Donaldson, C. H., & Guilford, C. (1982). Atlas of igneous rocks and their textures (Vol. 12). London: Longman.

Renne, P.R., Blaco, G., Ludwig, K.R., Mundil, R., Min, K. 2011, Response to the comment by W.H. Schwarz et al. on “Joint determination of 40K decay constants and 40Ar*/40K for the Fish Canyon sanidine standard, and improved accuracy for 40Ar/39Ar geochronology” by P.R. Renne et al. (2010). Geochimica et Coschimica Acta 75, 5097–5100.

Royse, K.R., Kempton, P.D., Darbyshire, D.P.F., 1998. Procedure for the analysis of rubidium–strontium and samarium–neodymium isotopes at the NERC Isotope Geosciences Laboratory. NIGL Report Series, 121, p.28

Todt, W., Cliff, R.A., Hanser, A., Hofmann, A.W., 1996. Evaluation of a 202Pb–205Pb double spike for high-precision lead isotope analysis. Earth Processes: Reading the Isotopic Code, pp. 429-437.

Verma, S.P., Verma, S.K., Rivera-Gómez, M.A., Torres-Sánchez, D., Díaz-González, L., Amezcua-Valdez, A., Rivera-Escoto, B.A., Rosales-Rivera, M., Armstrong-Altrin, J.S., López-Loera, H., Velasco-Tapia, F., Pandarinath, K., 2018. Statistically coherent calibration of X-ray fluorescence spectrometry for major elements in rocks and minerals. Journal of Spectroscopy, 1–13.

Vernon, R. H. (2004). A practical guide to rock microstructure. Cambridge university press.

**Tabla A.1.-** Información petrográfica de las rocas volcánicas del Complejo Volcánico de la Sierra de San Miguelito.

| Muestra | Unidad | Lat (N)° | Long(W)° | Textura | Fenocristales | | | | | | | Matriz | Tipo de desequilibrio | |
|---|---|---|---|---|---|---|---|---|---|---|---|---|---|---|
| | | | | | Ol | Plg | Opx | Cpx | Qz | FldK | Op | | Qz+R | Pl-N-S |
| SLP-01 | Cabras | 21°55'17" | 101°11'50" | P | 4 | 10 | 4 | 6 | | | 26 | 50 | * | * |
| SLP1713 | Cabras | 21°55'17" | 101°10'50" | P | 5 | 10 | 3 | 8 | | | 24 | 50 | * | * |
| SLP1724 | Cantera | 22°05'26" | 101°06'34" | P | | | 3 | 6 | 24 | 20 | 6 | 41 | | |
| SLP1724 | Cantera | 22°05'26" | 101°06'34" | P | | | 3 | 6 | 24 | 20 | 6 | 41 | | |
| SLP-07 | El Zapote | 22°04'12" | 101°04'45" | P | | 44 | 4 | 4 | 26 | 15 | | 7 | | |
| SLP1728 | El Zapote | 22°05'14" | 101°05'45" | P | | 42 | 6 | 3 | 26 | 15 | | 8 | | |
| SLP-02 | La Placa | 21°46'45" | 101°03'11" | P | 6 | 68 | | 20 | | | 5 | 1 | | |
| SLP-03 | La Placa | 21°49'47" | 101°04'42" | P | 3 | 19 | 7 | 3 | | | 1 | 67 | * | * |
| SLP1714 | La Placa | 21°46'46" | 101°02'11" | P | 8 | 64 | 1 | 20 | | | 6 | 1 | | |
| SLP1720 | La Placa | 21°49'48" | 101°05'43" | P | 3 | 18 | 6 | 4 | | | 2 | 67 | * | * |
| SLP1715 | Panalillo | 21°46'47" | 101°02'13" | P | 2 | 10 | 18 | 35 | 15 | 15 | 1 | 4 | | |
| SLP-04 | Panalillo | 21°48'45" | 101°04'11" | P | 2 | 2 | 9 | 11 | 32 | 14 | 4 | 26 | | |
| SLP1719 | Panalillo | 21°49'02" | 101°06'08" | P | | | 4 | | 16 | 22 | 9 | 49 | | |
| SLP1723 | Panalillo | 22°06'06" | 101°06'35" | P | | 43 | 1 | | 38 | 15 | | 3 | | |
| SLP1715 | Panalillo | 21°46'47" | 101°02'13" | P | 2 | 10 | 18 | 35 | 15 | 15 | 1 | 4 | | |
| SLP1716 | Panalillo | 21°48'46" | 101°05'11" | P | | 2 | 10 | 12 | 32 | 14 | 4 | 26 | | |
| SLP1719 | Panalillo | 21°49'02" | 101°06'08" | P | | | 4 | | 16 | 22 | 9 | 49 | | |
| SLP1723 | Panalillo | 22°06'06" | 101°06'35" | P | | 43 | 1 | | 38 | 15 | | 3 | | |
| SLP-05 | San José | 22°01'20" | 101°04'44" | P | | | 4 | 2 | 16 | 21 | 5 | 52 | | |
| SLP1729 | San José | 22°01'23" | 101°05'44' | P | | | 6 | 3 | 16 | 20 | 5 | 50 | | |
| SLP-06 | San Miguelito | 22°05'23" | 101°13'06" | P | | | 3 | 1 | 41 | 15 | 30 | 10 | | |
| SLP1712 | San Miguelito | 22°00'03" | 101°10'51" | P | | 3 | 1 | | 46 | 10 | 36 | 4 | | |
| SLP1711 | San Miguelito | 22°06'23" | 101°14'06" | P | | | 5 | | 40 | 15 | 30 | 10 | | |

Datos modales están representados en porcentaje. Textura: P= porfirítica. Ol: olivino; Plg: plagioclasas; Opx: ortopiroxeno; Cpx: clinopiroxeno; Qz: cuarzo; FldK: feldespato potásico; Op: minerales opacos. Tipo de desequilibrio: Qz+R = cuarzo con aros de reacción, Pl-N-S = plagioclasas con textura normal y de criba.

**Tabla A.2.-** Composición de elementos mayores de las rocas volcánicas del Complejo Volcánico Sierra de San Miguelito. Mediciones elaboradas en el Instituto Potosino de Investigación Científica y Tecnológica, San Luis Potosí.

| **Muestra** | SLP-01 | SLP-02 | SLP1718 | SLP-03 | SLP17-01 | SLP17-02 | SLP17-06 | SLP17-07 |
|---|---|---|---|---|---|---|---|---|
| **Unidad** | Cabras | La Placa | La Placa | La Placa | Panalillo | Panalillo | Cantera | Panalillo |
| **Roca(TAS)** | Foidita, melaefelinita | Foidita, melaefelinita | Traquibasalto Potásico | Basalto alcalino | Riolita | Riolita | Riolita | Riolita |
| **Long. (°W)** | 101°11'50" | 101°03'11" | 101°05'12' | 101°04'42" | 101°06'34" | 101°09'23" | 101°02'11" | 101°05'43" |
| **Lat. (°N)** | 21°55'17" | 21°46'45" | 21°49'47" | 21°49'47" | 22°05'26" | 22°05'09" | 21°46'46" | 21°49'48" |
| ***n*** | 12 | 12 | 12 | 12 | 12 | 12 | 12 | 12 |
| $SiO_2$ | 39.11 ± 1.50 | 37.38 ± 1.44 | 44.76 ± 1.5 | 46.34 ± 1.54 | 71.01 ± 1.94 | 72.73 ± 1.91 | 66.91 ± 168 | 71.6 ± 1.94 |
| $TiO_2$ | 3.9991 ± 0.039 | 1.7453±0.0225 | 1.7345 ± 0.021 | 2.1155 ± 0.0256 | 0.1137 ± 0.011 | 0.196 ± 0.011 | 0.187 ± 0.0113 | 0.1045 ± 0.0112 |
| $Al_2O_3$ | 15.76 ± 0.314 | 18.556 ± 0.305 | 17.139 ± 0.297 | 15.616 ± 0.302 | 11.245 ± 0.304 | 11.388 ± 0.301 | 18.445 ±0.303 | 12.726 ± 0.319 |
| $Fe_2O_3^t$ | 14.898 ± 0.131 | 14.657 ± 0.12 | 10.977 ± 0.105 | 11.721 ± 0.111 | 1.608 ± 0.078 | 1.613 ± 0.078 | 2.385 ± 0.079 | 1.611 ± 0.079 |
| MnO | 0.38551 ± 0.003 | 0.34943 ± 0.003 | 0.34366 ± 0.003 | 0.34362 ± 0.003 | 0.01435 ± 0.002 | 0.01786 ± 0.002 | 0.04815 ± 0.00234 | 0.02757 ± 0.0023 |
| MgO | 4.513 ± 0.255 | 6.025 ± 0.251 | 5.177 ± 0.249 | 4.488 ± 0.249 | 0.841 ± 0.263 | 0.845 ± 0.236 | 0.339 ± 0.236 | 0.722 ± 0.236 |
| CaO | 14.355 ± 0.175 | 15.963 ± 0.159 | 12.486 ± 0.143 | 11.74 ± 0.148 | 2.134 ± 0.119 | 2.217 ± 0.119 | 1.035 ± 0.118 | 2.052 ± 0.119 |
| $Na_2O$ | 2.082 ± 0.077 | 2.333 ± 0.073 | 2.642 ± 0.075 | 2.142 ± 0.074 | 0.482 ± 0.069 | 0.613 ± 0.069 | 2.95 ± 0.074 | 0.45 ± 0.069 |
| $K_2O$ | 1.984 ± 0.048 | 1.403 ± 0.045 | 2.406 ± 0.048 | 2.255 ± 0.048 | 5.366 ± 0.065 | 4.012 ± 0.056 | 6.774 ± 0.065 | 4.842 ± 0.061 |
| $P_2O_5$ | 2.4266 ± 0.043 | 0.8962 ± 0.013 | 0.6307 ± 0.010 | 0.7638 ± 0.013 | 0.0442 ± 0.007 | 0.0592 ± 0.007 | 0.1049 ± 0.0068 | 0.0501 ± 0.0067 |
| LOI | 0.496 | 0.692 | 1.703 | 2.481 | 7.146 | 6.31 | 0.824 | 5.818 |
| Sum | 100.005 | 99.999 | 99.998 | 100.005 | 100.004 | 100.001 | 100.002 | 100.003 |
| Q | | | | | 44.63 | 50.71 | 20.74 | 47.33 |
| Or | 11.93 | | 14.59 | 13.81 | 34.19 | 25.34 | 40.43 | 30.42 |
| Ab | 0.44 | | 5.67 | 16.65 | 4.40 | 5.54 | 25.21 | 4.05 |
| An | 28.28 | 36.73 | 28.53 | 27.28 | 11.10 | 11.34 | 4.49 | 10.47 |
| Ne | 9.48 | 10.91 | 9.36 | 1.15 | | | | |
| C | | | | | 0.94 | 2.29 | 4.67 | 3.33 |
| Di-Mg | 11.58 | 2.92 | 15.01 | 11.91 | | | | |
| Di-Fe | 11.76 | 2.78 | 10.28 | 11.22 | | | | |
| Hy-Mg | | | | | 2.26 | 2.25 | 0.85 | 1.91 |
| Hy-Fe | | | | | 1.36 | 1.21 | 1.91 | 1.38 |
| Mt | 3.35 | 3.30 | 3.47 | 2.68 | 0.78 | 0.78 | 1.08 | 0.77 |
| Il | 7.73 | 3.38 | 3.38 | 4.16 | 0.23 | 0.40 | 0.36 | 0.21 |
| Ap | 5.72 | 2.12 | 1.50 | 1.83 | 0.11 | 0.15 | 0.25 | 0.12 |
| Mg# | 41.46 | 49.00 | 54.26 | 47.23 | 60.04 | 60.08 | 28.99 | 56.28 |
| $FeO^t/MgO$ | 2.97 | 2.19 | 1.91 | 2.35 | 1.72 | 1.72 | 6.33 | 2.01 |

**Tabla A.2.-** *(Continuación)*

| **Muestra** | SLP17-08 | SLP17-09 | SLP-04 | SLP17-17 | SLP17-25 | SLP-05 | CR17-04 |
|---|---|---|---|---|---|---|---|
| **Unidad** | Panalillo | Panalillo | Panalillo | Panalillo | Panalillo | San José | San Miguelito |
| **Roca(TAS)** | Riolita | Riolita | Riolita | Riolita | Riolita | Riolita | Riolita |
| **Long. (°W)** | 101°09'24" | 101°09'2" | 101°04'11" | 101°05'11" | 101°05'45' | 101°04'44" | 101°12'33" |
| **Lat. (°N)** | 22°05'10" | 22°05'07" | 21°48'45" | 21°48'46" | 22°05'14" | 22°01'20" | 22°00'48" |
| ***n*** | 12 | 12 | 12 | 12 | 12 | 12 | 12 |
| $SiO_2$ | 70.98 ± 1.76 | 72.69 ± 1.89 | 78.88 ± 2.01 | 69.4 ± 1.81 | 71.98 ± 1.94 | 68.68 ± 1.63 | 74.32 ± 2.16 |
| $TiO_2$ | 0.2157 ± 0.0113 | 0.2019 ± 0.0114 | 0.0796 ± 0.0111 | 0.2344 ± 0.0115 | 0.1484 ± 0.0112 | 0.1627 ± 0.0112 | 0.0595 ± 0.0111 |
| $Al_2O_3$ | 14.692 ± 0.298 | 13.978 ± 0.309 | 10.895 ± 0.295 | 15.567 ± 0.304 | 10.129 ± 0.297 | 16.971 ± 0.291 | 14.004 ± 0.348 |
| $Fe_2O_3^t$ | 2.627 ± 0.079 | 2.401 ± 0.079 | 1.096 ± 0.078 | 2.484 ± 0.079 | 1.619 ± 0.078 | 2.15 ± 0.078 | 1.407 ± 0.079 |
| MnO | 0.02747 ± 0.00233 | 0.03816 ± 0.00235 | 0.03232 ± 0.0023 | 0.11047 ± 0.0023 | 0.0173 ± 0.0023 | 0.04593 ± 0.0023 | 0.01724 ± 0.0023 |
| MgO | 0.076 ± 0.236 | 0.045 ± 0.236 | 0.155 ± 0.236 | 0.737 ± 0.236 | 0.783 ± 0.236 | 0.096 ± 0.236 | 0.019 ± 0.236 |
| CaO | 0.606 ± 0.118 | 0.516 ± 0.118 | 0.924 ± 0.118 | 2.081 ± 0.119 | 2.397 ± 0.119 | 1.075 ± 0.118 | 0.328 ± 0.118 |
| $Na_2O$ | 3.189 ± 0.077 | 2.946 ± 0.079 | 2.416 ± 0.077 | 3.378 ± 0.078 | 0.42 ± 0.069 | 2.822 ± 0.073 | 3.467 ± 0.106 |
| $K_2O$ | 6.61 ± 0.064 | 6.458 ± 0.066 | 4.836 ± 0.058 | 4.948 ± 0.058 | 5.291 ± 0.063 | 6.647 ± 0.061 | 5.554 ± 0.073 |
| $P_2O_5$ | 0.0786 ± 0.0067 | 0.0669 ± 0.0067 | 0.0574 ± 0.0067 | 0.1068 ± 0.0068 | 0.0509 ± 0.0067 | 0.1133 ± 0.0067 | 0.0342 ± 0.0067 |
| LOI | 0.9 | 0.654 | 0.627 | 0.954 | 7.165 | 1.239 | 0.791 |
| Sum | 100.001 | 99.994 | 99.998 | 100.000 | 100.000 | 100.001 | 100.000 |
| Q | 25.30 | 29.25 | 44.17 | 24.92 | 46.25 | 24.25 | 32.01 |
| Or | 39.49 | 38.48 | 28.78 | 29.57 | 33.72 | 39.83 | 33.12 |
| Ab | 27.28 | 25.14 | 20.59 | 28.91 | 3.83 | 24.21 | 29.60 |
| An | 2.52 | 2.14 | 4.24 | 9.74 | 10.92 | 4.66 | 1.42 |
| Ne | | | | | | | |
| C | 1.39 | 1.37 | 0.14 | 1.14 | | 3.50 | 1.79 |
| Di-Mg | | | | | 0.82 | | |
| Di-Fe | | | | | 0.44 | | |
| Hy-Mg | 0.19 | 0.11 | 0.39 | 1.86 | 1.72 | 0.24 | 0.05 |
| Hy-Fe | 2.04 | 1.87 | 0.90 | 2.03 | 1.08 | 1.74 | 1.19 |
| Mt | 1.19 | 1.09 | 0.50 | 1.13 | 0.79 | 0.98 | 0.64 |
| Il | 0.41 | 0.39 | 0.15 | 0.45 | 0.30 | 0.31 | 0.11 |
| Ap | 0.18 | 0.16 | 0.13 | 0.25 | 0.13 | 0.27 | 0.08 |
| Mg# | 7.67 | 5.11 | 28.89 | 46.01 | 58.14 | 11.37 | 3.73 |
| $FeO^t/MgO$ | 31.10 | 48.01 | 6.36 | 3.03 | 1.86 | 20.15 | 66.63 |

**Tabla A.2.-** *(Continuación)*

| **Muestra** | SLP17-03 | SLP17-04 | SLP17-05 | SLP-06 | SLP-07 | SLP17-30 | SLP17-31 | SM17-03 |
|---|---|---|---|---|---|---|---|---|
| **Unidad** | San Miguelito | San Miguelito | San Miguelito | San Miguelito | El Zapote | Zapote | Zapote | San Miguelito |
| **Roca(TAS)** | Riolita | Riolita | Riolita | Traquidacita | Riolita | Riolita | Riolita | Riolita |
| **Long. (°W)** | 101°07'00" | 101°07'36" | 101°07'31" | 101°13'06" | 101°04'45" | 101°06'43" | 100°58'08" | 101°14'07' |
| **Lat. (°N)** | 22°07'02" | 22°07'04" | 22°07'07" | 22°05'23" | 22°04'12" | 22°00'40" | 22°05'28" | 22°06'23" |
| ***n*** | 12 | 12 | 12 | 12 | 12 | 12 | 12 | 12 |
| $SiO_2$ | 69.43 ± 1.84 | 70.85 ± 1.88 | 68.12 ± 1.64 | 63.75 ± 1.67 | 68.57 ± 1.78 | 72.82 ± 1.96 | 72.36 ± 1.77 | 69.95 ±2.02 |
| $TiO_2$ | 0.1305 ± 0.0112 | 0.1299 ± 0.0112 | 0.1458 ± 0.0112 | 0.1911 ± 0.0113 | 0.1436 ±0.0112 | 0.1302 ± 0.0112 | 0.1352 ± 0.0112 | 0.1334 ± 0.0112 |
| $Al_2O_3$ | 17.153 ± 0.329 | 15.643 ± 0.317 | 16.264 ± 0.289 | 21.064 ± 0.317 | 18.084 ± 0.322 | 15.101 ± 0.326 | 14.863 ± 0.295 | 17.027 ± 0.357 |
| $Fe_2O_3^t$ | 1.668 ± 0.079 | 1.645 ± 0.078 | 2.052 ± 0.079 | 1.919 ± 0.078 | 1.771 ± 0.078 | 1.693 ± 0.079 | 1.627 ± 0.078 | 1.456 ± 0.078 |
| MnO | 0.03938 ± 0.0023 | 0.03955 ± 0.0024 | 0.0575 ± 0.0023 | 0.04941 ± 0.00235 | 0.03128 ± 0.00235 | 0.02178 ± 0.0023 | 0.03287 ± 0.0023 | 0.02497 ± 0.00235 |
| MgO | 0.362 ± 0.236 | 0.258 ± 0.236 | 0.194 ± 0.236 | 0.451 ± 0.236 | 0.136 ± 0.236 | 0.071 ± 0.236 | 0.046 ± 0.236 | 0.313 ± 0.236 |
| CaO | 0.751 ± 0.118 | 0.971 ± 0.118 | 1.828 ± 0.118 | 1.097 ± 0.118 | 0.76 ± 0.118 | 0.692 ± 0.118 | 1.018 ± 0.118 | 0.699 ± 0.118 |
| $Na_2O$ | 2.743 ± 0.079 | 2.393 ± 0.078 | 2.764 ± 0.073 | 3.117 ± 0.075 | 3.229 ± 0.079 | 2.938 ± 0.082 | 3.346 ± 0.081 | 2.745 ± 0.082 |
| $K_2O$ | 6.357 ± 0.069 | 6.519 ± 0.071 | 7.082 ± 0.064 | 7.43 ± 0.067 | 6.165 ± 0.064 | 5.812 ± 0.066 | 5.857 ± 0.068 | 6.547 ±0.073 |
| $P_2O_5$ | 0.0531 ± 0.0067 | 0.0507 ±0.0066 | 0.0952 ± 0.0067 | 0.1104 ± | 0.0669 ± 0.0067 | 0.0608 ± 0.0067 | 0.0748 ± 0.0067 | 0.0664 ± 0.0068 |
| LOI | 1.316 | 1.496 | 1.395 | 0.822 | 1.047 | 0.663 | 0.64 | 1.036 |
| Sum | 100.002 | 99.995 | 99.997 | 100.000 | 100.003 | 100.002 | 99.999 | 99.997 |
| Q | 26.92 | 29.54 | 20.55 | 13.94 | 24.20 | 31.72 | 28.07 | 26.95 |
| Or | 38.11 | 39.16 | 42.51 | 44.33 | 36.86 | 34.62 | 34.88 | 39.14 |
| Ab | 23.55 | 20.58 | 23.75 | 26.63 | 27.64 | 25.06 | 28.53 | 23.49 |
| An | 3.43 | 4.56 | 8.58 | 4.77 | 3.37 | 3.06 | 4.60 | 3.07 |
| Ne | | | | | | | | |
| C | 4.59 | 3.06 | 0.97 | 6.22 | 4.93 | 2.89 | 1.36 | 4.36 |
| Di-Mg | | | | | | | | |
| Di-Fe | | | | | | | | |
| Hy-Mg | 0.91 | 0.65 | 0.49 | 1.13 | 0.34 | 0.18 | 0.12 | 0.79 |
| Hy-Fe | 1.35 | 1.33 | 1.70 | 1.48 | 1.40 | 1.33 | 1.28 | 1.12 |
| Mt | 0.76 | 0.75 | 0.94 | 0.87 | 0.81 | 0.77 | 0.74 | 0.66 |
| Il | 0.25 | 0.25 | 0.28 | 0.37 | 0.28 | 0.25 | 0.26 | 0.26 |
| Ap | 0.12 | 0.12 | 0.22 | 0.26 | 0.16 | 0.14 | 0.17 | 0.16 |
| Mg# | 38.40 | 31.06 | 21.36 | 40.30 | 18.07 | 10.75 | 7.51 | 38.17 |
| $FeO^t/MgO$ | 4.15 | 5.74 | 9.52 | 3.83 | 11.72 | 21.46 | 31.83 | 4.19 |

**Tabla A.3.-** Composiciones de elementos traza y tierras raras de las rocas volcánicas del Complejo Volcánico Sierra de San Miguelito. Muestras analizadas en el laboratorio ALS Chem, Canadá.

| **Muestra** | SLP-01 | SLP-02 | SLP1718 | SLP-03 | SLP17-01 | SLP17-02 | SLP17-06 | SLP17-07 | SLP17-08 | SLP17-09 | SLP-04 | SLP17-17 |
|---|---|---|---|---|---|---|---|---|---|---|---|---|
| **Unidad** | Cabras | La Placa | La Placa | La Placa | Panalillo | Panalillo | Cantera | Panalillo | Panalillo | Panalillo | Panalillo | Panalillo |
| **Roca(TAS)** | Foidita, melaefelinita | Foidita, melaefelinita | Traquibasalto Potásico | Basalto alcalino | Riolita | Riolita | Riolita | Riolita | Riolita | Riolita | Riolita | Riolita |
| **Long. (°W)** | 101°11'50" | 101°03'11" | 101°05'12' | 101°04'42" | 101°06'34" | 101°09'23" | 101°02'11" | 101°05'43" | 101°09'24" | 101°09'2" | 101°04'11" | 101°05'11" |
| **Lat. (°N)** | 21°55'17" | 21°46'45" | 21°49'47" | 21°49'47" | 22°05'26" | 22°05'09" | 21°46'46" | 21°49'48" | 22°05'10" | 22°05'07" | 21°48'45" | 21°48'46" |
| Ba | 376 | 288 | 691 | 966 | 392 | 171 | 219 | 308 | 70 | 54.7 | 28.5 | 389 |
| Co | 43 | 32 | 22 | 27 | 2 | | | | | 1 | | 3 |
| Cr | 240 | 100 | 230 | 240 | | 10 | | | | | | 10 |
| Cs | 0.37 | 1.11 | 6.48 | 1.35 | 14.15 | 13.75 | 13.25 | 25.5 | 5.74 | 6.11 | 13.3 | 10.3 |
| Cu | 35 | 11 | 10 | 10 | 3 | 3 | 2 | 3 | 4 | 2 | 2 | 4 |
| Ga | 25.1 | 21.2 | 19.5 | 20.3 | 19.2 | 17.2 | 21 | 22.3 | 23.8 | 24.8 | 18.5 | 18.4 |
| Hf | 6 | 4.3 | 6.1 | 5.9 | 5 | 5.2 | 6 | 6.1 | 8.7 | 8.6 | 3.8 | 4.9 |
| Nb | 27.1 | 13.6 | 12.4 | 13.6 | 20.4 | 17.9 | 22.8 | 19.6 | 38.4 | 38.6 | 18.2 | 16.5 |
| Ni | 92 | 7 | 26 | 46 | 3 | 2 | 2 | 2 | | | | 2 |
| Pb | 4 | 8 | 11 | 10 | 26 | 19 | 38 | 25 | 35 | 34 | 22 | 26 |
| Rb | 14.2 | 21.7 | 94 | 90.1 | 248 | 203 | 349 | 249 | 271 | 274 | 369 | 282 |
| Sc | 23 | 28 | 21 | 21 | 7 | 6 | 8 | 8 | 2 | 2 | 4 | 5 |
| Sr | 519 | 371 | 435 | 441 | 511 | 221 | 30.2 | 367 | 7.8 | 7.2 | 15.2 | 72.4 |
| Ta | 1.7 | 0.9 | 0.8 | 0.8 | 1.9 | 1.6 | 2 | 2 | 2.6 | 2.7 | 2.1 | 1.8 |
| Th | 2.1 | 2.56 | 7.14 | 6.24 | 19.8 | 20.9 | 29.9 | 30.5 | 27.8 | 27.4 | 35.2 | 23.8 |
| U | 0.84 | 0.66 | 1.36 | 1.34 | 4.84 | 4.08 | 7.68 | 6.63 | 4.83 | 5.66 | 9.01 | 6.94 |
| V | 229 | 161 | 145 | 138 | 11 | 8 | 8 | 5 | 39 | 33 | 41 | 13 |
| Y | 32.8 | 27 | 24.7 | 35.7 | 41.3 | 45.7 | 67 | 64.8 | 47.3 | 55.5 | 75.9 | 55.3 |
| Zn | 125 | 110 | 100 | 104 | 97 | 75 | 70 | 99 | 127 | 106 | 42 | 55 |
| Zr | 277 | 177 | 242 | 254 | 112 | 158 | 181 | 169 | 251 | 249 | 73 | 129 |
| La | 28.8 | 16.5 | 27 | 33.6 | 20.3 | 60.2 | 60.9 | 52.8 | 60.4 | 78.6 | 19.9 | 22.1 |
| Ce | 61.7 | 37 | 59 | 68.8 | 43.1 | 66.1 | 136.5 | 102 | 102.5 | 138 | 50.1 | 51.9 |
| Pr | 8.38 | 4.85 | 7.49 | 8.87 | 6.58 | 15.55 | 17.15 | 16.25 | 15.45 | 19.85 | 7.02 | 6.67 |
| Nd | 37.4 | 22.1 | 32.5 | 37.7 | 27.9 | 58.9 | 66.7 | 63.4 | 55.3 | 74.3 | 29.5 | 26.4 |
| Sm | 8.53 | 5.11 | 6.86 | 8.03 | 8.76 | 14.15 | 16.3 | 14.95 | 10.95 | 14.15 | 9.46 | 7.45 |
| Eu | 2.54 | 1.79 | 1.57 | 1.82 | 0.27 | 0.47 | 0.39 | 0.38 | 0.16 | 0.19 | 0.08 | 0.35 |
| Gd | 7.6 | 5.36 | 5.91 | 7.45 | 8.11 | 10.85 | 13.6 | 13.2 | 8.99 | 10.95 | 10.7 | 7.72 |
| Tb | 1.15 | 0.84 | 0.88 | 0.8 | 1.29 | 1.55 | 2.16 | 2.1 | 1.47 | 1.75 | 1.99 | 1.38 |
| Dy | 6.72 | 5.65 | 5.24 | 6.89 | 7.88 | 8.89 | 12.7 | 12.9 | 9.59 | 10.8 | 13.25 | 9.32 |
| Ho | 1.24 | 1.05 | 0.96 | 1.35 | 1.55 | 1.65 | 2.51 | 2.48 | 1.9 | 2.17 | 2.68 | 1.9 |
| Er | 3.47 | 2.85 | 2.77 | 3.81 | 4.38 | 4.49 | 6.89 | 6.79 | 5.3 | 5.94 | 7.83 | 5.59 |
| Tm | 0.48 | 0.4 | 0.36 | 0.51 | 0.68 | 0.67 | 1.01 | 1.1 | 0.9 | 0.97 | 1.24 | 0.91 |
| Yb | 2.83 | 2.84 | 2.5 | 3.39 | 4.28 | 4.22 | 6.64 | 6.71 | 5.53 | 6.31 | 7.72 | 5.81 |
| Lu | 0.39 | 0.4 | 0.35 | 0.5 | 0.62 | 0.59 | 0.88 | 0.96 | 0.82 | 0.93 | 1.1 | 0.84 |

**Tabla A.3.-** *(Continuación)*

| **Muestra** | SLP17-25 | SLP-05 | CR17-04 | SLP17-03 | SLP17-04 | SLP17-05 | SLP-06 | SLP-07 | SLP17-30 | SLP17-31 | SM17-03 |
|---|---|---|---|---|---|---|---|---|---|---|---|
| **Unidad** | Panalillo | San José | San Miguelito | San Miguelito | San Miguelito | San Miguelito | San Miguelito | El Zapote | Zapote | Zapote | San Miguelito |
| **Roca(TAS)** | Riolita | Riolita | Riolita | Riolita | Riolita | Riolita | Traquidacita | Riolita | Riolita | Riolita | Riolita |
| **Long. (°W)** | 101°05'45' | 101°04'44" | 101°12'33" | 101°07'00" | 101°07'36" | 101°07'31" | 101°13'06" | 101°04'45" | 101°06'43" | 100°58'08" | 101°14'07' |
| **Lat. (°N)** | 22°05'14" | 22°01'20" | 22°00'48" | 22°07'02" | 22°07'04" | 22°07'07" | 22°05'23" | 22°04'12" | 22°00'40" | 22°05'28" | 22°06'23" |
| Ba | 410 | 119.5 | 6.8 | 21.2 | 34.8 | 167.5 | 255 | 62.1 | 107 | 47.8 | 254 |
| Co | 2 | | | 2 | | 1 | | 1 | 1 | | 1 |
| Cr | | 10 | 10 | | | | | | | | |
| Cs | 9.05 | 11.75 | 5.18 | 18.1 | 17.35 | 20.4 | 11.9 | 14.8 | 13.25 | 13.5 | 13.05 |
| Cu | 3 | 2 | 5 | 2 | 2 | 2 | 2 | 3 | 2 | 2 | 2 |
| Ga | 15.9 | 23.1 | 42.8 | 24.6 | 23.2 | 23.1 | 22.2 | 23 | 21.6 | 23.1 | 22.7 |
| Hf | 4.6 | 6 | 8.9 | 4.8 | 4.4 | 4 | 4.8 | 5.8 | 5.6 | 5.4 | 5.6 |
| Nb | 13.3 | 23 | 100.5 | 26.1 | 24.5 | 25.1 | 20.8 | 23.3 | 21.3 | 25.2 | 21.6 |
| Ni | 1 | | 2 | 1 | | | 2 | 1 | 2 | | 2 |
| Pb | 22 | 35 | 62 | 37 | 36 | 33 | 32 | 40 | 33 | 38 | 33 |
| Rb | 183 | 336 | 397 | 407 | 390 | 403 | 319 | 368 | 330 | 369 | 315 |
| Sc | 5 | 7 | | 10 | 10 | 10 | 7 | 8 | 8 | 9 | 8 |
| Sr | 648 | 19.9 | 5.6 | 16 | 158.5 | 117.5 | 32.8 | 14.5 | 18.1 | 12.9 | 30.2 |
| Ta | 1.2 | 2.1 | 9.7 | 2.5 | 2.4 | 2.5 | 1.9 | 2.2 | 2 | 2.4 | 2 |
| Th | 21.9 | 34 | 18.25 | 33.8 | 31.2 | 31 | 25.3 | 29.2 | 26.7 | 37.9 | 30.8 |
| U | 6.15 | 6.31 | 6.65 | 6.78 | 6.58 | 5.74 | 4.23 | 4.48 | 5.33 | 6.22 | 5.17 |
| V | 17 | 26 | | | | | 8 | | 5 | | 8 |
| Y | 37.6 | 69.7 | 16.9 | 68.7 | 56.3 | 57.8 | 39 | 14.4 | 26 | 70.1 | 51.3 |
| Zn | 62 | 64 | 130 | 71 | 96 | 75 | 70 | 76 | 69 | 65 | 68 |
| Zr | 132 | 161 | 135 | 120 | 108 | 92 | 121 | 147 | 144 | 143 | 152 |
| La | 55.9 | 76 | 6.6 | 61.7 | 47.2 | 43.5 | 37.9 | 22 | 44.9 | 73.5 | 54.5 |
| Ce | 88 | 107 | 16.6 | 132 | 113.5 | 107 | 86.5 | 63.4 | 90.5 | 127 | 107 |
| Pr | 14.5 | 20.6 | 1.25 | 17.85 | 13.1 | 12.5 | 10.05 | 3.51 | 13.2 | 20.4 | 16.3 |
| Nd | 53 | 77.4 | 4 | 67.6 | 49.6 | 46.7 | 37.1 | 10.1 | 49.3 | 76.3 | 62.2 |
| Sm | 10.2 | 15.8 | 1.18 | 15.3 | 11.15 | 10.2 | 8.39 | 1.82 | 10.4 | 16.75 | 13.9 |
| Eu | 0.36 | 0.33 | 0.05 | 0.13 | 0.11 | 0.07 | 0.43 | 0.22 | 0.37 | 0.18 | 0.38 |
| Gd | 7.86 | 13.2 | 1.4 | 12.55 | 9.15 | 8.92 | 7.7 | 1.8 | 7.6 | 13.8 | 11.55 |
| Tb | 1.21 | 2.03 | 0.35 | 1.99 | 1.57 | 1.61 | 1.23 | 0.44 | 1.15 | 2.21 | 1.79 |
| Dy | 7.22 | 12.6 | 2.64 | 13.05 | 10.2 | 10.6 | 7.67 | 2.86 | 6.66 | 13.75 | 10.7 |
| Ho | 1.4 | 2.49 | 0.61 | 2.59 | 2.06 | 2.22 | 1.5 | 0.64 | 1.24 | 2.56 | 2 |
| Er | 3.82 | 6.67 | 2.03 | 7.24 | 6.19 | 6.43 | 4.1 | 2.09 | 3.33 | 7.22 | 5.23 |
| Tm | 0.61 | 1.06 | 0.35 | 1.15 | 1 | 1.06 | 0.61 | 0.39 | 0.56 | 1.12 | 0.8 |
| Yb | 3.61 | 6.38 | 2.59 | 7.16 | 6.17 | 6.61 | 3.9 | 2.69 | 3.62 | 6.92 | 4.8 |
| Lu | 0.55 | 0.94 | 0.36 | 1.01 | 0.91 | 0.99 | 0.56 | 0.41 | 0.51 | 1.02 | 0.71 |

**Tabla A.4.-** Composiciones de elementos mayores, traza y tierras raras de las rocas volcánicas del Complejo Volcánico Sierra de San Miguelito. Muestras analizadas en la Universidad de Leicester, Inglaterra.

| **Muestra** | SLP17-11 | SLP17-12 | SLP17-29 | SLP17-28 | SLP17-24 | SLP17-10 | SLP17-14 | SLP17-20 | SMB17-01 | SMB17-02 |
|---|---|---|---|---|---|---|---|---|---|---|
| **Unidad** | San Miguelito | | San José | El Zapote | Cantera | | | La Placa | | |
| **Roca (TAS)** | Riolita | Riolita | Riolita | Riolita | Riolita | Andesita | Basalto | Andesita | Andesita | Andesita |
| **Long. (°W)** | 101°14'06" | 101°10'51" | 101°05'44' | 101°05'45" | 101°06'34" | 101°09'23" | 101°02'11" | 101°05'43" | 101°09'24" | 101°09'2" |
| **Lat. (°N)** | 22°06'23" | 22°00'03" | 22°01'23" | 22°05'14" | 22°05'26" | 22°05'09" | 21°46'46" | 21°49'48" | 22°05'10" | 22°05'07" |
| $SiO_2$ | 77.63 | 76.53 | 79.15 | 77.07 | 78.01 | 62.88 | 51.23 | 56.89 | 61.86 | 61.27 |
| $TiO_2$ | 0.13 | 0.06 | 0.11 | 0.11 | 0.10 | 0.89 | 1.96 | 1.49 | 0.91 | 0.92 |
| $Al_2O_3$ | 12.57 | 13.75 | 11.54 | 12.69 | 12.20 | 16.73 | 16.34 | 15.79 | 15.57 | 16.12 |
| $Fe_2O_3^t$ | 1.39 | 1.34 | 1.25 | 1.24 | 1.28 | 6.55 | 11.80 | 8.23 | 6.78 | 7.02 |
| MnO | 0.02 | 0.02 | 0.01 | 0.01 | 0.01 | 0.11 | 0.17 | 0.14 | 0.11 | 0.12 |
| MgO | 0.18 | 0.07 | 0.04 | 0.07 | 0.17 | 2.84 | 6.23 | 5.65 | 3.25 | 3.07 |
| CaO | 0.45 | 0.29 | 0.37 | 0.37 | 0.38 | 5.46 | 8.84 | 6.94 | 5.56 | 6.18 |
| $Na_2O$ | 2.26 | 3.41 | 2.08 | 2.44 | 1.59 | 2.70 | 2.73 | 2.41 | 2.66 | 2.54 |
| $K_2O$ | 5.43 | 4.57 | 5.12 | 5.44 | 5.38 | 3.15 | 0.94 | 1.71 | 3.11 | 2.89 |
| $P_2O_5$ | 0.02 | 0.01 | 0.02 | 0.01 | 0.01 | 0.22 | 0.28 | 0.39 | 0.23 | 0.23 |
| LOI | 0.63 | 0.76 | 0.96 | 0.89 | 1.23 | 0.53 | 0.31 | 1.19 | 0.60 | 0.76 |
| Sum | 100.70 | 100.81 | 100.65 | 100.35 | 100.37 | 102.07 | 100.84 | 100.83 | 100.65 | 101.12 |
| Q | 42.06 | 38.01 | 46.42 | 41.02 | 47.14 | 17.35 | 1.50 | 12.30 | 16.80 | 16.60 |
| Or | 32.09 | 27.02 | 30.38 | 32.35 | 32.10 | 18.43 | 5.58 | 10.21 | 18.47 | 17.11 |
| Ab | 19.13 | 28.87 | 17.67 | 20.78 | 13.58 | 22.61 | 23.21 | 20.60 | 22.62 | 21.53 |
| An | 2.10 | 1.37 | 1.71 | 1.78 | 1.84 | 23.98 | 29.70 | 27.49 | 21.46 | 24.09 |
| Ne | 2.20 | 2.69 | 1.96 | 2.15 | 3.12 | | | | | |
| C | 1.50 | 1.30 | 1.04 | 1.11 | 1.42 | 12.04 | 22.71 | 18.95 | 12.14 | 11.74 |
| Di-Mg | 0.63 | 0.60 | 0.56 | 0.56 | 0.58 | 2.25 | 2.62 | 2.89 | 2.37 | 2.44 |
| Di-Fe | 0.25 | 0.11 | 0.21 | 0.21 | 0.19 | 1.67 | 3.74 | 2.86 | 1.74 | 1.75 |
| Hy-Mg | 0.05 | 0.02 | 0.05 | 0.02 | 0.02 | 0.50 | 0.65 | 0.91 | 0.54 | 0.53 |
| Hy-Fe | 27.11 | 13.05 | 8.42 | 13.95 | 27.61 | 53.04 | 55.24 | 64.14 | 55.53 | 53.25 |
| Mt | 6.95 | 17.22 | 28.12 | 15.94 | 6.78 | 2.08 | 1.70 | 1.31 | 1.88 | 2.06 |
| Il | 42.06 | 38.01 | 46.42 | 41.02 | 47.14 | 17.35 | 1.50 | 12.30 | 16.80 | 16.60 |
| Ap | 32.09 | 27.02 | 30.38 | 32.35 | 32.10 | 18.43 | 5.58 | 10.21 | 18.47 | 17.11 |
| Mg# | 19.13 | 28.87 | 17.67 | 20.78 | 13.58 | 22.61 | 23.21 | 20.60 | 22.62 | 21.53 |
| $FeO^t/MgO$ | 2.10 | 1.37 | 1.71 | 1.78 | 1.84 | 23.98 | 29.70 | 27.49 | 21.46 | 24.09 |
| Ba | 197.987 | 3.993 | 84.426 | 56.488 | 93.939 | 553.860 | 243.011 | 815.147 | 541.437 | 561.683 |
| Co | 1.174 | 0.681 | 0.745 | 0.879 | 0.684 | 16.790 | 33.135 | 27.095 | 2.581 | 17.910 |
| Cr | 11.381 | 11.365 | 34.817 | 12.732 | 14.384 | 103.450 | 92.022 | 238.981 | 20.717 | 108.275 |
| Cs | 9.426 | 3.656 | 4.574 | 11.994 | 7.751 | 3.245 | 0.950 | 0.945 | 0.583 | 2.853 |
| Cu | 2.102 | 4.915 | 2.438 | 3.041 | 2.502 | 8.883 | 13.950 | 10.996 | 7.900 | 8.300 |
| Ga | 22.550 | 48.024 | 21.436 | 23.497 | 22.506 | 19.931 | 25.484 | 19.267 | 19.600 | 20.900 |
| Hf | 6.364 | 11.285 | 6.022 | 6.772 | 6.043 | 6.308 | 4.290 | 6.412 | 5.817 | 5.578 |
| Nb | 22.111 | 124.387 | 21.488 | 23.509 | 23.281 | 13.252 | 13.638 | 12.944 | 12.872 | 12.091 |
| Ni | 1.355 | 1.576 | 2.337 | 1.025 | 2.036 | 6.921 | 3.483 | 42.683 | 6.800 | 3.500 |
| Pb | 26.661 | 51.671 | 28.743 | 29.351 | 27.019 | 10.886 | 4.164 | 8.495 | 10.723 | 9.958 |
| Rb | 213.350 | 290.797 | 144.259 | 250.091 | 181.507 | 66.264 | 15.721 | 60.949 | 50.935 | 42.022 |

| | | | | | | | | | | |
|---|---|---|---|---|---|---|---|---|---|---|
| Sc | 15.384 | 8.264 | 1.316 | 7.121 | 2.242 | 24.478 | 34.975 | 24.756 | 21.682 | 23.251 |
| Sr | 27.560 | 2.458 | 14.007 | 16.071 | 23.189 | 276.837 | 311.042 | 390.274 | 252.612 | 294.668 |
| Th | 28.959 | 44.084 | 27.782 | 30.295 | 25.802 | 9.562 | 2.751 | 7.037 | 9.073 | 8.010 |
| U | 4.414 | 6.664 | 5.752 | 4.297 | 5.005 | 2.766 | 0.599 | 1.242 | 2.721 | 2.653 |
| V | 7.029 | 2.210 | 16.231 | 1.605 | 2.670 | 91.165 | 140.290 | 116.680 | 105.382 | 99.617 |
| Y | 45.551 | 22.808 | 43.756 | 13.331 | 33.373 | 25.781 | 28.204 | 37.810 | 22.901 | 27.477 |
| Zn | 52.222 | 163.443 | 52.300 | 59.009 | 63.020 | 82.635 | 82.039 | 91.125 | 79.200 | 81.000 |
| Zr | 170.859 | 166.115 | 158.115 | 165.630 | 152.773 | 237.990 | 182.985 | 266.598 | 235.385 | 217.393 |
| La | 40.62 | 6.26 | 50.45 | 19.69 | 22.90 | 24.98 | 16.50 | 33.71 | 21.63 | 22.46 |
| Ce | 96.46 | 11.68 | 80.28 | 58.29 | 58.65 | 56.28 | 36.23 | 68.91 | 46.83 | 46.21 |
| Pr | 11.61 | 1.34 | 15.58 | 3.43 | 7.02 | 7.42 | 4.85 | 9.06 | 6.69 | 6.66 |
| Nd | 48.15 | 5.11 | 67.79 | 11.13 | 30.04 | 32.71 | 23.30 | 41.11 | 5.04 | 30.33 |
| Sm | 10.73 | 1.76 | 14.24 | 2.13 | 6.80 | 7.21 | 5.48 | 8.64 | 1.05 | 6.43 |
| Eu | 0.51 | 0.09 | 0.29 | 0.27 | 0.27 | 1.62 | 1.99 | 2.33 | 0.26 | 1.58 |
| Gd | 10.35 | 2.38 | 12.77 | 2.58 | 7.41 | 7.06 | 5.87 | 8.72 | 6.41 | 6.69 |
| Tb | 1.68 | 0.58 | 2.07 | 0.46 | 1.45 | 1.04 | 0.97 | 1.29 | 0.99 | 1.01 |
| Dy | 9.91 | 4.24 | 12.32 | 3.23 | 9.39 | 6.07 | 5.72 | 7.39 | 5.51 | 6.01 |
| Ho | 1.91 | 0.93 | 2.38 | 0.68 | 1.91 | 1.16 | 1.15 | 1.46 | 1.08 | 1.19 |
| Er | 5.59 | 3.01 | 6.81 | 2.25 | 5.52 | 3.30 | 3.30 | 4.25 | 3.14 | 3.50 |
| Tm | 0.69 | 0.44 | 0.75 | 0.29 | 0.62 | 0.34 | 0.39 | 0.51 | 0.28 | 0.33 |
| Yb | 5.01 | 3.68 | 5.89 | 2.75 | 5.14 | 3.00 | 2.99 | 3.57 | 2.86 | 3.07 |
| Lu | 0.75 | 0.55 | 0.88 | 0.41 | 0.78 | 0.45 | 0.46 | 0.58 | 0.45 | 0.47 |
| TREE | 229.90 | 37.45 | 254.17 | 103.42 | 146.27 | 144.05 | 101.66 | 181.26 | 125.46 | 127.95 |
| $(La/Yb)_{CN}$ | 5.51 | 1.16 | 5.82 | 4.87 | 3.03 | 5.66 | 3.75 | 6.41 | 5.13 | 4.97 |
| $(La/Sm)_{CN}$ | 2.47 | 2.18 | 2.26 | 5.82 | 2.04 | 2.21 | 1.91 | 2.43 | 2.02 | 2.14 |
| $(Gd/Yb)_{CN}$ | 1.67 | 0.52 | 1.75 | 0.76 | 1.17 | 1.90 | 1.59 | 1.97 | 1.81 | 1.76 |
| $(La/Yb)_{PM}$ | 5.52 | 1.16 | 5.83 | 4.88 | 3.03 | 5.67 | 3.76 | 6.42 | 5.14 | 4.98 |
| $(La/Sm)_{PM}$ | 2.48 | 2.19 | 2.27 | 5.84 | 2.04 | 2.22 | 1.92 | 2.43 | 2.02 | 2.15 |
| $(Gd/Yb)_{PM}$ | 1.68 | 0.53 | 1.76 | 0.76 | 1.17 | 1.91 | 1.59 | 1.98 | 1.82 | 1.76 |
| (Eu/Eu*) | 0.15 | 0.13 | 0.07 | 0.36 | 0.11 | 0.70 | 1.09 | 0.82 | 0.12 | 0.73 |
| (Nb/Nb*) | 0.70 | 35.38 | 0.69 | 1.76 | 1.37 | 0.32 | 0.64 | 0.22 | 0.33 | 0.29 |
| (Ti/Ti*) | 0.04 | 0.06 | 0.03 | 0.13 | 0.04 | 0.39 | 1.02 | 0.51 | 0.43 | 0.42 |

**Tabla A.4.-** *(Continuación)*

| **Muestra** | SLP17-15 | SLP17-16 | SLP17-19 | SLP17-23 | SLP17-13 |
|---|---|---|---|---|---|
| **Unidad** | | Panalillo | | | Cabras |
| **Roca (TAS)** | Riolita | Riolita | Riolita | Riolita | Basalto |
| **Long. (°W)** | 101°02'13" | 101°05'11" | 101°06'08" | 101°06'35" | 101°10'50" |
| **Lat. (°N)** | 21°46'47" | 21°48'46" | 21°49'02" | 22°06'06" | 21°55'17" |
| $SiO_2$ | 75.93 | 82.28 | 76.62 | 78.25 | 47.76 |
| $TiO_2$ | 0.20 | 0.06 | 0.24 | 0.15 | 2.83 |
| $Al_2O_3$ | 12.24 | 9.74 | 11.99 | 11.23 | 15.59 |
| $Fe_2O_3^t$ | 2.43 | 0.92 | 2.34 | 1.66 | 13.73 |
| MnO | 0.03 | 0.02 | 0.02 | 0.01 | 0.20 |
| MgO | 0.12 | 0.08 | 0.03 | 0.02 | 5.64 |
| CaO | 1.13 | 0.51 | 0.44 | 0.30 | 8.87 |
| $Na_2O$ | 2.53 | 2.55 | 2.51 | 2.61 | 3.39 |
| $K_2O$ | 5.02 | 3.94 | 5.12 | 5.49 | 1.27 |
| $P_2O_5$ | 0.05 | 0.01 | 0.04 | 0.02 | 0.71 |
| LOI | 0.64 | 0.47 | 0.92 | 0.70 | 0.39 |
| Sum | 100.32 | 100.57 | 100.27 | 100.43 | 100.38 |
| Q | 38.88 | 50.82 | 41.11 | 41.03 | 0.00 |
| Or | 29.81 | 23.27 | 30.50 | 32.57 | 7.59 |
| Ab | 21.51 | 21.57 | 21.41 | 22.17 | 29.03 |
| An | 5.31 | 2.46 | 1.94 | 1.36 | 23.85 |
| Ne | 0.71 | 0.38 | 1.63 | 0.50 | - |
| C | 2.18 | 0.95 | 1.80 | 1.29 | 2.58 |
| Di-Mg | 1.10 | 0.41 | 1.06 | 0.75 | 3.07 |
| Di-Fe | 0.38 | 0.11 | 0.46 | 0.29 | 5.44 |
| Hy-Mg | 0.12 | 0.02 | 0.09 | 0.05 | 1.66 |
| Hy-Fe | 12.42 | 19.98 | 3.55 | 3.34 | 48.99 |
| Mt | 18.22 | 10.35 | 70.19 | 74.68 | 2.19 |
| Il | 38.88 | 50.82 | 41.11 | 41.03 | 0.00 |
| Ap | 29.81 | 23.27 | 30.50 | 32.57 | 7.59 |
| Mg# | 21.51 | 21.57 | 21.41 | 22.17 | 29.03 |
| $FeO^t/MgO$ | 5.31 | 2.46 | 1.94 | 1.36 | 23.85 |
| Ba | 518.985 | 23.390 | 499.326 | 37.639 | 304.315 |
| Co | 2.026 | 0.853 | 1.115 | 0.593 | 43.183 |
| Cr | 18.347 | 14.968 | 11.565 | 12.659 | 234.352 |
| Cs | 8.323 | 9.347 | 1.596 | 1.843 | 0.333 |
| Cu | 3.919 | 1.670 | 4.026 | 2.862 | 36.438 |
| Ga | 18.087 | 19.209 | 24.249 | 23.983 | 26.990 |
| Hf | 6.578 | 4.276 | 11.171 | 9.380 | 6.068 |
| Nb | 15.766 | 19.431 | 34.377 | 40.481 | 25.028 |
| Ni | 1.861 | 3.599 | 0.904 | 1.674 | 83.257 |
| Pb | 22.503 | 16.621 | 21.886 | 26.949 | 3.066 |
| Rb | 157.642 | 237.321 | 85.363 | 121.351 | 10.359 |
| Sc | 13.620 | 4.740 | 0.896 | 1.349 | 26.952 |

| | | | | | |
|---|---|---|---|---|---|
| Sr | 64.817 | 12.268 | 29.233 | 5.279 | 425.171 |
| Th | 23.395 | 36.907 | 17.217 | 25.063 | 2.130 |
| U | 5.197 | 8.373 | 4.350 | 5.222 | 0.740 |
| V | 8.874 | 32.621 | 9.936 | 37.868 | 183.768 |
| Y | 49.555 | 75.276 | 35.823 | 39.647 | 32.536 |
| Zn | 53.115 | 27.636 | 93.980 | 85.772 | 98.530 |
| Zr | 239.542 | 85.699 | 428.562 | 274.831 | 266.834 |
| La | 89.25 | 20.22 | 45.42 | 46.26 | 26.45 |
| Ce | 195.11 | 52.90 | 104.44 | 98.96 | 55.06 |
| Pr | 22.48 | 7.46 | 14.60 | 14.99 | 7.73 |
| Nd | 91.68 | 34.91 | 64.06 | 64.10 | 37.28 |
| Sm | 16.08 | 10.37 | 12.40 | 12.52 | 8.18 |
| Eu | 1.23 | 0.11 | 0.94 | 0.16 | 2.75 |
| Gd | 15.27 | 11.60 | 11.87 | 11.87 | 8.42 |
| Tb | 2.00 | 2.30 | 1.86 | 1.91 | 1.24 |
| Dy | 11.05 | 14.47 | 10.65 | 11.44 | 7.00 |
| Ho | 1.99 | 2.98 | 2.06 | 2.26 | 1.30 |
| Er | 5.57 | 8.94 | 5.95 | 6.63 | 3.47 |
| Tm | 0.60 | 1.08 | 0.63 | 0.69 | 0.38 |
| Yb | 4.63 | 8.56 | 5.35 | 6.17 | 2.79 |
| Lu | 0.70 | 1.24 | 0.82 | 0.92 | 0.45 |
| TREE | 439.75 | 159.82 | 265.58 | 262.77 | 152.84 |
| $(La/Yb)_{CN}$ | 3.59 | 1.21 | 2.24 | 2.29 | 2.05 |
| $(La/Sm)_{CN}$ | 2.67 | 1.10 | 1.79 | 1.56 | 2.44 |
| $(Gd/Yb)_{CN}$ | 13.13 | 1.61 | 5.78 | 5.11 | 6.44 |
| $(La/Yb)_{PM}$ | 3.60 | 1.21 | 2.25 | 2.30 | 2.06 |
| $(La/Sm)_{PM}$ | 2.68 | 1.10 | 1.80 | 1.56 | 2.44 |
| $(Gd/Yb)_{PM}$ | 0.25 | 0.03 | 0.24 | 0.04 | 1.03 |
| (Eu/Eu*) | 0.21 | 1.63 | 0.69 | 1.53 | 0.84 |
| (Nb/Nb*) | 0.04 | 0.01 | 0.06 | 0.04 | 1.07 |
| (Ti/Ti*) | 13.10 | 1.60 | 5.77 | 5.10 | 6.43 |

**Tabla A.5.-** Datos isotópicos de roca total de Sr-Nd de las rocas volcánicas del Complejo Volcánico de la Sierra de San Miguelito.

| Muestra | Unidad | Edad | Rb (ppm) | Sr (ppm) | $^{87}Rb/^{86}Sr$ | $^{87}Sr/^{86}Sr$ | ±2 σ | $^{87}Sr/^{86}Sr_{(i)}$ | Sm (ppm) | Nd (ppm) | $^{147}Sm/^{144}Nd$ | $^{143}Nd/^{144}Nd$ | ±2σ | $^{143}Nd/^{144}Nd_{(i)}$ | $\varepsilon Nd_t$ |
|---|---|---|---|---|---|---|---|---|---|---|---|---|---|---|---|
| SLP17-13 | Cabras | 22.21 | 10.36 | 425.17 | 0.07049 | 0.70346 | 6 | 0.70344 | 8.18 | 37.28 | 0.13271 | 0.51289 | 10 | 0.51287 | +5.2 |
| SLP17-14 | La Placa | 30.13 | 15.72 | 311.04 | 0.14622 | 0.70502 | 6 | 0.70496 | 5.48 | 23.30 | 0.14210 | 0.51266 | 18 | 0.51264 | +0.9 |
| SLP17-10 | La Placa | 32.67 | 66.26 | 276.84 | 0.69248 |  | – | | 7.21 | 32.71 | 0.13330 | 0.51249 | 9 | 0.51246 | -2.5 |
| SLP17-20 | La Placa | 27.5 | 60.95 | 390.27 | 0.45181 | 0.70557 | 6 | 0.70540 | 8.64 | 41.11 | 0.12707 | 0.51252 | 7 | 0.51249 | -2.0 |
| SMB17-01 | La Placa | 30 | 50.94 | 252.61 | 0.58333 | 0.70606 | 7 | 0.70581 | 1.05 | 5.04 | 0.12628 | 0.51249 | 13 | 0.51247 | -2.4 |
| SMB17-02 | La Placa | 30 | 42.02 | 294.67 | 0.41257 | 0.70592 | 20 | 0.70575 | 6.43 | 30.33 | 0.12822 | 0.51252 | 7 | 0.51249 | -1.8 |
| SLP17-11 | San Miguelito | 33.17 | 213.35 | 27.56 | 22.39592 | 0.71995 | 7 | 0.70940 | 10.73 | 48.15 | 0.13474 | 0.51249 | 6 | 0.51246 | -2.5 |
| SLP17-12 | San Miguelito | 33 | 290.80 | 2.46 | 342.26587 | – | – | – | 1.76 | 5.11 | 0.20808 | 0.51262 | 8 | 0.51258 | -0.2 |
| SLP17-15 | Panalillo | 28.65 | 157.64 | 64.82 | 7.03621 | 0.71005 | 6 | 0.70719 | 16.08 | 91.68 | 0.10608 | 0.51248 | 8 | 0.51245 | -2.7 |
| SLP17-16 | Panalillo | 28.65 | 237.32 | 12.27 | 55.96519 | 0.73354 | 7 | 0.71078 | 10.37 | 34.91 | – | – | – | – | – |
| SLP17-19 | Panalillo | 31.05 | 85.36 | 29.23 | 8.44796 | 0.71258 | 8 | 0.70886 | 12.40 | 64.06 | 0.11702 | 0.51254 | 8 | 0.51252 | -1.4 |
| SLP17-23 | Panalillo | 29.4 | 121.35 | 5.28 | 66.50392 | 0.74749 | 11 | 0.71973 | 12.52 | 64.10 | 0.11812 | 0.51254 | 8 | 0.51251 | -1.4 |
| SLP17-24 | Cantera | 32.1 | 181.51 | 23.19 | 22.64472 | 0.72170 | 7 | 0.71138 | 6.80 | 30.04 | 0.13698 | 0.51249 | 8 | 0.51247 | -2.3 |
| SLP17-28 | El Zapote | 33.48 | 250.09 | 16.07 | 45.02054 | 0.73799 | 6 | 0.71659 | 2.13 | 11.13 | 0.11587 | 0.51249 | 8 | 0.51247 | -2.3 |
| SLP17-29 | San José | 33.95 | 144.26 | 14.01 | 29.79568 | – | – | – | 14.24 | 67.79 | 0.12706 | 0.51248 | 9 | 0.51245 | -2.6 |

**Tabla A.6.-**Datos isotópicos de roca total de Pb de las rocas volcánicas del Complejo Volcánico de la Sierra de San Miguelito.

| Muestra | Unidad | Edad | Th (ppm) | U (ppm) | Pb (ppm) | $^{206}Pb/^{204}Pb$ | $^{207}Pb/^{204}Pb$ | $^{208}Pb/^{204}Pb$ | $^{206}Pb/^{204}Pb_{(i)}$ | $^{207}Pb/^{204}Pb_{(i)}$ | $^{208}Pb/^{204}Pb_{(i)}$ |
|---|---|---|---|---|---|---|---|---|---|---|---|
| SLP17-13 | Cabras | 22.21 | 2.13 | 0.74 | 3.066 | 18.928 | 15.614 | 38.571 | 18.925 | 15.329 | 38.571 |
| SLP17-14 | La Placa | 30.13 | 2.751 | 0.599 | 4.164 | 18.965 | 15.665 | 38.909 | 18.962 | 15.303 | 38.909 |
| SLP17-10 | La Placa | 32.67 | 9.562 | 2.766 | 10.886 | 18.939 | 15.667 | 38.902 | 18.934 | 15.149 | 38.902 |
| SLP17-20 | La Placa | 27.5 | 7.037 | 1.242 | 8.495 | 18.894 | 15.664 | 38.864 | 18.891 | 15.248 | 38.864 |
| SMB17-01 | La Placa | 30 | 9.073 | 2.721 | 10.723 | 18.936 | 15.666 | 38.894 | 18.932 | 15.205 | 38.893 |
| SMB17-02 | La Placa | 30 | 8.01 | 2.653 | 9.958 | 18.938 | 15.665 | 38.889 | 18.933 | 15.227 | 38.889 |
| SLP17-11 | San Miguelito | 33.17 | 28.959 | 4.414 | 26.661 | 18.900 | 15.666 | 38.885 | 18.897 | 15.016 | 38.885 |
| SLP17-12 | San Miguelito | 33 | 44.084 | 6.664 | 51.671 | 18.905 | 15.661 | 38.831 | 18.903 | 15.154 | 38.831 |
| SLP17-15 | Panalillo | 28.65 | 23.395 | 5.197 | 22.503 | 18.909 | 15.665 | 38.881 | 18.906 | 15.122 | 38.881 |
| SLP17-16 | Panalillo | (28.65) | 36.907 | 8.373 | 16.621 | 19.013 | 15.680 | 39.016 | 19.005 | 14.521 | 39.016 |
| SLP17-19 | Panalillo | 31.05 | 17.217 | 4.35 | 21.886 | 18.896 | 15.660 | 38.858 | 18.892 | 15.217 | 38.858 |
| SLP17-23 | Panalillo | 29.4 | 25.063 | 5.222 | 26.949 | 18.897 | 15.659 | 38.861 | 18.894 | 15.162 | 38.861 |
| SLP17-24 | Cantera | 32.1 | 25.802 | 5.005 | 27.019 | 18.907 | 15.666 | 38.889 | 18.903 | 15.112 | 38.889 |
| SLP17-28 | El Zapote | 33.48 | 30.295 | 4.297 | 29.351 | 18.892 | 15.668 | 38.876 | 18.889 | 15.045 | 38.876 |
| SLP17-29 | San José | 33.95 | 27.782 | 5.752 | 28.743 | 18.922 | 15.669 | 38.913 | 18.918 | 15.078 | 38.913 |

**Tabla A.7.-** Datos de edades $^{40}Ar/^{39}Ar$ age data para las unidades del Complejo Volcánico de la Sierra de San Miguelito

| Step no | Power (%) | $^{40}Ar$ | $\pm\sigma_{40}$ | $^{39}Ar$ | $\pm\sigma_{39}$ | $^{38}Ar$ | $\pm\sigma_{38}$ | $^{37}Ar$ | $\pm\sigma_{37}$ | $^{36}Ar$ | $\pm\sigma_{36}$ | $^{40}Ar^{*}/^{39}Ar$ | $\pm\sigma$ | Age (Ma) | $\pm\sigma$ (Ma) |
|---|---|---|---|---|---|---|---|---|---|---|---|---|---|---|---|
| ***SLP17-11 (San Miguelito) sanidine, grain size 0.1-0.3 mm, 0.1062mg, J=0.009790695 ± 4.89535E-05*** | | | | | | | | | | | | | | | |
| 1 | 1.2 | 0.08104 | 0.00434 | 0.00483 | 0.00050 | 0.00001 | 0.00025 | -0.00151 | 0.00403 | 0.00015 | 0.00021 | 7.27882 | 13.16002 | 124.00983 | 216.67689 |
| 2 | 1.5 | 0.22769 | 0.00471 | 0.04797 | 0.00056 | 0.00137 | 0.00025 | 0.01221 | 0.00404 | 0.00097 | 0.00021 | -1.29137 | -1.33035 | -22.92000 | 23.76272 |
| 3 | 2.0 | 0.68898 | 0.00690 | 0.26534 | 0.00390 | 0.00743 | 0.00028 | 0.05568 | 0.00404 | 0.00218 | 0.00022 | 0.14526 | 0.24824 | 2.55999 | 4.37181 |
| 4 | 2.6 | 0.21664 | 0.00457 | 0.09143 | 0.00072 | 0.00150 | 0.00026 | 0.00931 | 0.00404 | 0.00051 | 0.00021 | 0.70128 | 0.69783 | 12.32573 | 12.22357 |
| 5 | 3.4 | 1.09766 | 0.00897 | 0.51532 | 0.00399 | 0.01106 | 0.00035 | 0.06600 | 0.00404 | 0.00201 | 0.00021 | 0.96793 | 0.12588 | 16.99040 | 2.20081 |
| 6 | 4.2 | 0.87296 | 0.01186 | 0.42920 | 0.00239 | 0.00755 | 0.00028 | 0.04290 | 0.00405 | 0.00183 | 0.00021 | 0.75956 | 0.15008 | 13.34636 | 2.62822 |
| 7 | 5.2 | 2.53212 | 0.00988 | 1.23526 | 0.00256 | 0.01399 | 0.00042 | 0.02160 | 0.00539 | 0.00048 | 0.00031 | 1.93330 | 0.07474 | 33.77807 | 1.30450 |
| 8 | 6.5 | 2.10912 | 0.00600 | 1.01864 | 0.00242 | 0.01205 | 0.00040 | 0.02112 | 0.00539 | 0.00061 | 0.00031 | 1.89104 | 0.09029 | 33.04634 | 1.57202 |
| 9 | 8.0 | 4.04445 | 0.00666 | 1.92434 | 0.01180 | 0.02295 | 0.00044 | 0.03731 | 0.00539 | 0.00140 | 0.00031 | 1.88482 | 0.04965 | 32.93863 | 0.87514 |

| | | | MSWD | % $^{39}Ar$ | Initial Ratio |
|---|---|---|---|---|---|
| **Plateau age** | **33.17** | **0.67** | 0.15 | 80.1 | na |
| **Isochron age** | **34.8** | **5.3** | 13 | na | 86±66 |

| Step no | Power (%) | $^{40}Ar$ | $\pm\sigma_{40}$ | $^{39}Ar$ | $\pm\sigma_{39}$ | $^{38}Ar$ | $\pm\sigma_{38}$ | $^{37}Ar$ | $\pm\sigma_{37}$ | $^{36}Ar$ | $\pm\sigma_{36}$ | $^{40}Ar^{*}/^{39}Ar$ | $\pm\sigma$ | Age (Ma) | $\pm\sigma$ (Ma) |
|---|---|---|---|---|---|---|---|---|---|---|---|---|---|---|---|
| ***SLP17-29 (San Jose) sanidine, grain size 0.1-0.3 mm, 0.0328mg, J=0.00973613± 4.86807E-05*** | | | | | | | | | | | | | | | |
| 1 | 0.5 | 0.00888 | 0.00154 | 0.00080 | 0.00018 | 0.00001 | 0.00002 | -0.00044 | 0.00049 | 0.00004 | 0.00002 | -5.52252 | -6.86829 | -99.70682 | 127.49589 |
| 2 | 0.9 | 0.33317 | 0.00240 | 0.12370 | 0.00049 | 0.00150 | 0.00007 | 0.00254 | 0.00049 | 0.00036 | 0.00002 | 1.81540 | 0.06275 | 31.60848 | 1.09423 |
| 3 | 1.2 | 1.21558 | 0.00555 | 0.19103 | 0.00150 | 0.00273 | 0.00008 | 0.00476 | 0.00049 | 0.00290 | 0.00005 | 1.82595 | 0.08747 | 31.79064 | 1.51775 |
| 4 | 1.5 | 0.66775 | 0.01100 | 0.08937 | 0.00155 | 0.00135 | 0.00003 | 0.00295 | 0.00014 | 0.00163 | 0.00005 | 2.01781 | 0.21708 | 35.09868 | 3.74348 |
| 5 | 2.0 | 0.56452 | 0.00504 | 0.15207 | 0.00171 | 0.00189 | 0.00007 | 0.00376 | 0.00014 | 0.00088 | 0.00003 | 1.97997 | 0.06417 | 34.44671 | 1.11894 |
| 6 | 2.7 | 0.96233 | 0.01134 | 0.37882 | 0.00504 | 0.00437 | 0.00009 | 0.00638 | 0.00014 | 0.00066 | 0.00003 | 2.01889 | 0.04499 | 35.11721 | 0.79422 |
| 7 | 3.4 | 0.79170 | 0.00781 | 0.26101 | 0.00282 | 0.00312 | 0.00007 | 0.00359 | 0.00014 | 0.00096 | 0.00003 | 1.93237 | 0.05334 | 33.62618 | 0.93451 |
| 8 | 4.4 | 1.30307 | 0.01938 | 0.38188 | 0.00436 | 0.00473 | 0.00008 | 0.00594 | 0.00014 | 0.00188 | 0.00004 | 1.94107 | 0.06482 | 33.77612 | 1.12991 |
| 9 | 5.6 | 1.09343 | 0.00769 | 0.48988 | 0.00343 | 0.00572 | 0.00014 | 0.00612 | 0.00014 | 0.00044 | 0.00003 | 1.96282 | 0.02606 | 34.15118 | 0.47991 |
| 10 | 7.0 | 1.81151 | 0.01455 | 0.74657 | 0.00512 | 0.00885 | 0.00016 | 0.01047 | 0.00014 | 0.00126 | 0.00004 | 1.92234 | 0.02916 | 33.45333 | 0.52933 |
| 11 | 8.5 | 1.77599 | 0.01152 | 0.75081 | 0.00150 | 0.00914 | 0.00010 | 0.00966 | 0.00014 | 0.00097 | 0.00002 | 1.97942 | 0.01753 | 34.43713 | 0.34689 |
| 12 | 10.0 | 1.53159 | 0.00675 | 0.59982 | 0.00378 | 0.00725 | 0.00011 | 0.01120 | 0.00014 | 0.00131 | 0.00005 | 1.90119 | 0.03087 | 33.08856 | 0.55710 |
| 13 | 12.0 | 3.04731 | 0.01155 | 1.37643 | 0.00426 | 0.01596 | 0.00015 | 0.03779 | 0.00014 | 0.00132 | 0.00006 | 1.92688 | 0.01695 | 33.53151 | 0.33619 |
| 14 | 14.0 | 1.87358 | 0.00615 | 0.88109 | 0.00505 | 0.01009 | 0.00008 | 0.03943 | 0.00014 | 0.00047 | 0.00003 | 1.96619 | 0.01756 | 34.20913 | 0.34680 |

| | | | MSWD | % $^{39}Ar$ | Initial Ratio |
|---|---|---|---|---|---|
| **Plateau age** | **33.95** | **0.44** | 1.3 | 98.1 | na |
| **Isochron age** | **34.09** | **0.48** | 1.7 | na | 292.7±8.7 |

| Step no | Power (%) | $^{40}Ar$ | $\pm\sigma_{40}$ | $^{39}Ar$ | $\pm\sigma_{39}$ | $^{38}Ar$ | $\pm\sigma_{38}$ | $^{37}Ar$ | $\pm\sigma_{37}$ | $^{36}Ar$ | $\pm\sigma_{36}$ | $^{40}Ar^{*}/^{39}Ar$ | $\pm\sigma$ | Age (Ma) | $\pm\sigma$ (Ma) |
|---|---|---|---|---|---|---|---|---|---|---|---|---|---|---|---|
| ***SLP17-28 (El Zapote) sanidine, grain size 0.1-0.3 mm, 0.0212mg, J=0.009768395 ± 4.8842E-05*** | | | | | | | | | | | | | | | |
| 1 | 0.5 | 0.00738 | 0.00108 | 0.00096 | 0.00025 | 0.00002 | 0.00002 | 0.00135 | 0.00046 | 0.00003 | 0.00002 | -3.10003 | -7.45942 | -55.47598 | 135.56241 |
| 2 | 0.9 | 0.07025 | 0.00118 | 0.01356 | 0.00026 | 0.00021 | 0.00002 | 0.00173 | 0.00046 | 0.00015 | 0.00002 | 1.77793 | 0.52476 | 31.06330 | 9.09123 |
| 3 | 1.2 | 0.11742 | 0.00153 | 0.04273 | 0.00037 | 0.00051 | 0.00003 | 0.00596 | 0.00047 | 0.00014 | 0.00002 | 1.74555 | 0.16836 | 30.50239 | 2.92120 |
| 4 | 1.5 | 0.41147 | 0.00338 | 0.20242 | 0.00207 | 0.00251 | 0.00008 | 0.00953 | 0.00047 | 0.00009 | 0.00002 | 1.89642 | 0.03463 | 33.11472 | 0.62127 |
| 5 | 2.0 | 1.06346 | 0.00621 | 0.54646 | 0.00264 | 0.00651 | 0.00011 | 0.01847 | 0.00047 | 0.00020 | 0.00002 | 1.83678 | 0.01929 | 32.08245 | 0.36982 |
| 6 | 2.7 | 1.20920 | 0.00867 | 0.49321 | 0.00560 | 0.00585 | 0.00011 | 0.01396 | 0.00047 | 0.00103 | 0.00003 | 1.82740 | 0.03353 | 31.92016 | 0.60167 |
| 7 | 3.4 | 0.87898 | 0.01766 | 0.39921 | 0.00621 | 0.00481 | 0.00011 | 0.00965 | 0.00023 | 0.00030 | 0.00006 | 1.97935 | 0.06893 | 34.54895 | 1.20389 |
| 8 | 4.4 | 2.65836 | 0.02502 | 1.25026 | 0.01111 | 0.01443 | 0.00019 | 0.02536 | 0.00023 | 0.00085 | 0.00006 | 1.92248 | 0.03015 | 33.56555 | 0.54735 |
| 9 | 5.6 | 3.41673 | 0.02704 | 1.70051 | 0.00807 | 0.01961 | 0.00030 | 0.03241 | 0.00023 | 0.00047 | 0.00006 | 1.92647 | 0.02093 | 33.63460 | 0.39854 |
| 10 | 7.0 | 3.50570 | 0.02306 | 1.70700 | 0.00668 | 0.01977 | 0.00015 | 0.02880 | 0.00023 | 0.00070 | 0.00006 | 1.93088 | 0.01886 | 33.71082 | 0.36653 |
| 11 | 8.5 | 3.33876 | 0.02567 | 1.67506 | 0.01357 | 0.01899 | 0.00031 | 0.02633 | 0.00023 | 0.00061 | 0.00006 | 1.88396 | 0.02393 | 32.89902 | 0.44498 |
| 12 | 10.0 | 3.38770 | 0.02731 | 1.66010 | 0.00553 | 0.01956 | 0.00028 | 0.02540 | 0.00023 | 0.00075 | 0.00006 | 1.90519 | 0.02083 | 33.26649 | 0.39626 |
| 13 | 12.0 | 3.25444 | 0.02156 | 1.59914 | 0.00881 | 0.01835 | 0.00018 | 0.02407 | 0.00023 | 0.00056 | 0.00006 | 1.92988 | 0.02067 | 33.69363 | 0.39459 |
| 14 | 14.0 | 4.33748 | 0.01755 | 2.02317 | 0.00948 | 0.02328 | 0.00013 | 0.02936 | 0.00023 | 0.00156 | 0.00006 | 1.91337 | 0.01544 | 33.40791 | 0.31417 |

| | | | MSWD | % $^{39}Ar$ | Initial Ratio |
|---|---|---|---|---|---|
| **Plateau age** | **33.48** | **0.43** | 0.61 | 90.2 | na |
| **Isochron age** | **33.4** | **0.68** | 2.2 | na | 279±20 |

| Step no | Power (%) | $^{40}Ar$ | $\pm\sigma_{40}$ | $^{39}Ar$ | $\pm\sigma_{39}$ | $^{38}Ar$ | $\pm\sigma_{38}$ | $^{37}Ar$ | $\pm\sigma_{37}$ | $^{36}Ar$ | $\pm\sigma_{36}$ | $^{40}Ar^{*}/^{39}Ar$ | $\pm\sigma$ | Age (Ma) | $\pm\sigma$ (Ma) |
|---|---|---|---|---|---|---|---|---|---|---|---|---|---|---|---|
| ***SLP17-24 (Cantera) sanidine, grain size 0.1-0.3 mm, 0.028mg, J=0.009832925 ±4.91646E-05*** | | | | | | | | | | | | | | | |
| 1 | 0.2 | -0.00179 | 0.00225 | -0.00045 | 0.00052 | -0.00003 | 0.00003 | -0.00042 | 0.00017 | 0.00000 | 0.00003 | 4.75258 | 18.38306 | 82.39704 | 311.54490 |
| 2 | 0.5 | 0.00955 | 0.00225 | 0.00007 | 0.00052 | 0.00001 | 0.00003 | 0.00026 | 0.00017 | 0.00004 | 0.00003 | -36.79198 | -283.81485 | -810.14036 | 7888.55861 |
| 3 | 0.9 | 0.21885 | 0.00503 | 0.03799 | 0.00067 | 0.00060 | 0.00004 | 0.00775 | 0.00018 | 0.00057 | 0.00003 | 1.28869 | 0.24179 | 22.71693 | 4.23707 |
| 4 | 1.2 | 0.71505 | 0.01081 | 0.33857 | 0.00522 | 0.00396 | 0.00011 | 0.00518 | 0.00018 | 0.00028 | 0.00003 | 1.86532 | 0.04853 | 32.78983 | 0.86081 |
| 5 | 1.5 | 1.19073 | 0.01459 | 0.50088 | 0.00587 | 0.00610 | 0.00016 | 0.00798 | 0.00018 | 0.00092 | 0.00004 | 1.82948 | 0.04435 | 32.16539 | 0.78906 |
| 6 | 2.0 | 2.22496 | 0.01774 | 1.03458 | 0.00838 | 0.01228 | 0.00023 | 0.01616 | 0.00018 | 0.00117 | 0.00003 | 1.81387 | 0.02462 | 31.89338 | 0.45723 |
| 7 | 2.7 | 1.70031 | 0.01269 | 0.83209 | 0.00663 | 0.00967 | 0.00014 | 0.01247 | 0.00018 | 0.00056 | 0.00003 | 1.84329 | 0.02307 | 32.40593 | 0.43289 |
| 8 | 3.4 | 4.36778 | 0.00777 | 1.99192 | 0.00445 | 0.02478 | 0.00026 | 0.02515 | 0.00018 | 0.00244 | 0.00005 | 1.82636 | 0.00968 | 32.11092 | 0.23190 |
| 9 | 4.4 | 1.72001 | 0.00812 | 0.89714 | 0.00388 | 0.01065 | 0.00015 | 0.01080 | 0.00018 | 0.00023 | 0.00003 | 1.84126 | 0.01476 | 32.37054 | 0.30306 |
| 10 | 5.6 | 1.98469 | 0.00727 | 1.04858 | 0.00378 | 0.01233 | 0.00020 | 0.01922 | 0.00018 | 0.00029 | 0.00003 | 1.81130 | 0.01357 | 31.84843 | 0.28439 |
| 11 | 6.5 | 3.49835 | 0.03090 | 0.81744 | 0.00902 | 0.01086 | 0.00013 | 0.00834 | 0.00018 | 0.00716 | 0.00009 | 1.66495 | 0.05367 | 29.29592 | 0.94795 |
| 12 | 7.0 | 1.69258 | 0.01521 | 0.88070 | 0.00594 | 0.01037 | 0.00015 | 0.00868 | 0.00018 | 0.00025 | 0.00002 | 1.83751 | 0.02219 | 32.30532 | 0.41854 |
| 13 | 7.7 | 1.23284 | 0.00987 | 0.63760 | 0.00257 | 0.00768 | 0.00011 | 0.00868 | 0.00018 | 0.00011 | 0.00003 | 1.88261 | 0.02099 | 33.09095 | 0.40072 |
| 14 | 8.5 | 1.32019 | 0.00771 | 0.68473 | 0.00216 | 0.00819 | 0.00008 | 0.01026 | 0.00018 | 0.00017 | 0.00003 | 1.85462 | 0.01689 | 32.60343 | 0.33572 |

| | | | MSWD | % $^{39}Ar$ | Initial Ratio |
|---|---|---|---|---|---|
| **Plateau age** | **32.1** | **0.38** | 1.6 | 86 | na |
| **Isochron age** | **32.5** | **0.39** | 1.3 | na | 277.4±9.4 |

| Step no | Power (%) | $^{40}Ar$ | $\pm\sigma_{40}$ | $^{39}Ar$ | $\pm\sigma_{39}$ | $^{38}Ar$ | $\pm\sigma_{38}$ | $^{37}Ar$ | $\pm\sigma_{37}$ | $^{36}Ar$ | $\pm\sigma_{36}$ | $^{40}Ar^{*}/^{39}Ar$ | $\pm\sigma$ | Age (Ma) | $\pm\sigma$ (Ma) |
|---|---|---|---|---|---|---|---|---|---|---|---|---|---|---|---|
| ***SLP17-10 (La Placa) whole rock, grain size 0.3-0.5 mm, 0.0382 mg, J=0.009703865±0.0000485193*** | | | | | | | | | | | | | | | |
| 1 | 0.3 | 0.03155 | 0.0023 | 0.00028 | 0.0003 | 0.00003 | 0.00002 | -0.00043 | 0.0008 | 0.00005 | 0.00002 | 61.73442 | 75.8479 | 846.87 | 830.3885 |
| 2 | 0.6 | 1.00104 | 0.0121 | 0.11786 | 0.0012 | 0.00195 | 0.0001 | 0.08319 | 0.0005 | 0.00265 | 0.00003 | 1.77302 | 0.1344 | 30.78 | 2.3181 |
| 3 | 0.9 | 3.21498 | 0.0189 | 0.99477 | 0.0061 | 0.01312 | 0.0001 | 0.72982 | 0.0005 | 0.00483 | 0.0001 | 1.78178 | 0.0328 | 30.93 | 0.5855 |
| 4 | 1.2 | 3.75210 | 0.0131 | 1.59263 | 0.0085 | 0.01932 | 0.0001 | 1.16933 | 0.0005 | 0.00284 | 0.0001 | 1.82443 | 0.0161 | 31.66 | 0.3178 |
| 5 | 1.5 | 3.78826 | 0.0108 | 1.95757 | 0.0121 | 0.02224 | 0.0002 | 1.32950 | 0.0005 | 0.00028 | 0.00003 | 1.89207 | 0.0139 | 32.82 | 0.2888 |
| 6 | 2.1 | 5.01006 | 0.0217 | 2.57457 | 0.0081 | 0.02939 | 0.0003 | 1.61104 | 0.0005 | 0.00050 | 0.00003 | 1.88822 | 0.0110 | 32.76 | 0.2497 |
| 7 | 2.7 | 4.69989 | 0.0222 | 2.46109 | 0.0099 | 0.02744 | 0.0002 | 1.54289 | 0.0005 | 0.00026 | 0.00003 | 1.87861 | 0.0122 | 32.59 | 0.2643 |
| 8 | 3.3 | 4.15327 | 0.0275 | 2.15567 | 0.0096 | 0.02463 | 0.0002 | 1.41606 | 0.0005 | 0.00023 | 0.00003 | 1.89485 | 0.0157 | 32.87 | 0.3153 |
| 9 | 4.4 | 3.00030 | 0.0183 | 1.56726 | 0.0075 | 0.01786 | 0.0002 | 1.02738 | 0.0005 | 0.00030 | 0.00003 | 1.85668 | 0.0160 | 32.21 | 0.3185 |
| 10 | 5.7 | 2.48388 | 0.0137 | 1.27463 | 0.0053 | 0.01510 | 0.0002 | 0.92318 | 0.0005 | 0.00046 | 0.00003 | 1.84087 | 0.0154 | 31.94 | 0.3082 |
| 11 | 7.7 | 2.77713 | 0.0193 | 1.41388 | 0.0078 | 0.01679 | 0.0002 | 1.06198 | 0.0005 | 0.00054 | 0.00003 | 1.84940 | 0.0185 | 32.09 | 0.3552 |

| | | | MSWD | % $^{39}Ar$ | Initial Ratio |
|---|---|---|---|---|---|
| **Plateau age** | **32.67** | **0.39** | 1.01 | 66.5 | na |
| **Isochron age** | **32.51** | **0.48** | 2.4 | na | 290±9.6 |

| Step no | Power (%) | $^{40}Ar$ | $\pm\sigma_{40}$ | $^{39}Ar$ | $\pm\sigma_{39}$ | $^{38}Ar$ | $\pm\sigma_{38}$ | $^{37}Ar$ | $\pm\sigma_{37}$ | $^{36}Ar$ | $\pm\sigma_{36}$ | $^{40}Ar^{*}/^{39}Ar$ | $\pm\sigma$ | Age (Ma) | $\pm\sigma$ (Ma) |
|---|---|---|---|---|---|---|---|---|---|---|---|---|---|---|---|
| ***SLP17-14 (La Placa) whole rock, grain size 0.3-0.5 mm, 0. 0565mg, J=0.009639335 ± 4.81967E-05*** | | | | | | | | | | | | | | | |
| 1 | 0.3 | 0.02598 | 0.00073 | 0.00029 | 0.00003 | 0.00002 | 0.00002 | 0.00072 | 0.00011 | 0.00013 | 0.00002 | -40.37230 | -23.92136 | -889.27221 | 681.04773 |
| 2 | 0.6 | 0.20920 | 0.00154 | 0.00680 | 0.00009 | 0.00026 | 0.00003 | 0.02014 | 0.00011 | 0.00075 | 0.00001 | -2.19379 | -0.66779 | -38.55931 | 11.86549 |
| 3 | 0.9 | 0.23900 | 0.00233 | 0.01835 | 0.00030 | 0.00036 | 0.00003 | 0.05965 | 0.00011 | 0.00067 | 0.00002 | 2.12006 | 0.38822 | 36.49646 | 6.61845 |
| 4 | 1.2 | 0.49609 | 0.00198 | 0.04977 | 0.00039 | 0.00087 | 0.00004 | 0.18338 | 0.00011 | 0.00135 | 0.00005 | 1.88467 | 0.30904 | 32.48046 | 5.28072 |
| 5 | 1.5 | 1.22369 | 0.00389 | 0.35070 | 0.00191 | 0.00443 | 0.00006 | 1.27254 | 0.00011 | 0.00181 | 0.00005 | 1.94940 | 0.04610 | 33.58567 | 0.80437 |
| 6 | 2.1 | 1.01341 | 0.00470 | 0.42019 | 0.00214 | 0.00520 | 0.00010 | 1.44765 | 0.00011 | 0.00070 | 0.00004 | 1.91272 | 0.03289 | 32.95943 | 0.58494 |
| 7 | 2.7 | 1.27038 | 0.00730 | 0.65120 | 0.00324 | 0.00777 | 0.00010 | 1.99388 | 0.00139 | 0.00038 | 0.00003 | 1.77739 | 0.02117 | 30.64726 | 0.39249 |
| 8 | 3.3 | 1.34030 | 0.00625 | 0.71380 | 0.00366 | 0.00850 | 0.00009 | 2.50620 | 0.00139 | 0.00032 | 0.00003 | 1.74279 | 0.01654 | 30.05553 | 0.31967 |
| 9 | 4.4 | 1.24149 | 0.00965 | 0.66867 | 0.00566 | 0.00793 | 0.00013 | 2.35863 | 0.00139 | 0.00028 | 0.00004 | 1.73089 | 0.02819 | 29.85202 | 0.50440 |
| 10 | 5.7 | 1.27088 | 0.00694 | 0.69090 | 0.00435 | 0.00832 | 0.00014 | 2.78995 | 0.00139 | 0.00026 | 0.00002 | 1.72824 | 0.01698 | 29.80674 | 0.32587 |
| 11 | 7.7 | 1.78673 | 0.00873 | 0.96382 | 0.00607 | 0.01148 | 0.00023 | 3.95772 | 0.00139 | 0.00031 | 0.00003 | 1.75844 | 0.01784 | 30.32314 | 0.34009 |

| | | | MSWD | % $^{39}Ar$ | Initial Ratio |
|---|---|---|---|---|---|
| **Plateau age** | **30.13** | **0.42** | 1.02 | 81.5 | na |
| **Isochron age** | **30.47** | **0.99** | 3.5 | na | 311±17 |

| Step no | Power (%) | $^{40}Ar$ | $\pm\sigma_{40}$ | $^{39}Ar$ | $\pm\sigma_{39}$ | $^{38}Ar$ | $\pm\sigma_{38}$ | $^{37}Ar$ | $\pm\sigma_{37}$ | $^{36}Ar$ | $\pm\sigma_{36}$ | $^{40}Ar^{*}/^{39}Ar$ | $\pm\sigma$ | Age (Ma) | $\pm\sigma$ (Ma) |
|---|---|---|---|---|---|---|---|---|---|---|---|---|---|---|---|
| ***SLP17-20 (La Placa) whole rock, grain size 0.3-0.5 mm, 0. 0396mg, J=0.00960707± 4.80354E-05*** | | | | | | | | | | | | | | | |
| 1 | 0.3 | 0.24840 | 0.00288 | 0.03033 | 0.00038 | 0.00064 | 0.00004 | 0.01713 | 0.00084 | 0.00073 | 0.00003 | 0.97190 | 0.33630 | 16.76678 | 5.77541 |
| 2 | 0.6 | 2.95426 | 0.01134 | 0.56369 | 0.00244 | 0.00959 | 0.00013 | 0.17396 | 0.00084 | 0.00757 | 0.00011 | 1.23057 | 0.06226 | 21.20301 | 1.07161 |
| 3 | 0.9 | 4.60960 | 0.03390 | 1.28911 | 0.00837 | 0.02091 | 0.00028 | 0.50612 | 0.00084 | 0.00941 | 0.00006 | 1.39559 | 0.03124 | 24.02744 | 0.54748 |
| 4 | 1.2 | 5.21865 | 0.03792 | 2.32888 | 0.01178 | 0.03682 | 0.00042 | 1.44776 | 0.00084 | 0.00654 | 0.00006 | 1.40189 | 0.01943 | 24.13520 | 0.35323 |
| 5 | 1.5 | 4.65527 | 0.02151 | 2.04198 | 0.01039 | 0.03270 | 0.00026 | 1.90737 | 0.00084 | 0.00512 | 0.00008 | 1.53084 | 0.01767 | 26.33920 | 0.32891 |
| 6 | 2.1 | 3.20456 | 0.01473 | 1.42063 | 0.00596 | 0.02313 | 0.00021 | 1.94331 | 0.00084 | 0.00334 | 0.00006 | 1.55321 | 0.01780 | 26.72119 | 0.33168 |
| 7 | 2.7 | 5.98247 | 0.05629 | 2.14008 | 0.01690 | 0.03594 | 0.00035 | 3.54177 | 0.00084 | 0.00901 | 0.00011 | 1.53858 | 0.03284 | 26.47137 | 0.57611 |
| 8 | 3.3 | 3.35366 | 0.01395 | 1.28933 | 0.00319 | 0.02079 | 0.00026 | 2.93116 | 0.00084 | 0.00437 | 0.00005 | 1.58892 | 0.01664 | 27.33097 | 0.31471 |
| 9 | 4.4 | 2.75433 | 0.00829 | 0.95072 | 0.00308 | 0.01552 | 0.00014 | 3.02233 | 0.00084 | 0.00408 | 0.00007 | 1.61682 | 0.02460 | 27.80721 | 0.44200 |
| 10 | 5.7 | 1.57253 | 0.00621 | 0.57229 | 0.00192 | 0.00904 | 0.00015 | 2.09047 | 0.00084 | 0.00206 | 0.00004 | 1.67109 | 0.02517 | 28.73319 | 0.45244 |

| | | | MSWD | % $^{39}Ar$ | Initial Ratio |
|---|---|---|---|---|---|
| **Plateau age** | **-** | **-** | **-** | **-** | na |
| **Isochron age** | **28** | **2** | 20 | na | 274±23 |

| Step no | Power (%) | $^{40}Ar$ | $\pm\sigma_{40}$ | $^{39}Ar$ | $\pm\sigma_{39}$ | $^{38}Ar$ | $\pm\sigma_{38}$ | $^{37}Ar$ | $\pm\sigma_{37}$ | $^{36}Ar$ | $\pm\sigma_{36}$ | $^{40}Ar^{*}/^{39}Ar$ | $\pm\sigma$ | Age (Ma) | $\pm\sigma$ (Ma) |
|---|---|---|---|---|---|---|---|---|---|---|---|---|---|---|---|
| ***SLP17-15 (Panalillo) sanidine, grain size 0.1-0.3 mm, 0.031mg, J=0.009805594 ± 4.9028E-05*** | | | | | | | | | | | | | | | |
| 1 | 0.6 | 0.06139 | 0.00547 | 0.00076 | 0.00182 | 0.00011 | 0.00081 | 0.00196 | 0.01193 | 0.00024 | 0.00055 | -12.12323 | -217.39499 | -228.31733 | 4364.56779 |
| 2 | 0.9 | 0.44042 | 0.00591 | 0.00358 | 0.00182 | 0.00016 | 0.00081 | -0.00234 | 0.01194 | 0.00128 | 0.00055 | 16.49613 | 46.67272 | 270.48744 | 710.68724 |
| 3 | 1.2 | 1.83239 | 0.01375 | 0.07646 | 0.00191 | 0.00291 | 0.00081 | 0.02519 | 0.01194 | 0.00645 | 0.00055 | -1.22180 | -2.15707 | -21.74418 | 38.62148 |
| 4 | 1.5 | 0.59943 | 0.00678 | 0.06489 | 0.00187 | 0.00180 | 0.00081 | 0.01472 | 0.01195 | 0.00226 | 0.00055 | -1.17485 | -2.53015 | -20.90370 | 45.28017 |
| 5 | 2.0 | 0.81205 | 0.00753 | 0.13470 | 0.00192 | 0.00388 | 0.00081 | 0.03002 | 0.01195 | 0.00282 | 0.00055 | -0.21980 | -1.22387 | -3.89247 | 21.69710 |
| 6 | 2.6 | 1.30151 | 0.00758 | 0.42205 | 0.00301 | 0.00786 | 0.00082 | 0.05572 | 0.01196 | 0.00242 | 0.00055 | 1.37028 | 0.38920 | 24.07886 | 6.79479 |
| 7 | 3.3 | 0.99706 | 0.00822 | 0.47237 | 0.00274 | 0.00773 | 0.00082 | 0.06322 | 0.01197 | 0.00138 | 0.00055 | 1.23840 | 0.34778 | 21.77538 | 6.07935 |
| 8 | 4.2 | 0.91676 | 0.00696 | 0.44748 | 0.00338 | 0.00794 | 0.00082 | 0.07602 | 0.01197 | 0.00122 | 0.00055 | 1.23683 | 0.36770 | 21.74801 | 6.42753 |
| 9 | 5.2 | 0.72760 | 0.00504 | 0.37326 | 0.00134 | 0.00437 | 0.00012 | 0.03228 | 0.00142 | 0.00028 | 0.00009 | 1.72864 | 0.07036 | 30.32339 | 1.23308 |
| 10 | 6.5 | 1.06992 | 0.00566 | 0.52859 | 0.00291 | 0.00652 | 0.00018 | 0.03859 | 0.00142 | 0.00062 | 0.00008 | 1.67153 | 0.04897 | 29.32976 | 0.86455 |
| 11 | 8.0 | 1.37878 | 0.00863 | 0.68703 | 0.00509 | 0.00838 | 0.00016 | 0.07806 | 0.00142 | 0.00094 | 0.00009 | 1.59675 | 0.04115 | 28.02777 | 0.73012 |
| 12 | 10.0 | 2.17588 | 0.01757 | 1.04632 | 0.00559 | 0.01265 | 0.00016 | 0.09548 | 0.00142 | 0.00149 | 0.00008 | 1.65464 | 0.03035 | 29.03570 | 0.54759 |
| 13 | 12.0 | 2.73692 | 0.03948 | 0.93503 | 0.01304 | 0.01219 | 0.00014 | 0.07494 | 0.00142 | 0.00436 | 0.00010 | 1.53346 | 0.05718 | 26.92508 | 1.00537 |
| 14 | 14.0 | 2.06103 | 0.00493 | 0.97727 | 0.00232 | 0.01172 | 0.00020 | 0.05451 | 0.00142 | 0.00109 | 0.00009 | 1.77596 | 0.02707 | 31.14635 | 0.49543 |

| | | | MSWD | % $^{39}Ar$ | Initial Ratio |
|---|---|---|---|---|---|
| **Plateau age** | **28.65** | **0.37** | 1.4 | 83.4 | na |
| **Isochron age** | **30.6** | **2** | 3.2 | na | 256±61 |

| Step no | Power (%) | $^{40}Ar$ | $\pm\sigma_{40}$ | $^{39}Ar$ | $\pm\sigma_{39}$ | $^{38}Ar$ | $\pm\sigma_{38}$ | $^{37}Ar$ | $\pm\sigma_{37}$ | $^{36}Ar$ | $\pm\sigma_{36}$ | $^{40}Ar^{*}/^{39}Ar$ | $\pm\sigma$ | Age (Ma) | $\pm\sigma$ (Ma) |
|---|---|---|---|---|---|---|---|---|---|---|---|---|---|---|---|
| ***SLP17-16 (Panalillo) sanidine, grain size 0.1-0.3 mm, 0.0269mg, J=0.009820493 ± 4.91025E-05*** | | | | | | | | | | | | | | | |
| 1 | 0.5 | 0.02426 | 0.00907 | 0.00232 | NaN | 0.00003 | 0.00002 | 0.00000 | 0.00015 | 0.00007 | NaN | 2.09582 | 3.91234 | 36.75451 | 67.91703 |
| 2 | 0.9 | 2.40244 | 0.02241 | 0.01263 | 0.00028 | 0.00167 | 0.00005 | 0.00176 | 0.00015 | 0.00800 | 0.00010 | 0.99850 | 2.95614 | 17.60420 | 51.86521 |
| 3 | 1.2 | 2.65762 | 0.02510 | 0.02576 | 0.00053 | 0.00198 | 0.00009 | 0.00228 | 0.00015 | 0.00909 | 0.00011 | -2.23650 | -1.59661 | -40.06552 | 28.92304 |
| 4 | 1.5 | 2.15042 | 0.02180 | 0.06898 | 0.00051 | 0.00213 | 0.00008 | 0.00913 | 0.00015 | 0.00719 | 0.00010 | 0.04354 | 0.53577 | 0.77132 | 9.48806 |
| 5 | 2.0 | 4.93083 | 0.03821 | 0.30654 | 0.00289 | 0.00634 | 0.00011 | 0.01350 | 0.00015 | 0.01545 | 0.00021 | 1.03626 | 0.24343 | 18.26656 | 4.27033 |
| 6 | 2.7 | 7.10684 | 0.02717 | 0.52825 | 0.00222 | 0.01021 | 0.00005 | 0.03844 | 0.00015 | 0.02155 | 0.00010 | 1.27106 | 0.07659 | 22.37987 | 1.34482 |
| 7 | 3.4 | 8.17871 | 0.04307 | 1.01427 | 0.00792 | 0.01590 | 0.00019 | 0.05275 | 0.00029 | 0.02419 | 0.00014 | 0.94426 | 0.05992 | 16.65228 | 1.05517 |
| 8 | 4.4 | 10.59831 | 0.05862 | 1.53740 | 0.00695 | 0.02271 | 0.00023 | 0.07512 | 0.00029 | 0.02864 | 0.00028 | 1.33181 | 0.06680 | 23.44260 | 1.17394 |
| 9 | 5.6 | 4.31153 | 0.01491 | 0.66515 | 0.00301 | 0.00994 | 0.00014 | 0.03266 | 0.00029 | 0.01134 | 0.00008 | 1.39135 | 0.04373 | 24.48364 | 0.77391 |
| 10 | 7.0 | 3.63643 | 0.00890 | 0.55492 | 0.00163 | 0.00798 | 0.00008 | 0.03921 | 0.00029 | 0.00969 | 0.00007 | 1.33983 | 0.04251 | 23.58288 | 0.75254 |
| 11 | 8.5 | 3.23238 | 0.01429 | 0.47113 | 0.00242 | 0.00687 | 0.00011 | 0.01833 | 0.00029 | 0.00872 | 0.00011 | 1.33803 | 0.07737 | 23.55146 | 1.35808 |
| 12 | 10.0 | 4.81527 | 0.01324 | 0.77867 | 0.00293 | 0.01140 | 0.00014 | 0.04136 | 0.00029 | 0.01244 | 0.00010 | 1.41455 | 0.04297 | 24.88907 | 0.76102 |
| 13 | 12.0 | 5.87268 | 0.01458 | 1.06564 | 0.00418 | 0.01474 | 0.00015 | 0.04920 | 0.00029 | 0.01441 | 0.00011 | 1.47455 | 0.03467 | 25.93719 | 0.61899 |
| 14 | 14.0 | 3.31117 | 0.00987 | 0.86639 | 0.00197 | 0.01115 | 0.00016 | 0.02512 | 0.00029 | 0.00642 | 0.00007 | 1.60830 | 0.02779 | 28.27137 | 0.50464 |

| | | | MSWD | % $^{39}Ar$ | Initial Ratio |
|---|---|---|---|---|---|
| **Plateau age** | **24.15** | **0.82** | 0.58 | 51.5 | na |
| **Isochron age** | **29.6** | **3.5** | 7.5 | na | 282±12 |

| Step no | Power (%) | $^{40}Ar$ | $\pm\sigma_{40}$ | $^{39}Ar$ | $\pm\sigma_{39}$ | $^{38}Ar$ | $\pm\sigma_{38}$ | $^{37}Ar$ | $\pm\sigma_{37}$ | $^{36}Ar$ | $\pm\sigma_{36}$ | $^{40}Ar^{*}/^{39}Ar$ | $\pm\sigma$ | Age (Ma) | $\pm\sigma$ (Ma) |
|---|---|---|---|---|---|---|---|---|---|---|---|---|---|---|---|
| ***SLP17-19 (Panalillo) sanidine, grain size 0.1-0.3 mm, 0.0764mg, J=0.009835392 ± 4.9177E-05*** | | | | | | | | | | | | | | | |
| 1 | 1.2 | 1.98129 | 0.00733 | 0.04116 | 0.00096 | 0.00160 | 0.00009 | 0.00143 | 0.00068 | 0.00644 | 0.00006 | 1.41969 | 0.49982 | 25.01641 | 8.74755 |
| 2 | 1.5 | 0.68167 | 0.00710 | 0.02308 | 0.00095 | 0.00070 | 0.00006 | 0.00076 | 0.00068 | 0.00216 | 0.00005 | 1.58525 | 0.67412 | 27.91129 | 11.77865 |
| 3 | 2.0 | 2.71789 | 0.00749 | 0.07134 | 0.00098 | 0.00253 | 0.00004 | 0.00255 | 0.00068 | 0.00882 | 0.00006 | 1.18508 | 0.28900 | 20.90624 | 5.06988 |
| 4 | 2.5 | 2.25194 | 0.00774 | 0.10096 | 0.00110 | 0.00246 | 0.00008 | 0.00501 | 0.00068 | 0.00709 | 0.00005 | 1.34010 | 0.15706 | 23.62308 | 2.75311 |
| 5 | 3.0 | 1.37325 | 0.00720 | 0.24516 | 0.00105 | 0.00361 | 0.00007 | 0.00838 | 0.00068 | 0.00339 | 0.00004 | 1.47472 | 0.05491 | 25.97915 | 0.96896 |
| 6 | 3.7 | 1.18737 | 0.00727 | 0.25232 | 0.00117 | 0.00336 | 0.00007 | 0.00838 | 0.00068 | 0.00246 | 0.00005 | 1.79663 | 0.07164 | 31.60064 | 1.25895 |
| 7 | 4.5 | 0.90857 | 0.00715 | 0.35482 | 0.00118 | 0.00411 | 0.00008 | 0.01197 | 0.00068 | 0.00097 | 0.00004 | 1.74645 | 0.03806 | 30.72557 | 0.68125 |
| 8 | 5.5 | 1.02138 | 0.00694 | 0.39584 | 0.00125 | 0.00472 | 0.00012 | 0.01018 | 0.00068 | 0.00113 | 0.00005 | 1.72942 | 0.03932 | 30.42838 | 0.70235 |
| 9 | 6.5 | 1.42872 | 0.00805 | 0.60905 | 0.00186 | 0.00712 | 0.00014 | 0.01803 | 0.00068 | 0.00105 | 0.00004 | 1.83304 | 0.02341 | 32.23540 | 0.43826 |
| 10 | 7.7 | 1.82092 | 0.00700 | 0.87933 | 0.00209 | 0.01030 | 0.00015 | 0.02432 | 0.00068 | 0.00090 | 0.00004 | 1.76374 | 0.01565 | 31.02703 | 0.31335 |
| 11 | 9.0 | 3.59243 | 0.01041 | 1.62078 | 0.00331 | 0.01907 | 0.00010 | 0.04856 | 0.00068 | 0.00256 | 0.00005 | 1.74528 | 0.01251 | 30.70515 | 0.26609 |
| 12 | 10.5 | 2.31103 | 0.00754 | 1.09677 | 0.00194 | 0.01299 | 0.00012 | 0.03174 | 0.00068 | 0.00122 | 0.00005 | 1.77436 | 0.01465 | 31.21232 | 0.29862 |
| 13 | 12.5 | 3.88175 | 0.00807 | 1.68664 | 0.00269 | 0.01936 | 0.00024 | 0.07554 | 0.00068 | 0.00310 | 0.00007 | 1.75258 | 0.01417 | 30.83248 | 0.29055 |
| 14 | 14.5 | 3.09208 | 0.00845 | 1.49707 | 0.00343 | 0.01744 | 0.00022 | 0.05468 | 0.00068 | 0.00147 | 0.00005 | 1.77299 | 0.01152 | 31.18842 | 0.25355 |

| | | | MSWD | % $^{39}Ar$ | Initial Ratio |
|---|---|---|---|---|---|
| **Plateau age** | **31.05** | **0.37** | 1.7 | 94.6 | na |
| **Isochron age** | **30.99** | **0.49** | 3 | na | 292.3±4.9 |

| Step no | Power (%) | $^{40}Ar$ | $\pm\sigma_{40}$ | $^{39}Ar$ | $\pm\sigma_{39}$ | $^{38}Ar$ | $\pm\sigma_{38}$ | $^{37}Ar$ | $\pm\sigma_{37}$ | $^{36}Ar$ | $\pm\sigma_{36}$ | $^{40}Ar^{*}/^{39}Ar$ | $\pm\sigma$ | Age (Ma) | $\pm\sigma$ (Ma) |
|---|---|---|---|---|---|---|---|---|---|---|---|---|---|---|---|
| ***SLP17-23 (Panalillo) sanidine, grain size 0.1-0.3 mm, 0.0325mg, J=0.009850291 ± 7.987E-05*** | | | | | | | | | | | | | | | |
| 1 | 0.2 | 0.00043 | 0.00082 | -0.00008 | 0.00009 | 0.00003 | 0.00002 | 0.00007 | 0.00012 | 0.00001 | 0.00002 | 22.24100 | 95.01483 | 357.38182 | 1385.04533 |
| 2 | 0.5 | 0.12195 | 0.00096 | 0.00603 | 0.00013 | 0.00013 | 0.00003 | 0.00040 | 0.00012 | 0.00035 | 0.00002 | 3.02345 | 1.24353 | 52.94425 | 21.46345 |
| 3 | 0.9 | 0.40041 | 0.00183 | 0.05776 | 0.00074 | 0.00092 | 0.00005 | 0.00160 | 0.00012 | 0.00109 | 0.00004 | 1.31317 | 0.22334 | 23.18635 | 3.92272 |
| 4 | 1.2 | 0.31489 | 0.00207 | 0.07448 | 0.00065 | 0.00102 | 0.00004 | 0.00106 | 0.00012 | 0.00069 | 0.00003 | 1.47309 | 0.13754 | 25.98969 | 2.41833 |
| 5 | 1.5 | 0.83210 | 0.00676 | 0.32756 | 0.00301 | 0.00398 | 0.00010 | 0.00808 | 0.00012 | 0.00097 | 0.00002 | 1.66041 | 0.03425 | 29.26794 | 0.64341 |
| 6 | 2.0 | 0.30119 | 0.00266 | 0.11910 | 0.00055 | 0.00158 | 0.00003 | 0.00292 | 0.00012 | 0.00029 | 0.00003 | 1.81017 | 0.08718 | 31.88453 | 1.54349 |
| 7 | 2.7 | 0.97335 | 0.00700 | 0.44556 | 0.00388 | 0.00520 | 0.00007 | 0.01128 | 0.00012 | 0.00070 | 0.00002 | 1.71247 | 0.02733 | 30.17796 | 0.53569 |
| 8 | 3.4 | 1.51208 | 0.01509 | 0.77432 | 0.00889 | 0.00887 | 0.00020 | 0.01546 | 0.00012 | 0.00061 | 0.00003 | 1.71627 | 0.03057 | 30.24434 | 0.58697 |
| 9 | 4.4 | 1.64429 | 0.02375 | 0.80701 | 0.01190 | 0.00947 | 0.00025 | 0.01470 | 0.00012 | 0.00094 | 0.00003 | 1.68843 | 0.04049 | 29.75780 | 0.74706 |
| 10 | 5.6 | 0.95267 | 0.00380 | 0.37110 | 0.00097 | 0.00438 | 0.00007 | 0.00854 | 0.00012 | 0.00120 | 0.00003 | 1.60553 | 0.02910 | 28.30819 | 0.55771 |
| 11 | 7.0 | 0.30115 | 0.00215 | 0.15658 | 0.00095 | 0.00183 | 0.00003 | 0.00326 | 0.00012 | 0.00014 | 0.00003 | 1.66279 | 0.06602 | 29.30959 | 1.17810 |
| 12 | 8.5 | 2.46656 | 0.02733 | 1.12168 | 0.01341 | 0.01312 | 0.00030 | 0.02132 | 0.00012 | 0.00207 | 0.00003 | 1.64751 | 0.03257 | 29.04241 | 0.61560 |
| 13 | 9.0 | 0.98904 | 0.00374 | 0.41378 | 0.00176 | 0.00515 | 0.00009 | 0.00910 | 0.00012 | 0.00104 | 0.00004 | 1.64341 | 0.03282 | 28.97065 | 0.61952 |

| | | | MSWD | % $^{39}Ar$ | Initial Ratio |
|---|---|---|---|---|---|
| **Plateau age** | **29.4** | **0.5** | 1.8 | 100 | na |
| **Isochron age** | **30.4** | **0.74** | 0.99 | na | 272±15 |

| Step no | Power (%) | $^{40}Ar$ | $\pm\sigma_{40}$ | $^{39}Ar$ | $\pm\sigma_{39}$ | $^{38}Ar$ | $\pm\sigma_{38}$ | $^{37}Ar$ | $\pm\sigma_{37}$ | $^{36}Ar$ | $\pm\sigma_{36}$ | $^{40}Ar^{*}/^{39}Ar$ | $\pm\sigma$ | Age (Ma) | $\pm\sigma$ (Ma) |
|---|---|---|---|---|---|---|---|---|---|---|---|---|---|---|---|
| ***SLP17-13 (Cabras) whole rock, grain size 0.3-0.5 mm, 0.0559mg, J=0.0096716± 4.8358E-05*** | | | | | | | | | | | | | | | |
| 1 | 0.3 | 0.07913 | 0.00180 | 0.00075 | 0.00071 | 0.00004 | 0.00003 | 0.00019 | 0.00144 | 0.00027 | 0.00002 | -2.60297 | -10.38043 | -45.99895 | 185.79856 |
| 2 | 0.6 | 1.28527 | 0.00769 | 0.08301 | 0.00102 | 0.00192 | 0.00008 | 0.12907 | 0.00144 | 0.00405 | 0.00006 | 0.92590 | 0.24093 | 16.08350 | 4.16731 |
| 3 | 0.9 | 1.18678 | 0.00381 | 0.30154 | 0.00153 | 0.00454 | 0.00010 | 0.44766 | 0.00145 | 0.00279 | 0.00006 | 1.17033 | 0.06272 | 20.30554 | 1.08684 |
| 4 | 1.2 | 1.68241 | 0.01130 | 0.83760 | 0.00555 | 0.00968 | 0.00011 | 1.21463 | 0.00145 | 0.00196 | 0.00006 | 1.31005 | 0.02724 | 22.71454 | 0.48272 |
| 5 | 1.5 | 1.37243 | 0.01110 | 0.96489 | 0.00733 | 0.01137 | 0.00022 | 1.47190 | 0.00145 | 0.00048 | 0.00003 | 1.27335 | 0.01825 | 22.08204 | 0.33313 |
| 6 | 2.1 | 1.67691 | 0.00596 | 1.23491 | 0.00334 | 0.01501 | 0.00020 | 2.62228 | 0.00145 | 0.00039 | 0.00004 | 1.26441 | 0.01191 | 21.92801 | 0.23236 |
| 7 | 2.7 | 1.69995 | 0.00506 | 1.23201 | 0.00443 | 0.01527 | 0.00019 | 3.23687 | 0.00145 | 0.00040 | 0.00004 | 1.28194 | 0.01207 | 22.23018 | 0.23558 |
| 8 | 3.3 | 0.94035 | 0.00357 | 0.66871 | 0.00272 | 0.00874 | 0.00011 | 2.19228 | 0.00145 | 0.00030 | 0.00003 | 1.27196 | 0.01670 | 22.05819 | 0.30803 |
| 9 | 4.4 | 1.75785 | 0.00671 | 1.25177 | 0.00216 | 0.01603 | 0.00012 | 4.59718 | 0.00145 | 0.00045 | 0.00003 | 1.29615 | 0.00996 | 22.47498 | 0.20479 |
| 10 | 5.7 | 1.32664 | 0.00913 | 1.01058 | 0.00442 | 0.01294 | 0.00019 | 3.59353 | 0.00084 | 0.00034 | 0.00004 | 1.21363 | 0.01632 | 21.05253 | 0.30034 |
| 11 | 7.7 | 1.47146 | 0.00911 | 1.11524 | 0.00786 | 0.01442 | 0.00011 | 4.13878 | 0.00084 | 0.00044 | 0.00003 | 1.20135 | 0.01475 | 20.84070 | 0.27468 |

| | | | MSWD | % $^{39}Ar$ | Initial Ratio |
|---|---|---|---|---|---|
| **Plateau age** | **22.21** | **0.29** | 1.6 | 75.6 | na |
| **Isochron age** | **21.93** | **0.59** | 5.9 | | 293±15 |

## Tabla A.8.- Información de química mineral. Abreviaciones B= análisis en borde; C= análisis en el centro.

Composición representativa de feldespatos alcalinos de las rocas félsicas del CVSSM

| **Muestra** | SLP1711 | SLP1711 | SLP1711 | SLP1711 | SLP1711 | SLP1711 | SLP1728 | SLP1728 | SLP1728 | SLP1728 | SLP1728 | SLP1728 |
|---|---|---|---|---|---|---|---|---|---|---|---|---|
| **Análisis** | B | B | C | C | B | B | B | B | C | C | B | B |
| **Unidad** | SSM | SSM | SSM | SSM | SSM | SSM | Zapote | Zapote | Zapote | Zapote | Zapote | Zapote |
| **Roca (TAS)** | Riolita | Riolita | Riolita | Riolita | Riolita | Riolita | Riolita | Riolita | Riolita | Riolita | Riolita | Riolita |
| $SiO_2$ | 65.304 | 65.088 | 66.015 | 64.88 | 65.354 | 66.273 | 66.146 | 66.913 | 66.136 | 66.184 | 67.31 | 66.297 |
| $TiO_2$ | 0.04 | -0.028 | 0.003 | 0.029 | 0.001 | 0.058 | -0.013 | -0.033 | 0.012 | 0.067 | 0.008 | -0.045 |
| $Al_2O_3$ | 18.817 | 19.041 | 19.128 | 18.92 | 18.963 | 19.004 | 18.468 | 19.033 | 18.606 | 18.846 | 18.672 | 18.679 |
| $Fe_2O_3^t$ | 0.018 | 0.021 | 0.011 | 0.029 | 0.021 | 0.036 | 0.038 | 0.003 | 0.06 | 0.04 | -0.002 | 0.063 |
| MnO | -0.036 | 0.016 | -0.015 | 0.003 | 0.002 | 0.026 | 0.008 | 0.002 | -0.01 | -0.012 | 0.008 | 0.003 |
| MgO | 0.024 | 0.016 | 0.019 | -0.019 | -0.037 | -0.004 | -0.031 | -0.008 | 0.016 | -0.007 | -0.002 | -0.018 |
| CaO | 0.241 | 0.205 | 0.197 | 0.208 | 0.231 | 0.245 | 0.293 | 0.293 | 0.365 | 0.339 | 0.302 | 0.298 |
| $Na_2O$ | 3.658 | 3.549 | 3.509 | 3.551 | 3.515 | 4.139 | 4.426 | 4.239 | 4.178 | 4.178 | 4.637 | 4.211 |
| $K_2O$ | 11.391 | 11.455 | 11.466 | 11.415 | 11.575 | 10.903 | 10.546 | 10.589 | 10.49 | 10.743 | 10.151 | 10.806 |
| $P_2O_5$ | 0.007 | -0.017 | 0.017 | -0.014 | -0.003 | -0.01 | -0.017 | -0.007 | 0.003 | -0.01 | -0.044 | -0.02 |
| Total | 99.464 | 99.346 | 100.35 | 99.002 | 99.622 | 100.67 | 99.864 | 101.024 | 99.856 | 100.368 | 101.04 | 100.274 |
| | | | | | | | | | | | | |
| %Ab | 32.41 | 31.69 | 31.44 | 31.77 | 31.22 | 36.15 | 38.40 | 37.29 | 37.03 | 36.54 | 40.38 | 36.66 |
| %An | 1.18 | 1.01 | 0.98 | 1.03 | 1.13 | 1.18 | 1.40 | 1.42 | 1.79 | 1.64 | 1.45 | 1.43 |
| %Or | 66.41 | 67.30 | 67.59 | 67.20 | 67.65 | 62.66 | 60.20 | 61.29 | 61.18 | 61.82 | 58.16 | 61.90 |

Composición representativa de clinopiroxenos de las rocas intermedias del CVSSM

| **Muestra** | SLP1720 | SLP1720 | SLP1720 | SLP1720 | SLP1720 | SLP1720 | SLP1710 | SLP1710 | SLP1710 |
|---|---|---|---|---|---|---|---|---|---|
| **Análisis** | B | B | C | C | B | B | B | C | B |
| **Unidad** | La Placa | La Placa | La Placa | La Placa | La Placa | La Placa | La Placa | La Placa | La Placa |
| **Roca (TAS)** | Andesita | Andesita | Andesita | Andesita | Andesita | Andesita | Andesita | Andesita | Andesita |
| $SiO_2$ | 52.553 | 49.773 | 49.312 | 49.374 | 50.791 | 51.336 | 51.139 | 51.236 | 51.272 |
| $TiO_2$ | 0.491 | 0.955 | 1.111 | 1.027 | 0.791 | 0.913 | 0.437 | 0.297 | 0.451 |
| $Al_2O_3$ | 2.285 | 3.464 | 3.998 | 3.823 | 3.549 | 1.37 | 2.824 | 2.265 | 2.484 |
| $Fe_2O_3^t$ | 11.023 | 11.81 | 12.031 | 11.665 | 12.378 | 11.613 | 6.384 | 6.701 | 6.233 |
| MnO | 0.238 | 0.271 | 0.29 | 0.3 | 0.331 | 0.28 | 0.178 | 0.186 | 0.165 |
| MgO | 14.276 | 13.533 | 13.472 | 13.477 | 13.461 | 15.936 | 17.541 | 18.217 | 18.048 |
| CaO | 17.926 | 19.142 | 18.933 | 18.809 | 18.972 | 17.32 | 19.6 | 18.721 | 19.683 |
| $Na_2O$ | 0.246 | 0.388 | 0.371 | 0.327 | 0.363 | 0.166 | 0.317 | 0.281 | 0.206 |
| $K_2O$ | 0.449 | -0.009 | 0.001 | -0.011 | 0.006 | 0.037 | -0.013 | -0.008 | 0.004 |
| $P_2O_5$ | 0.023 | 0.016 | -0.01 | 0.00 | 0.00 | -0.02 | 0.017 | 0.017 | 0.056 |
| Total | 99.51 | 99.343 | 99.509 | 98.791 | 100.642 | 98.951 | 98.424 | 97.913 | 98.602 |
| | | | | | | | | | |
| %Wo | 38.5 | 40.4 | 40.1 | 40.2 | 39.9 | 35.5 | 39.92 | 37.89 | 39.55 |
| %En | 42.7 | 39.8 | 39.7 | 40.0 | 39.4 | 45.5 | 49.71 | 51.30 | 50.47 |
| %Fs | 18.8 | 19.8 | 20.2 | 19.8 | 20.7 | 18.9 | 10.37 | 10.81 | 9.98 |

Composición representativa de clinopiroxenos de las rocas básicas del CVSSM

| **Muestra** | SLP1713 | SLP1713 | SLP1713 | SLP1713 | SLP1713 | SLP1713 |
|---|---|---|---|---|---|---|
| **Análisis** | B | B | B | B | C | C |
| **Unidad** | Cabras | Cabras | Cabras | Cabras | Cabras | Cabras |
| **Roca (TAS)** | Basalto | Basalto | Basalto | Basalto | Basalto | Basalto |
| $SiO_2$ | 50.974 | 51.593 | 51.596 | 51.757 | 51.997 | 51.322 |
| $TiO_2$ | 0.981 | 1.064 | 1.181 | 1.001 | 0.896 | 0.936 |
| $Al_2O_3$ | 1.579 | 1.598 | 1.336 | 1.729 | 1.509 | 1.575 |
| $Fe_2O_3^t$ | 10.782 | 10.95 | 11.732 | 9.769 | 10.515 | 11.448 |
| MnO | 0.245 | 0.269 | 0.292 | 0.267 | 0.3 | 0.302 |
| MgO | 16.264 | 15.957 | 15.807 | 15.95 | 16.338 | 16.241 |
| CaO | 18.416 | 17.851 | 17.572 | 18.897 | 17.799 | 17.522 |
| $Na_2O$ | 0.209 | 0.188 | 0.234 | 0.252 | 0.215 | 0.251 |
| $K_2O$ | -0.009 | -0.009 | -0.012 | -0.017 | 0.007 | -0.012 |
| $P_2O_5$ | 0.02 | 0.013 | -0.033 | -0.016 | 0.02 | 0.026 |
| Total | 99.461 | 99.474 | 99.705 | 99.589 | 99.596 | 99.611 |
| | | | | | | |
| %Wo | 37.13 | 36.61 | 35.94 | 38.66 | 36.38 | 35.59 |
| %En | 45.63 | 45.54 | 44.98 | 45.41 | 46.47 | 45.90 |
| %Fs | 17.25 | 17.85 | 19.08 | 15.93 | 17.15 | 18.52 |

Composición representativa de ortopiroxenos de las rocas intermedias del CVSSM

| **Muestra** | SLP1720 | SLP1720 | SLP1720 | SLP1720 | SLP1720 | SLP1720 | SLP1710 | SLP1710 | SLP1710 | SLP1710 |
|---|---|---|---|---|---|---|---|---|---|---|
| **Análisis** | B | C | C | C | B | B | B | C | C | B |
| **Unidad** | La Placa | La Placa | La Placa | La Placa | La Placa | La Placa | La Placa | La Placa | La Placa | La Placa |
| **Roca (TAS)** | Andesita | Andesita | Andesita | Andesita | Andesita | Andesita | Andesita | Andesita | Andesita | Andesita |
| $SiO_2$ | 53.346 | 53.21 | 53.527 | 54.086 | 52.994 | 52.868 | 52.93 | 54.039 | 53.918 | 54.449 |
| $TiO_2$ | 0.488 | 0.425 | 0.325 | 0.331 | 0.368 | 0.397 | 0.404 | 0.486 | 0.197 | 0.232 |
| $Al_2O_3$ | 3.625 | 2.664 | 1.678 | 2.38 | 2.994 | 2.254 | 2.761 | 2.917 | 2.713 | 2.588 |
| $Fe_2O_3^t$ | 11.641 | 11.513 | 11.605 | 10.137 | 10.858 | 14.717 | 20.453 | 19.366 | 9.831 | 10.569 |
| MnO | 0.21 | 0.178 | 0.21 | 0.197 | 0.198 | 0.283 | 0.023 | -0.012 | 0.212 | 0.19 |
| MgO | 28.397 | 29.712 | 29.743 | 30.998 | 29.802 | 27.648 | 5.059 | 5.573 | 30.657 | 30.669 |
| CaO | 2.874 | 1.698 | 1.896 | 1.323 | 1.797 | 1.493 | 1.218 | 1.486 | 1.672 | 1.727 |
| $Na_2O$ | 0.061 | 0.032 | 0.072 | 0.074 | 0.009 | 0.018 | 0.143 | 0.158 | 0.024 | 0.022 |
| $K_2O$ | -0.009 | -0.007 | 0.006 | -0.001 | -0.009 | 0.01 | 1.418 | 1.195 | 0.01 | -0.002 |
| $P_2O_5$ | 0.024 | 0.028 | -0.003 | 0.014 | 0.017 | 0.024 | 0.072 | 0.078 | 0.028 | -0.003 |
| | 100.657 | 99.453 | 99.059 | 99.539 | 99.028 | 99.712 | 84.481 | 85.286 | 99.262 | 100.441 |
| | | | | | | | | | | |
| %Wo | 5.57 | 3.26 | 3.61 | 2.52 | 3.47 | 2.89 | 5.05 | 6.13 | 3.21 | 3.27 |
| %En | 76.61 | 79.34 | 78.91 | 82.20 | 79.99 | 74.56 | 29.17 | 31.98 | 81.84 | 80.90 |
| %Fs | 17.82 | 17.40 | 17.48 | 15.28 | 16.54 | 22.55 | 65.79 | 61.89 | 14.95 | 15.82 |

Composición representativa de clinopiroxenos de las rocas básicas del CVSSM

| **Muestra** | SLP1713 | SLP1713 | SLP1713 | SLP1713 | SLP1713 | SLP1713 | SLP1713 |
|---|---|---|---|---|---|---|---|
| **Análisis** | B | B | C | C | C | B | B |
| **Unidad** | Cabras | Cabras | Cabras | Cabras | Cabras | Cabras | Cabras |
| **Roca (TAS)** | Basalto | Basalto | Basalto | Basalto | Basalto | Basalto | Basalto |
| $SiO_2$ | 49.94 | 52.61 | 51.17 | 52.789 | 51.884 | 52.926 | 51.447 |
| $TiO_2$ | 0.544 | 0.478 | 0.468 | 0.426 | 0.415 | 0.532 | 0.462 |
| $Al_2O_3$ | 0.845 | 0.707 | 0.702 | 0.682 | 0.491 | 0.556 | 0.566 |
| $Fe_2O_3^t$ | 20.099 | 20.267 | 17.654 | 17.578 | 19.732 | 21.004 | 22.247 |
| MnO | 0.471 | 0.443 | 0.449 | 0.406 | 0.511 | 0.472 | 0.525 |
| MgO | 17.87 | 21.263 | 22.047 | 21.782 | 22.162 | 21.847 | 20.644 |
| CaO | 7.451 | 4.201 | 5.674 | 5.911 | 3.613 | 2.248 | 3.124 |
| $Na_2O$ | 0.187 | 0.044 | 0.125 | 0.086 | 0.049 | 0.06 | 0.007 |
| $K_2O$ | -0.009 | -0.013 | -0.006 | -0.017 | -0.019 | -0.017 | -0.006 |
| $P_2O_5$ | 0.033 | 0.013 | -0.047 | -0.02 | 0.051 | -0.017 | 0.02 |
| Total | 97.431 | 100.013 | 98.236 | 99.623 | 98.889 | 99.611 | 99.036 |
| | | | | | | | |
| %Wo | 15.43 | 8.43 | 11.26 | 11.78 | 7.20 | 4.56 | 6.31 |
| %En | 51.51 | 59.35 | 60.87 | 60.41 | 61.48 | 61.65 | 58.01 |
| %Fs | 33.06 | 32.23 | 27.87 | 27.81 | 31.31 | 33.79 | 35.68 |

**Tabla A9.- Geotermómetros en equilibrio. Ecuaciones tomadas de Putirka (2008)**

| | |
|---|---|
| **Feldespato-liquido en equilibrio** | $\frac{10^4}{T(K)} = 17.3 - 1.03ln\left[\frac{X_{Ab}^{afs}}{X_{NaO0.5}^{liq} X_{AlO1.5}^{liq} \left(X_{SiO2}^{liq}\right)^3}\right] - 200\left(X_{Ab}^{afs}\right)$ $-2.42\left(X_{NaO0.5}^{liq}\right) - 28.8\left(X_{AlO1.5}^{liq}\right) + 13500\left(X_{CaO}^{liq} - 0.0037\right)^2$ $-550\left(X_{KO0.05}^{liq} - 0.056\right)\left(X_{NaO0.5}^{liq} - 0.089\right) - 0.078P(kbar)$ |
| **Ortopiroxeno-líquido en equilibrio** | $\frac{10^4}{T(K)} = 4.07 - 0.329[P(GPa)] + 0.12\left(H2O^{liq}\right)$ $+0.567ln\left[\frac{X_{Fm2Si2O6}^{opx}}{\left(X_{SiO2}^{liq}\right)^2 \left(X_{FeO}^{liq} + X_{MnO}^{liq} + X_{MgO}^{liq}\right)^2}\right]$ $-3.06\left[X_{MgO}^{liq}\right] - 6.17\left[X_{KO0.05}^{liq}\right] + 1.89\left[Mg\#^{liq}\right] + 2.57\left[X_{Fe}^{opx}\right]$ |
| **Clinopiroxeno-líquido en equilibrio** | $T(°C) = \frac{93100 + 544P(kbar)}{61.1 + 36.6\left(X_{Ti}^{cpx}\right) + 10.9\left(X_{Fe}^{cpx}\right) - 0.95\left(X_{Al}^{cpx} + X_{Cr}^{cpx} - X_{Na}^{cpx} - X_{K}^{cpx}\right) + 0.395\left[\ln\left(a_{En}^{cpx}\right)\right]^2}$ |
| **Líquidos en equilibrio con ol+plg+cpx** | $T(°C) = -583 + 3141\left[X_{SiO2}^{liq}\right] + 15779\left[X_{Al2O3}^{liq}\right] + 1338.6\left[X_{MgO}^{liq}\right]$ $-31440\left[X_{SiO2}^{liq} \cdot X_{Al2O3}^{liq}\right] + 77.67[P(GPa)]$ |